

An unknown input observation approach for torque-sensorless assistance in electric bicycles

Dissertation zur Erlangung des Grades des Doktors der
Ingenieurwissenschaften der Naturwissenschaftlich-Technischen
Fakultät der Universität des Saarlandes

von
Riccardo Mandriota

Saarbrücken
2024

Tag des Kolloquiums: 29.04.2025

Dekan: Prof. Dr.-Ing. Dirk Bähre

Berichterstatter: Prof. Dr.-Ing. Matthias Nienhaus
Jun.-Prof. Dr. Gianluca Rizzello

Akad. Mitglied: Dr. Michael Roland

Vorsitz: Prof. Dr.-Ing. Michael Vielhaber

Acknowledgments

This doctoral thesis was developed during the time that I spent as a scientific researcher at the Laboratory of Actuation Technology (LAT) under the guidance, support, and supervision of Prof. Matthias Nienhaus. I am extremely grateful to him for the opportunity that he gave me to carry on this project and to expand my knowledge. I am also thankful to Prof. Hartmut Janocha for his support and the insightful advice provided during these years.

I wish to extend my gratitude to my friend and mentor Prof. Emanuele Grasso for his guidance and help in the development of this work as well as in all my other publications.

Special thanks also to my friend and colleague Dr. Niklas König. Discussions with him have been fundamental to developing the ideas behind this work and the electric bicycle prototype. I am really thankful to him for his help in difficult times. I wish to extend my sincere thanks to my friend, colleague, and former office mate Dr. Stefano Fabbri for the constructive discussions that we had and the great time we spent together in the past years in Saarbrücken. Many thanks also to my friend and colleague Saeed Farzami. His help was determinant to perform the experimental validation of this work.

I also want to thank my other colleagues at LAT and WELLGO for creating a comfortable and constructive environment. In particular, Dr. Klaus Schuhmacher, Jonah Vennemann, Carsten Klein, and Christopher May for the productive discussions that we had that helped me considerably during the development of this work. I also wish to thank Elke Zarbock for the harmony that she brings at LAT every day.

My sincere gratitude goes also to the students who worked on this project: Marcello de Nicolo, Rosario Gandolfo, and Mohammed Seddik. Special thanks also to all the other people who participated in the survey that I did not mention before: Simon Nimsgern, Daniel Becker, Justin Lambert, Roxanne Bohgdjalian, Sahil Sihag, Till Schlüter, Alessandro Erba, and Eric Peleikis. Also, many thanks to Patrick Christoffell and Maximilian Junk for developing the electric bicycle motor board and to my friend Ivan Funaro for gifting me the bicycle I used as prototype.

Special thanks go to all my other friends here in Germany and Italy for making my life easier, lighter, and funnier.

I also wish to thank my parents Domenico and Mariarosaria, my sister Raffaella, my aunt and uncle Mara and Saverio, and my grandfather Nino for their support and encouragement during good and bad times. I dedicate this work to them and all my other grandparents Lella, Raffaella, and Giuseppe for their unconditional support in my entire life that made this goal and the previous ones possible.

Eventually, I would like to extend my dedication and express my gratitude to Lucía for her continued love and for the enormous support and encouragement that she gives me every day.

Riccardo Mandriota

Abstract

Nowadays, to counteract global warming, reduce air pollution, and traffic congestion in our cities, worldwide government policies are promoting light electric vehicles as viable means of transportation. Among them, electric bicycles may also be helpful to encourage physical activity at reduced effort levels compared to standard cycling or for rehabilitation purposes. Nevertheless, high costs make them not affordable to a large part of the population. To reduce prices and simplify the vehicle mechanical design, electrical assistance control strategies that avoid the installation of expensive torque sensors have received particular attention in the last decade. These strategies are based on the pedaling torque estimation employing unknown system input or disturbance estimation approaches. This work lies in this field and proposes a state observation approach based on Kalman filtering to estimate the cycling torque and provide electrical assistance accordingly. In particular, two different pedaling torque models are analyzed highlighting the necessity of an improved mathematical description to enhance the system performances. The proposed approaches based on the bicycle longitudinal dynamics model and in-vehicle measurements are later validated in a realistic riding environment characterized by variable slopes and curves. From this analysis, it emerges that a pedaling effort reduction similar to the one obtainable when employing a torque sensor is achievable especially when an enhanced pedaling modeling is considered.

Kurzzusammenfassung

Um der globalen Erwärmung entgegenzuwirken, die Luftverschmutzung zu reduzieren und die Verkehrsstaus in unseren Städten zu verringern, fördern die Regierungen weltweit die Nutzung von leichten Elektrofahrzeugen als praktikables Transportmittel. Elektrofahrräder können auch dazu beitragen, die körperliche Aktivität bei geringerer Anstrengung im Vergleich zum normalen Radfahren zu fördern oder zu Rehabilitationszwecken eingesetzt werden. Aufgrund der hohen Kosten sind sie jedoch für einen großen Teil der Bevölkerung nicht erschwinglich. Um die Preise zu senken und die mechanische Konstruktion des Fahrzeugs zu vereinfachen, wurde in der letzten Dekade besonderes Augenmerk auf Strategien zur Regelung der elektrischen Unterstützung gelegt, die den Einbau von teuren Drehmomentsensoren vermeiden. Diese Strategien basieren auf der Schätzung des Pedaldrehmoments unter Verwendung von Ansätzen zur Schätzung unbekannter Eingangsgrößen oder Störungen. Die vorliegende Arbeit ist in diesem Bereich angesiedelt und schlägt einen Ansatz zur Zustandsbeobachtung auf der Grundlage der Kalman-Filterung vor, um das Drehmoment beim Radfahren zu schätzen und eine entsprechende elektrische Unterstützung anzubieten. Insbesondere werden zwei verschiedene Modelle des Pedaldrehmoments analysiert, wobei die Notwendigkeit einer besseren mathematischen Beschreibung des Pedaldrehmoments zur Verbesserung der Systemleistung hervorgehoben wird. Die vorgeschlagenen Ansätze, die auf dem Modell der Fahrradlängsdynamik und fahrzeuginternen Messungen basieren, werden dann in einer realistischen Fahrumgebung mit variablen Steigungen und Kurven validiert. Aus dieser Analyse geht hervor, dass eine ähnliche Reduzierung der Pedalleistung bei der Verwendung eines Pedaldrehmomentsensors erreicht werden kann, insbesondere wenn eine verbesserte Pedaliermodellierung berücksichtigt wird.

Abbreviations

AC	Alternating Current
ADC	Analog-to-Digital Converter
APPR	Average Pedaling Power Reduction
BDC	Bottom Dead Center
BEMF	Back ElectroMotive Force
BLDC	BrushLess Direct Current Motor
BMS	Battery Management System
BPF	Band-Pass Filter
BSU	Bicycle Supervision Unit
CAN	Controller Area Network
CoG	Center of Gravity
CPTO	Constant Pedaling Torque Observer
DAC	Disturbance Accommodation Control
DC	Direct Current
DOB	Disturbance OBserver
EKF	Extended Kalman Filter
FOC	Field Oriented Control
FLC	Fuzzy Logic Controller
GNSS	Global Navigation Satellite System
HDMI	High Definition Multimedia Interface
IM	Induction Motor
IMU	Inertial Measurement Unit
IMUB	Inertial Measurement Unit Board
KF	Kalman Filter
LAT	Laboratory of Actuation Technology
Li-Ion	Lithium-Ion Battery
LPF	Low-Pass Filter

MCU	Motor Control Unit
MEMS	Micro-ElectroMechanical System
MOSFET	Metal-Oxide-Semiconductor Field-Effect Transistor
MPPR	Maximum Pedaling Power Reduction
NRMSE	Normalized Root Mean Square Error
PAS	Pedal-Assist System
PDU	Power Distribution Unit
PEDELEC	Pedal Electric Cycle
PER	Pedaling Energy Reduction
PID	Proportional-Integral-Derivative
PMSM	Permanent Magnet Synchronous Motor
PTO	Pedaling Torque Observer
PWM	Pulse Width Modulation
RC	Repetitive Controller
RFO	Reaction Force Observer
RL	Reinforcement Learning
RLS	Recursive Least Squares
RMSE	Root Mean Square Error
RTPM	Real-Time Power Mapping
SoC	State of Charge
SPI	Serial Peripheral Interface
SPTO	Sinusoidal Pedaling Torque Observer
SRM	Switched Reluctance Motor
SynRM	Synchronous Reluctance Motor
TDC	Top Dead Center
TF	Torque Filling
UIO	Unknown Input Observer
UKF	Unscented Kalman Filter
USB	Universal Serial Bus

Contents

1	Introduction	9
1.1	Electric bicycle sensorless control	10
1.1.1	Unknown input or disturbance observation	11
1.1.2	Pedaling torque estimation state of the art	12
1.2	Contributions of the work	14
1.3	Structure of the work	16
2	Electric bicycles	19
2.1	Design	19
2.1.1	System domain	20
2.1.2	Mechanical domain	22
2.1.3	Electrical domain	24
2.2	Pedaling torque sensors	26
2.3	Control strategies	30
3	Mathematical modeling of bicycle dynamics	35
3.1	Bicycle longitudinal dynamics	35
3.1.1	Driving forces	36
3.1.2	Pedaling torque	42
3.1.3	Motor torque	44
3.1.4	Gravity force	46
3.1.5	Rolling friction force	47
3.1.6	Aerodynamic drag force	48
3.1.7	Bump force	49
3.1.8	Braking force	50
3.1.9	Global considerations	50
3.2	Resisting forces sensitivity analysis	51
4	Pedaling torque estimation	57
4.1	State observation theory	57
4.1.1	State-space models and observability	57
4.1.2	Kalman filtering	60
4.2	Pedaling torque observers	63
4.2.1	Modeling hypotheses	63
4.2.2	State-space models	64
4.2.3	Kalman filtering	67
4.2.4	System observability proof	69
4.3	Pedaling torque observers inputs and measurements	70
4.3.1	Motor torque	70
4.3.2	Road slope	70

4.3.3	Bicycle speed	78
4.4	Pedaling torque observers simulation	78
4.4.1	Effect of Kalman filter tuning	79
4.4.2	Effect of modeling simplifications	85
4.4.3	Effect of parametric variations	89
4.4.4	Considerations	92
5	Experimental results	97
5.1	Bicycle prototype	97
5.1.1	System description	97
5.1.2	Mechanical design	98
5.1.3	Electrical design	99
5.2	Road slope estimation	100
5.2.1	Kalman filter tuning	101
5.2.2	Level ground riding	104
5.2.3	Variable sloped environment	105
5.2.4	Riding in a curve	106
5.3	Torque-sensorless control	108
5.3.1	Pedaling torque observers tuning	109
5.3.2	Pedaling torque estimation analysis	114
5.3.3	Riding performance analysis	119
5.3.4	Qualitative analysis	132
5.3.5	Final considerations	135
6	Conclusions and outlooks	137
6.1	Content summary	137
6.2	Conclusions	137
6.3	Outlooks	139
7	Appendix	143
7.1	IMU calibration and mounting offset correction	143
7.2	Prototype control electronics description	145
8	List of symbols	151
	Bibliography	157

1 Introduction

The invention of the first bicycle is attributed to the German Baron Karl von Drais from Mannheim in 1817. This vehicle was the first two-wheeled vehicle that allowed the rider to keep balance thanks to a steerable front wheel. From this initial invention, which was forbidden in many countries due to its riskiness in 1821, bicycles have progressively evolved into safer and more efficient vehicles. Pedals were added to the front wheel and higher speeds were achieved thanks to the advent of tension-spoked wheels in the late 1860s. About twenty years later, safety and riding comfort were enhanced when inventions in the field of pneumatic tires and chain drives made bicycles with wheels of the same diameter possible. [1]

At the same time, progress in the electrical machines field brought the idea of electrifying a bicycle to increase its reachable speed and reduce riding efforts. The first inventions in the electric bicycle field took place in the USA in 1895 when Odgen Bolton patented the first electric bicycle [2]. It was a vehicle with a 10 V battery and a six-pole hub brushed Direct Current (DC) motor mounted on the back wheel. One year later, Charles Theryc created the first bicycle planetary-gear DC motor [3] and in 1899, John Schnepf invented the first friction drive where the motor power was transmitted to the back wheel through a concentric roller [4]. For almost a century, the provided motor assistance was independent on pedaling, until in 1982 the German Egon Gelhard developed the first electric bicycle in which the rider is helped by the electrical traction of the engine only when pedaling [5]. However, only in 1993 this kind of bicycle began gaining notoriety thanks to the Japanese company *Yamaha* commercially spreading the vehicles with the name of *Pedal-Assist System* (PAS). These bicycles, relying on torque and speed sensors, were capable of electrically assisting the rider with a human power amplification of 200 % up to $15 \frac{km}{h}$ and a gradual reduction to 0 % at $24 \frac{km}{h}$. Later on, these bicycles were named *Pedal Electric Cycles* (Pedelects) [1]. In the 1990s, many sensors and control strategies for electric bicycles were developed as well as new kinds of more durable batteries. In 2005, with the boom of lithium batteries, a reduction of weight and increased electrical autonomy was achieved. Therefore, the innovations in the battery field caused a sudden growth in the electric bicycle market. In 2009, more than 21 million electric bicycles were circulating in China outnumbering cars (9.4 million). Later in 2015, worldwide electric bicycle sales amounted to 40 million, 90 % of them in China [5]. In the last decade, easy-to-install kits that allow the conversion of standard bicycles into electric bicycles started gaining popularity contributing to an increase in this booming market. The first all-in-wheel conversion kit was patented by researchers of the Massachusetts Institute of Technology in 2015 and named *Copenhagen Wheel* [6]. This spoked-wheel integrates a motor, a battery, the controller, and the necessary sensors. Thanks to the ongoing green revolution, the electric bicycle market is rapidly growing. In 2021, the worldwide market reached 25 billion USD with an expected annual growth rate of circa 10% between 2021 and 2028 [7].

There is a wide range of assets associated with the popularization of electric bicycles.

Several studies have shown the physical and psychological benefits of electric cycling on health [8]. Since the efforts required by cycling might not always be sustainable for the elderly or people with physical problems, electric bicycles could be employed to encourage exercise and to rehabilitate [9, 10]. Electric bicycle employment can encourage long-distance commuting, decrease traffic congestion, and improve the air quality in our cities. Switching to bicycles can save insurance, registration, licenses, and parking costs. As shown in [11], riding an electric bicycle reduces the energy cost per distance traveled compared to other means of transportation. Worldwide government policies support the circulation of light electric vehicles such as electric bicycles and scooters to reduce fuel consumption, air pollution, and global warming [12]. However, the population acceptance of electric bicycles is limited by safety, vehicle weight, battery autonomy, and weather dependence concerns. Other factors that discourage the adoption of electric bicycles are the short-term reliability of the electronics, the difficulties in reparation of proprietary electronic systems, and the short life of the batteries that degrade even when not used. Furthermore, the cost of electric bicycles can represent a barrier to accessing them by part of the population.

The price of electric bicycles depends on their design since electrical assistance can be provided in different ways according to the type of motor, sensors, and controller mounted on them. However, there are limitations on the maximum power and speed at which the bicycle can be electrically powered that vary from country to country. For example, in the EU, “*pedal cycles with pedal assistance which are equipped with an auxiliary electric motor having a maximum continuous rated power of less than or equal to 250 W, where the output of the motor is cut off when the cyclist stops pedalling and is otherwise progressively reduced and finally cut off before the vehicle speed reaches 25 $\frac{km}{h}$* ” do not need approval and thus a plate number [13]. In the USA, the regulations are less strict but differ between the federal states. Moreover, there can be limits on the maximum vehicle weight, like in China, where the limit is 40 kg, or on the allowed kind of assistance, like in Japan and the EU, which admit only pedelecs. Therefore, torque and cadence sensors are installed to control the motor power and verify that the electrical assistance respects the regulations.

These sensors cannot be always easily mounted on a bicycle. Their installation often requires a proper design of the bicycle frame depending on their space requirement and working principles. Moreover, they are typically mounted on parts of the bicycle where the pedaling force, vibrations, and external shocks are directly applied. Consequently, these sensors must be designed to be robust to mechanical stress determining the increase in their cost. High-quality sensors can cost around 10 - 15 % of the overall cost of an electric bicycle. Therefore, in recent years, research in the field of *sensorless* control for electric bicycles has been conducted with the focus on providing motor electrical assistance without relying on sensor measurements reducing the cost of an electric bicycle without losing assistance capability and decreasing the riding safety.

1.1 Electric bicycle sensorless control

The term *sensorless* or *torque-sensorless* control in the electric bicycle field refers mainly to pedelec control strategies that provide electrical assistance without employing a torque sensor to measure the pedaling input. However, it has to be remarked that this definition refers only to the removal of torque-sensing elements. Low-cost sensors such as current, rotor

position, speed sensors, or Inertial Measurement Units (IMUs) are still required to estimate the human input and electrically aid the cyclist. The main purpose of electrical assistance in electric bicycles is to reduce cycling efforts. This means that a rejection or reduction of the effect of external disturbances acting on the bicycle dynamics such as gravity and friction and an amplification of the cycling torque must be achieved. To amplify the human input avoiding the employment of an expensive torque sensor, pedaling torque estimation techniques are required. The assumption on which these methods are based consists of considering human cycling as an unknown input or disturbance acting on the system that needs to be extracted from the total disturbance acting on the vehicle dynamics. Following, a historical overview of disturbance estimation approaches is provided. Then, the problem of unknown input estimation is particularized to the case of electric vehicles and specifically to the pedaling torque in electric bicycles.

1.1.1 Unknown input or disturbance observation

The first attempts to estimate unknown or unmeasured inputs can be dated back to 1970 when Bryson and Luenberger [14] proposed a state observer able to estimate an unknown bias error augmenting the state of the system with a zero-order model of the disturbance, i.e. considering the derivative of the disturbance equal to zero. Three years later, this concept was extended in the work of Meditch and Hostetter [15] that proposed Unknown Input Observers (UIOs) to estimate unknown non-constant inputs whose variations are slow relative to the natural response of the observer. In the same years, Johnson proposed an optimal robust controller, called Disturbance Accommodation Controller (DAC), that allows set-point regulation in the presence of a broad class of realistic external disturbances [16]. In particular, the author described the external disturbance employing a differential equation, the so-called disturbance state modeling, showing that the effectiveness of DACs is dependent on how well the disturbances are described by the employed model. Nevertheless, due to the mathematical complexity of the DAC, the practical significance of these results was not noticed in those years [17]. In 1983, Ohnishi first proposed the Disturbance Observer (DOB) to estimate external disturbances using a reduced-order observer and optimal control to suppress plant uncertainties [18]. The great advantage of this approach consists in shifting the disturbance analysis from the time to the frequency domain. This allows a simple description of the disturbance estimation dynamics as the bandwidth of a Low-Pass Filter (LPF). Later, the same author formalized the 2-degrees-of-freedom structure of the DOB in the Laplace domain [19, 20]. Nevertheless, as shown in [17, 21, 22], a DOB can be expressed in the Laplace domain or with a state-space representation. In fact, since there exist infinite state variable realizations of a transfer function, the first is a generalization of the second. For the sake of clarity, although conceptually identical, disturbance estimation methods expressed in the Laplace domain will be referred to as DOBs whereas approaches that employ state-space representations will be called UIOs in this thesis. In the first works on DOBs, the method was applied to the field of brushed DC motors [18, 23] and multi-degree of freedom manipulators control [19] to estimate and compensate the effects of external load forces. These works show how the compensation of the estimated external disturbance obtained with a DOB improves the dynamic performances of feedback control loops even in the presence of model parametric variations. Later, Murakami proposed a DOB-based technique that allows force or torque estimation employing simultaneously two DOBs. One

of them achieves the robustness of the feedback control loop like a classical DOB and the other, the so-called Reaction Force Observer (RFO), estimates the contact forces avoiding the employment of force sensors [24]. Nevertheless, the RFO has a model-based control structure that deteriorates the force estimation accuracy when external disturbances such as gravity, friction, and model parametric variations are not correctly identified [25]. In the early 2000s, disturbance estimation approaches were applied to electrical-assisted vehicles such as electric wheelchairs [26, 27] and electric bicycles [28, 29] to estimate and compensate environmental disturbances affecting the vehicle dynamics such as friction and gravity. In other works, disturbances are estimated in steer-by-wire systems [30] or in self-sustaining control of bicycles [31, 32].

1.1.2 Pedaling torque estimation state of the art

In the last decade, disturbance estimation approaches were applied in the electric bicycle field to estimate the pedaling torque and provide electrical assistance accordingly. In all methods known in the literature, the extraction of the pedaling torque from the total disturbance torque acting on the bicycle dynamics requires the employment of a pre-measured or estimated dynamic model of the vehicle whose accuracy affects the correctness of the human input estimation. Moreover, models of different complexity may be employed to describe the pedaling torque. Therefore, in the following, a classification of the torque-sensorless approaches based on the employed disturbance modeling is proposed. Figure 1.1 contains a timeline of electric bicycle sensorless control strategies based on this classification. Two main categories can be defined:

- Constant pedaling torque model;
- Periodic pedaling torque model.

Constant pedaling torque model:

Methods that employ a constant pedaling torque model can be further divided depending on the utilized estimation method in DOBs, RFOs, and UIOs. Among DOB-based estimation approaches, the work of Sankaranarayanan and Ravichandran [33] estimates the human input using only one DOB. However, this simple structure allows the pedaling torque estimation solely when the environmental forces are negligible. More complexity is introduced by Kawajiri et al. [34], who proposed a pedaling torque estimation for a dual motors power-assisted bicycle. This work employs two DOBs to estimate external disturbances on the front and rear wheels combined with a Recursive Least Squares (RLS) algorithm that evaluates the ratio between the reaction forces on the front and rear wheels to extract the applied pedaling torque. However, this method employs two motors, two rotary encoders, and an accelerometer increasing system complexity and costs. Li et al. [35] proposed an estimation strategy, still not experimentally validated, that determines the human torque by analyzing the dynamics of the crankset mechanism relying on IMU measurements to extract the angular speed of the rotating parts of the system. Additionally, a DOB estimates and compensates for environmental disturbance forces acting on the vehicle dynamics.

RFO-based estimation methods such as the work of Cheon and Nam [36] implement an inner DOB to estimate and reject the total external disturbance acting on the motor, whereas

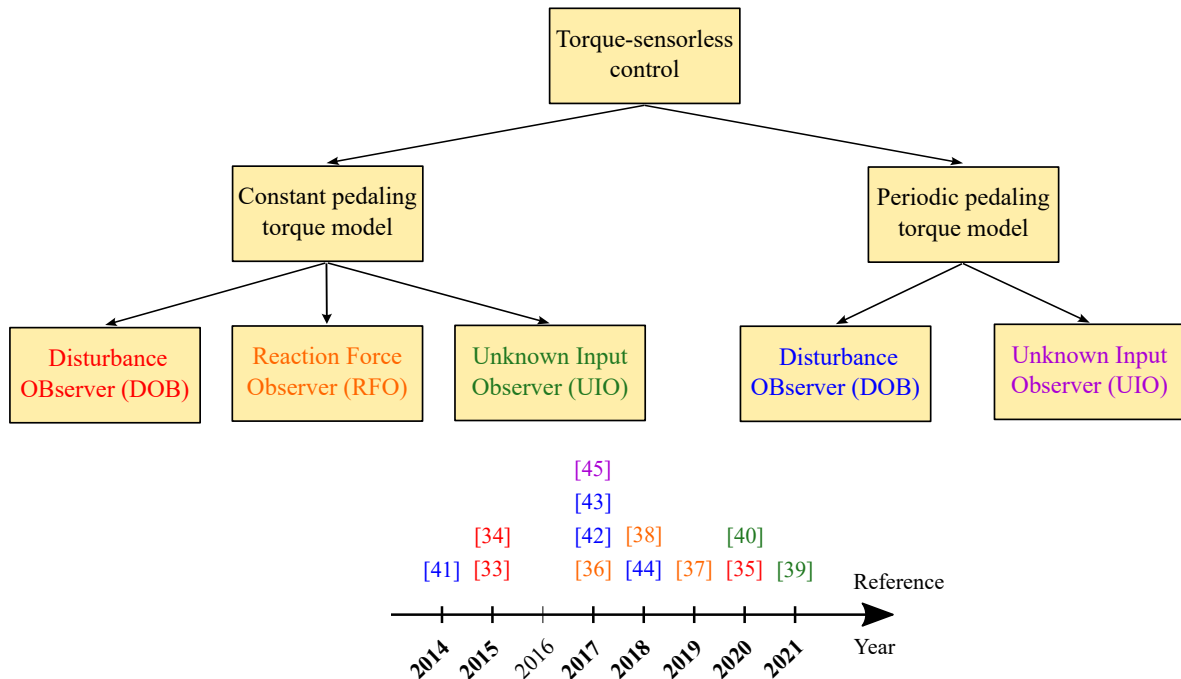


Figure 1.1: Classification and timeline of electric bicycles torque-sensorless control strategies.

the outer one, called RFO, estimates the pedaling torque thanks to its lower bandwidth tuned according to pedaling torque frequency considerations. Then, the estimated torque is used to generate the speed reference for a feedback control loop in a model impedance control. Although the method minimizes the speed tracking error, the accuracy of the pedaling torque estimation is guaranteed purely when the environmental components are known or negligible. Likewise, in Padmagirisan et al. [37], the method proposed in [33] is enhanced with a Band-Pass Filter (BPF) that allows the extraction of the human contribution from the total disturbance torque. Nevertheless, the work lacks a pedaling torque estimation validation in realistic scenarios. A similar approach that employs a BPF as RFO to extract the pedaling torque from the total disturbance torque is proposed by Li et al. in [38]. Differently from [37], this work utilizes another mathematical formulation and bandwidth of the RFO.

The estimation of the pedaling torque relying on UIOs has been already investigated by the author of this thesis in [39] where the pedaling torque is extracted from the motor load torque estimated with a Kalman Filter (KF) under laboratory riding conditions. Misgeld et al. [40] estimate the pedaling torque by combining an Unscented Kalman Filter (UKF) with the road slope information obtained from an adaptive orthogonal filter that takes as input the three-dimensional accelerations and angular velocities measured with an IMU. Nevertheless, the experimental results of both UIO-based works show that they can only approximately estimate the average value of the pedaling torque.

Periodic pedaling torque model:

As previously stated, utilizing a more detailed disturbance modeling can improve the accuracy of the estimation. Hence the idea of exploiting the pseudo-periodicity of the pedaling

torque to extract it from the total estimated environmental torque obtained either with a DOB or an UIO. This approach was first applied to electric bicycle sensorless control in the work of Fujimoto et al. [41] that employs a pedaling torque estimator based on Fourier analysis of the total disturbance torque given by a DOB. However, in the proposed approach, the torque cannot be estimated in real-time during the first pedaling cycle since the output of the DOB in the previous cycle is used to perform a Fourier analysis and extract the pedaling torque. Moreover, the work neglects the effect of gravity on vehicle dynamics. Therefore, other works of the same authors [42, 43] consider the environmental conditions employing a RLS with multiple forgetting factors to estimate the external disturbances online. In [44], the authors propose methods to improve the estimation during the first pedaling cycle. Nevertheless, all these works based on the Fourier analysis estimate only the pedaling torque approximately with a significant performance degradation when the estimated torque is employed to provide the electrical assistance.

Hatada et al. [45] considers the periodicity of the pedaling torque to distinguish it from the environmental disturbance components. Here, the periodic DOB for varying frequency first proposed by Narikiyo et al. in [46] is applied to the case of electric bicycles. The basic idea of this work is to model the disturbance as the sum of a sine with variable frequency plus a bias. The proposed periodic disturbance estimation relies on a state augmentation of a Luenberger observer plus an online pedaling frequency estimation obtained with an adaptive notch filter. Thus, this method can be considered an UIO that employs a periodic pedaling torque model.

1.2 Contributions of the work

Although several torque-sensorless approaches for pedelecs have been proposed in the last decade, there are still extensive improvement prospects. As seen in the previous section, the pedaling torque estimation problem has been addressed in the literature relying on DOBs, RFOs, or UIOs. Among them, this work focuses on UIO utilization, namely on state observation approaches. Following, the contributions of this work are reported:

- **Electric bicycle design analysis:** The comprehension of the torque-sensorless pedelec system requires knowledge of the components, sensor technologies, and control strategies commonly utilized in standard electric bicycles. In this work, a thorough analysis is presented. Moreover, a novel classification of control strategies commonly used in electric bicycles is proposed. These control strategies are typically classified based on the sensor used to measure the human input and provide electrical assistance. However, this gives only general information for the final user and does not provide sufficient information for the control system designer. Therefore, to address this problem, a classification based on the control strategy optimization focus is here proposed.
- **Bicycle longitudinal dynamics generalization:** The generation of the sensorless electrical assistance is based on the analysis of the bicycle longitudinal dynamics. However, in the majority of the works, the employed mathematical model depends on the design characteristics of the specific employed motor assembly and loses its validity in the case of other system configurations. Thus, in this work, a mathematical

generalization of the vehicle dynamic model valid for mid-drive, hub, and friction motor electric bicycle assemblies is proposed.

- **Variable environmental and riding conditions:** The majority of the literature limits the analysis to specific environmental and riding conditions. Many works neglect indeed the effects of variable inclines on the offered electrical assistance. The effects of system parametric variations including variable mass and friction conditions are also often ignored. Furthermore, the impact of variable wind conditions and bumps is also usually disregarded. Additionally, propulsive human forces not applied at the pedals are never considered. In this work, all the aforementioned components are taken into account in bicycle modeling. Moreover, their impact on the vehicle motion is discussed through a sensitivity analysis to derive a simplified mathematical model that allows torque-sensorless assistance. Afterwards, the validity of these assumptions is extensively analyzed using simulations and experimental results performed in a real scenario.
- **Pedaling torque model complexity analysis:** A comparison of the pedaling torque estimation and electrical assistance performances obtained when relying on a constant or periodic pedaling torque modeling is still missing in the literature. Indeed, the advantages and disadvantages of increasing the unknown input or disturbance model complexity have still not been discussed in this field. Therefore, in this work, two pedaling torque estimation methods, named Pedaling Torque Observers (PTOs), that rely either on a Constant (CPTO) or a Sinusoidal (SPTO) human input description are mathematically formalized and compared.
- **UIO selection and tuning:** Differently from DOB approaches, the tuning of UIOs is usually more complex and requires deeper control theory knowledge. While the former can be easily tuned by selecting the bandwidth of a LPF based on considerations on the typical cycling frequency, in UIOs a more complex pole placement is often required, like in [45] where a complicated tuning of a Luenberger observer is described. Moreover, as discussed in [40], to handle the bicycle dynamic model nonlinearities, the employment of a nonlinear state observation approach is necessary. Among the possible approaches, an Extended Kalman Filter (EKF) has been selected in this work because of its capacity to easily handle nonlinear systems through a linearization around the nominal state trajectory. Since in the case of non-severe nonlinear systems, like the one under investigation, the linearization error can be considered negligible, the employment of an EKF represents a simple and comprehensible solution to the problem. Moreover, this work provides intelligible guidelines on the selection of the filter covariance matrices, based on the confidence on the model and the measurements, to maximize the estimation performances.
- **Simplified road slope estimation:** Among the environmental components that act on the vehicle dynamics, the effects of variable road slopes are known to have the highest impact [11]. Therefore, to obtain acceptable torque-sensorless assistance performances in a variable sloped environment, an estimation of the road angle is necessary. This is typically achieved by relying on inertial measurements and complex estimation algorithms. The importance of accomplish an online low-cost and low-computational-effort road slope estimation is pointed out in this work. In particular, here the problem

is addressed by utilizing a KF based on the wheel speed and a reduced set of inertial measurements obtained with a low-cost IMU.

- **Electrical assistance analysis:** Many works do not present a clear comparison of the electrical assistance performance obtained with torque-sensorless and sensed techniques. The analysis is usually limited to the minimization of the pedaling torque estimation error using torque sensors to perform the validation. In many cases, a metric to evaluate the quality of the received electrical assistance is missing. Additionally, the cycling feeling in torque-sensorless pedelecs, expressed in terms of experienced assistance delays, received undesired aid, or global safety sensation has never been investigated. Therefore, this work proposes a method to evaluate the generated torque-sensorless electrical assistance performance based on the delivered pedaling power and energy reduction. Moreover, for the first time in this field, user-dependent quantities are evaluated through a survey. In each condition, the assistance obtained with and without pedaling torque sensor are compared.

1.3 Structure of the work

In this section, the structure of the work and the content of each chapter is explained in detail.

To get a full understanding of torque-sensorless control, a general description of the electric bicycle system components is given in Chapter 2. In particular, functionality and selection criteria are analyzed to evaluate their influence on the global system performances and costs. Furthermore, a deep analysis of the technologies used in the commercial torque sensors employed to control electric bicycles is provided. This clarifies the importance of switching to torque-sensorless solutions to reduce the final cost of the system. Moreover, a novel classification of the main strategies known in the literature employed to control electric bicycles is proposed in this work. Such a working framework provides the necessary background and guidelines to the electric bicycle system designer and specifically to the developer of torque-sensorless control methods.

Among the possible models employable to mathematically describe the motion of a bicycle, the necessity of limiting the analysis to the longitudinal one is pointed out in Chapter 3. Then, the force components that characterize the vehicle longitudinal dynamics are deeply analyzed by considering the typical electromechanical configurations of the system. Moreover, a mathematical description of the human forces interacting when riding a bicycle is given. Finally, a sensitivity analysis that provides a complete understanding of the impact of the various components operating on the bicycle longitudinal dynamics at different vehicle speed levels is also presented.

In Chapter 4, after a brief introduction to state observation theory, the PTOs expressed in the form of EKFs are described. Firstly, the assumed modeling simplifications, based on the indications provided by the sensitivity analysis, are derived. Then, the mathematical framework on which the PTOs are based is presented and deeply analyzed. Particular focus is given to inputs and measurements of the state observers since their accuracy is fundamental for improving the quality of the torque estimation. In particular, the importance of an accurate online road slope estimation is highlighted. A KF is here proposed as a possible

low-cost approach to accomplish this purpose. Then, a method to compensate for slope estimation errors caused by modeling simplifications while cornering is also presented. Afterwards, the effectiveness of the PTOs is evaluated in simulation to provide guidelines on the KF tuning and point out the impact of modeling simplifications and parametric variations on the pedaling torque estimation.

An experimental validation of the proposed torque-sensorless control for pedelecs is presented in Chapter 5. After describing and motivating the choices made in the design phase of the pedelec prototype utilized in this analysis, the proposed road slope estimation approach performances are validated with outdoor tests. Here, a particular focus is given to the tuning of the KF and the estimation error in the presence of vehicle accelerations and rapid road angle variations. Then, the proposed PTOs are analyzed. In particular, the tuning of the algorithms and the torque estimation performances are evaluated in different scenarios. Afterwards, the torque-sensorless control performances expressed in terms of delivered power and energy reduction are compared to the ones achieved when using a torque sensor on a defined testing track. Finally, a user-oriented analysis carried out utilizing a survey is presented. The latter gives indications about the riding feeling of the proposed sensorless control approaches compared to the sensor-based one.

Conclusions that summarize the results obtained in this work are drawn in Chapter 6. Eventually, the outlooks on possible system and performance improvements of the proposed torque-sensorless approaches are presented.

The appendix to this work provides a detailed description of the IMU calibration and mounting offset correction processes as well as the electronics utilized in the developed pedelec prototype. Also, the reader can find the questionnaire used in the performed torque-sensorless control survey.

2 Electric bicycles

The understanding of electric bicycle sensorless control requires a deep analysis of the design characteristics of the mechatronic system. In the following, the functionality of the single components that make up an electric bicycle and their design criteria are evaluated to analyze their impact on the system performance, reliability, safety, maintenance, and costs. Afterwards, the sensors employed to measure the human input are analyzed to highlight assets and drawbacks of the different torque sensor technologies in the electric bicycle field. Then, the control strategies commonly employed to provide electrical assistance in electric bicycles are thoroughly analyzed. In particular, this thesis proposes a novel classification of pedelec control strategies based on the control system focus.

2.1 Design

The parts that constitute an electric bicycle can appear in different configurations. Each configuration has its assets and drawbacks that will be discussed in this section. The elements that compose the electric bicycle system are divided into battery, electric motor, sensors, controller, and the bicycle itself. The battery transforms chemical energy into electrical energy. Afterwards, the motor turns this energy into mechanical energy to assist the bicycle motion. Then, sensors like throttle, cadence, torque, and brake sensors measure human inputs. Eventually, the outputs of the sensors are sent to the controller that commands and supervises the entire system. Figure 2.1 contains a generic representation of the above mentioned elements. It has to be remarked, that these elements can be located also in different positions within the bicycle respect to the ones reported in the figure.

Electric bicycle costs can vary considerably depending on the technology, the quality, and the brand of the single components. The most expensive part of the system is typically the battery. Its cost amounts to around 25 % of the overall price. The cost of the motor and the sensors is circa 15 % while the controller value amounts to circa 10 % of the total. The remaining costs are related to the mechanical parts of the bicycle (frame, drivetrain, wheels, tires, etc.). Therefore, removing sensors may decrease the final cost of the product. It is thus worth analyzing techniques that allow bicycle electrical assistance without relying on expensive sensors.

As stated in [47], the design of an electric bicycle is divided into three domains: the system, the mechanical, and the electrical domain. The system design domain relates to the choice of the electric vehicle topology, the type of electrical assistance, and the possibility of recuperating energy while braking. The mechanical domain concerns the motor positioning and its assembly, whereas the electrical domain includes choices about the type of energy storage source, motor, and control strategies. Figure 2.2 provides a synthetic representation of the mentioned design domains that are discussed later in this section.

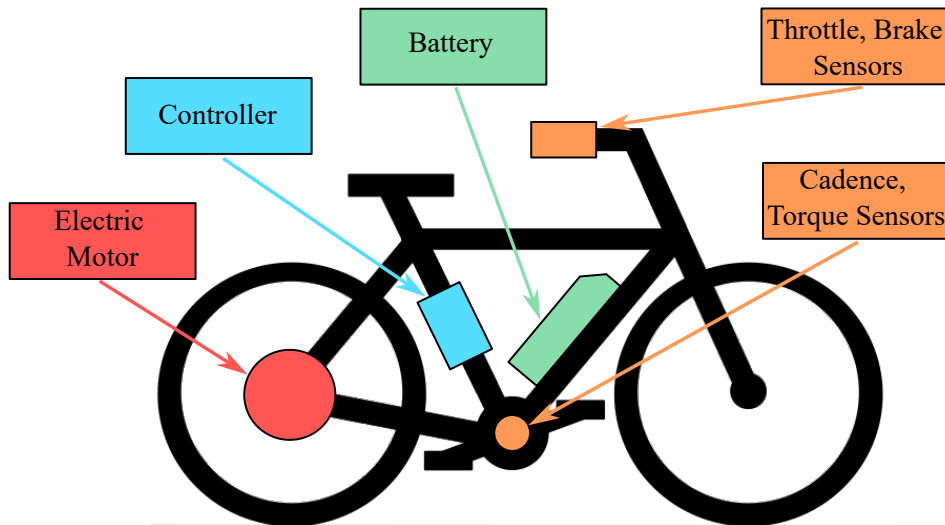


Figure 2.1: Generic representation of the elements that make up an electric bicycle.

2.1.1 System domain

- **Topology:** Considering the system domain, an electric bicycle can be designed following a serial or a parallel topology. Serial electric bicycles are characterized by the absence of a mechanical drivetrain. In these vehicles, human and electric power are coupled in the electrical domain. The pedals are connected directly to a generator electrically coupled with a battery and a motor. An example of a series electric bicycle is the Italian *SeNZA* [48]. The parallel topology is the most common configuration and is thus the one investigated in this work. In such vehicles, human and motor powers are combined in the mechanical domain. The human power is transmitted to the wheel through the pedals and the drivetrain while the electrical assistance of the motor is summed to it. [7]
- **Electrical assistance:** Another important choice in the design of the electric bicycle system is the selection of the electrical assistance strategy. Electric bicycles can be divided into power-on-demand and pedelecs depending on their control approach. In power-on-demand bicycles, the rider requires electrical assistance through a throttle that regulates the motor power by pressing a lever or twisting a grip mounted on the handlebar. Although it represents the easiest and cheapest way to control an electric bicycle, this configuration presents several drawbacks. Riders might tire or feel pain when pressing or twisting the throttle, especially in long-distance travel. In power-on-demand bicycles, the rider is not rewarded with electrical assistance when pedaling. Therefore, these bicycles do not encourage physical activity. On the other hand, pedelecs provide electrical assistance only when the bicycle is pedaled rewarding the rider with motor propulsion that depends on the control strategy and the desired assistance level. To measure the human power input, sensors, such as cadence and torque sensors, are installed increasing the complexity and the costs of the system. The choice of the electrical assistance type depends on the preferences and demands of the user while riding. As previously stated, torque-sensorless approaches aim at re-

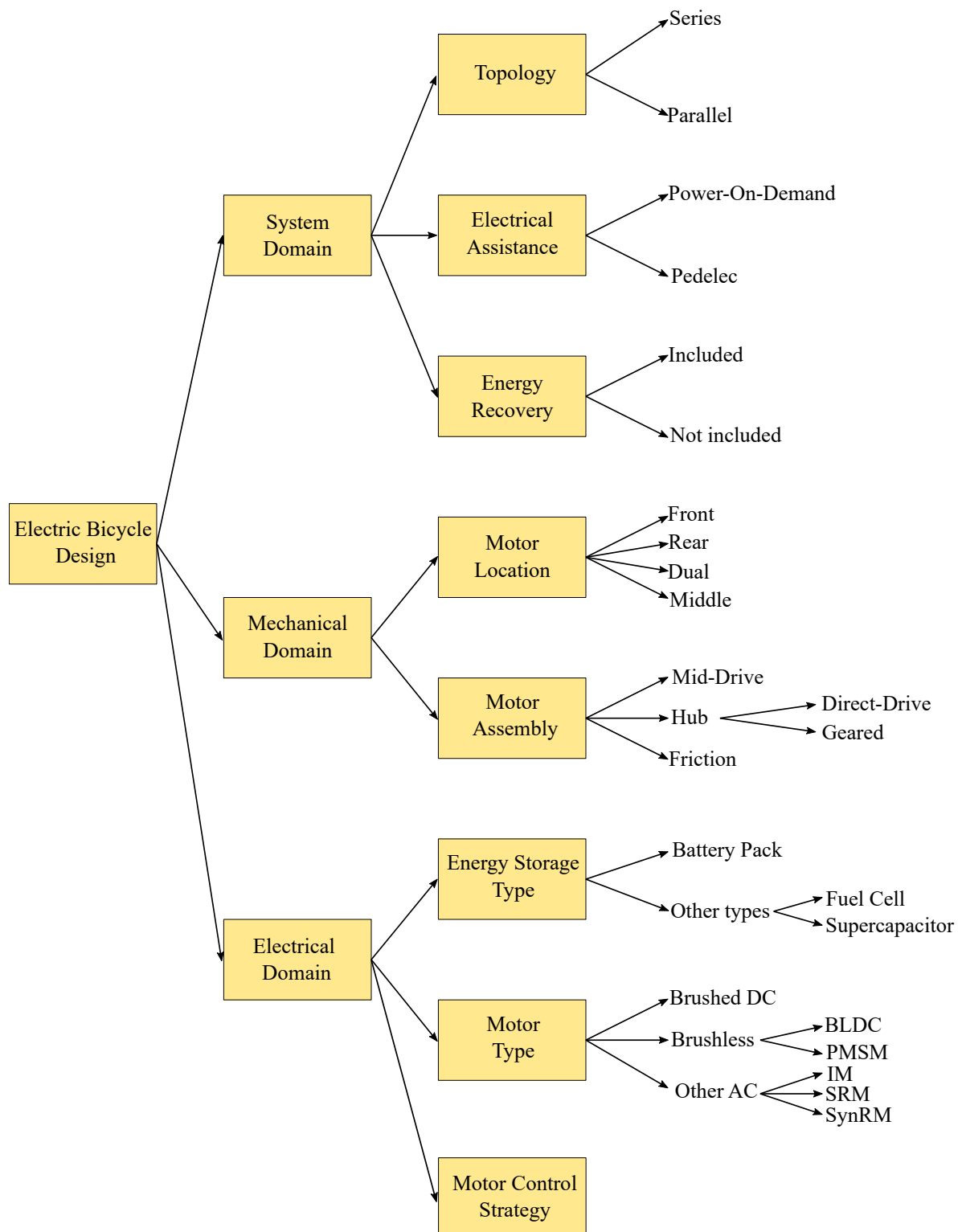


Figure 2.2: Design domains classification used for the project of electric bicycles based on the one proposed in [47].

moving sensing elements in pedelecs. For this reason, this work will limit the analysis only to bicycles that use this kind of electrical aid.

- **Energy recovery:** Another feature that belongs to the system design domain is regenerative braking. Bicycles that integrate this operating mode require electric brakes to sense the brake input of the rider. Electric brakes are standard bicycle brakes that, when actuated, generate an electrical output that is sent to the controller to activate the regenerative mode. In this status, the motor operates as a generator producing a braking electromagnetic torque and energy that can be used to recharge the battery. Regenerative braking has a potential benefit of circa 10 % depending on the individual behavior of the rider and the considered track [49]. Where the potential benefit is defined as the percentage of recovered energy compared to the total input energy (battery plus rider) on a specific track. Furthermore, electric braking reduces the wear of mechanical brakes because they are less stressed in braking operations. However, including regenerative braking requires a non-freewheeling motor and a controller that allows the bidirectional energy flow between the battery and the motor increasing the complexity of the system. Since this work focuses on the sensorless electrical assistance capability rather than the vehicle electrical autonomy, the possibility of recovering energy will not be considered to reduce the system complexity.

2.1.2 Mechanical domain

- **Motor location:** In the mechanical design of an electric bicycle, the first important aspect regards the selection of the motor location. As depicted in Figure 2.3, motors can be mounted in the front or rear wheels, or the middle of the bicycle. Front-wheel motors offer an easier installation because there is no need to check the compatibility between the motor and the drivetrain. Since they can be easily assembled and disassembled, they also simplify maintenance. Furthermore, they have the advantage of providing a better weight distribution of the bicycle. However, bicycles with front-wheel motors have less traction especially when high-power motors are mounted because, in combination with a light front wheel weight, they can cause wheels to slip. On the other hand, back-wheel motors allow better traction at the cost of bicycle weight unbalance and a more complex installation and maintenance. Electric bicycles with dual motors overcome the issues related to the two previous configurations like the one described in [50], but the costs, weight, and control system complexity increase in this configuration. Motors mounted in the middle directly connected to the drivetrain solve problems related to weight unbalance.
- **Motor assembly:** Another aspect that belongs to the mechanical domain is the selection of the motor assembly. Motors can be mid-drive, hub, or friction type. Mid-drive motors are typically the most performing ones because they multiply the drivetrain power and thus take advantage of the existing gears. However, they are more expensive and require a bicycle frame designed to integrate them. This means that they cannot be easily adapted to electric bicycle conversion kits. Moreover, they increase the wear of the bicycle chain that is not designed to handle the combined electro-human power. Hub motors are mounted into the wheel and can be of two types: direct-drive or geared. In the first configuration, the motor is directly connected to the wheel axle while

in the second the motor connects to the axle through a planetary gear. Direct-drive hub motors are heavy and have a large diameter to provide sufficient power without a mechanical transmission between the motor and the wheel. These motors are silent and hardly subjected to overheating thanks to their dimensions, allow regenerative braking, and rarely damage the mechanical transmission. Nevertheless, this configuration is more suitable to assist the bicycle at high speed than producing high torque at low velocity. Therefore, direct drive motors are typically not suggested for hill climbing. On the other hand, geared hubs are light and tiny motors that rotate at high speeds connected to planetary gears with the function of multiplying the torque and reducing the output speed. This configuration is typically recommended for hill climbing and has less friction when electric power is not applied because they integrate an internal freewheel mechanism. However, these motors are usually louder than direct-drive motors, have more complex maintenance, tend to overheat, and do not allow regenerative braking due to the freewheel clutch. The less-performing motor assembly is the friction one. In this configuration, the motor transmits the power directly to the tire using a friction connection. The assets of this assembly consist of the reduced cost and its lightweight. However, this configuration is less efficient due to the friction losses and tends to wear out rapidly the tire.

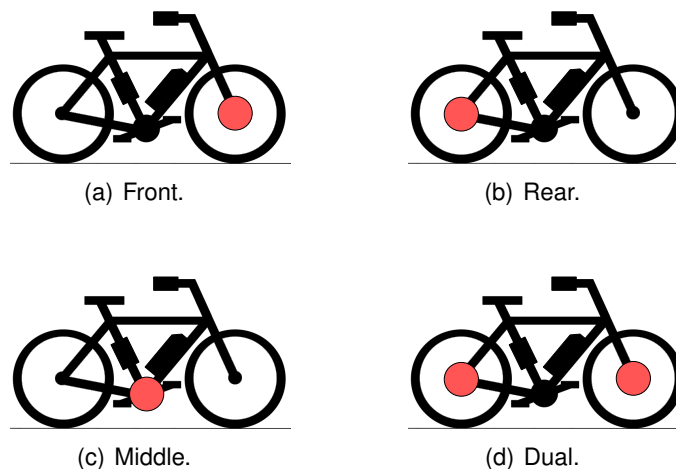


Figure 2.3: Different motor position configurations in electric bicycles.

Other aspects of the mechanical design domain of an electric bicycle are related to the frame design which has to consider the positioning of the battery, the sensors, and the electronics as well as the drivetrain and tire selection. For sake of brevity, the author does not discuss these aspects here since their analysis goes beyond the purpose of this work. The interested reader can refer to reference books for the design of standard and electric bicycles [1, 51]. The considerations made in this section will be used to derive a generic expression of the driving forces that account for all the typical motor assemblies and locations in Chapter 3 and to select the mechanical characteristics of the electric bicycle prototype used to perform the experimental validation of the proposed torque-sensorless approaches

in Chapter 5.

2.1.3 Electrical domain

- **Energy storage type:** The first important aspect to consider in the electric bicycle electrical design is the selection of the energy storage source. In these vehicles, the most common energy storage type is the battery or battery pack constituted by the connection of several low-voltage cells that determine the output voltage and the capacity of the pack expressed in *Wh* or *Ah*. Many kinds of batteries are employed in electric bicycle applications characterized by different chemical compositions. Each electrochemistry affects the energy content, the service life, the cost, and the charge-discharge characteristic of the battery [51]. Nowadays, the most common batteries for electric bicycles are the Lithium-Ion (Li-Ion) packs characterized by high energy density, fast recharge time, no memory effect, and a longer lifetime than the other technologies. However, lithium cells are sensitive to temperature and can be damaged when overcharged or rapidly discharged [7]. Thus, cell-by-cell monitoring is necessary. This is performed by employing a Battery Management System (BMS) that controls the battery charge and discharge to prevent overloading, overheating, and explosions [52]. Recently, energy sources, such as hydrogen fuel cells [53–55] and supercapacitors [56, 57], have been analyzed as alternative energy storage for electric bicycles. Although promising, these technologies are still not popular among commercial electric bicycle applications. Since they are nowadays the standard energy storage type employed in electric bicycles, this work will consider only Li-Ion battery packs with integrated BMS. More information about energy storage sources as well as battery charging technologies can be found in [51].
- **Motor type:** Another fundamental aspect of the electrical design of electric bicycles is the choice of motor. In the past, brushed DC motors were the standard for electric bicycles thanks to their easy control and low cost. However, these motors are heavy, have a large diameter due to the presence of the brushes-commutator system, and require periodic maintenance because the brushes wear out rapidly. Thanks to the availability of rare-earth permanent magnets and solid-state variable-frequency power supplies, these motors have been replaced by brushless motors with permanent magnets that can be either BrushLess-DCs (BLDCs) [58–61] or Permanent Magnets Synchronous Motors (PMSMs) [62–65]. Both types are three-phase synchronous motors with a different induced Back-ElectroMotive Force (BEMF) distribution. In fact, BLDCs have a trapezoidal induced BEMF distribution and PMSMs have a sinusoidal one. Brushless motors are typically more expensive than brushed DC motors due to the presence of permanent magnets, except in the case of permanent-magnet-excited brushed DC motors. However, they are more reliable, have a higher power density, and can be easily controlled. Nevertheless, BLDCs exhibit a high torque ripple not suitable for high-performance applications. Thus, these motors are replaced in high-quality electric bicycles by PMSMs characterized by a lower torque ripple. Other Alternating Current (AC) motors are rarely used in electric bicycle applications. An application of Induction Motors (IMs) in electrical bicycles is shown in [66]. Although IMs are more reliable and cheaper than brushless motors, they are characterized by low power density and effi-

ciency. Therefore, their application in light electric vehicles is not so popular. Switched Reluctance Motors (SRMs) could also be employed in electric bicycles [67, 68] exploiting their good fault tolerance, low cost, and easy sensorless control. Nonetheless, they have the disadvantage of a lower efficiency and power density, are noisier, and have a larger ripple than brushless motors. As shown in [69, 70], Synchronous Reluctance Machines (SynRMs) might also be used for electric bicycle applications. These motors are cheaper than PMSMs because they do not employ permanent magnets to produce the rotor magnetic flux but they are rarely employed due to their lower power density and more complex control than other brushless motors. Although several motor technologies can be implemented, in the following, only brushless motors will be considered since they are nowadays the standard for electric bicycles.

- **Motor control strategy:** The choice of the motor control strategy depends on the position-sensing technique and the power conversion strategy. Brushless motors in electric bicycle applications are typically powered by a three-phase inverter constituted by three pairs of power semiconductors arranged in a bridge configuration and controlled with a Pulse Width Modulation (PWM). Figure 2.4 contains a schematic representation of a three-phase power inverter used to control a brushless motor. In particular, this figure represents the case in which Metal-Oxide-Semiconductor Field-Effect Transistors (MOSFETs) are employed to power a three-phase star-connected brushless motor. In the figure, U_{DC} is the DC bus voltage, S_i with $i \in [1;6]$ are the MOSFETs, $\{a, b, c\}$ are the terminals of the three-phase brushless motor, and L_i with $i \in \{a, b, c\}$ are the phase inductances. BLDCs are typically controlled using an electronic commutation in which a continuous current with a duration of 120 electrical degrees is supplied to the machine. Since the rotor position information is needed only at the commutation points [71], low-cost Hall effect position sensors can be employed to control the machine. On the other hand, PMSMs require continuous rotor position feedback to supply the motor with sinusoidal voltages and currents [71]. Thus, rotor position information given by an encoder or a resolver is required. In this way, it is possible to control the machine either with a scalar or a more performing vectorial control, also known as Field Oriented Control (FOC). Furthermore, brushless motors can also be controlled by relying on sensorless techniques. These techniques, typically based either on the estimation of the BEMFs or on the exploitation of the machine anisotropy, save costs and space at the price of reduced dynamic performances [71]. To achieve high-quality motor dynamic performance and reduce the torque ripple, this thesis will focus on the utilization of PMSMs controlled with a FOC that rely on the rotor position information given by an encoder.

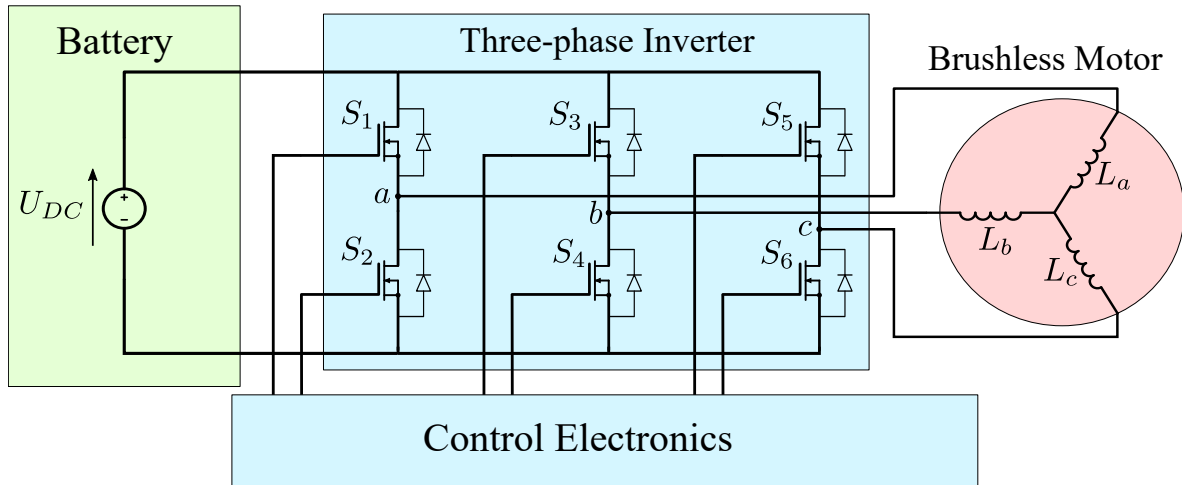


Figure 2.4: Schematic representation of a three-phase power inverter used to control brushless motors.

2.2 Pedaling torque sensors

Electric bicycle sensors are used to evaluate the human power input and provide the motor electrical assistance according to the chosen control strategy and the local regulations. In the case of pedelecs, cadence and/or torque sensors are required. Among them, the following analysis focuses on pedaling torque sensors since sensorless control approaches aim mainly at their removal.

Pedaling torque sensors can be located in different positions within the bicycle and can exploit several physical effects. In the following, a classification based on the measured physical quantity is proposed. Assets and drawbacks of each configuration are summarized in Table 2.1. As depicted in Figure 2.5, torque sensors can measure the torque across the bottom bracket spindle, the reaction force on the bottom bracket, the chain tension, the reaction force on the rear dropout, the rear axle deflection torque, or the forces on the pedals or crankarms.

- **Bottom bracket spindle torque:** Sensors measuring the torque across the bottom bracket spindle commonly exploit piezoresistive, optical, or magnetic principles. In piezoresistive sensors, such as [72, 73], one or more strain gauges are glued on the spindle. Whenever a pedaling torque is applied, a strain on the spindle generates a variation of resistance in the gauges measured with Wheatstone bridge circuitry and analogically amplified. Although this technology is very accurate, the installation of strain gauges requires particular care. Moreover, a slip-ring or wireless communication is required to transfer power and data to the rotating axis where the piezoresistive sensing elements are installed determining an increase in costs and complexity. Alternatively, the torque on the spindle can be measured optically, like in the sensor [74], by evaluating the phase shift of a light beam when passing through radially slotted disks mounted on both sides of the bottom bracket that are aligned when no torque is applied. The accuracy of these sensors is comparable to the piezoresistive ones.

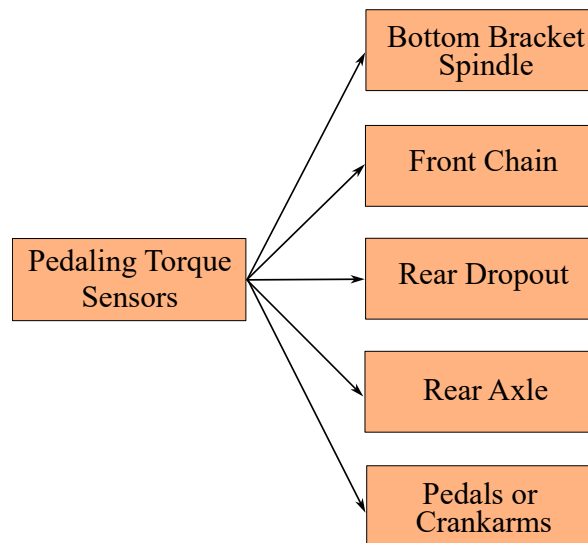


Figure 2.5: Pedaling torque sensor classification based on the position of the sensing device within the electric bicycle.

Nevertheless, optical sensors are susceptible to contamination of the lenses and require thus periodic cleaning. The great advantage of these sensors is that they do not need electronics on the rotating part. Bottom bracket spindle torque sensors can also exploit magnetic properties such as magnetostriction to evaluate the applied torque. In these sensors, such as [75], the axle presents a magnetized magnetostrictive ferromagnetic material that changes its magnetic properties with an applied strain. Although they do not require electronics on the rotating part, complex magnetization and calibration of the ferromagnetic material are necessary. Moreover, their accuracy is typically worse than optical and piezoresistive bottom bracket spindle torque sensors. As stated in [76], the main drawback of measuring the bottom bracket spindle torque is that it allows sensing only the force that the rider applies on the left pedal because the right pedal effort is applied directly to the chainring without passing through the spindle. To overcome this issue and measure the global applied pedaling torque, some sensors, like [73], couple the bottom bracket spindle with the front chainring employing a spider. Although accurate in measuring the pedaling torque, all the sensors seen up to this point are characterized by high costs and complexity.

- **Bottom bracket spindle deflection force:** When pedaling, a backward pull on the right side of the bottom bracket is generated. This force can be measured by evaluating the backward deflection of the spindle using a magnet and an inexpensive Hall effect sensor, as done in [77]. Although this technology is cheaper than the previously mentioned ones, it has the drawback that the torque is not measured directly. Thus, the performance of the control system may be altered by errors in the measurement of the human input. Besides, these sensors require particular care in the mounting process because an alignment in the direction of the chain tension is necessary for correct operation.

- **Front chain tension:** Another possibility to sense the human torque is to measure the tension of the front chain introducing additional idler pulleys in the drivetrain exploiting either piezoresistive [78] or hall effect [79] principles. In this approach, knowing the measured chain tension and the chainring radius allows the indirect calculation of the pedaling torque.
- **Rear dropout reaction force:** Other sensors, like [80,81], derive the torque measuring the rear dropout forward reaction force caused by the pulling of the chain through a strain gauge load cell. When the radius of the rear sprocket is known, they allow an indirect calculation of the pedaling torque. Although these sensors are simple and inexpensive, their installation requires customization of the bicycle frame.
- **Rear axle forward deflection torque:** The pedaling torque may be also measured from the rear axle forward deflection obtained with a sensor mounted in the motor hub [82]. When pedaling, the torque is transmitted from the chain to the rear sprocket and from the latter to the rotor via a torsional spring. The connection with the spring causes a phase shift between the sprocket and the rotor when a torque is applied that can be measured using Hall effect sensors.
- **Pedals/Crankarms forces:** A different approach to sensing the torque consists of measuring the forces acting on the pedals or the crank arms using piezoresistive or piezoelectric [83] sensors. In literature, many examples of piezoresistive sensors that evaluate the forces acting on the pedals [84–86] or on the crank arms [87–89] can be found. However, evaluating the pedaling torque from the forces applied on the pedals or crank arms is not trivial because not all the force components contribute to torque generation. Therefore, many sensing elements are installed to evaluate the single contributions. Since these forces are measured in a rotating frame, the sensors require a wireless data transfer and customized pedals or crank arms designed to protect and power the electronics increasing system complexity and costs. For the above-mentioned reasons, such sensors are rather employed as cycling power meters to analyze the pedaling performances than to sense the human input in electric bicycle control systems.

From the considerations made in this section, it emerges that depending on the mounting position and the exploited physical principle, pedaling torque sensors may increase the costs of an electric bicycle when high-quality sensors are utilized. The employment of cheaper sensing technologies based on indirect measurements of the human input might reduce the costs but increases the bicycle mechanical design complexity. Additionally, their utilization might degrade the overall control performance of the system. Therefore, it is worth analyzing torque-sensorless control approaches to avoid the installation of such sensors.

Measured quantity	Physical principle	Advantages	Disadvantages
Bottom bracket spindle torque	Piezoresistive [72, 73]	High accuracy	Expensive Rotating frame Complex installation
	Optical [74]	High accuracy No rotating frame	Expensive Lenses contamination
	Magnetostrictive [75]	No rotating frame	Expensive Magnetization process Calibration process
Bottom bracket spindle deflection force	Hall effect [77]	Cheap	Indirect measurement Complex installation
Front chain tension	Piezoresistive [78] Hall effect [79]	Cheap	Indirect measurement Drivetrain modification
Rear dropout reaction force	Piezoresistive [80, 81]	Cheap	Indirect measurement Frame modification
Rear axle forward deflection torque	Hall effect [82]	Cheap	Indirect measurement Motor modification
Pedals/Crankarms forces	Piezoresistive [84–89]	High accuracy	Rotating frame Many sensing elements Crankset modification Expensive
	Piezoelectric [83]	High accuracy	Rotating frame Crankset modification Expensive

Table 2.1: Pedaling torque sensors classification based on the measured quantity and the exploited physical principle.

2.3 Control strategies

This section analyzes the different control strategies used to power-assist an electric bicycle. In its simplest form, a controller is an on-off switch that provides a constant voltage to the motor. Thus, when no pedaling torque is applied, the vehicle speed depends only on the motor characteristics and environmental load. An upgrade to this control approach is to use a rheostat to control the motor current providing different levels of assistance. Although this method is simple, it wastes battery energy. Therefore, modern controllers reduce energy losses by relying on a PWM. Power-on-demand bicycle controllers generate the corresponding assistance level depending on the throttle signal. Differently from this, pedelec controllers combine the measurements of cadence and/or torque sensors to produce electrical assistance. In its basic form, the pedelec controller is just an on/off switch that turns on the power assistance when a cadence or a torque sensor senses a human input. In its more complex forms, a pedelec controller can combine many inputs: pedaling cadence and torque, motor speed and torque, road slope, bicycle acceleration, cyclist heart rate, etc. to provide a desired relationship between human and motor power. [1]

Focusing on pedelec control strategies, a commonly used classification is based on the sensors that measure the human power input. Two categories are typically distinguished namely cadence-sensor-based and torque-sensor-based control strategies. However, the definition of the best approach is not straightforward since it depends mainly on the preferences of the cyclist and demands while cycling. Moreover, as said before, the control strategies can also rely on both sensors. When considering strategies that employ either cadence or torque information, cadence-sensor-based pedelecs are claimed to be more suitable for cyclists that ride an electric bicycle to minimize the effort without interest in physical training. Whereas, torque-sensor-based pedelecs seem to suit better people that do not want to lose the training aspect while riding an electric bicycle. The commonly used classification previously proposed gives only general information for the final user of the bicycle and does not provide sufficient information to the controller designer. Following, the author discusses a classification based on the optimization focus. However, it is necessary to remark that a control strategy can belong to more than one category and thus a clear distinction cannot always be done. As illustrated in Figure 2.6, the author has classified the control strategies into four main categories, namely power-, speed-, cyclist-, and energy-oriented control approaches. Table 2.2 contains a summary and a comparison of the analyzed pedelec control strategies.

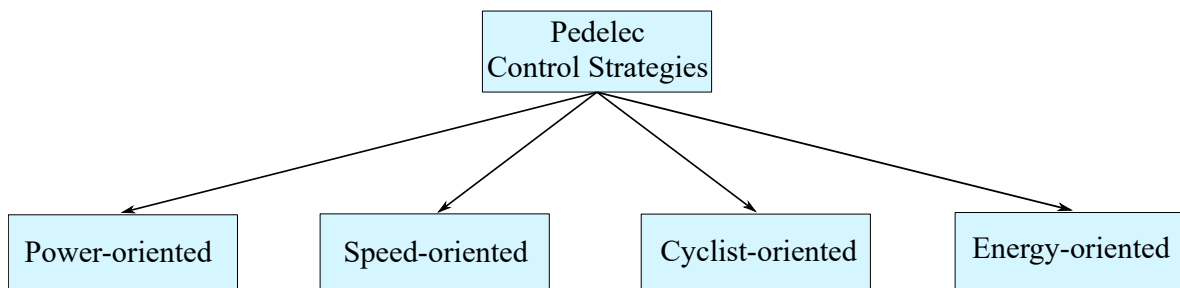


Figure 2.6: Pedelec control strategies classification based on the optimization focus.

- **Power-oriented control strategies:** To power-oriented strategies belong elementary control approaches such as the previously mentioned on/off switching and fixed-gain ones. In fixed-gained approaches, the motor power or torque is set as a fixed percentage of the pedaling input. This is typically done by the user that selects the desired level of assistance and thus determines the system performance [90]. Moreover, to respect the legislation, the assistance ratio can be reduced with the increasing bicycle speed. Other approaches that belong to power-oriented strategies are Real-Time Power Mapping (RTPM) strategies, such as the one proposed in [90]. In RTPM strategies, the rider chooses a desired total target power which is then ensured by the control system. In other words, the sum of the human and motor contributions is set to a desired level. The main asset of power-oriented strategies is the simplicity of their implementation. Nevertheless, such methods do not consider the environmental load that affects the final vehicle speed. Actually, there can be situations in which the combined human and motor power may not be sufficient to overcome the external load. For this reason, [28] exploits a DOB that estimates and compensates for the environmental disturbance torque. In this work, the motor assistance is composed of a term proportional to the cyclist input plus the estimated environmental load given by a DOB. Moreover, the works [29, 91, 92] address the robust estimation of external disturbances using DOBs. Another drawback of power-oriented techniques is that they amplify the ripple of the pedaling torque and thus the vehicle speed fluctuations leading to dangerous situations, especially with high amplification gain on a flat or downhill road. To avoid speed fluctuations, Torque Filling (TF) approaches can be implemented [90, 93]. The idea behind TF strategies is to ensure that the total torque is constant across the whole pedal cycle and compensate for the fluctuating profile of the pedaling torque with the motor action. In this way, the control action eliminates the torque ripple related to the torque amplification and the consequent speed fluctuation.
- **Speed-oriented control strategies:** In speed-oriented strategies, the control system or the rider select a target bicycle speed. The motor provides the power accordingly to track the speed reference. Therefore, in these approaches, the desired speed profile can be followed independently from the environmental conditions. The work [94] proposes a bicycle speed trajectory tracking. In particular, this work implements a feed-forward controller obtained from the vehicle mathematical model along with a standard feedback Proportional-Integral-Derivative (PID) controller. Whereas, in [95], a state feedback optimal control which is robust to disturbances and model uncertainties tracks the desired speed. The works [96, 97] express the bicycle speed control in terms of optimization of H_∞ performances. In other works, Fuzzy Logic Controllers (FLCs) [98–100] allow to track the target speed generating an electrical assistance that depends on several inputs using a linguistic approach. In [101], an adaptive FLC adjusts online the fuzzy parameters to guarantee better riding comfort and safety. Moreover, the work [102] compares the velocity tracking performances between standard PID, Fuzzy PID, and Hybrid Fuzzy-PID controllers. Although FLC strategies allow to provide the electrical assistance in a more readable way similar to human reasoning, their implementation on microcontrollers is generally computationally heavier than standard trajectory tracking control strategies. The pedaling torque profile introduces oscillations in the bicycle speed even in a speed-oriented control. The reduction of speed fluctu-

ation in bicycle speed control has been addressed in literature relying on Repetitive Controllers (RCs) [103, 104]. A RC exploits the periodic nature of the pedaling torque to reduce the speed fluctuations rejecting periodic disturbances. Furthermore, another possible approach to reduce speed fluctuations analyzed in [105] uses an adaptive notch filter. The experimental results show that the proposed adaptive notch filter reduces the velocity oscillations more than a standard RC.

- **Cyclist-oriented control strategies:** Cyclist-oriented control strategies focus on keeping a physiological variable at a constant level independently from the environmental load encountered while cycling. Some works [106, 107] measure the oxygen uptake or ventilation rate to evaluate the effort while cycling and provide electrical assistance accordingly. Nevertheless, these strategies require complex hardware that can be used only in laboratory experiments. According to Fick principle, oxygen consumption can be related to heart rate. Therefore, as stated in [90], many works [108, 109] use heart rate dynamic models to predict the heart rate of the cyclist at particular environmental conditions and apply power assistance to keep the heart rate and thus the physical effort at desired target values. However, controlling the heart rate of the cyclist is not trivial since its dynamics can differ from one person to the other and can be dependent on variables that are not necessarily related to physical activity. Other works [110, 111] focus on providing the power assistance granting the comfort of ride using Reinforcement Learning (RL) approaches. In these works, the RL agent applies different levels of assistance and gets a reward for trying to solve the comfort of ride problem. After a trial-and-error period, the RL agent learns to provide electrical assistance to enhance the comfort of ride.
- **Energy-oriented control strategies:** Energy-oriented control strategies aim at efficiently managing the energy flows within the electric bicycle system. In particular, they address the issue of extending the battery range limiting its discharge, and recovering energy when braking or during high-efficiency pedaling. For example, in [112], the energy is recovered when the cyclist is most efficient and returned during low-efficiency pedaling with the objective of keeping the State of Charge (SoC) of the battery constant and thus increasing the battery autonomy. Another work [113] aims at reducing energy consumption by imposing a desired battery discharge rate and thus regulating its SoC. In other works [114, 115], the energy management optimization in electric bicycles has been formulated using FLCs.

As previously shown, several control strategies of different complexity may be employed to electrical assist pedelecs. With some modifications, many of these approaches can be also applied to torque-sensorless systems to achieve specific desired control targets. Among the possible applicable control strategies, this thesis will focus on the power-oriented ones because they reduce the mechatronic system complexity and allow easier analysis of the torque-sensorless performance. In particular, a simple fixed-gain strategy is utilized later in this work.

Strategy	Focus	Advantages	Disadvantages	References
On/off switching	Power	Easy implementation	Not environmental adaptive	[1, 51]
Fixed gain	Power	Easy implementation Input power amplification	Not environmental adaptive Speed fluctuations	[28, 51, 90]
RTPM	Power	Easy implementation	Not environmental adaptive Speed fluctuations	[90]
DOB	Power	Environmental adaptive	Speed fluctuations	[28, 29, 91, 92]
TF	Power	No speed fluctuations	Not environmental adaptive	[90]
Speed trajectory tracking	Speed	Environmental adaptive	Speed fluctuations	[94–97]
FLC	Speed	Environmental adaptive Easy linguistic approach	Speed fluctuations Computationally heavy	[98–102]
RC	Speed	Environmental adaptive Reduced speed fluctuations		[103, 104]
Adaptive Notch Filter	Speed	Environmental adaptive No speed fluctuations		[105]
Ventilation rate based	Cyclist	Reduced cycling effort	Complex measurements	[106, 107]
Heart rate based	Cyclist	Reduced cycling effort	Cyclist dependent	[108, 109]
RL	Cyclist	Improved riding comfort	Learning time	[110, 111]
SoC optimization	Energy	Electrical autonomy		[112, 113]
Fuzzy SoC optimization	Energy	Electrical autonomy Easy linguistic approach	Computationally heavy	[114, 115]

Table 2.2: Summary and comparison of the analyzed pedelec control strategies.

3 Mathematical modeling of bicycle dynamics

A bicycle can be mathematically described with models of different complexity depending on the purpose of the analysis. A detailed bicycle model may be elaborate because the system has many degrees of freedom and intricate geometry. Thus, when modeling a bicycle, it is fundamental to choose the modeled components, the tire-road interaction, and the complexity of the rider [116]. Bicycles are statically unstable, but when controlled by the human steering action and thanks to mechanical design aspects such as the front fork offset stabilizing effect, they may be stabilized. In the design of electric bicycles, the mathematical model is used to evaluate the combined human-motor power needed for hill-climbing and overcoming the wind and rolling resistances [51]. Since the rider performs the vehicle stabilization, the vehicle dynamics analysis can be reduced to the one in the longitudinal direction [104]. The following sections express the bicycle longitudinal dynamics mathematically. In particular, they analyze the propulsive and resisting forces acting on the bicycle dynamics and their parametric variability. In such a way a generic mathematical expression of the vehicle longitudinal dynamics is derived. Eventually, this chapter contains a sensitivity analysis of the resisting forces to evaluate the variability of the power needed to overcome them in different realistic scenarios. The former provides indications that will be utilized in Chapter 4 to simplify the proposed mathematical model for the pedaling torque estimation.

3.1 Bicycle longitudinal dynamics

The pedaling purpose is to apply a driving force that equals the total forces resisting forward motion to maintain a constant speed [1]. When the driving force exceeds or is smaller than the resisting ones, a bicycle acceleration or deceleration is caused. This section analyses the bicycle longitudinal dynamics in the specific case of an electric bicycle with parallel topology. It is assumed that the bicycle moves only along the longitudinal direction x , the rider has a fixed position and orientation, the mass of the system is concentrated at its mass center, and the leaning of the vehicle is neglected. Under these hypotheses, the bicycle longitudinal dynamics, graphically represented in Figure 3.1, can be expressed with the equation:

$$F_d - F_g - F_r - F_a - F_b - F_B = F_I, \quad (3.1)$$

where F_d , F_g , F_r , F_a , F_b , F_B and F_I are the driving, the gravity, the rolling friction, the aerodynamic drag, the bump, the braking and the inertia forces, respectively. In the following sections, the terms that compose equation (3.1) are analyzed in details.

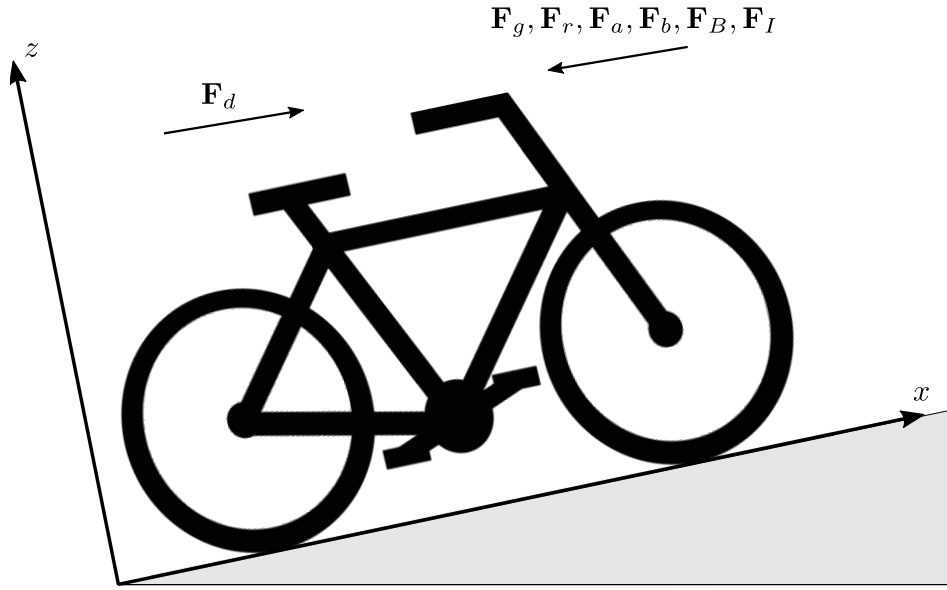


Figure 3.1: Bicycle longitudinal dynamics including the effects of driving and resisting forces.

3.1.1 Driving forces

The propulsive power in an electric bicycle is generated by the combined action of the cyclist and the motor:

$$F_d = F_h + F_m, \quad (3.2)$$

where F_h and F_m are the human and motor force contributions to the longitudinal dynamics. In the case of a standard bicycle, where no electrical assistance is available ($F_m = 0 \text{ N}$), equation (3.2) reduces to $F_d = F_h$. In a bicycle, the majority of human power is generated by applying a force to the pedals F_p that is converted in a torque T_{pc} by the crankset mechanism, whose cogwheel rotates at an angular speed ω_c . This torque is then transmitted to the rear-wheel T_{pw} through a chain transmission. In drivetrains with a freewheel mechanism, the torque is transmitted only in forward pedaling. On the contrary, in backward pedaling, the wheel is disengaged from the drivetrain and free to rotate at a different speed from the rear cogwheel. Therefore, under the hypotheses of engaged drivetrain and no wheel-slipping, the angular speed at the rear-cogwheel ω_w equals the angular speed of the wheel ω . Figure 3.2 reports a schematized representation of a bicycle drivetrain. In this figure, r_c and r_w represent the radii of the front- and back-cogwheels of the drivetrain and r the radius of the rear wheel.

Under these hypotheses, a relation between the delivered pedaling power at the crankset $P_{pc} = T_{pc}\omega_c$ and the one transmitted to the rear-cogwheel $P_{pw} = T_{pw}\omega_w = T_{pw}\omega$ can be defined:

$$T_{pw}\omega = \eta_d T_{pc}\omega_c, \quad (3.3)$$

where η_d represents the efficiency of the chain-transmission whose value is typically in the range $\eta_d \in [0.85; 0.97]$ [1]. Neglecting the power losses in equation (3.3), the drivetrain gear

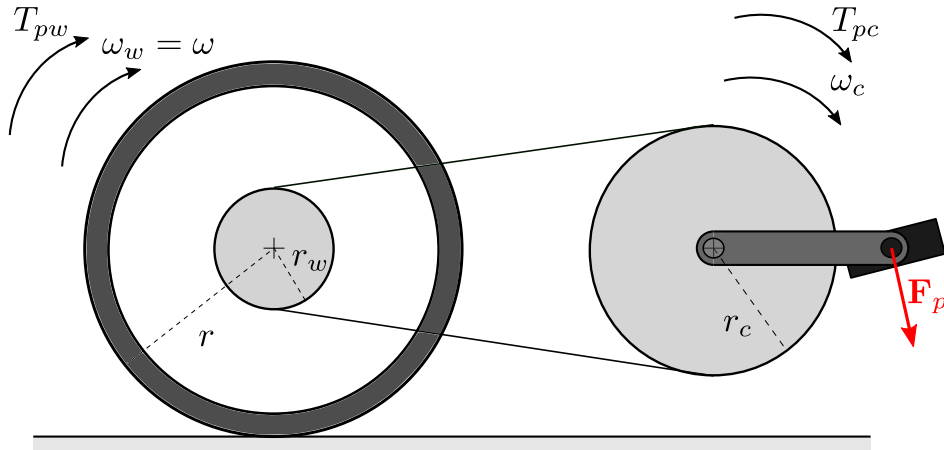


Figure 3.2: Schematic representation of a bicycle drivetrain in case of forward pedaling and no wheel-slipping.

ratio τ_d can be expressed as follows:

$$\tau_d = \frac{\omega}{\omega_c} = \frac{T_{pc}}{T_{pw}}. \quad (3.4)$$

Alternatively, this gear ratio can be expressed as the ratio of the number of teeth or the ratio of the radii of the front and rear cogwheels:

$$\tau_d = \frac{z_c}{z_w} = \frac{r_c}{r_w}. \quad (3.5)$$

It has to be remarked that, in bicycle drivetrains, the gear ratio is typically meant to reflect how many times the rear wheel turns for each complete turn of the pedals, namely as the ratio of the output to the input angular speeds. Hereafter, to simplify the mathematical modeling, this assumption will be applied to all analyzed gear ratios. From equations (3.3) and (3.4) the pedaling torque transmitted to the rear-wheel can be expressed as:

$$T_{pw} = \eta_d \frac{T_{pc}}{\tau_d}. \quad (3.6)$$

Thus, the human force contribution to the longitudinal motion results:

$$F_h = \frac{T_{pw}}{r} = \eta_d \frac{T_{pc}}{r\tau_d}. \quad (3.7)$$

In case of an electric bicycle, the motor contributes to propel the vehicle. This contribution depends on the considered motor assembly leading to different expressions of the driving force.

Mid-drive motor assembly:

In case of mid-drive motors, both the pedaling and motor torques are applied to the crankset.

3.1 Bicycle longitudinal dynamics

In particular, the motor can be directly connected to the crankset or connected to it through a gearbox that multiplies the motor torque. In case of geared motors, the relation between the motor power $P_m = T_m \omega_m$ and the motor power transmitted to the crankset $P_{mc} = T_{mc} \omega_c$ results:

$$T_{mc} \omega_c = \eta_g T_m \omega_m, \quad (3.8)$$

where T_m is the motor torque, T_{mc} is the motor torque transmitted to the crankset, ω_m is the motor mechanical speed, and η_g is the efficiency of the gearbox. Geared transmission are typically characterized by high efficiency $\eta_g \in [0.94; 0.98]$. Neglecting the power losses in equation (3.8), the gear ratio of the gearbox τ_g results:

$$\tau_g = \frac{\omega_c}{\omega_m} = \frac{T_m}{T_{mc}}. \quad (3.9)$$

Depending on the internal configuration of the gearbox, the transmission ratio can be related to the number of teeth of the cogwheels. In geared motors, planetary gears are typically employed because they provide higher torque at the same dimension compared to ordinary gears. From equations (3.8) and (3.9), the expression of the motor torque applied to the crankset results:

$$T_{mc} = \eta_g \frac{T_m}{\tau_g}. \quad (3.10)$$

In case no gearbox is inserted between the motor and the crankset, the transmission ratio and its efficiency result $\tau_g = \eta_g = 1$ and thus $T_{mc} = T_m$ and $\omega_c = \omega_m$. Considering the bicycle drivetrain, a relation between the total input power at the crankset $P_{\Sigma c} = T_{\Sigma c} \omega_c$ and the total output power at the rear-wheel $P_{\Sigma w} = T_{\Sigma w} \omega$ can be defined:

$$T_{\Sigma w} \omega = \eta_d T_{\Sigma c} \omega_c, \quad (3.11)$$

where $T_{\Sigma c}$ is the total torque at the crankset and $T_{\Sigma w}$ is the total torque transmitted to the wheel. These two torques can be decomposed in contributions related to the motor and the human pedaling:

$$T_{\Sigma c} = T_{pc} + T_{mc} \quad T_{\Sigma w} = T_{pw} + T_{mw}, \quad (3.12)$$

where T_{mw} is the motor torque transmitted to the rear-wheel. Therefore, equation (3.11) becomes:

$$(T_{pw} + T_{mw}) \omega = \eta_d (T_{pc} + T_{mc}) \omega_c. \quad (3.13)$$

Using the superposition principle, the contributions of the pedaling and motor power can be considered separately. Considering only the effect of the motor torque on the drivetrain, the transmitted motor torque to the rear-cogwheel results:

$$T_{mw} = \eta_d \frac{T_{mc}}{\tau_d}. \quad (3.14)$$

Thus, the motor force contribution results:

$$F_m = \frac{T_{mw}}{r} = \eta_d \frac{T_{mc}}{r\tau_d} = \eta_d \eta_g \frac{T_m}{r\tau_d\tau_g}. \quad (3.15)$$

Figure 3.3 presents the power flow block diagram of a mid-drive motor assembly.

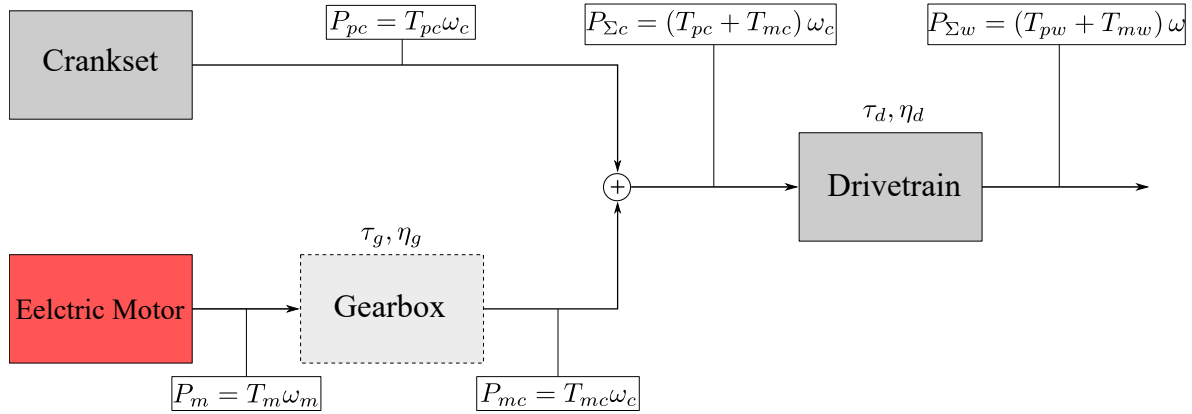


Figure 3.3: Power flow block diagram of a mid-drive motor assembly.

Hub motor assembly:

In case of hub motor assembly, the motor is not connected to the crankset. Therefore, the motor force contribution is independent from the drivetrain. In case of geared hub motors, the torque transmitted to the wheel results:

$$T_{mw} = \eta_g \frac{T_m}{\tau_g}. \quad (3.16)$$

Thus, the motor force contribution results:

$$F_m = \frac{T_{mw}}{r} = \eta_g \frac{T_m}{r\tau_g}. \quad (3.17)$$

In case of a direct-drive motor, where no gearbox is present ($\tau_g = \eta_g = 1$) between the motor and the wheel $T_m = T_{mw}$, the force contribution results:

$$F_m = \frac{T_m}{r}. \quad (3.18)$$

It has to be remarked that the motor force contribution of a hub motor assembly does not depend on its mounting position in the bicycle system, namely in the front or rear wheel. Figure 3.4 shows the power flow block diagram of a hub motor assembly mounted in the rear wheel.

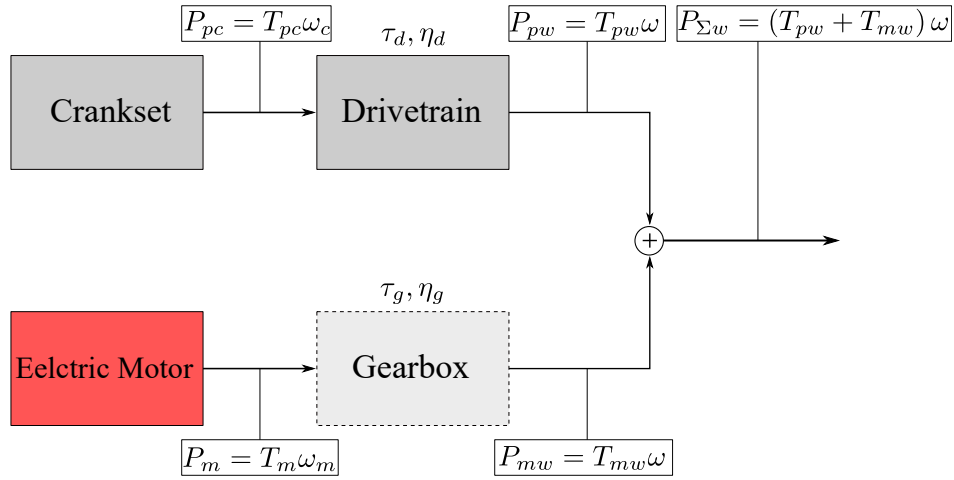


Figure 3.4: Power flow block diagram of a hub motor assembly mounted in the rear wheel.

Friction motor assembly:

In case of a friction motor assembly, the power is transmitted from the motor to the front or rear wheel with a friction drive. Figure 3.5 reports a schematized representation of bicycle friction drive where r_f represents the radius of the motor friction-wheel. The relation between the motor power $P_m = T_m \omega_m$ and the power transmitted to the wheel $P_{mw} = T_{mw} \omega$ can be expressed as:

$$T_{mw} \omega = \eta_f T_m \omega_m, \quad (3.19)$$

where η_f is the efficiency of the friction transmission. Neglecting power losses, the friction drive transmission ratio τ_f can be expressed as:

$$\tau_f = \frac{\omega}{\omega_m} = \frac{T_m}{T_{mw}}. \quad (3.20)$$

In case of adherence between the two friction-wheels, equation (3.20) can be related to the geometry of the friction-wheels:

$$\tau_f = \frac{r_f}{r}. \quad (3.21)$$

From equations (3.19) and (3.20), the expression of the motor torque transmitted to the wheel can be expressed as:

$$T_{mw} = \eta_f \frac{T_m}{\tau_f}. \quad (3.22)$$

Therefore, the motor force contribution in a friction motor assembly results:

$$F_m = \frac{T_{mw}}{r} = \eta_f \frac{T_m}{r \tau_f}. \quad (3.23)$$

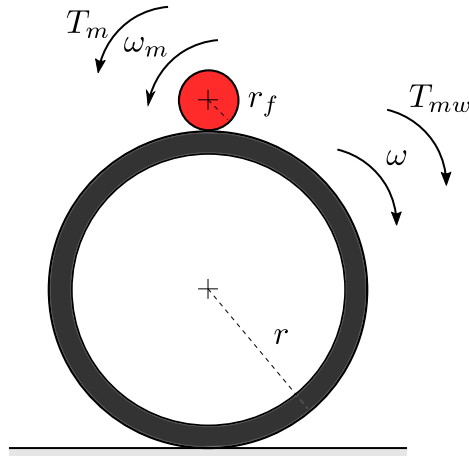


Figure 3.5: Friction motor assembly.

Figure 3.6 shows a block diagram of the power flow in a friction motor assembly. Table 3.1 reports a summary of the obtained driving forces expressions in electric bicycles with different motor assemblies. It can be seen that the motor force contribution can be expressed with a generic expression valid for the three motor assemblies:

$$F_m = \eta_m \frac{T_m}{r \tau_m}, \quad (3.24)$$

where $\eta_m = \prod \eta_i$ is the global motor mechanical transmission efficiency, $\tau_m = \prod \tau_i$ its transmission ratio, and i the generic involved mechanical transmission. In the following sections, the pedalling torque T_p and the motor torque T_m are analyzed in details.

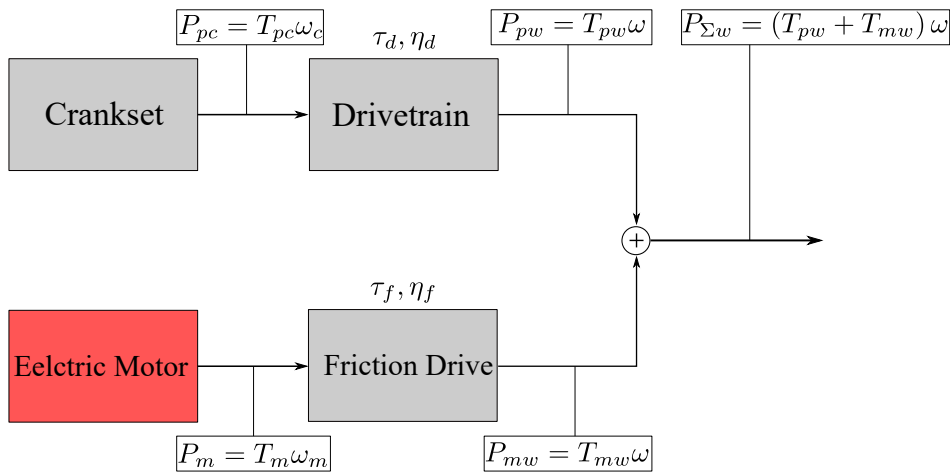


Figure 3.6: Power flow block diagram of a friction motor assembly.

Motor assembly type	Human force contribution F_h	Motor force contribution F_m
Mid-drive		$\eta_d \eta_g \frac{T_m}{r \tau_d \tau_g}$
Hub	$\eta_d \frac{T_{pc}}{r \tau_d}$	$\eta_g \frac{T_m}{r \tau_g}$
Friction		$\eta_f \frac{T_m}{r \tau_f}$

Table 3.1: Driving forces expressions in different electric bicycle motor assemblies.

3.1.2 Pedaling torque

The pedaling torque applied to the crankset T_{pc} has a time-variant profile that depends on the geometry of the crankset, the intensity, and the direction of the applied pedaling forces. This torque is the sum of the contributions of the left T_{pc}^l and right pedals T_{pc}^r :

$$T_{pc} = T_{pc}^l + T_{pc}^r. \quad (3.25)$$

These torque contributions are generated by the pedaling force applied on the left \mathbf{F}_p^l and right \mathbf{F}_p^r pedals. However, these forces do not contribute entirely to the torque generation. They can be decomposed in a tangential component to the pedal motion \mathbf{F}_{pT}^i and a radial one \mathbf{F}_{pR}^i , where $i \in \{l, r\}$. Among them, the tangential component is the one responsible for torque generation and it is also called effective component while the radial force is referred to as ineffective component. The single torque contribution can be written as:

$$T_{pc}^i = F_{pT}^i l_c, \quad (3.26)$$

where l_c is the length of the crank arm. Therefore, the single torque contribution depends on the intensity and direction of the applied pedaling force and the crankset angle θ_c . Figure 3.7 represents the single pedal torque contribution during one crank revolution. During the first half period (I and II quarters) a propulsive torque is applied $T_{pc}^i > 0$. Thus, the first half period represents a propulsive phase also called downstroke phase. In particular, a typical pedaling torque profile increases in the I quarter and decreases in the II one. During the second half period (III and IV quarters), the torque contribution may be negative because non-professional cyclists do not lift the leg while pushing the pedal with the other one [117]. Indeed, the weight of the passive leg generates a negative torque contribution $T_{pc}^i < 0$ when the slight tendency to lift the resting pedal does not overcome the weight of the leg. Therefore, the second half period represents a recovery phase also called upstroke phase. Figure 3.8 contains the typical profile over one crank revolution of the single pedal tangential and radial force components whose values are inspired by the ones shown in [1].

Considering the global effect, each pedal alternates a propulsive or a recovery phase. In other words, when one leg pushes on a pedal, the other recovers. In this way, the cyclist generates a quasi-periodic pedaling torque profile similar to a sinusoidal signal with an offset [43, 45, 105]. Figure 3.9 represents a typical pedaling torque profile over one crank revolution

inspired by the one shown in [118]. Defining $\theta_c = 0$ rad when the pedal is in the vertical position or at the Top Dead Center (TDC), the pedaling profile shows two maximums when the pedals are close to the horizontal position, where $\theta_c \simeq \frac{\pi}{2}$ rad and $\theta_c \simeq \frac{3\pi}{2}$ rad. This torque peak typically occurs during the transition of each pedal from the I to the II quarter. On the contrary, close to the TDC and the Bottom Dead Center (BDC), where $\theta_c = \pi$ rad, the pedaling torque presents its minimum values.

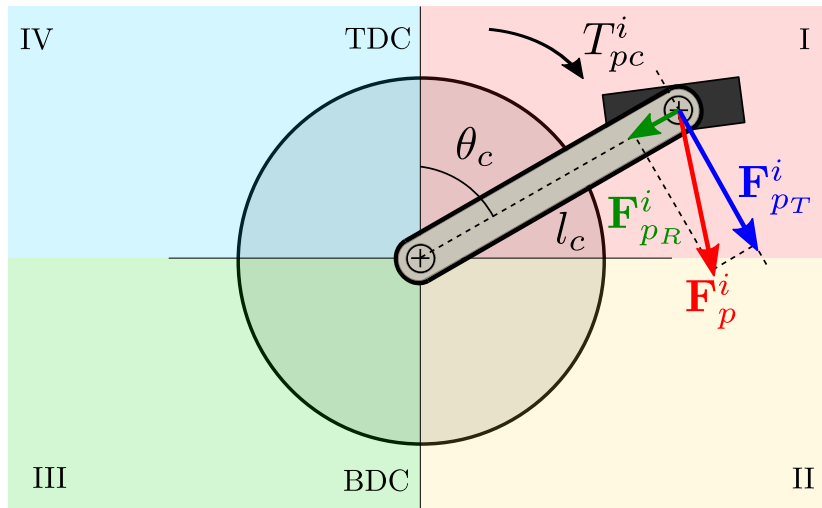


Figure 3.7: Single pedal contribution T_{pc}^i to the pedaling torque T_{pc} over one crank revolution.

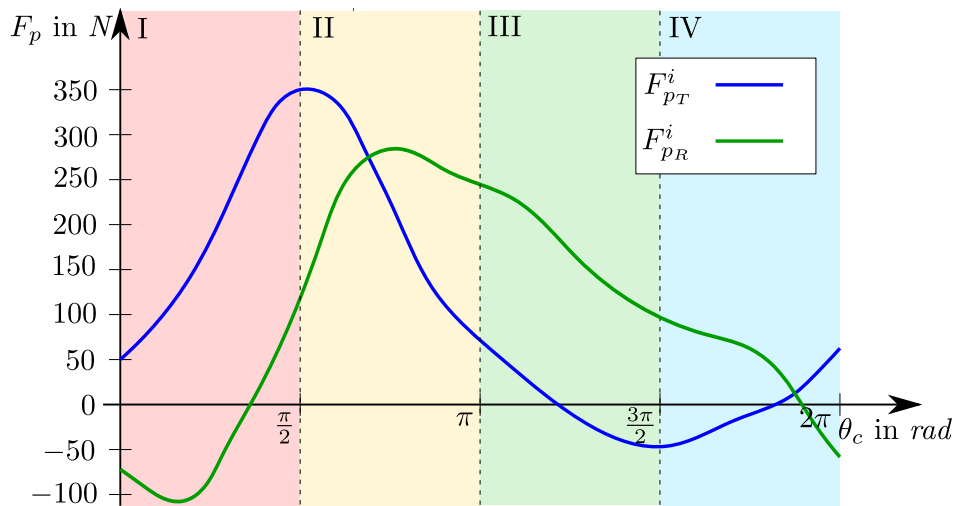


Figure 3.8: Typical single pedal tangential F_{pT}^i and radial F_{pR}^i force components over one crank revolution.

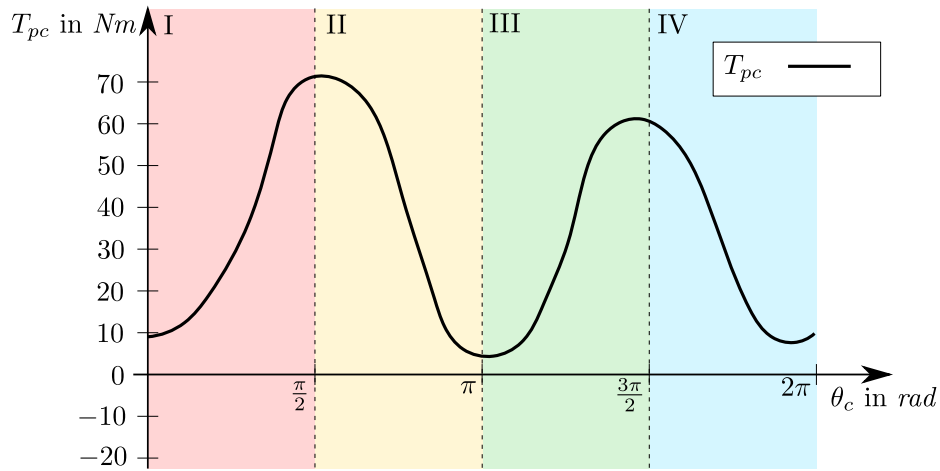


Figure 3.9: Typical pedaling torque profile T_{pc} over one crank revolution.

Pedaling torque profiles are variable depending on the riding conditions, the cyclist pedaling style, inter-subject variability, and the mechanical configuration of the bicycle. Environmental conditions affect the final torque profile because they influence the magnitude of force needed to accelerate the vehicle to the desired speed. As shown in [118], the pedaling torque profile varies with the cycling cadence and the environmental conditions. Besides, a cyclist can turn the pedals with any variety of pedaling styles determining different pedaling torque profiles. For example, the upright cycling torque profile differs from the one obtained in standing-up pedaling. Moreover, the cyclist capability of propelling a bike varies depending on the fitness level, age, and sex. Furthermore, asymmetries between the two legs are quite common for most cyclists generating a difference between the two torque maximums over a crank revolution. Other factors that influence the pedaling torque profile are related to the mechanics of the bicycle. Indeed, the saddle height, its inclination, and the length of the crankarms affect the average and peak pedaling torque over one crank revolution [1, 119].

Nevertheless, pedaling is not the only human propulsion source in a bicycle. Cyclists exploit muscles other than the legs to propel the vehicle generating driving forces indicated with F_h^e in this work. Tilting the bicycle away from the pedal in downstroke allows the rider to perform substantial arm work easily. Besides, pulling the torso forward, from the saddle toward the handlebar, during the pedaling downstroke permits to use of the arms powerfully especially when starting. Moreover, standing while pedaling allows for an increase in the short-term applied power because it adds work produced by other muscles. [1]

Thus, the global expression of the human force contribution results:

$$F_h = \eta_d \frac{T_{pc}}{r\tau_d} + F_h^e. \quad (3.27)$$

3.1.3 Motor torque

The motor torque T_m depends on the type of motor used to propel the bicycle. As stated in chapter 2, many kinds of motors can be employed in an electric bicycle. In the following, the analysis is limited to three-phase brushless motors since they are nowadays the standard for electric bicycle applications. In Figure 3.10, a schematic representation of a brushless motor

is reported. Different coordinate systems can be defined to model the machine, namely phase abc -, stator $\alpha\beta$ -, and rotor dq - reference frames. The phase coordinate system is related to the physics of the machine and constituted of three axes with $\frac{2\pi}{3}$ rad phase shift. Quantities expressed in this coordinate system can be transformed into the stator frame, where the α -axis is aligned to the a one and the β -axis is orthogonal to it. The rotor frame is defined with the d -axis aligned to the permanent magnet axis and the q - one orthogonal to it. This coordinate system rotates synchronously with the rotor $\omega_{dq} = \omega_e$, where ω_e is the electrical angular speed of the rotor.

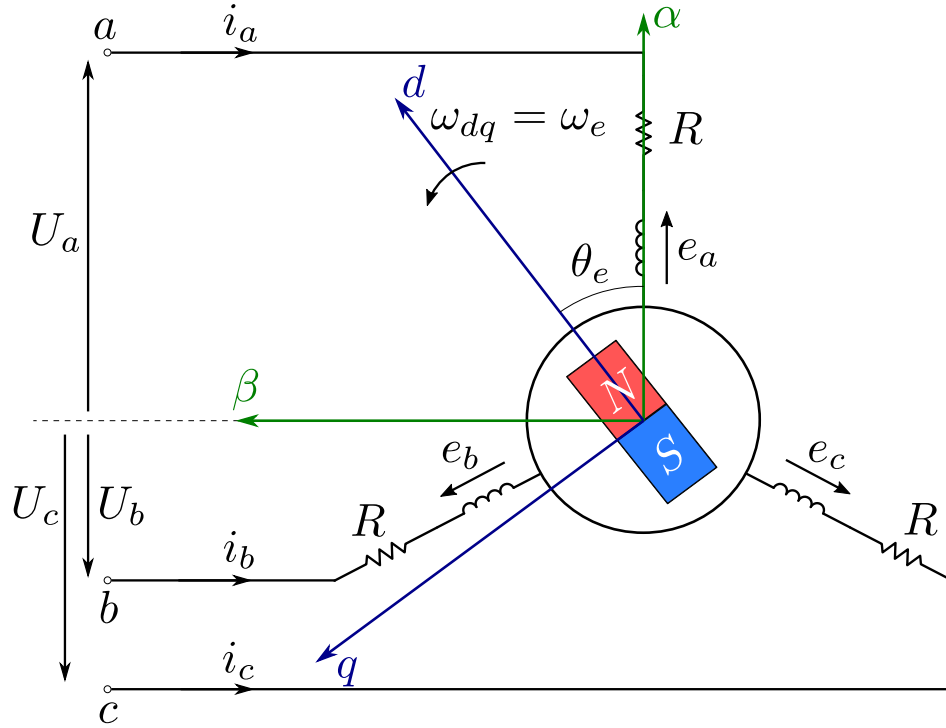


Figure 3.10: Schematic representation of a brushless motor.

The number of pole pairs of the machine n_p defines the relation between electrical and mechanical quantities:

$$\theta_m = \frac{\theta_e}{n_p} \quad \omega_m = \frac{\omega_e}{n_p}, \quad (3.28)$$

where θ_m and θ_e are the mechanical and electrical positions.

Furthermore, $\mathbf{U}_{abc} = [U_a \ U_b \ U_c]^T$ and $\mathbf{i}_{abc} = [i_a \ i_b \ i_c]^T$ are the voltage and current vectors in the phase reference frame, R is the phase resistance, and $\mathbf{e}_{abc} = [e_a \ e_b \ e_c]^T = \frac{d\boldsymbol{\Psi}_{abc}}{dt}$ are the induced electromotive forces equal to the derivative of the magnetic flux linked with each phase $\boldsymbol{\Psi}_{abc} = [\Psi_a \ \Psi_b \ \Psi_c]^T$. These fluxes are generated by the combined effects of the permanent magnets, self-induction, and mutual-induction. For the sake of brevity, the equations of brushless motors are not derived in this work. For further information on brushless motor models, the interested reader can refer to [120]. Using the Clarke and Park transformations, a vector in the phase reference system can be transformed in the stator

3.1 Bicycle longitudinal dynamics

or rotor frames, respectively. In the case of PMSMs, the motor or electromagnetic torque expressed in the rotor reference frame assumes the following expression:

$$T_m = \underbrace{\frac{3}{2}n_p\Psi_{PM}i_q}_{\text{synchronous torque}} + \underbrace{\frac{3}{2}n_p(L_d - L_q)i_d i_q}_{\text{reluctance torque}}, \quad (3.29)$$

where Ψ_{PM} is the permanent magnet flux linkage, L_d and L_q are the inductance expressed in the rotor reference frame, while i_d and i_q are the currents in the same coordinate system. Equation (3.29) is constituted by a component related to the interaction of the permanent magnet and the q -axis current called synchronous torque and a term related to the reluctance variation called reluctance torque. In the case of isotropic machines, such as PMSMs with superficially mounted magnets, $L_d \simeq L_q$ and thus equation (3.29) can be written as:

$$T_m = K_T i_q, \quad (3.30)$$

where $K_T = \frac{3}{2}n_p\Psi_{PM}$ is the torque constant of the motor. Moreover, in the FOC of PMSMs, the machine is typically controlled with a current reference $i_d^* = 0$ A, and thus expression (3.30) stands even in case anisotropies are present. For the sake of brevity, the analysis will be limited to PMSMs since they are the kind of motor employed in the experimental validation of the proposed torque-sensorless control in Chapter 4. The interested reader can find further information about BLDCs in [120].

3.1.4 Gravity force

Gravity affects the bicycle longitudinal dynamics in the presence of a road slope. In particular, its component in the longitudinal direction of motion F_g has a resisting effect in uphill riding $F_g < 0$ and a propulsive effect in downhill riding $F_g > 0$. The gravity force expression can be written as follows:

$$F_g = mg \sin(\beta), \quad (3.31)$$

where m is the total mass of the vehicle equal to the sum of the masses of the bicycle, the cyclist, and the carried cargo, $g = 9.80665 \frac{m}{s^2}$ is the gravitational acceleration on earth, and β is the road slope angle. Figure 3.11 shows the bicycle gravity force in case of uphill and downhill riding, where the weight mg is applied to the Center of Gravity (CoG) of the system and \mathbf{N} is the normal to the surface weight force component.

The steepness, slope, gradient, or grade of the road can be defined either as an angle β or as a ratio of elevation increase or rise h per unit distance traveled horizontally or run d and typically expressed as a percentage $\beta\%$:

$$\beta\% = \frac{h}{d} \cdot 100. \quad (3.32)$$

The road slope angle can be obtained from equation (3.32) as follows:

$$\beta = \arctan\left(\frac{\beta\%}{100}\right). \quad (3.33)$$

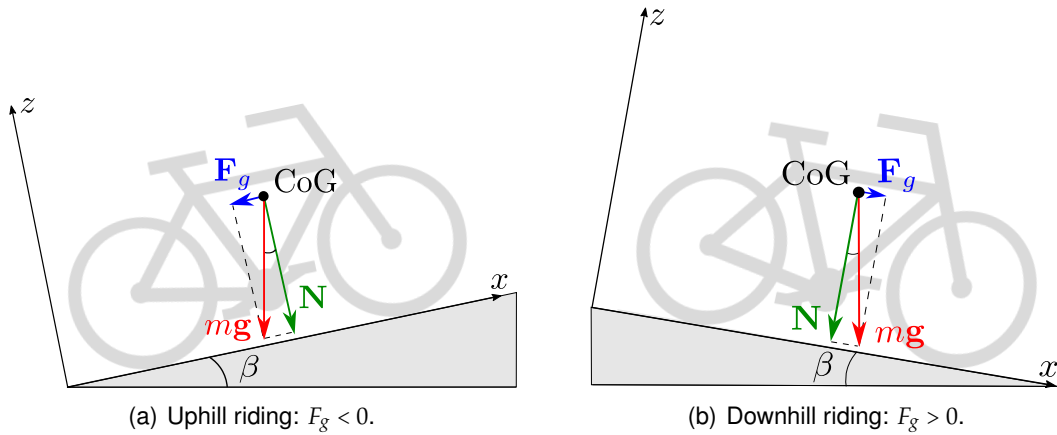


Figure 3.11: Gravity force F_g in bicycle longitudinal dynamics.

Small inclines around $\beta_{\%} = 0.1\%$ can be barely sensed by a cyclist. Modest hills have a grade ranging between $\beta_{\%} \in [3;6]\%$. Slopes $\beta_{\%} \geq 12\%$ are considered hard to ascend with a bicycle. Some roads can have short stretches whose steepness reaches $\beta_{\%} \in [20;25]\%$. Moreover, the slope on rough terrain can be $\beta_{\%} \geq 25\%$. The steepest listed road in the world is in Harlech, Wales, with a grade of $\beta_{\%} = 37.5\%$. [1]

3.1.5 Rolling friction force

The rolling friction force F_r is the force required to roll a loaded wheel at a constant speed. This friction force is commonly defined as follows:

$$F_r = \mu N = \mu mg \cos(\beta), \quad (3.34)$$

where μ is the rolling friction coefficient. Equation (3.34) represents a commonly accepted empirical approximation. Nonetheless, no proof of its validity and its independence from the vehicle speed exists. The rolling friction can be caused by the tire resistance when conforming to a harder road or by the ground resistance encountered when the tires sink into softer ground. Tire rolling resistance is the most commonly encountered and is caused by the energy losses in the deformation and rubbing of the rolling tires on the road. This deformation has a hysteretic behavior that strongly depends on the tire material, its geometry, frequency of deformation, inflation pressure, and temperature. Concerning ground rolling, the resisting force is caused by the additional work needed to press the tires into the surface. The rolling friction coefficient μ ranges from 0.002 in high-quality racing tires with high pressure to circa 0.01 in tires of utility bicycles with low pressure [1]. The rolling friction coefficient is not constant with the tire speed, temperature, and pressure. Indeed, its value increases slightly with increasing velocity. However, higher speeds increase the tire temperature and hence its pressure. An increment in temperature and pressure reduces the rolling friction coefficient balancing the effect of velocity. Other sources of rolling friction in bicycles are related to the bearings and mounting imperfections of the wheels. The impact of bearings on rolling friction is negligible compared to the effect of the wheels unless they are mounted too tightly. More-

over, imperfect wheels, a misaligned mounting, or an uneven tire can considerably increase the rolling resistance.

3.1.6 Aerodynamic drag force

The aerodynamic drag force F_a is the resisting force caused by the motion of the bicycle relative to air. This resisting force is composed of two main components: the pressure drag and the skin-friction drag. The first is caused by pushing and accelerating aside the air directly ahead of the rider. The second is generated by the fluid friction on the object surface moving through the air. However, in bicycles without fairings, the skin-friction drag can be considered negligible compared to the pressure one. Evaluating the work done by the cyclist to accelerate and push aside a mass of air directly ahead of the cyclist, the resisting force can be expressed as:

$$F_a = \text{sgn}(v_{a_x}) \frac{1}{2} \rho C_d A v_{a_x}^2, \quad (3.35)$$

where ρ is the density of air, C_d is the drag coefficient, A is the frontal area of the cyclist plus the bicycle, and v_{a_x} is the relative air velocity along the longitudinal direction of motion. In reality, the frontal area does not encounter all air evenly. Thus, the drag coefficient represents a correction term employed to account for the imperfection of the formula in a real scenario. The effective encountered area commonly used to model this imperfection is the drag area $A_d = C_d A$. When the skin-friction is negligible, the drag coefficient C_d is almost constant with velocity. Nevertheless, the drag coefficient, the frontal area, and hence the drag area vary with the rider dimensions, position while riding, bicycle shape, and dressed clothes. For instance, riding a bicycle in the upright position, in the so-called touring position (with the hands on a dropped handlebar), or a crouched position changes the drag area considerably. For the aforementioned reasons, racing bicycles are typically optimized to reduce this area compared to commuting bicycles. Moreover, professional cyclists wear tight clothes to minimize the drag area. Table 3.2 reports typical values of drag coefficients taken from [1].

Rider and bicycle	Drag coefficient C_d	Frontal area A in m^2	Drag area A_d in m^2
Upright position, commuting bicycle	1.15	0.55	0.63
Touring position, road bicycle	1	0.4	0.4
Crouched position, tight clothes, racing bicycle	0.88	0.36	0.32

Table 3.2: Typical values of drag coefficients in bicycles [1].

Another parameter that affects the aerodynamic drag force is the density of air whose value is not constant and varies with temperature, humidity, and altitude. In the case of dry

air, the expression of air density is obtained from the ideal gas law:

$$\rho = \frac{p}{R_s \Theta} \quad (3.36)$$

where p is the absolute pressure expressed in Pa , $R_s = 287.05 \frac{J}{kgK}$ is the specific gas constant for dry air, and Θ is the absolute temperature expressed in K . Thus, the air density decreases with the increasing air temperature and increases with the increasing atmospheric pressure. The value of dry air density at room temperature of $\Theta = 20^\circ C$ at the sea level is $\rho = 1.2 \frac{kg}{m^3}$. The air density also decreases with increasing humidity because the molar mass of water vapor is smaller than the one of dry air. Furthermore, in the troposphere, an increasing altitude reduces the air temperature and atmospheric pressure leading to a decrease in the air density.

The aerodynamic drag force also depends on the apparent wind v_a and particularly on its component along the longitudinal direction v_{a_x} . This speed equals the bicycle ground speed v when the wind is neglected: $v_{a_x} = v$. In the presence of wind, it increases in case of headwind $v_{w_x} > 0$ leading to an increase in the aerodynamic drag and decreases in case of tailwind $v_{w_x} < 0$ causing a decrease of the drag force or a sailing force when $|v_{w_x}| > |v|$. Figure 3.12 contains two examples of airspeed \mathbf{v}_a calculation in case of head and tailwind speed \mathbf{v}_w and ground speed of the bicycle \mathbf{v} . For simplicity in the representation, the wind has been considered acting in the horizontal plane $x - y$ and expressed in the wind reference frame where a headwind is considered with a positive sign. It can be seen that the component of the airspeed along the longitudinal direction can be expressed as the sum of the ground speed of the bicycle plus the projection of the real wind speed along the longitudinal direction:

$$\mathbf{v}_{a_x} = \mathbf{v} + \mathbf{v}_{w_x} \quad (3.37)$$

It has to be remarked, that equation (3.37) is valid even when considering a three-dimensional wind speed vector.

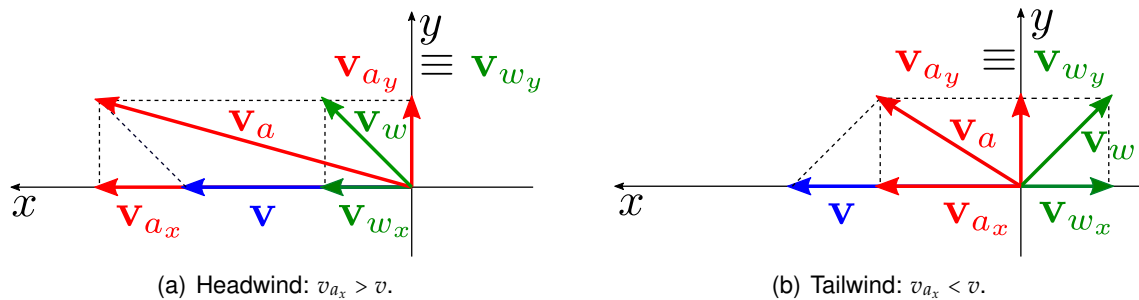


Figure 3.12: Air velocity \mathbf{v}_a in the presence of wind \mathbf{v}_w and bicycle speed \mathbf{v} in the horizontal plane.

3.1.7 Bump force

The presence of bumps on the road affects the motion of the bicycle. In the case of reduced bumpiness, bump losses are commonly treated as rolling friction even if the energy losses do

not occur in the wheels. Small bump losses dissipate in the frame, suspensions, and cyclist body. On the other hand, large bumps can cause a system center of mass variation that may lead to a change of the vehicle motion direction and significant energy losses. In bicycles, the rider mass absorbs, intentionally or not, a considerable amount of vibrations leading to energy losses. In particular, according to [121], energy absorption correlates with discomfort perception. Thus, an improvement in the perceived comfort while riding reduces the energy losses related to bumps. The speed losses caused by bumps can be minimized by the tires, suspensions, and intentional movements of the rider. However, an analytic expression to describe the bump losses does not exist. Since most roads are reasonably smooth and the effect of bump losses is not predictable or quantifiable, they will be covered by the rolling friction in the mathematical formulation reported in this work.

3.1.8 Braking force

The purpose of braking is to reduce the bicycle speed and thus its kinetic energy. This energy can be dissipated as heat into the environment or converted into electrical energy in the case of regenerative braking. When braking a bicycle, a resisting force F_B is applied. In standard bicycles, the braking force is caused by friction in contact surfaces that occur in the brake-wheel and wheel-road contacts. Braking forces are produced when the contact surfaces slip between each other, namely in kinetic friction conditions. The ratio between the normal force that presses the two surfaces \mathcal{F}_{f_N} and the frictional resistance to motion \mathcal{F}_{f_P} is called kinetic friction coefficient $\mu_f = \frac{\mathcal{F}_{f_P}}{\mathcal{F}_{f_N}}$. This coefficient depends on the contact material type, lubrication, and temperature. There exist many technologies of friction bicycle brakes that can be classified into five types: plunger, drum, coaster, disk, and rim brakes. Among them, the rim brakes are the most worldwide spread type. In this kind of brake, a rubber pad is forced against the surface of the wheel rim generating a braking torque. In addition, the wheel-road contact can generate a braking force in case of wheel-slipping. In this situation, the wheel-road kinetic friction coefficient depends on the tire type of rubber, the road roughness and wetness, and the contact surface temperature. Since the braking force depends on the particular braking system and wheel-road interaction, a generic mathematical expression of the braking force cannot be derived. Nevertheless, neglecting the wheels-slipping effect and assuming to know the total torque applied on the front and rear wheels by the brakes T_B , the braking force can be expressed as:

$$F_B = \frac{T_B}{r}. \quad (3.38)$$

3.1.9 Global considerations

When the driving forces differ from the resisting ones, a variation of kinetic energy and hence an acceleration or deceleration of the bicycle is caused. This force of acceleration or inertia force F_I is expressed as follows:

$$F_I = ma, \quad (3.39)$$

where a is the bicycle acceleration in the longitudinal direction. The caused variation of kinetic energy is equal to the product of the inertia force times the distance over which it is applied. Thus, this energy variation will be very high when starting the bicycle or braking it and will be zero in steady-state conditions where $a = 0 \frac{m}{s^2}$. From the consideration previously made about the driving and resisting forces, equation (3.1) can be expressed in its extended form:

$$\eta_d \frac{T_{pc}}{r\tau_d} + F_h^e + \eta_m \frac{T_m}{r\tau_m} - mg \sin(\beta) - \mu mg \cos(\beta) - \text{sgn}(v_{ax}) \frac{1}{2} \rho A_d v_{ax}^2 - \frac{T_B}{r} = ma. \quad (3.40)$$

3.2 Resisting forces sensitivity analysis

In this section, the effect of parametric variations on the required propulsive power needed to overcome the resisting forces is analyzed through a sensitivity analysis. In particular, the latter evaluates the power applied by the cyclist and the motor at given speeds in different realistic environmental scenarios. This analysis allows the evaluation of the parametric variability influence on the longitudinal dynamics (3.40) and of the error relevance when considering a typical value of each parameter instead of the actual value in the mathematical modeling. Based on the considerations made in this section, a simplified vehicle dynamic model is derived and utilized in the proposed pedaling torque estimators in Chapter 4.

In the following, the time-variant parameters of equation (3.40), namely the road grade $\beta_{\%}$, the system mass m , the rolling friction coefficient μ , the drag area A_d , the air density ρ , and the wind speed v_{w_x} , are discussed. Parameters such as the wheel radius r , the drivetrain transmission ratio τ_d , and the one of the motor τ_m are not analyzed since they are constant or known by design. Moreover, the drivetrain η_d and motor efficiencies η_m are here neglected because their typical value is close to 1. Additionally, the analysis is performed considering a gravity acceleration $g = 9.80665 \frac{m}{s^2}$. Depending on the analyzed parameter, the power variation is evaluated by varying the parameter of interest and fixing the others to typical values within their variability range. Table 3.3 reports the chosen fixed parameter values and the analyzed parametric variability range employed in this sensitivity analysis. Although, as stated in Section 3.1.4, steeper road grade may be experienced while riding, the analysis is here limited to the typical range of variation $\beta_{\%} \in [0; 10]$ %. Negative inclines are not considered here since they generate a propulsive force independently from the speed level, as clear from equation (3.31). A typical total system mass variability range $m \in [60; 140]$ kg (including the bicycle, the cyclist, and the cargo) has been considered. Based on the considerations of Section 3.1.5, the typical variability range of the rolling friction coefficient $\mu \in [0.002; 0.01]$ has been evaluated. Similarly, the common drag area range $A_d \in [0.32; 0.4]$ m², defined in Table 3.2, has been taken into account. An air density variability range $\rho \in [1.14; 1.3]$ $\frac{kg}{m^3}$ has been analyzed considering values of dry air density at sea level in the typical cycling temperature range $\Theta \in [0; 35]$ °C. The effect of an increasing altitude or humidity level is here neglected since it causes a reduction of the air density leading to similar results to a temperature variation. Furthermore, wind levels in the range $v_{w_x} \in [-10; 10]$ $\frac{km}{h}$ are examined. It is necessary to remark that values outside the above-defined ranges can rarely occur during cycling and therefore are not covered in this analysis. Following, the selection criteria of the fixed values are discussed. The average road slope $\beta_{\%} = 5$ % within the defined variability range has been picked. Whereas, a common system mass value

3.2 Resisting forces sensitivity analysis

$m = 100 \text{ kg}$ equal to the sum of a cyclist 70 kg , an electric bicycle 30 kg , and no cargo has been chosen. A rolling friction coefficient fixed value $\mu = 0.005$ representing an intermediate case between racing and commuting tires has been selected. Moreover, a fixed drag area value $A_d = 0.4 \text{ m}^2$ corresponding to a cyclist in a touring position riding a road bike has been picked as an intermediate value between commuting and race cycling. Additionally, a typical air density $\rho (20^\circ \text{C}) = 1.2 \frac{\text{kg}}{\text{m}^3}$ is taken into account. Ultimately, the absence of wind $v_{w_x} = 0 \frac{\text{km}}{\text{h}}$ has been considered as a commonly experienced riding condition and selected as fixed value in the sensitivity analysis.

Parameter	Fixed value	Variability range
Road slope $\beta_{\%}$ in %	5	[0;10]
System Mass m in kg	100	[60;140]
Rolling friction coefficient μ	0.005	[0.002;0.01]
Drag area A_d in m^2	0.4	[0.32;0.63]
Air density ρ in $\frac{\text{kg}}{\text{m}^3}$	1.2	[1.14;1.30]
Wind speed v_{w_x} in $\frac{\text{km}}{\text{h}}$	0	[-10;10]

Table 3.3: Parametric values employed in the sensitivity analysis and their typical variability range.

The following analysis, illustrated in Figure 3.13, compares the power required to overcome the single resisting forces within the typical cycling speed range $v \in [0; 30] \frac{\text{km}}{\text{h}}$, namely the gravity $P_g = F_g v$, the rolling friction $P_r = F_r v$, and the aerodynamic drag $P_a = F_a v$. It has to be remarked that sailing effects are not shown in the presence of tailwinds in Figure 3.13(f). As one can notice, the power needed to overcome the gravity force depends only on the slope and on the system mass. In particular, from Figures 3.13(a) and 3.13(b) it can be seen that slope variations have a higher influence than mass value modifications. Furthermore, Figure 3.13(a) shows that in level ground riding $\beta_{\%} = 0 \%$, the gravity does not influence the vehicle motion at all. As clear from equation (3.34), the power required to overcome the rolling friction depends also on the rolling friction coefficient. Figure 3.13(a) shows that the influence of the road slope on this resisting component is negligible since this term depends on the cosine of the slope angle. Whereas, in Figures 3.13(b) and 3.13(c) one can notice that variations of system mass and rolling friction coefficient influence the rolling resistance considerably. In particular, typical rolling friction coefficient variations have a higher impact than changes in system mass. Contrary to the previously seen resisting forces, the aerodynamics depends on the drag area, the air density, and the wind speed. It can be noticed that the presence of wind has the highest impact on the power needed to overcome the aerodynamic resistance, followed by variations of the drag area whose influence is significant, especially in the high-speed range. Figure 3.13(e) shows that the effects of air density variations are negligible compared to the other parametric variations and noticeable only at high speeds. Considering the resisting components simultaneously, it can be seen that, in the absence of wind and slope, at speeds lower than circa $v < 15 \frac{\text{km}}{\text{h}}$, the rolling resistance is

the dominant resisting component. While at speeds higher than circa $v > 15 \frac{km}{h}$, the majority of propulsive power is used to overcome the aerodynamic resistance. However, it has to be remarked that this speed threshold value can slightly vary depending on the chosen fixed parameters. Moreover, in the presence of a noticeable road grade, the propulsive power is employed primarily to overcome the effect of gravity.

Afterwards, the typical variability of the total power required to overcome the resisting forces $P_R = P_g + P_r + P_a$ is analyzed in Figure 3.14. It has to be remarked that in this figure, the total power required to overcome the resisting forces when the system presents the fixed parameters of Table 3.3 is reported in black. Moreover, for the sake of a more clear graphical representation, the effect of the parametric variation has been divided into two subfigures. Figure 3.14(a) represents the effect of road grade, vehicle mass, and rolling friction coefficient variations on the total required power, while Figure 3.14(b) analyses the same effect caused by variations of the drag area, air density, and wind speed. It can be seen that a variation in road grade has the largest impact on the total required power. A mass variation has a significant influence on the longitudinal dynamics. However, its impact is smaller than the one of a slope variation. At high speeds, the presence of wind can affect considerably the longitudinal dynamics with an impact comparable to a mass variation. Besides, as stated before, variations of the rolling friction coefficient have a bigger impact on the total required power at low speeds while variations of the drag area influence the dynamics more at high velocities. Furthermore, it can be seen that the effect of air density variations is negligible compared to variations of the other parameters. Eventually, one can conclude that all parametric variations have a bigger impact on bicycle dynamics at high speeds.

3.2 Resisting forces sensitivity analysis

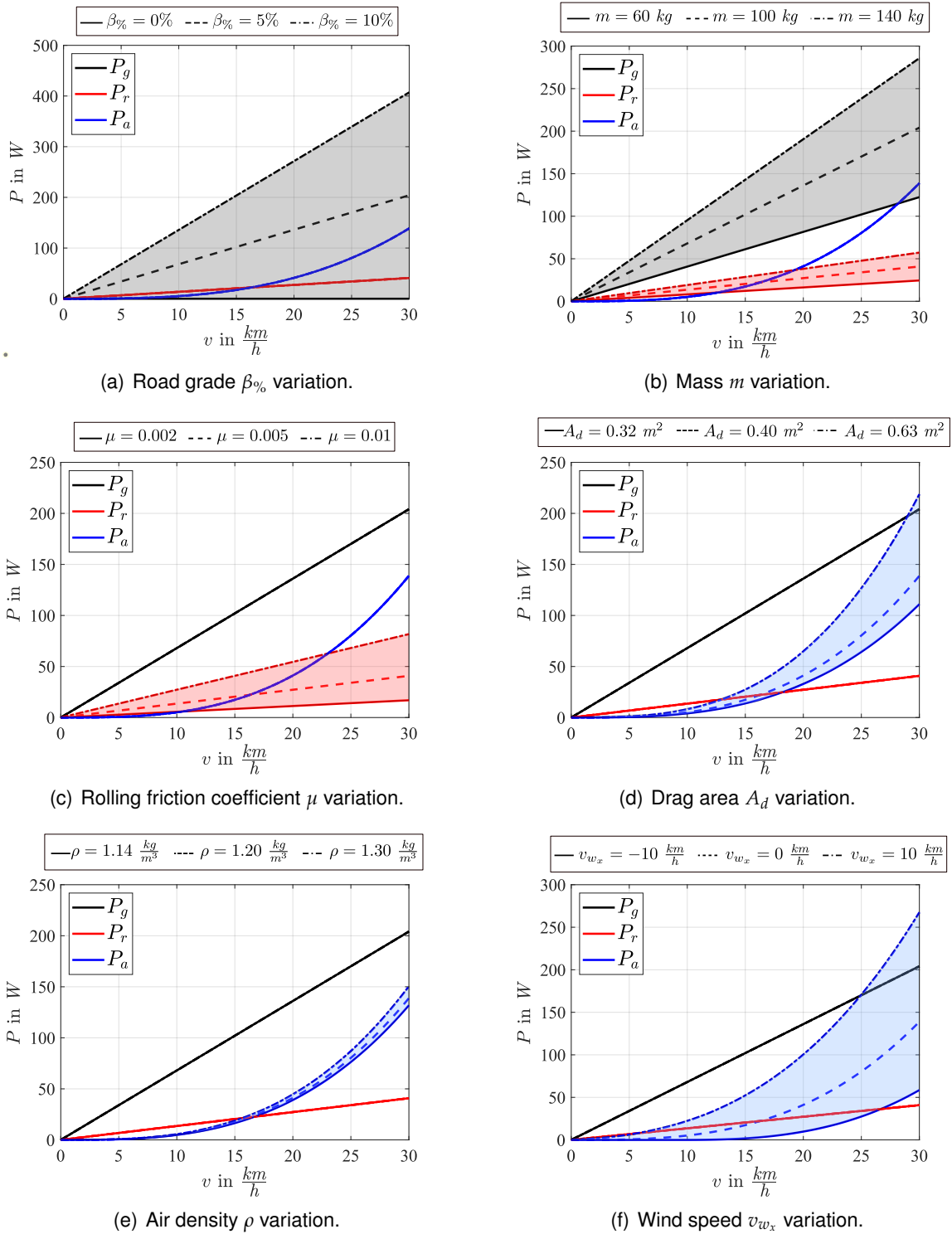
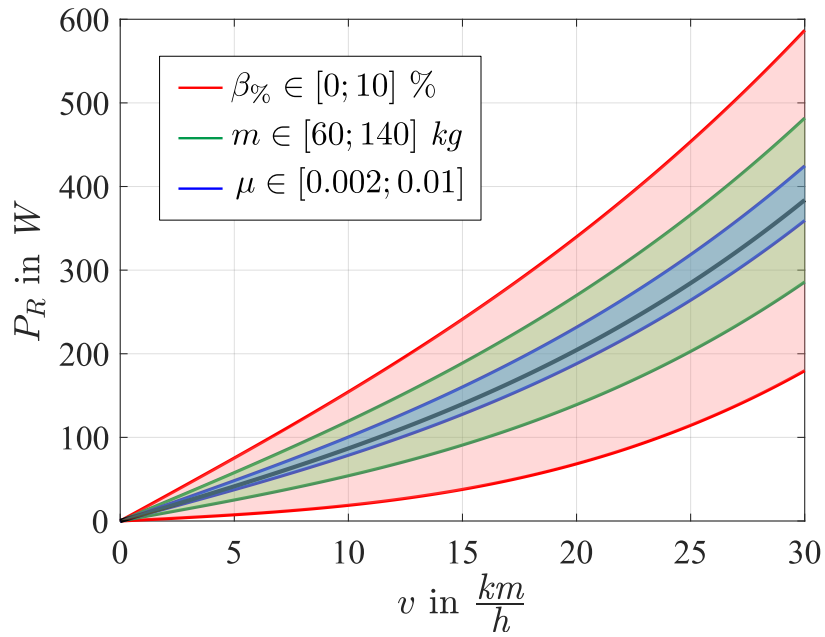
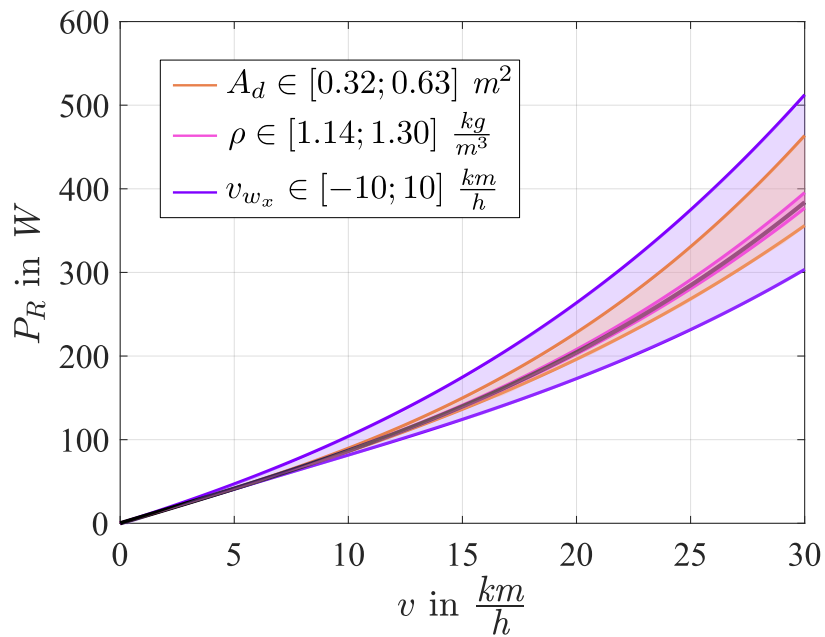


Figure 3.13: Parametric variability of the propulsive power required to overcome the single resisting forces (gravity P_g , rolling P_r , and aerodynamic P_a resistances) at different speed levels v .



(a) Effect of road grade $\beta_{\%}$, mass m , and rolling friction coefficient μ variations.



(b) Effect of drag area A_d , air density ρ , and wind speed v_{w_x} variations.

Figure 3.14: Range of parametric variability of the total power required to overcome the resisting forces P_R at different speed levels v .

4 Pedaling torque estimation

In this chapter, two UIO-based pedaling torque estimation techniques for pedelecs, named PTOs, are proposed and described in detail. Firstly, the state-space observation fundamentals applied to the case of linear and nonlinear systems and specifically the Kalman filtering theory are recalled. Afterwards, a state variables representation of the system that contains the bicycle longitudinal dynamics and the pedaling torque modeling is derived from the considerations made in Chapter 3. Simplifying assumptions are made on the bicycle longitudinal dynamics equation (3.40) to achieve a system description that allows a sufficiently accurate torque-sensorless pedaling torque estimation in the low-speed range with a reduced system complexity and number of employed sensors. To accomplish this purpose, two PTOs relying on different pedaling torque models are considered and compared, namely a constant (CPTO) and a sinusoidal one (SPTO). The two proposed nonlinear state-space representations are expressed as EKFs and rely on motor torque, road slope, and bicycle speed measurements. However, these quantities are indirectly measured and can be affected by errors that might deteriorate the pedaling torque estimation quality. Thus, this chapter analyzes the measurement process and possible sources of errors. Among them, the road grade has particular importance, since, as shown in Section 3.2, its variation can significantly affect the bicycle dynamics. After analyzing the road slope estimation techniques known in the literature, an UIO in the form of a KF that estimates the road slope without increasing system complexity and costs is proposed. Besides, a method to correct the road grade estimation error caused by the bicycle cornering is investigated. Eventually, the chapter contains simulations of the proposed PTOs that allow the evaluation of the KF tuning impact on the state estimation and the analysis of the employed modeling simplifications assets and drawbacks.

4.1 State observation theory

This section briefly introduces the reader to the theory of state observation and the particular case of Kalman filtering. Firstly, linear and nonlinear state-space models in continuous and discrete time domains are introduced. Then, linear systems observation made through the Luenberger observer is presented. After, the analysis focuses on the observability of linear and nonlinear systems. Later on, Kalman filtering is introduced. In particular, the KF and EKF algorithms and their application to discrete-time linear and nonlinear systems are discussed in detail.

4.1.1 State-space models and observability

As seen in Section 1.1, the pedaling torque T_{pc} can be estimated employing disturbance estimation approaches that, when using state observers, are referred as UIOs. A state observer is a system that estimates the internal state of another system \hat{x} from its input \mathbf{u} and

measured output \mathbf{y} . It is typically digital-implemented and thus expressed in the discrete-time domain. Figure 4.1 contains a schematic representation of a discrete-time state observer where $k \in \mathbb{Z}$ is the discrete time variable.

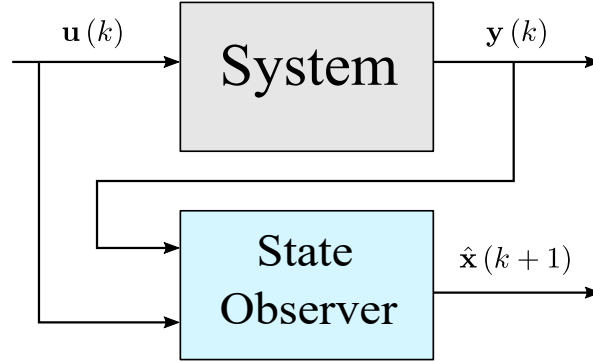


Figure 4.1: Schematic representation of a discrete-time state observer.

A continuous-time-invariant linear system can be expressed with a state-space representation:

$$\begin{aligned} \frac{d\mathbf{x}(t)}{dt} &= \mathbf{A}\mathbf{x}(t) + \mathbf{B}\mathbf{u}(t), \\ \mathbf{y}(t) &= \mathbf{C}\mathbf{x}(t) \end{aligned} \quad (4.1)$$

where $\mathbf{x}(t) \in \mathbb{R}^n$ is the state-space vector composed of n state variables, $\mathbf{u}(t) \in \mathbb{R}^m$ is the input vector composed of m input signals, $\mathbf{y}(t) \in \mathbb{R}^p$ is the output vector composed of the p measurements of the system, $\mathbf{A} \in \mathbb{R}^{n \times n}$ is the state matrix, $\mathbf{B} \in \mathbb{R}^{n \times m}$ is the input matrix, $\mathbf{C} \in \mathbb{R}^{p \times n}$ is the output matrix, and $t \in \mathbb{R}$ is the continuous time variable. It has to be remarked that models with input-output feedthrough are neglected in this work. The more general form of a continuous-time state-space model valid for a nonlinear system can be written as:

$$\begin{aligned} \frac{d\mathbf{x}(t)}{dt} &= f(\mathbf{x}(t), \mathbf{u}(t)), \\ \mathbf{y}(t) &= h(\mathbf{x}(t)) \end{aligned} \quad (4.2)$$

where $f(\cdot, \cdot)$ and $h(\cdot)$ are nonlinear functions. The digital implementation of a state observer requires the discretization of continuous-time state-space representation and a proper sampling time T_s selection according to the Nyquist-Shannon sampling theorem. The discretized version of the state-space model (4.1) can be written as:

$$\begin{aligned} \mathbf{x}(k+1) &= \mathbf{F}\mathbf{x}(k) + \mathbf{G}\mathbf{u}(k) \\ \mathbf{y}(k) &= \mathbf{H}\mathbf{x}(k) \end{aligned} \quad (4.3)$$

where $\mathbf{F} = e^{\mathbf{A}T_s}$ is the discretized state matrix, $\mathbf{G} = \int_0^{T_s} e^{\mathbf{A}\tau} d\tau \mathbf{B}$ is the discretized input matrix, and $\mathbf{H} = \mathbf{C}$ is the discretized output matrix. Due to heavy matrix exponentials and integrals calculations, the exact discretization may be complex to calculate. However, when selecting a sufficiently small sampling time, the discrete model can be simplified and easily calculated introducing a negligible approximation error. Methods like the forward Euler, the backward

Euler, and the Tustin one can be employed. For the simplicity of its approximation, the forward Euler method will be employed in this work. This method leads to the following expressions of the discretized matrices: $\mathbf{F} \simeq \mathbf{I} + T_s \mathbf{A}$, $\mathbf{G} \simeq T_s \mathbf{B}$, and $\mathbf{H} = \mathbf{C}$, where \mathbf{I} represents the identity matrix. Nevertheless, particular attention must be paid in the selection of the sampling time since in the forward Euler approximation a too large value may result in an unstable discretized system. In the generic case of a nonlinear system, the discretized state-space model can be written as:

$$\begin{aligned} \mathbf{x}(k+1) &= f_d(\mathbf{x}(k), \mathbf{u}(k)) \\ \mathbf{y}(k) &= h_d(\mathbf{x}(k)) \end{aligned} \quad (4.4)$$

where $f_d(\cdot, \cdot)$ and $h_d(\cdot)$ are nonlinear functions.

Considering a linear system, the continuous-time state observer, also called Luenberger observer, that allows the estimation of the system (4.1) state has the following expression:

$$\frac{d\hat{\mathbf{x}}(t)}{dt} = [\mathbf{A} - \mathbf{K}\mathbf{C}] \hat{\mathbf{x}}(t) + \mathbf{B}\mathbf{u}(t) + \mathbf{K}\mathbf{y}(t), \quad (4.5)$$

where $\hat{\mathbf{x}}(t)$ is the estimated state vector and $\mathbf{K} \in \mathbb{R}^{n \times p}$ is the Luenberger observer gain matrix [122]. Discretizing equation (4.5), the discretized version of the Luenberger observer can be obtained:

$$\hat{\mathbf{x}}(k+1) = [\mathbf{F} - T_s \mathbf{K}\mathbf{H}] \hat{\mathbf{x}}(k) + \mathbf{G}\mathbf{u}(k) + T_s \mathbf{K}\mathbf{y}(k). \quad (4.6)$$

The system internal state estimation is possible only if the system is completely observable. In particular, “a discrete-time system is observable if for any initial state $\mathbf{x}(k_i)$ and some final time k_f , the initial state can be uniquely determined by the knowledge of the input $\mathbf{u}(k)$, and output $\mathbf{y}(k)$ for $k \in [k_i, k_f]$ ” [123]. If the system is observable, the initial state and thus all states between the initial and the final times can be determined. To test the observability of the system, one possible approach consists in defining the observability matrix \mathcal{O} :

$$\mathcal{O} = [\mathbf{H} \quad \mathbf{H}\mathbf{F} \quad \dots \quad \mathbf{H}\mathbf{F}^{n-1}]^T. \quad (4.7)$$

The system results completely observable when the observability matrix of the system has full rank ($\text{rank}(\mathcal{O}) = n$).

In the case of nonlinear systems, the generic discrete-time Luenberger observer can be expressed as:

$$\hat{\mathbf{x}}(k+1) = f_d(\hat{\mathbf{x}}(k), \mathbf{u}(k)) + \mathbf{K}[\mathbf{y}(k) - h_d(\hat{\mathbf{x}}(k))]. \quad (4.8)$$

When considering nonlinear systems, the observability is much more complex to formalize [123]. A common approach used in nonlinear systems observation consists in linearizing the system around a reference trajectory and employing the linearized system to estimate the state. As stated in [124], the observability of a linearized system implies the local observability of the original nonlinear one, namely that a neighborhood of the initial state such that the system is completely observable exists.

4.1.2 Kalman filtering

The system internal state observation can rely on different kinds of state observers, as shown in [22]. Among them, the KF has been selected in this work due to its optimal estimation capability in the presence of noise and its comprehensible tuning based on the selection of the covariance matrices. Moreover, it allows to easily handle with nonlinear systems by employing the extended form of the algorithm. The KF digital implementation requires a representation of the system in the discretized linear system state-space model form (4.3). Compared to the Luenberger observer, a KF models the noise and uncertainties affecting the process and the measurements employing the following linear stochastic difference equations:

$$\begin{aligned} \mathbf{x}(k) &= \mathbf{F}\mathbf{x}(k-1) + \mathbf{G}\mathbf{u}(k-1) + \mathbf{w}(k-1) \\ \mathbf{y}(k) &= \mathbf{H}\mathbf{x}(k) + \mathbf{v}(k) \end{aligned} \quad (4.9)$$

where $\mathbf{w} \in \mathbb{R}^n$ represents disturbances and unmodelled dynamics acting on the system and $\mathbf{v} \in \mathbb{R}^p$ represents the noise acting on the measurements. In the KF, the stochastic processes \mathbf{w} and \mathbf{v} are white and Gaussian. Thus, they are zero-mean $E[\mathbf{w}] = E[\mathbf{v}] = \mathbf{0}$, uncorrelated $E[\mathbf{v}\mathbf{w}^T] = \mathbf{0}$, and have known covariance matrices $\mathbf{Q} = E[\mathbf{w}\mathbf{w}^T]$ and $\mathbf{R} = E[\mathbf{v}\mathbf{v}^T]$ respectively, where $E[\cdot]$ represents the statistic expected value operator and $\mathbf{0}$ the null matrix. Defining the estimation error vector $\boldsymbol{\varepsilon}(k) = \mathbf{x}(k) - \hat{\mathbf{x}}(k) \in \mathbb{R}^n$, the estimation error covariance matrix $\mathbf{P}(k) \in \mathbb{R}^{n \times n}$ is expressed as:

$$\mathbf{P}(k) = E[\boldsymbol{\varepsilon}(k)\boldsymbol{\varepsilon}^T(k)]. \quad (4.10)$$

In the KF algorithm, the state estimate $\hat{\mathbf{x}}(k)$ and the estimation error covariance matrix $\mathbf{P}(k)$ are propagated at each time instant k . This algorithm splits up into prediction and update tasks. At each time instant k during the prediction phase, the *a priori* state estimation $\hat{\mathbf{x}}^-(k)$ and the estimation error covariance matrix $\mathbf{P}^-(k)$ are calculated based on the previous knowledge of the process. During the update phase, the KF gain $\mathbf{K}(k)$ is calculated and used to evaluate the *a posteriori* state estimation $\hat{\mathbf{x}}^+(k)$ and the estimation error covariance matrix $\mathbf{P}^+(k)$ exploiting the measurement information. In the following, the KF algorithm steps are described in detail. Firstly, the algorithm is initialized considering the expected values of the state estimate and the estimation error covariance matrix:

$$\begin{aligned} \hat{\mathbf{x}}^+(0) &= E[\mathbf{x}(0)] \\ \mathbf{P}^+(0) &= E[\boldsymbol{\varepsilon}(0)\boldsymbol{\varepsilon}^T(0)] \end{aligned} \quad (4.11)$$

Then, at each $k \geq 1$, the prediction task takes place:

$$\mathbf{P}^-(k) = \mathbf{F}\mathbf{P}^+(k-1)\mathbf{F}^T + \mathbf{Q}, \quad (4.12)$$

$$\hat{\mathbf{x}}^-(k) = \mathbf{F}\hat{\mathbf{x}}^+(k-1) + \mathbf{G}\mathbf{u}(k-1). \quad (4.13)$$

After that, the update phase begins:

$$\mathbf{K}(k) = \mathbf{P}^-(k) \mathbf{H}^T [\mathbf{H} \mathbf{P}^-(k) \mathbf{H}^T + \mathbf{R}]^{-1}, \quad (4.14)$$

$$\hat{\mathbf{x}}^+(k) = \hat{\mathbf{x}}^-(k) + \mathbf{K}(k) [\mathbf{y}(k) - \mathbf{H} \hat{\mathbf{x}}^-(k)], \quad (4.15)$$

$$\mathbf{P}^+(k) = [\mathbf{I} - \mathbf{K}(k) \mathbf{H}] \mathbf{P}^-(k). \quad (4.16)$$

Under the KF hypotheses, the error covariance matrix is minimized at each step, namely the mean squared estimation error. Moreover, the KF is the best linear state observer that minimizes this matrix when the stochastic process acting on the system is white and Gaussian. Nevertheless, the KF optimality can be exploited with some modifications to the observer structure to estimate the system state even when the before-mentioned hypotheses are not fulfilled. [123]

In the case of nonlinear dynamical systems, the EKF can be employed to estimate the system state. In this approach, the nonlinear discrete-time system is linearized around a nominal state trajectory, employing the KF state estimate as a nominal trajectory. In other words, the nonlinear system is linearized around the state estimate obtained from the KF applied to the linearized system. The EKF estimates the state of a nonlinear discrete-time system described by the following stochastic difference equations:

$$\begin{aligned} \mathbf{x}(k) &= f_d(\mathbf{x}(k-1), \mathbf{u}(k-1), \mathbf{w}(k-1)) \\ \mathbf{y}(k) &= h_d(\mathbf{x}(k), \mathbf{v}(k)) \end{aligned} \quad (4.17)$$

The EKF algorithm initialization is performed as for the KF with equations (4.11). Then, for each $k \geq 1$, firstly the partial derivative or Jacobian matrices \mathbf{J}_F and \mathbf{J}_L are calculated as follows:

$$\begin{aligned} \mathbf{J}_F(k-1) &= \left. \frac{\partial f_d(\mathbf{x}(k-1), \mathbf{u}(k-1), \mathbf{w}(k-1))}{\partial \mathbf{x}} \right|_{\hat{\mathbf{x}}^+(k-1)} \\ \mathbf{J}_L(k-1) &= \left. \frac{\partial h_d(\mathbf{x}(k-1), \mathbf{u}(k-1), \mathbf{w}(k-1))}{\partial \mathbf{w}} \right|_{\hat{\mathbf{x}}^+(k-1)}. \end{aligned} \quad (4.18)$$

Then, the prediction phase takes place:

$$\mathbf{P}^-(k) = \mathbf{J}_F(k-1) \mathbf{P}^+(k-1) \mathbf{J}_F^T(k-1) + \mathbf{J}_L(k-1) \mathbf{Q} \mathbf{J}_L^T(k-1), \quad (4.19)$$

$$\hat{\mathbf{x}}^-(k) = f_d(\hat{\mathbf{x}}^+(k-1), \mathbf{u}(k-1), \mathbf{0}). \quad (4.20)$$

After that, the Jacobians \mathbf{J}_H and \mathbf{J}_M are calculated:

$$\begin{aligned} \mathbf{J}_H(k) &= \left. \frac{\partial h_d(\mathbf{x}(k), \mathbf{v}(k))}{\partial \mathbf{x}} \right|_{\hat{\mathbf{x}}^-(k)} \\ \mathbf{J}_M(k) &= \left. \frac{\partial h_d(\mathbf{x}(k), \mathbf{v}(k))}{\partial \mathbf{v}} \right|_{\hat{\mathbf{x}}^-(k)}. \end{aligned} \quad (4.21)$$

Finally, the update phase begins:

$$\mathbf{K}(k) = \mathbf{P}^-(k) \mathbf{J}_H^T(k) [\mathbf{J}_H(k) \mathbf{P}^-(k) \mathbf{J}_H^T(k) + \mathbf{J}_M(k) \mathbf{R} \mathbf{J}_M^T(k)]^{-1}, \quad (4.22)$$

$$\hat{\mathbf{x}}^+(k) = \hat{\mathbf{x}}^-(k) + \mathbf{K}(k) [\mathbf{y}(k) - h_d(\hat{\mathbf{x}}^-(k), \mathbf{0})], \quad (4.23)$$

$$\mathbf{P}^+(k) = [\mathbf{I} - \mathbf{K}(k) \mathbf{J}_H(k)] \mathbf{P}^-(k). \quad (4.24)$$

Since the EKF is based on the linearization of the system (4.17), the matrix \mathbf{P} does not exactly represent the estimation error covariance matrix. Nevertheless, in the case of non-severe nonlinear systems, like in the system under investigation, the linearization error is negligible. Thus, this matrix can be approximated to the estimation error covariance matrix. A schematic representation of the KF and EKF algorithms is reported in Figure 4.2. [123]

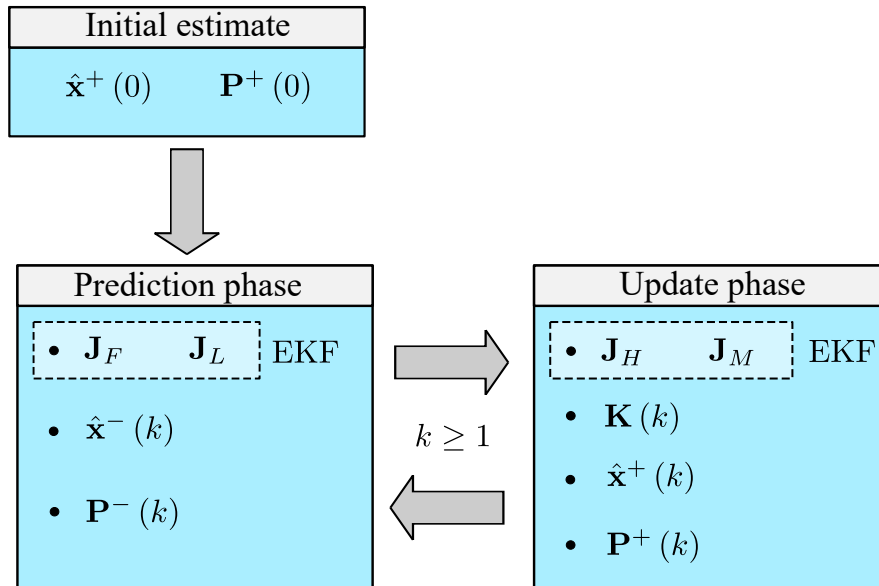


Figure 4.2: Block diagram of the KF including the EKF algorithm for nonlinear systems.

4.2 Pedaling torque observers

In this section, a state variables representation of the system is derived from equation (3.40) to obtain a model that can be used in a state observer structure to estimate the state of the system and particularly the pedaling torque T_{pc} . Firstly, the simplifying modeling hypotheses are expressed and discussed. Then, a state-space model is derived when a constant and a sinusoidal pedaling torque model is considered. Afterwards, the obtained models are expressed in the form of EKFs and their observability is proven.

4.2.1 Modeling hypotheses

Based on the considerations of Section 3.2 and the ones reported in [125], an analysis of the impact of parametric variations on the bicycle dynamics and their time variability allows us to make simplifying assumptions on the modeling equations. Table 4.1 contains the results of this qualitative analysis. It has to be remarked that the impact of parametric variations has been evaluated in the lower bicycle speed range $v \in [0; 15] \frac{km}{h}$ because more accuracy in the estimation of the pedaling torque is required at low speeds during the acceleration phases where the cyclist typically requires the highest electrical assistance rather than at high speeds where motor assistance can be dangerous or not admitted by the local legislation.

Parameter	Impact	Time variability
Mass m	Large	Very slow
Road slope β	Very large	Fast
Rolling friction coefficient μ	Medium	Medium
Air density ρ	Very small	Very slow
Drag Area A_d	Medium	Fast
Wind speed v_{w_x}	Medium	Very fast

Table 4.1: Parametric variability impact on the bicycle longitudinal dynamics.

The system mass m , the rolling friction coefficient μ , the drag area A_d , the air density ρ , and the wind speed v_{w_x} are considered time-invariant in this work. The system mass does not vary much once the cyclist starts pedaling and can thus be considered constant and equal to its initial value. In the case of the rolling friction coefficient, even if it can vary while riding depending on the factors analyzed in Section 3.1.5, its value is less time-variable and has a smaller impact than the road angle. The drag area may vary fast due to a change in the cyclist posture while riding but its influence on the longitudinal dynamics is small at low speeds. The air density, which depends on the air temperature, pressure, and humidity, varies slowly compared to the bicycle dynamics and has a negligible effect in the low-speed range. The air is rarely still and the wind can change direction unpredictably and rapidly within a few seconds [1]. Additionally, its longitudinal component can vary depending on

changes in riding direction and the influence of other vehicles on the road. However, the wind effect on the longitudinal dynamics is also typically small in the low-speed range. Thus, the wind speed is considered $v_{w_x} = 0 \frac{m}{s^2}$, i.e. $v_{a_x} = v$. Furthermore, for all the aforementioned parameters, an online measurement can hardly be performed without increasing the system complexity with additional sensors.

On the contrary, variations of the road slope occur very often while riding and have the highest impact on the longitudinal dynamics compared to the other parameters. Indeed, the road is rarely level or constant in slope. Moreover, slopes that seem to be smooth can vary in roughness [1]. Thus, the road slope angle $\beta(t)$ requires to be estimated during cycling. Additionally, in the system modeling other simplifying assumptions are made:

- Braking torques T_B and human propulsive forces not generated by pedaling F_h^e are not considered.
- Power losses in the mechanical transmissions are neglected $\eta_d = \eta_m = 1$.
- The model is derived under the assumption of no wheel-slipping and engaged drive-train.
- The gear ratios of the mechanical transmissions τ_d and τ_m are considered constant. Thus, gear variations are neglected.

4.2.2 State-space models

Under the hypotheses mentioned in section 4.2.1, equation (3.40) can be written as:

$$\frac{T_{pc}(t)}{r\tau_d} + \frac{T_m(t)}{r\tau_m} - mg \sin(\beta(t)) - \mu mg \cos(\beta(t)) - \frac{1}{2}\rho A_d v^2(t) = m \frac{dv(t)}{dt}, \quad (4.25)$$

where the bicycle acceleration is expressed as the derivative of the bicycle speed $a(t) = \frac{dv(t)}{dt}$. For the sake of a more compact mathematical representation, the effect of rolling resistance can be seen as the one of an apparent road slope with an apparent rise h_μ and run d_μ :

$$\mu = \frac{h_\mu}{d_\mu}. \quad (4.26)$$

Thus, it introduces an apparent slope angle:

$$\beta_\mu = \arctan(\mu). \quad (4.27)$$

Substituting (4.27) in (4.25) and applying trigonometric considerations, one obtains:

$$\frac{T_{pc}(t)}{r\tau_d} + \frac{T_m(t)}{r\tau_m} - \frac{mg}{\cos(\beta_\mu)} \sin(\beta(t) + \beta_\mu) - \frac{1}{2}\rho A_d v^2(t) = m \frac{dv(t)}{dt}. \quad (4.28)$$

Since within the range of possible realistic values of μ defined in section 3.1.5, $\mu \simeq \beta_\mu$ and $\cos(\beta_\mu) \simeq 1$, equation (4.28) can be written as:

$$\frac{T_{pc}(t)}{r\tau_d} + \frac{T_m(t)}{r\tau_m} - mg\alpha(t) - \frac{1}{2}\rho A_d v^2(t) = m \frac{dv(t)}{dt}, \quad (4.29)$$

where $\alpha(t) = \sin(\beta(t) + \mu)$. Assuming that all other quantities are known or measurable, the pedaling torque can be considered an external unknown disturbance that can be estimated employing an UIO. In the following, two different state variable representations that may be employed for pedaling torque estimation purposes are proposed. The first state-space model expresses the pedaling torque as a constant. In this case, a simple UIO may be employed to estimate the unknown disturbance as proposed in [15]. The second state variables representation employs a simplified sinusoidal model of the pedaling torque. In these conditions, an UIO with a similar structure to the one proposed in [45] can be applied to estimate the system state. Hereinafter, the UIO that estimates the pedaling torque relying on a constant model will be referred to as CPTO, whereas the one that utilizes a sinusoidal model will be called SPTO.

Constant pedaling torque model (CPTO):

According to the UIO theory [15], unknown non-constant inputs whose variations are slow relative to the natural response of the observer can be estimated by enhancing the system state. In particular, external disturbances can be considered constant compared to the system dynamics. In other words, the unknown disturbance bandwidth is assumed to be smaller than the natural response of the observer. In the case of pedaling torque estimation, the system (4.29) can be enhanced by the equation:

$$\frac{dT_{pc}(t)}{dt} = 0. \quad (4.30)$$

From equations (4.29) and (4.30), a continuous-time state-space system representation can be derived. Defining the system state $\mathbf{x}(t) = [v(t) \quad T_{pc}(t)]^T$, the system input $\mathbf{u}(t) = [T_m(t) \quad \alpha(t)]^T$, and the system outputs or measurements $y(t) = v(t)$, the following nonlinear state-space model is obtained:

$$\begin{cases} \frac{dv(t)}{dt} = -\frac{\rho A_d}{2m} v^2(t) + \frac{1}{mr\tau_d} T_{pc}(t) + \frac{1}{mr\tau_m} T_m(t) - g\alpha(t) \\ \frac{dT_{pc}(t)}{dt} = 0 \end{cases}, \quad (4.31)$$

$$y(t) = v(t). \quad (4.32)$$

Sinusoidal pedaling torque model (SPTO):

As stated in section 3.1.2, the pedaling torque has a pseudo-sinusoidal profile with an offset. In particular, since the pedaling torque profile has two maximums per crank revolution, it may be expressed as the sum of a continuous component or offset T_{pc_0} plus a 2nd harmonic of

4.2 Pedaling torque observers

the crank angle θ_c with amplitude T_{pc_2} . Thus, a simplified expression of the pedaling torque results:

$$T_{pc}(t) = T_{pc_0} - T_{pc_2} \cos[2\theta_c(t) + \theta_c(0)], \quad (4.33)$$

where $\theta_c(0)$ is the initial value of the crankset angle that depends on the initial position of the pedals when starting pedaling. Equation (4.33) can be included in the state variables representation enhancing the state of the system to:

$$\mathbf{x}(t) = [v(t) \quad \zeta_0(t) \quad \zeta_2^c(t) \quad \zeta_2^s(t)]^T, \quad (4.34)$$

where $\zeta_0(t) = T_{pc_0}$, $\zeta_2^c(t) = -T_{pc_2} \cos[2\theta_c(t) + \theta_c(0)]$, and $\zeta_2^s(t) = T_{pc_2} \sin[2\theta_c(t) + \theta_c(0)]$. Thus, the pedaling torque can be seen as the sum of two state variables:

$$T_{pc}(t) = \zeta_0(t) + \zeta_2^c(t). \quad (4.35)$$

The UIO theory can be applied for the estimation of the continuous component of the pedaling torque:

$$\frac{d\zeta_0(t)}{dt} = 0. \quad (4.36)$$

From equation (3.4) and expressing the angular speed of the wheel as a function of the bicycle speed $\omega(t) = \frac{v(t)}{r}$, the derivatives of $\zeta_2^c(t)$ and $\zeta_2^s(t)$ can be expressed as:

$$\frac{d\zeta_2^c(t)}{dt} = 2\omega_c(t) T_{pc_2} \sin[2\theta_c(t) + \theta_c(0)] = \frac{2}{r\tau_d} v(t) \zeta_2^s(t), \quad (4.37)$$

$$\frac{d\zeta_2^s(t)}{dt} = 2\omega_c(t) T_{pc_2} \cos[2\theta_c(t) + \theta_c(0)] = -\frac{2}{r\tau_d} v(t) \zeta_2^c(t). \quad (4.38)$$

Therefore, the following nonlinear continuous-time state-space model is obtained:

$$\begin{cases} \frac{dv(t)}{dt} = -\frac{\rho A_d}{2m} v^2(t) + \frac{1}{mr\tau_d} \zeta_0(t) + \frac{1}{mr\tau_d} \zeta_2^c(t) + \frac{1}{mr\tau_m} T_m(t) - g\alpha(t) \\ \frac{d\zeta_0(t)}{dt} = 0 \\ \frac{d\zeta_2^c(t)}{dt} = \frac{2}{r\tau_d} v(t) \zeta_2^s(t) \\ \frac{d\zeta_2^s(t)}{dt} = -\frac{2}{r\tau_d} v(t) \zeta_2^c(t) \end{cases}, \quad (4.39)$$

$$\mathbf{y}(t) = v(t). \quad (4.40)$$

4.2.3 Kalman filtering

This section presents the UIOs employed for the pedaling torque estimation in this work expressed in the form of EKFs. In particular, the UIOs formulation in the cases of a constant and sinusoidal pedaling torque model is derived.

Constant pedaling torque model (CPTO):

When considering a constant pedaling torque model, discretizing equations (4.31)-(4.32) with the sampling time T_s and expressing them in the form (4.17) one obtains:

$$\begin{cases} v(k) = \left[1 - \frac{\rho A_d T_s}{2m} v(k-1)\right] v(k-1) + \frac{T_s}{mr\tau_d} T_{pc}(k-1) + \frac{T_s}{mr\tau_m} T_m(k-1) \\ \quad - g T_s \alpha(k-1) + w_v(k-1) \\ T_{pc}(k) = T_{pc}(k-1) + w_{T_{pc}}(k-1) \end{cases}, \quad (4.41)$$

$$y(k) = v(k) + \nu_v(k), \quad (4.42)$$

where the white and Gaussian noises on the process $\mathbf{w}(k) = [w_v(k) \quad w_{T_{pc}}(k)]^T$ and the measurements $\nu(k) = \nu_v(k)$ are considered. These stochastic processes can be described by the covariance matrices:

$$\mathbf{Q} = \begin{bmatrix} \sigma_{w_v}^2 & 0 \\ 0 & \sigma_{w_{T_{pc}}}^2 \end{bmatrix}, \quad R = \sigma_{\nu_v}^2, \quad (4.43)$$

where $\sigma_{w_v}^2$, $\sigma_{w_{T_{pc}}}^2$, and $\sigma_{\nu_v}^2$ are the variances of the noises w_v , $w_{T_{pc}}$, and ν_v respectively. In the absence of previous knowledge of the system state, a practical choice for the EKF algorithm initialization is:

$$\hat{\mathbf{x}}^+(0) = \mathbf{0} \in \mathbb{R}^{2 \times 1}, \quad \mathbf{P}^+(0) = \mathbf{I} \in \mathbb{R}^{2 \times 2}. \quad (4.44)$$

At each step $k \geq 1$, the EKF algorithm shown in section 4.1.2 is performed. In particular, the following Jacobian matrices are calculated according to equations (4.18) and (4.21):

$$\mathbf{J}_F(k-1) = \begin{bmatrix} 1 - \frac{\rho A_d T_s}{m} \hat{v}^+(k-1) & \frac{T_s}{mr\tau_d} \\ 0 & 1 \end{bmatrix}, \quad \mathbf{J}_L = \mathbf{I} \in \mathbb{R}^{2 \times 2}, \quad (4.45)$$

$$\mathbf{J}_H = [1 \quad 0], \quad J_M = 1. \quad (4.46)$$

Sinusoidal pedaling torque model (SPTO):

When considering the simplified sinusoidal pedalling torque model, discretizing equations (4.39)-(4.40) with the sampling time T_s and expressing them in the form (4.17) one obtains:

$$\left\{ \begin{array}{l} v(k) = \left[1 - \frac{\rho A_d T_s}{2m} v(k-1) \right] v(k-1) + \frac{T_s}{mr\tau_d} \zeta_0(k-1) + \frac{T_s}{mr\tau_d} \zeta_2^c(k-1) \\ \quad + \frac{T_s}{mr\tau_m} T_m(k-1) - gT_s \alpha(k-1) + w_v(k-1) \\ \zeta_0(k) = \zeta_0(k-1) + w_{\zeta_0}(k-1) \\ \zeta_2^c(k) = \zeta_2^c(k-1) + \frac{2T_s}{r\tau_d} v(k-1) \zeta_2^s(k-1) + w_{\zeta_2^c}(k-1) \\ \zeta_2^s(k) = \zeta_2^s(k-1) - \frac{2T_s}{r\tau_d} v(k-1) \zeta_2^c(k-1) + w_{\zeta_2^s}(k-1) \end{array} \right. , \quad (4.47)$$

$$y(k) = v(k) + v_v(k), \quad (4.48)$$

where the white and Gaussian noises on the process $\mathbf{w}(k) = [w_v(k) \ w_{\zeta_0}(k) \ w_{\zeta_2^c}(k) \ w_{\zeta_2^s}(k)]^T$ and the measurements $v(k) = v_v(k)$ are considered. These stochastic processes can be described by the covariance matrices:

$$\mathbf{Q} = \begin{bmatrix} \sigma_{w_v}^2 & 0 & 0 & 0 \\ 0 & \sigma_{w_{\zeta_0}}^2 & 0 & 0 \\ 0 & 0 & \sigma_{w_{\zeta_2^c}}^2 & 0 \\ 0 & 0 & 0 & \sigma_{w_{\zeta_2^s}}^2 \end{bmatrix}, \quad R = \sigma_{v_v}^2, \quad (4.49)$$

where $\sigma_{w_{\zeta_0}}^2$, $\sigma_{w_{\zeta_2^c}}^2$, and $\sigma_{w_{\zeta_2^s}}^2$ are the variances of the noises w_{ζ_0} , $w_{\zeta_2^c}$, and $w_{\zeta_2^s}$ respectively. As previously shown, a practical initialization of the EKF algorithm is:

$$\hat{\mathbf{x}}^+(0) = \mathbf{0} \in \mathbb{R}^{4 \times 1}, \quad \mathbf{P}^+(0) = \mathbf{I} \in \mathbb{R}^{4 \times 4}. \quad (4.50)$$

At each step $k \geq 1$, the EKF algorithm shown in section 4.1.2 is performed. In particular, the Jacobian matrices are calculated according to equations (4.18) and (4.21):

$$\mathbf{J}_F(k-1) = \begin{bmatrix} 1 - \frac{\rho A_d T_s}{m} \hat{v}^+(k-1) & \frac{T_s}{rm\tau_d} & \frac{T_s}{rm\tau_d} & 0 \\ 0 & 1 & 0 & 0 \\ \frac{2T_s}{r\tau_d} \hat{\zeta}_2^{s+}(k-1) & 0 & 1 & \frac{2T_s}{r\tau_d} \hat{v}^+(k-1) \\ -\frac{2T_s}{r\tau_d} \hat{\zeta}_2^{c+}(k-1) & 0 & -\frac{2T_s}{r\tau_d} \hat{v}^+(k-1) & 1 \end{bmatrix}, \quad (4.51)$$

$$\mathbf{J}_L = \mathbf{I} \in \mathbb{R}^{4 \times 4}, \quad (4.52)$$

$$\mathbf{J}_H = [1 \ 0 \ 0 \ 0], \quad J_M = 1. \quad (4.53)$$

Therefore, at each iteration of the algorithm, the pedaling torque is obtained as:

$$\hat{T}_{pc}(k) = \hat{\xi}_0(k) + \hat{\xi}_2^c(k). \quad (4.54)$$

4.2.4 System observability proof

To estimate the system state with a state observer, the system must be completely observable. As stated in section 4.1, the observability of a linearized system implies the local observability of the nonlinear one. When using an EKF, the observability of a linear time-variant system must be proofed at each step k because the Jacobian matrices are time-variant. As stated in [126], to verify the observability of a linear time-variant system, the observability matrix \mathcal{O}_v must have full rank for each initial state $k_i \in [0; +\infty)$:

$$\mathcal{O}_v(k_i) = \begin{bmatrix} \mathbf{J}_H(k_i) \\ \mathbf{J}_H(k_i+1)\mathbf{J}_F(k_i) \\ \vdots \\ \mathbf{J}_H(k_i+n-1)\mathbf{J}_F(k_i+n-2)\dots\mathbf{J}_F(k_i) \end{bmatrix}. \quad (4.55)$$

Constant pedaling torque model (CPTO):

In the case of the CPTO, the observability matrix (4.55) becomes:

$$\mathcal{O}_v(k_i) = \begin{bmatrix} \mathbf{J}_H \\ \mathbf{J}_H\mathbf{J}_F(k_i) \end{bmatrix} = \begin{bmatrix} 0 \\ 1 - \frac{\rho A_d T_s}{m} \hat{\omega}^+(k_i) \quad \frac{T_s}{mr\tau_d} \end{bmatrix}. \quad (4.56)$$

Its determinant results:

$$|\mathcal{O}_v(k_i)| = \frac{T_s}{mr\tau_d} \neq 0. \quad (4.57)$$

The linearized system results completely observable and thus the nonlinear one local observable in a neighborhood of $\mathbf{x}(k_i)$ since $\text{rank}[\mathcal{O}_v(k_i)] = n = 2 \quad \forall k_i \in [0; +\infty)$.

Sinusoidal pedaling torque model (SPTO):

In the case of the SPTO, the observability matrix (4.55) becomes:

$$\mathcal{O}_v(k_i) = \begin{bmatrix} \mathbf{J}_H \\ \mathbf{J}_H\mathbf{J}_F(k_i) \\ \mathbf{J}_H\mathbf{J}_F(k_i+1)\mathbf{J}_F(k_i) \\ \mathbf{J}_H\mathbf{J}_F(k_i+2)\mathbf{J}_F(k_i+1)\mathbf{J}_F(k_i) \end{bmatrix}. \quad (4.58)$$

The expression of the observability matrix can be obtained by substituting the expressions of the Jacobians (4.45) and (4.46). However, for the sake of a compact mathematical representation, the complete expression of the observability matrix is not reported here. Nevertheless,

its determinant is evaluated:

$$|\mathcal{O}_v(k_i)| = \frac{8T_s^6 \hat{v}^{+2}(k_i) \hat{v}^+(k_i + 1)}{m^3 r^6 \tau_d^6}. \quad (4.59)$$

The determinant of the observability matrix results $|\mathcal{O}_v(k_i)| \neq 0$ when $\hat{v}^+(k_i) \neq 0$ and $\hat{v}^+(k_i + 1) \neq 0$. Therefore, in this case, the linearized system results completely observable and the non-linear one local observable in a neighborhood of $\mathbf{x}(k_i)$ since $\text{rank}[\mathcal{O}_v(k_i)] = n = 4 \quad \forall k_i \in [0; +\infty)$. This result indicates that the SPTO can correctly estimate the system state only when the bicycle moves $v \neq 0 \frac{m}{s}$. This result agrees with the expectations since the employed model describes the pedaling torque profile only in non-static conditions.

4.3 Pedaling torque observers inputs and measurements

In the previously proposed PTOs, the motor torque, the road slope, and the bicycle speed have been considered known measurable inputs and outputs of the system. This section analyzes their measurement process and the measurement error effect on the pedaling torque estimation and motor control.

4.3.1 Motor torque

As stated in section 3.1.3, the motor torque T_m is measured indirectly using equation (3.30) in the case of PMSMs. Correct motor torque measurements can be obtained when the permanent magnet flux linkage Ψ_{PM} is accurately known. Besides, high-performance motor torque control needs correct knowledge of the machine electrical parameters that may be identified through offline or online approaches. For further information about offline and online parameter identification techniques for synchronous machines, the interested reader can refer to [127]. Good current measurement accuracy is also fundamental because errors can lead to distorted currents and cause torque ripple when controlling the motor. A further source of error in the motor torque measurement is related to the electrical rotor position. Indeed, low-resolution position sensors or sensorless techniques can determine errors in the coordinate transformation and propagate to the measured torque.

4.3.2 Road slope

In vehicle applications, the road slope cannot be measured directly but is typically estimated by combining the measurements provided by different types of sensors including IMUs, wheel position or speed sensors, Global Navigation Satellite System (GNSS) receivers, force or torque sensors, and air pressure sensors. Some methods exploit external signals, such as GNSS information, to estimate the road angle. In particular, they employ the three-dimensional vehicle speed and altitude information provided by GNSS receivers [128, 129]. However, the estimation accuracy is limited by losses in satellite connections depending on the signal reception environment. Moreover, their reliability varies with the horizontal vehicle speed degrading in the low-speed range [130]. To overcome the problems related to the quality of the received GNSS signal, other methods employ in-vehicle sensors to estimate the road angle. These methods can be classified into different categories depending

on the utilized sensors. Some approaches exploit the vehicle longitudinal dynamic model combined with force and wheel acceleration measurements to extract the road angle information [131–135]. The accuracy of the estimation is dependent on knowledge of the model parameters that vary with the driving conditions. Furthermore, the estimation degrades in non-modeled driving scenarios such as braking and gear-shifting. Other approaches exploit measurements provided by IMUs and wheel position or speed sensors to estimate the road slope [40, 136–139]. Combining the information given by the sensors, the gravity acceleration measured by the IMU can be isolated from the vehicle acceleration and used to estimate the road slope even in dynamic conditions. However, these methods require strong low-pass filtering of the acceleration signals to remove the measurement noise introduced by vibrations and differentiation. Besides, since the IMUs are mounted on the vehicle, the road angle estimation may contain an error due to the pitch motion of the vehicle caused by accelerations and bumps [130]. Also, low-cost Micro-ElectroMechanical System (MEMS) IMUs are characterized by measurement drift caused by temperature variations and mechanical stress that can affect the angle estimation. Atmospheric pressure sensors can also be employed to estimate the road slope [140]. These methods exploit the relation between altitude and air pressure to extract the slope information. Nevertheless, they are characterized by limited accuracy and dependency on the meteorological conditions. As explained before, each road grade estimation approach has limitations under different operating conditions. To overcome these problems, sensor fusion approaches, that combine the estimation obtained with various methods, are often utilized [130, 141]. Although these methods provide reliable road grade information, they increase the complexity and costs of the entire system.

In this work, the intent of reducing costs and keeping the road slope estimation independent from GNSS signals reception and meteorological conditions has led to excluding GNSS-based, atmospheric pressure-based, and sensor fusion approaches. Furthermore, as stated in [137], model dynamics-based estimation methods require the measurement of the input torque to be observable. Therefore, these methods cannot be employed to estimate the road slope in this work, because a simultaneous estimation of the input torque is required. Based on the considerations above, methods that employ low-cost MEMS IMU measurements are considered. Among them, complex estimation algorithms that exploit 6-axes IMU measurements and a vehicle three-dimensional kinematic modeling can be utilized to extract the road slope information [137, 139]. However, as shown in [137], these approaches are based on the simplifying assumption that the accelerations are measured at the vehicle center of gravity inducing errors in the estimation. Since they achieve a comparable estimation accuracy reducing the computational complexity, methods based only on the vehicle longitudinal kinematic model are considered in this work. In these estimation approaches, 1-axis acceleration measurements might be sufficient to estimate the road slope. However, it is not always possible to mount the sensing device perfectly aligned with the longitudinal direction of motion. Thus, these simplified methods also require a 6-axes IMU to compensate for the mounting angles of the device and mitigate the effect of errors introduced by the vehicle model simplification.

Static road slope estimation:

IMU measurement-based road slope estimation algorithms require a correct transformation of the IMU acceleration and angular speed measurements in the vehicle or body reference

frame. Therefore, a calibration procedure and compensation for the mounting offset of the device are necessary. For the sake of brevity, detailed information about these two processes are reported in the appendix (Section 7.1).

After reporting the measurements from the sensor ($x^s - y^s - z^s$) to the bicycle reference frame ($x - y - z$), the road angle can be calculated from the measured accelerations in static conditions. Limiting the analysis to the only longitudinal motion of the bicycle, in the presence of a road slope $\beta \neq 0 \text{ deg}$ and absence of a longitudinal acceleration $a = 0 \frac{m}{s^2}$ and leaning of the bicycle $\varphi = 0 \text{ deg}$, the road slope angle can be calculated as:

$$\beta = \arctan\left(\frac{a_{s_x}}{a_{s_z}}\right) = \arctan\left(\frac{g_x}{g_z}\right), \quad (4.60)$$

where $\mathbf{a}_s = [a_{s_x} \ a_{s_y} \ a_{s_z}]^T$ are the measured accelerations and $\mathbf{g} = [g_x \ g_y \ g_z]^T$ are the gravity accelerations components expressed in the vehicle reference frame. Figure 4.3 contains an example of the IMU-measured acceleration components under the aforementioned hypotheses. For the sake of simplicity in the graphical representation, the roll φ_s and yaw ψ_s IMU mounting angles have been considered $\varphi_s = \psi_s = 0 \text{ deg}$, whereas a pitch mounting offset $\gamma_s \neq 0 \text{ deg}$ is present. It has to be remarked that a gravitational field component aligned along an accelerometer axis is read with a negative sign by the MEMS accelerometer. Thus, in Figure 4.3, the gravity acceleration components are reported in opposite direction.

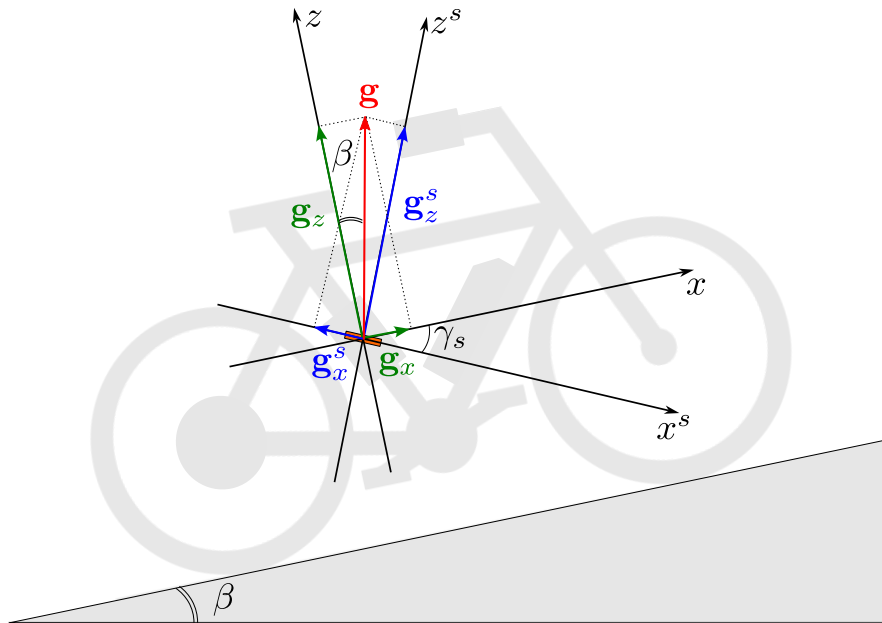


Figure 4.3: Measured acceleration components $\mathbf{a}_s = \mathbf{g}$ in the presence of a road slope ($\beta \neq 0 \text{ deg}$), no longitudinal acceleration ($a = 0 \frac{m}{s^2}$), and no leaning ($\varphi = 0 \text{ deg}$).

Dynamic road slope estimation:

When the vehicle accelerates or decelerates $a \neq 0 \frac{m}{s^2}$, equation (4.60) is no longer a valid expression for the computation of the road slope angle because the accelerometer measures the overall acceleration $\mathbf{a}_s = \mathbf{g} + \mathbf{a}$. Figure 4.4 contains an example of the IMU-measured ac-

Algebraic method II:

The second algebraic method employs the measured longitudinal acceleration $a(t)$ obtained differentiating the longitudinal speed of the vehicle to extract the road angle information. The measured acceleration in the longitudinal direction $a_{s_x}(t) = a(t) + g_x(t)$ can be written as:

$$a_{s_x}(t) = a(t) + g_x(t) = a(t) + g \sin[\beta(t)]. \quad (4.63)$$

Therefore, the road slope can be computed as:

$$\hat{\beta}(t) = \arcsin\left(\frac{a_{s_x}(t) - a(t)}{g}\right). \quad (4.64)$$

This method requires the computation of the longitudinal acceleration of the bicycle as the derivative of its speed. Thus, it is heavily affected by the accelerometer measurement noise and the one caused by the differentiation of the vehicle speed [137]. Moreover, in a real scenario, the accelerometer measures also the vibrations caused by bumps while riding the bicycle. Therefore, it is necessary to strongly low-pass filter the measurements to remove the effect of high-frequency noise and vibrations introducing time delays in the measured signals that may result in an inaccurate slope estimation.

Closed-loop method:

Closed-loop methods based on state observers are commonly preferred to algebraic ones because they grant a higher high-frequency disturbance rejection capability on the measured acceleration components. This means that, compared to algebraic methods, in closed-looped approaches, the acceleration signals can be filtered with a higher bandwidth reducing the introduced time delays on the slope estimation at the same performance level. In particular, this work proposes a state observer that models the bicycle longitudinal acceleration $a(t)$ and the gravity longitudinal component $g_x(t)$ as constants, namely with a lower bandwidth than the one of the state observer. Also, the system modeling assumes that the variation of these two quantities can be considered slower than the one of the vehicle speed $v(t)$. This simplification can be employed in an UIO structure to estimate the system state relying on measurements of the vehicle speed and the longitudinal acceleration reported in the bicycle frame measured with the accelerometer $a_{s_x}(t)$. Defining the state $\mathbf{x}(t) = [a(t) \quad v(t) \quad g_x(t)]^T$ and output $\mathbf{y}(t) = [v(t) \quad a_{s_x}(t)]^T$ vectors, a continuous-time linear state-space model can be derived:

$$\begin{cases} \frac{da(t)}{dt} = 0 \\ \frac{dv(t)}{dt} = a(t) \\ \frac{dg_x(t)}{dt} = 0 \end{cases}, \quad (4.65)$$

$$\begin{cases} y_1(t) = v(t) \\ y_2(t) = a_{s_x}(t) = a(t) + g_x(t) \end{cases} \quad (4.66)$$

Discretizing with the sampling time T_s , one obtains the following discrete-time state-space model expressed in terms of matrices in the form (4.3):

$$\begin{bmatrix} a(k+1) \\ v(k+1) \\ g_x(k+1) \end{bmatrix} = \begin{bmatrix} 1 & 0 & 0 \\ T_s & 1 & 0 \\ 0 & 0 & 1 \end{bmatrix} \begin{bmatrix} a(k) \\ v(k) \\ g_x(k) \end{bmatrix}, \quad (4.67)$$

$$\begin{bmatrix} y_1(k) \\ y_2(k) \end{bmatrix} = \begin{bmatrix} 0 & 1 & 0 \\ 1 & 0 & 1 \end{bmatrix} \begin{bmatrix} a(k) \\ v(k) \\ g_x(k) \end{bmatrix}. \quad (4.68)$$

From (4.7), the observability matrix can be derived:

$$\mathcal{O} = \begin{bmatrix} \mathbf{H} \\ \mathbf{HF} \\ \mathbf{HF}^2 \end{bmatrix} = \begin{bmatrix} 0 & 1 & 0 \\ 1 & 0 & 1 \\ T_s & 1 & 0 \\ 1 & 0 & 1 \\ 2T_s & 1 & 0 \\ 1 & 0 & 1 \end{bmatrix}. \quad (4.69)$$

It can be seen that the system is completely observable since $\text{rank}(\mathcal{O}) = n = 3$. Therefore, a state observer can be employed to estimate the system state. In particular, a KF has been considered in this work. The system (4.67)-(4.68) can be expressed in the form (4.9):

$$\begin{bmatrix} a(k) \\ v(k) \\ g_x(k) \end{bmatrix} = \begin{bmatrix} 1 & 0 & 0 \\ T_s & 1 & 0 \\ 0 & 0 & 1 \end{bmatrix} \begin{bmatrix} a(k-1) \\ v(k-1) \\ g_x(k-1) \end{bmatrix} + \begin{bmatrix} w_a(k-1) \\ w_v(k-1) \\ w_{g_x}(k-1) \end{bmatrix}, \quad (4.70)$$

$$\begin{bmatrix} y_1(k) \\ y_2(k) \end{bmatrix} = \begin{bmatrix} 0 & 1 & 0 \\ 1 & 0 & 1 \end{bmatrix} \begin{bmatrix} a(k) \\ v(k) \\ g_x(k) \end{bmatrix} + \begin{bmatrix} v_v(k) \\ v_{a_{s_x}}(k) \end{bmatrix}, \quad (4.71)$$

where the white and Gaussian noises on the process $\mathbf{w}(k) = [w_a(k) \quad w_v(k) \quad w_{g_x}(k)]^T$ and on the measurements $\mathbf{v}(k) = [v_v(k) \quad v_{a_{s_x}}(k)]^T$ are considered. These stochastic processes can be described by the covariance matrices:

$$\mathbf{Q} = \begin{bmatrix} \sigma_{w_a}^2 & 0 & 0 \\ 0 & \sigma_{w_v}^2 & 0 \\ 0 & 0 & \sigma_{w_{g_x}}^2 \end{bmatrix}, \quad \mathbf{R} = \begin{bmatrix} \sigma_{v_v}^2 & 0 \\ 0 & \sigma_{v_{a_{s_x}}}^2 \end{bmatrix}, \quad (4.72)$$

4.3 Pedaling torque observers inputs and measurements

where $\sigma_{w_a}^2$, $\sigma_{w_v}^2$, $\sigma_{w_{g_x}}^2$, $\sigma_{v_v}^2$, and $\sigma_{v_{a_{s_x}}}$ are the variances of the noises w_a , w_v , w_{g_x} , v_v , and $v_{a_{s_x}}$ respectively. As previously shown, a practical initialization of the KF algorithm is:

$$\hat{\mathbf{x}}^+(0) = \mathbf{0} \in \mathbb{R}^{3 \times 1}, \quad \mathbf{P}^+(0) = \mathbf{I} \in \mathbb{R}^{3 \times 3}. \quad (4.73)$$

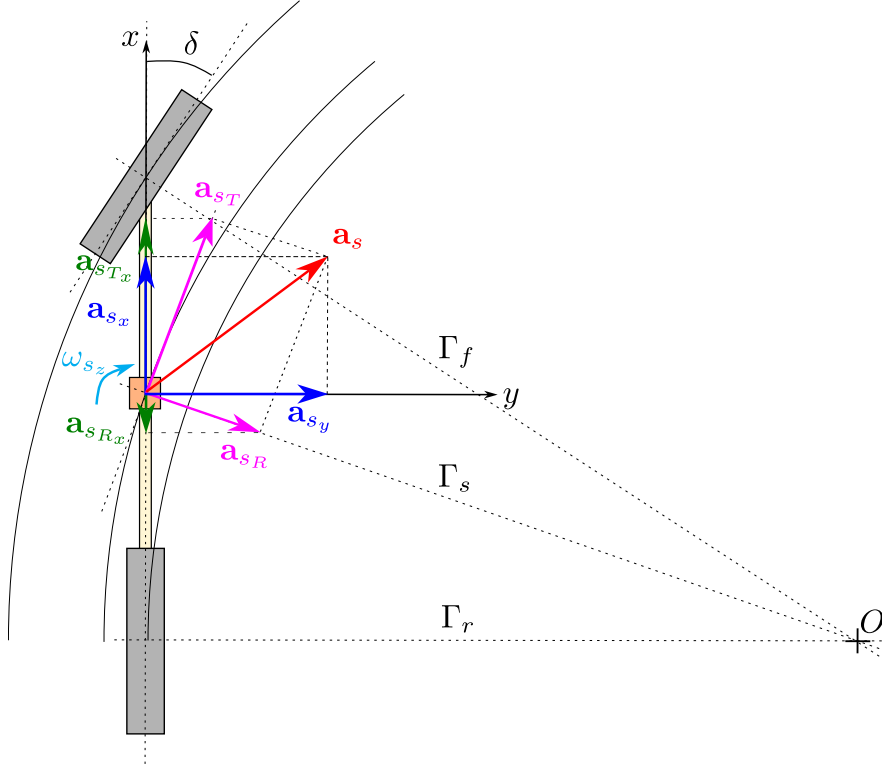
At each $k \geq 1$, the KF filter algorithm is performed as shown in section 4.1.2. Furthermore, at each step, the state estimate can be employed to evaluate the road angle using the expression:

$$\hat{\beta}(k) = \arcsin\left(\frac{\hat{g}_x(k)}{g}\right). \quad (4.74)$$

Estimation methods based only on the longitudinal motion of the vehicle are limited by modeling simplifications. Indeed, the proposed model neglects the effect of cornering while riding which introduces centrifugal acceleration components that can affect the estimation accuracy. Therefore, in the next paragraph, the employment of angular speed measurements provided by the IMU gyroscope is used to mitigate the effects of cornering on the road slope estimation.

Curve effect correction:

Modeling a bicycle in a curve requires the employment of a two-dimensional model that considers the steering effect of the front wheel. Cornering introduces a centrifugal acceleration component a_{s_R} that is measured by the accelerometer. This component can cause errors in the slope estimation depending on the mounting position of the IMU on the bicycle. Figure 4.5 contains a schematic two-dimensional representation of a bicycle during cornering with the IMU, reported in orange, mounted onto the bicycle frame. The bicycle cornering is generated by the rotation of the handlebar by an angle δ , called steering angle, relative to the longitudinal direction of motion x . Neglecting the slip angles of the tires, the instantaneous center of rotation O of the bicycle corresponds to the intersection between the straight lines perpendicular to the orientation of the two wheels, as reported in Figure 4.5. Thus, the front wheel travels the trajectory imposed by the steering angle with radius Γ_f , the rear wheel the concentric trajectory of radius Γ_r , and the IMU the intermediate trajectory of radius Γ_s . One can notice that, after the mounting offset correction, the longitudinal direction of the accelerometer always corresponds to the direction of the bicycle frame and can differ from the instantaneous trajectory depending on the mounting position of the accelerometer within the bicycle. Therefore, the centrifugal acceleration, which is perpendicular to the instantaneous trajectory, could be not perpendicular to the longitudinal direction of the accelerometer affecting the measurement with a negative offset that propagates onto the estimated road slope. To avoid this error, the IMU should be mounted into the wheels where the longitudinal direction of the accelerometer would correspond to the instantaneous trajectory. However, this is not a good practical solution because the accelerations measured at the wheels are more affected by vibrations since they are in direct contact with the uneven surface of the road. Hence, a stronger low-pass filtering of the measured acceleration would be required. The reduction of the cornering effect on the road angle estimation when the IMU is mounted on the bicycle frame is performed in this work considering a method taken from [137]. The idea is to weigh the confidence on the estimated road angle depending on the cornering state


 Figure 4.5: Effect of cornering on the measured acceleration a_s .

of the vehicle. This is done by employing a time-variable LPF whose bandwidth changes depending on the aggressiveness of the curve. In particular, the slope estimation is filtered with a lower bandwidth while riding in more aggressive curves. As shown in [137], the angular rate ω_{s_z} measured with the IMU can be used to quantify the curve aggressiveness. In particular, the following index is considered:

$$\Lambda = G_{\omega_{s_z}}(s) |\omega_{s_z}|, \quad (4.75)$$

where $G_{\omega_{s_z}}(s)$ is a LPF expressed in the Laplace s -domain and the absolute value of the angular speed is considered to treat left and right-hand turns equally. The index (4.75) is employed to calculate the cutoff frequency f_{c_β} of an additional LPF $G_\beta(s)$ that filters the slope estimation:

$$f_{c_\beta} = \frac{f_{c_\beta}^{max}}{c(\Lambda - \Lambda_{th})} \quad \text{with} \quad f_{c_\beta} \in [f_{c_\beta}^{max}; f_{c_\beta}^{min}], \quad (4.76)$$

where Λ_{th} is a threshold for the index Λ used to trigger the filter bandwidth variation and c is a coefficient used to tune the rapidity of this variation.

4.3.3 Bicycle speed

The proposed pedaling torque and road slope estimation algorithms are based on the knowledge of the vehicle speed v . However, this quantity is not directly measured with a sensor but is obtained from rotor position measurements. In particular, the vehicle speed can be calculated from the electrical rotor position as follows:

$$v = \omega_m r = \frac{\omega_e r}{n_p}, \quad (4.77)$$

where the electrical angular speed is obtained evaluating the derivative of the measured electrical rotor position $\omega_e = \frac{d\theta_e}{dt}$. However, as previously stated, differentiating results in high-frequency noise amplification. Therefore, a low pass filtering of the signals is necessary to reduce the noise resulting in a delayed vehicle speed measurement. The introduced delay may propagate onto the estimation algorithms affecting their accuracy and thus the responsiveness of the motor control. This means that a trade-off filter bandwidth must be chosen depending on the characteristics of the used rotor position measurements and the desired control system performance.

4.4 Pedaling torque observers simulation

In this section, the proposed PTOs employed for the pedaling torque estimation are simulated to analyze the effects of the KF tuning, modeling errors, and parametric variations on the estimated pedaling torque. The simulations are performed in *MATLAB* environment with a fixed simulation step $T_{sim} = 10 \mu s$. Moreover, the state observers are digitally implemented with a sampling frequency of $f_s = 500 \text{ Hz}$ and thus a sampling period of $T_s = 2 \text{ ms}$. In all simulations, the bicycle is modeled under the hypotheses of Section 4.2.1. In particular, a bicycle with 28" wheels and no provided electrical assistance $T_m = 0 \text{ Nm}$ is considered. Besides, the simulations are performed in a flat road scenario $\beta = 0 \text{ deg}$ and thus considering $\alpha = \sin(\mu)$. Table 4.2 contains the bicycle model fixed parameter values employed as standard values in all simulations.

Figure 4.6 contains a schematic representation of the simulated bicycle longitudinal dynamics. As one can see, the cycling is simulated with a bicycle speed feedback control loop. In particular, a reference speed of $v^* = 20 \frac{km}{h}$ is tracked employing a PI controller. The controller is tuned to generate realistic pedaling torque and bicycle acceleration profiles. The output of the PI controller y_{PI} is the input of the pedaling torque generator that produces a simulated pedaling torque T_{pc} in the form (4.33). In particular, the following pedaling torque expression is employed in the simulations:

$$T_{pc}(t) = \frac{3}{4}y_{PI}(t) - \frac{1}{2}y_{PI}(t)\cos[2\theta_c(t)], \quad (4.78)$$

where an initial crank angle $\theta_c(0) = 0 \text{ rad}$ is considered. A pedaling torque model with a continuous component higher than the 2nd harmonic $|T_{pc0}| > |T_{pc2}|$ is employed to obtain a positive pedaling torque profile $T_{pc} \geq 0 \text{ Nm}$. Figure 4.7 contains the simulated pedaling torque and bicycle speed profiles obtained under the above-mentioned conditions.

In the following simulation results, a comparison between the simulated pedaling torque

Parameter	Value
Road slope β	0 deg
Mass m	100 kg
Gravity acceleration g	9.80665 $\frac{m}{s^2}$
Rolling friction coefficient μ	0.005
Drag area A_d	0.4 m^2
Air density ρ	1.2 $\frac{kg}{m^3}$
Wind speed v_{w_x}	0 $\frac{km}{h}$
Drivetrain transmission ratio τ_d	2.8
Wheel radius r	0.3556 m

Table 4.2: Fixed parameter values employed in the PTO simulations.

and the estimated one \hat{T}_{pc} obtained using the proposed methods is presented. Moreover, the estimation error $\varepsilon_{T_{pc}} = T_{pc} - \hat{T}_{pc}$ is analyzed in each scenario to provide information regarding the accuracy of the estimation. In addition, to evaluate the dependency of the pedaling torque estimation error on the vehicle speed, in each scenario the simulated bicycle velocity is reported. The quality of the estimation is evaluated using the Root Mean Square Error (RMSE). It has to be remarked that the calculated RMSE is reported at the back wheel since the transmitted torque value T_{pw} is the one typically employed to generate the electrical assistance. The RMSE is an index that calculates the square root of the average squared estimation errors over a finite number of samples. Compared to other metrics employed to evaluate the accuracy of predictive models, the RMSE is quite sensitive to outliers, i.e. errors with a large absolute value. Thus, the RMSE penalizes more models characterized by significant deviations from the true values [142]. Following, the expression of the RMSE is reported:

$$RMSE = \sqrt{\frac{\sum_{i=1}^n (\chi_i - \hat{\chi}_i)^2}{n}}, \quad (4.79)$$

where χ_i is the actual or measured value, $\hat{\chi}_i$ is the estimated value, and n represents the number of considered observations.

4.4.1 Effect of Kalman filter tuning

This section analyzes the effects of the KF tuning on the pedaling torque estimation considering the two proposed PTOs. When implementing a KF in real applications, the system model may be not perfectly known as well as its covariance matrices. Moreover, the noises that affect the process and the measurements can be not pure white, zero mean, and un-

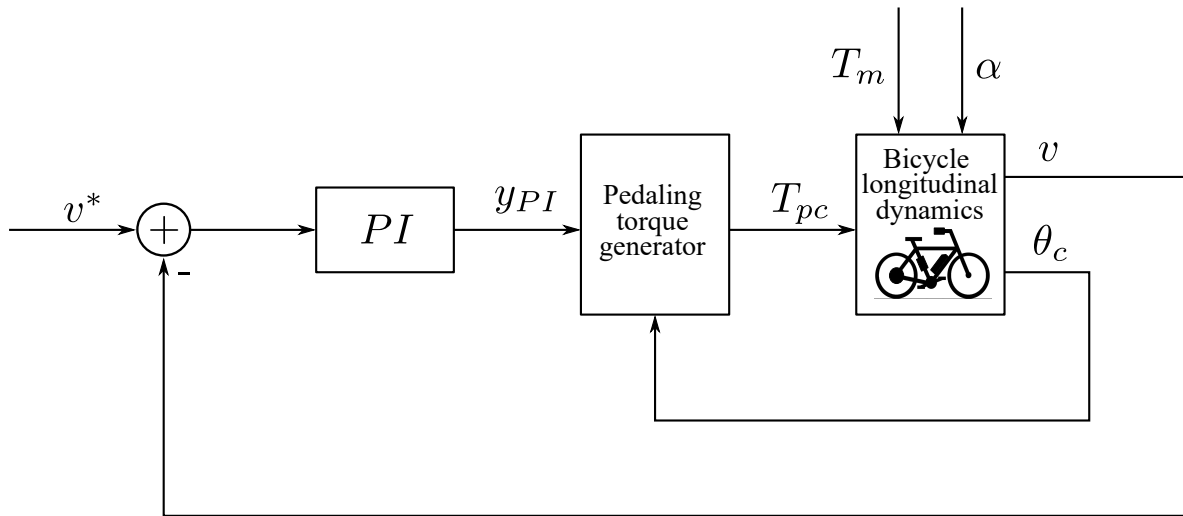


Figure 4.6: Schematic representation of the simulated bicycle longitudinal dynamics.

correlated. Under these conditions, a KF might not work even if it is correctly implemented. The models proposed in the previous sections for the pedaling torque estimation are based on simplified pedaling torque models and thus intrinsically contain a modeling error that can lead to a wrong pedaling torque estimation when the KFs are not correctly tuned. A practical strategy employed to compensate for modeling errors in a KF consists of adding fictitious process noise to the uncertain equations [123]. In this way, the filter has less confidence in its model and places more emphasis on the measurements to improve the state estimation. This can be done by increasing the variance of the noise on the process compared to the one of the noise on the measurements. In such a way, the Kalman gain converges to a larger steady-state value making the filter more responsive to the measurements. In this application, the modeling simplifications of the proposed state observers may be compensated by adding fictitious noise on the process, namely by increasing the noise variance corresponding to the pedaling torque model equations. In this way, the filter emphasizes the bicycle longitudinal dynamics model and the vehicle speed measurement to estimate the pedaling torque.

Constant pedaling torque model (CPTO):

In the case of the CPTO, the variances $\sigma_{w_v}^2 = 10^{-2} \frac{m^2}{s^2}$ and $\sigma_{v_v}^2 = 10^{-3} \frac{m^2}{s^2}$ have been selected to emphasize the bicycle longitudinal model and the speed measurement compared to the pedaling torque model. Also, a variance $\sigma_{w_v}^2 > \sigma_{v_v}^2$ has been chosen to give more confidence to the measured speed rather than the bicycle longitudinal dynamics that can be affected by modeling errors and parametric variations that may reduce the estimation accuracy. Figure 4.8 contains the simulation results obtained considering the covariance matrices:

$$\mathbf{Q} = \begin{bmatrix} 10^{-2} & 0 \\ 0 & \sigma_{w_{T_{pc}}}^2 \end{bmatrix}, \quad R = 10^{-3}, \quad (4.80)$$

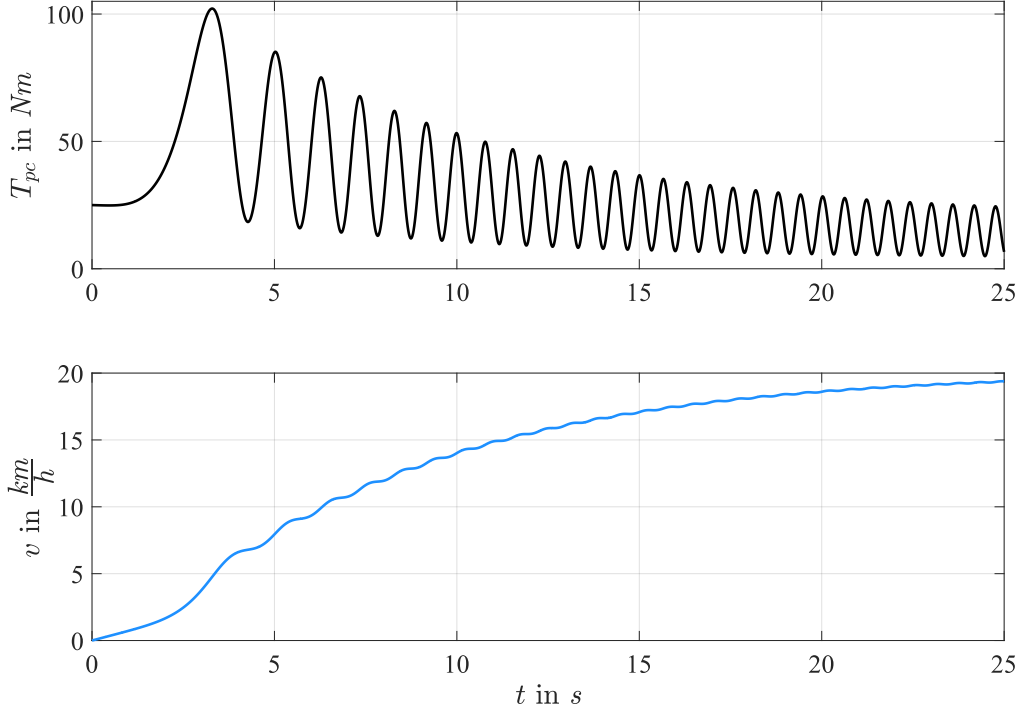


Figure 4.7: Simulated pedaling torque T_{pc} and bicycle speed v profiles.

with $\sigma_{w_{T_{pc}}}^2 \in \{10^3, 10^5\} N^2 m^2$. As one can see, the filter correctly estimates the pedaling torque average value T_{pc_0} in both conditions. Nevertheless, the estimation presents a non-null instantaneous estimation error that oscillates around the pedaling torque average value. In the two considered cases, the RMSE reported at the back wheel has been calculated resulting in 4.51 Nm in the case $\sigma_{w_{T_{pc}}}^2 = 10^3 N^2 m^2$ and 1.11 Nm in the case $\sigma_{w_{T_{pc}}}^2 = 10^5 N^2 m^2$. Thus, a RMSE reduction of circa 75% is obtained in the second case. As one can notice, the pedaling torque estimation improves when increasing the covariance $\sigma_{w_{T_{pc}}}^2$ because the filter becomes more responsive to the measured speed and the bicycle longitudinal dynamics model.

Sinusoidal pedaling torque model (SPTO):

Even in the case of the SPTO, the fictitious noise addition on the pedaling torque equations can compensate for the modeling errors and improve the pedaling torque estimation. In the following, the covariances $\sigma_{w_v}^2$ and $\sigma_{v_v}^2$ are selected analogously to the CPTO. Figure 4.9 contains the simulation results obtained when considering the covariance matrices:

$$\mathbf{Q} = \begin{bmatrix} 10^{-2} & 0 & 0 & 0 \\ 0 & \sigma_{w_{\xi}}^2 & 0 & 0 \\ 0 & 0 & \sigma_{w_{\xi}}^2 & 0 \\ 0 & 0 & 0 & \sigma_{w_{\xi}}^2 \end{bmatrix}, \quad R = 10^{-3}, \quad (4.81)$$

4.4 Pedaling torque observers simulation

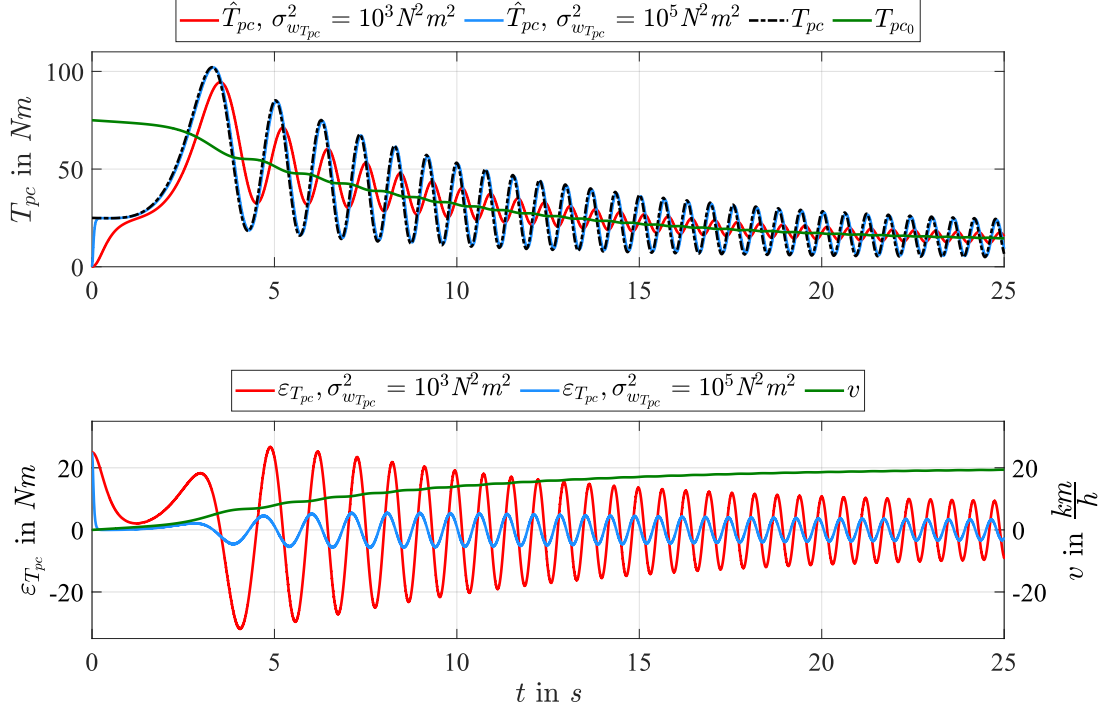


Figure 4.8: Simulated effect of the KF tuning on the pedaling torque estimation using the CPTO. From top to bottom: Pedaling torque estimation \hat{T}_{pc} ; corresponding pedaling torque estimation error $\varepsilon_{T_{pc}}$ and bicycle speed v .

with $\sigma_{w_{\xi}}^2 = \sigma_{w_{\xi_0}}^2 = \sigma_{w_{\xi_2}}^2 = \sigma_{w_{\xi_5}}^2 \in \{10^3, 10^5\} N^2 m^2$. Also in this case, the pedaling torque average value can be correctly estimated and the estimate presents a reduced oscillation around the true value compared to the CPTO. It can be seen that higher values of $\sigma_{w_{\xi}}^2$ increase the convergence rapidity and thus improve the pedaling torque estimation. In both conditions, the RMSE reported at the back wheel has been calculated resulting in 1.32 Nm in the case $\sigma_{w_{\xi}}^2 = 10^3 N^2 m^2$ and 0.29 Nm in the case $\sigma_{w_{\xi}}^2 = 10^5 N^2 m^2$. Therefore, a RMSE reduction of circa 78% is obtained when increasing $\sigma_{w_{\xi}}^2$. Comparing the obtained results with the ones of the CPTO, one can notice the similarity between the effect of increasing $\sigma_{w_{T_{pc}}}^2$ and $\sigma_{w_{\xi}}^2$ on the estimation error reduction. Table 4.3 contains the pedaling torque RMSEs reported at the back wheel analyzed in the previously considered scenarios. One can notice that the employment of a sinusoidal model improves the estimation of circa 71% and 74% for $\sigma_{w_{T_{pc}}}^2 = \sigma_{w_{\xi}}^2 = 10^3 N^2 m^2$ and $\sigma_{w_{T_{pc}}}^2 = \sigma_{w_{\xi}}^2 = 10^5 N^2 m^2$, respectively.

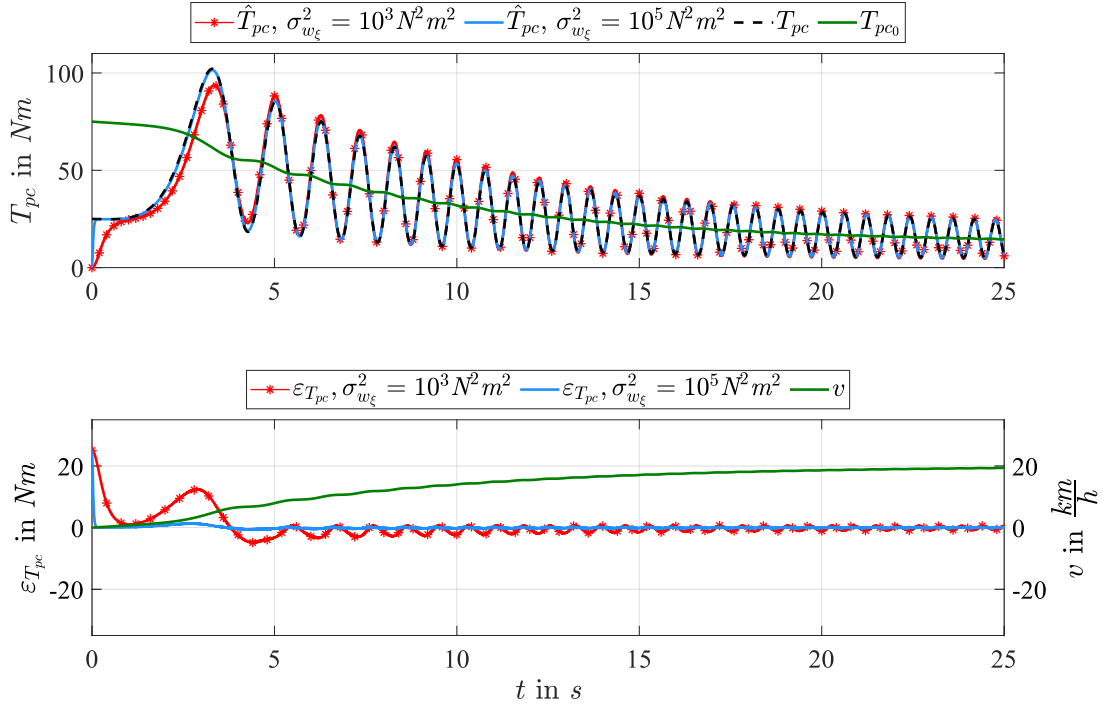


Figure 4.9: Simulated effect of the KF tuning on the pedaling torque estimation using the SPTO. From top to bottom: Pedaling torque estimation \hat{T}_{pc} ; corresponding pedaling torque estimation error $\varepsilon_{T_{pc}}$ and bicycle speed v .

RMSE in Nm		
PTO	$\sigma_{w_{T_{pc}}}^2 = \sigma_{w_{\xi}}^2 = 10^3 N^2 m^2$	$\sigma_{w_{T_{pc}}}^2 = \sigma_{w_{\xi}}^2 = 10^5 N^2 m^2$
CPTO	4.51	1.11
SPTO	1.32	0.29

Table 4.3: Simulated effect of KF tuning on the pedaling torque RMSE reported at the back wheel (evaluated considering T_{pw}).

Measurement noise effect:

The previous results indicate that indefinitely increasing the filter variance $\sigma_{w_{T_{pc}}}^2 = \sigma_{w_{\xi}}^2$ would result in a more accurate pedaling torque estimation. However, in a realistic scenario, the noise affects the measured signals employed as inputs and outputs of the PTOs. In these conditions, the selection range of the covariance matrix values is limited depending on the noise level of the measurements. To analyze this effect, a measured speed with an additional normal distributed noise of variance $\sigma_v^2 = 10^{-8} \frac{m^2}{s^2}$ has been considered in the performed

4.4 Pedaling torque observers simulation

simulations. Figure 4.10 and 4.11 contain the results of this analysis in the case a CPTO and a SPTO are employed, respectively. As one can see, for increasing variance levels $\sigma_{w_{T_{pc}}}^2 = \sigma_{w_{\xi}}^2$, the pedaling torque estimation is more affected by the measurement noise and might be not suitable to generate references for the motor torque control. Thus, in practical applications, where noise and errors affect the measurements, infinitely high variance values $\sigma_{w_{T_{pc}}}^2 = \sigma_{w_{\xi}}^2$ cannot be chosen because the PTOs would rely too much on noisy measurements degrading the pedaling torque estimation. Also, it can be noticed that, at the same variance level, the SPTO estimation worsens more in the presence of measurement noise compared to the CPTO one.

Based on the considerations above, in a realistic scenario, where smaller variance values need to be employed, the CPTO only allows approximately the estimation of the average pedaling torque and not its instantaneous value. Whereas, a SPTO, although more responsive to torque variations, might be more susceptible to measurement noise and errors. Therefore, in the following simulations only the state observers tuned with $\sigma_{w_{T_{pc}}}^2 = \sigma_{w_{\xi}}^2 = 10^3 \text{ N}^2 \text{ m}^2$ will be considered. Moreover, it has to be remarked that to evaluate the effect of modeling errors and parametric variations on the estimation independently from measurement noise, the latter will be neglected in the subsequent simulations.

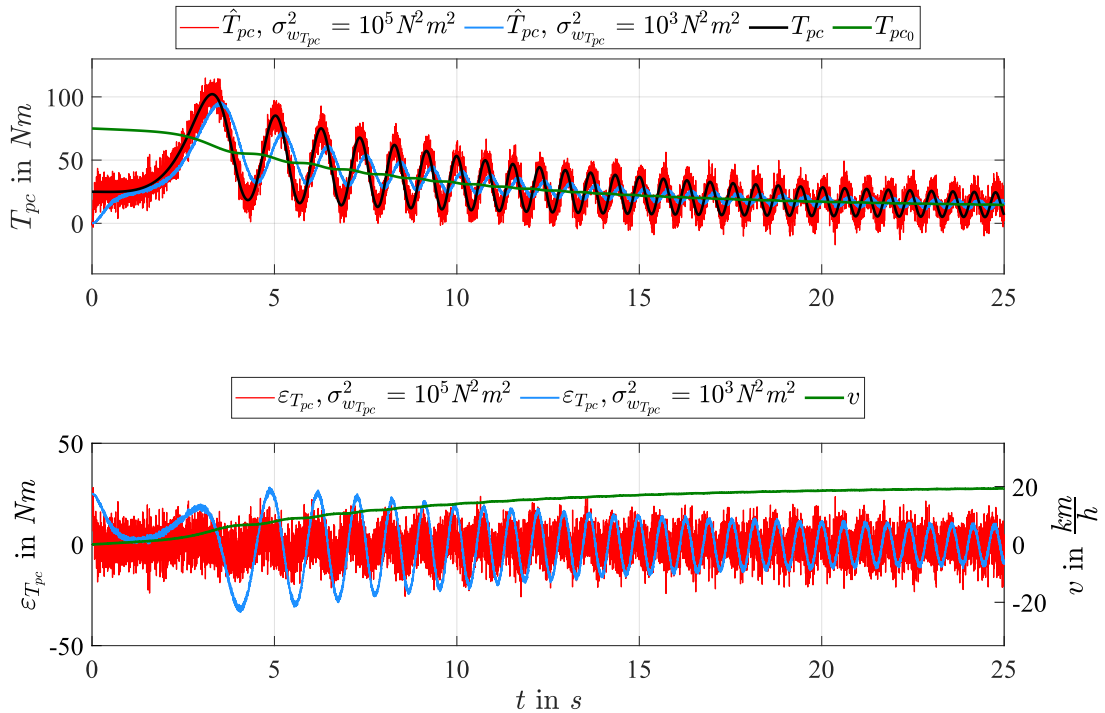


Figure 4.10: Simulated effect of the speed measurement noise on the CPTO tuning. From top to bottom: Pedaling torque estimation \hat{T}_{pc} ; corresponding pedaling torque estimation error $\varepsilon_{T_{pc}}$ and bicycle speed v .

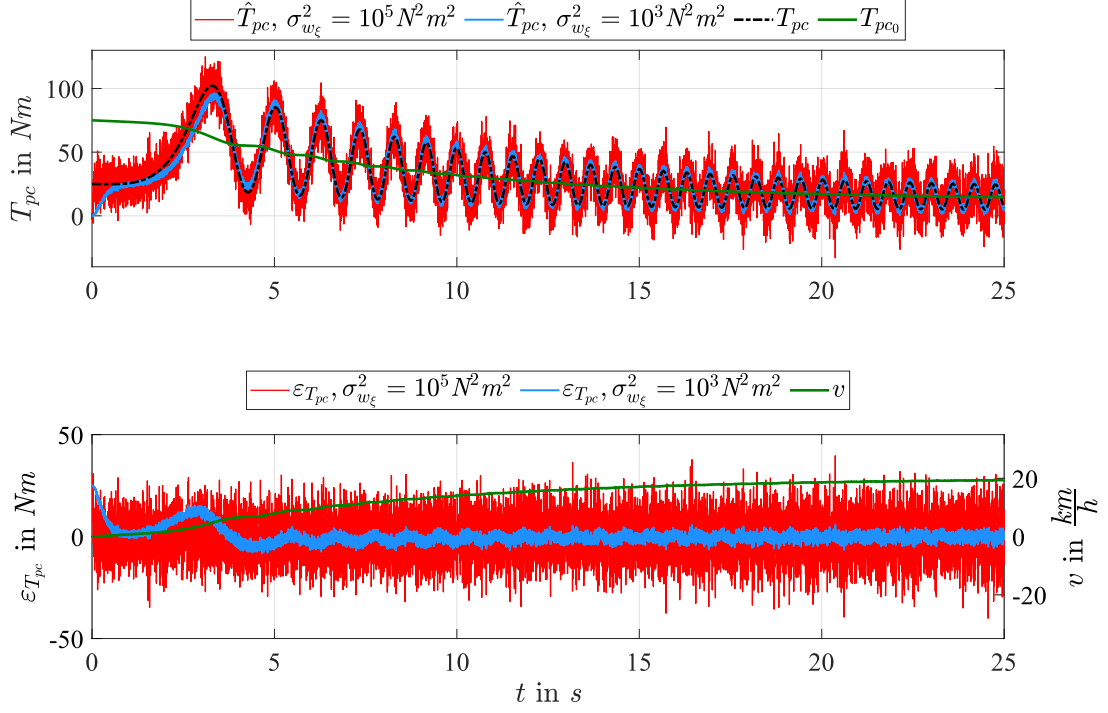


Figure 4.11: Simulated effect of the speed measurement noise on the SPTO tuning. From top to bottom: Pedaling torque estimation \hat{T}_{pc} ; corresponding pedaling torque estimation error $\varepsilon_{T_{pc}}$ and bicycle speed v .

4.4.2 Effect of modeling simplifications

This section analyzes the effects of model simplifications on the pedaling torque estimation. In particular, unmodelled pedaling torque high-order harmonics, neglected mechanical transmission losses, unmodelled external forces, and wind acting on the bicycle longitudinal dynamics are evaluated.

Pedaling torque high-order harmonics:

As stated in Section 3.1.2, pedaling torque profiles can be highly variable and challenging to describe mathematically. Indeed, equation (4.33) represents a simplified model of the pedaling torque profile. Cycling torques are not perfectly sinusoidal because they are affected by high-order harmonics that depend on the specific applied pedaling pattern. Figure 4.12 shows the simulation results obtained considering the effect of pedaling torque high-order harmonics when considering the two proposed PTOs. In this simulation, it has been assumed that the pedaling torque presents a small 4th harmonic component $|T_{pc4}| < |T_{pc2}|$ and can be described by the following expression:

$$T_{pc}(t) = \frac{3}{4}y_{PI}(t) - \frac{1}{2}y_{PI}(t)\cos[2\theta_c(t)] - \frac{1}{8}y_{PI}(t)\cos[4\theta_c(t)]. \quad (4.82)$$

4.4 Pedaling torque observers simulation

Under these hypotheses, the RMSE reported to the back wheel has been evaluated resulting in 4.64 Nm in the case of the CPTO, and 1.55 Nm in the case of the SPTO. Therefore, even in the presence of pedaling torque high-order harmonics, the sinusoidal model performs better than the constant one with an RMSE reduction of circa 66%. Furthermore, comparing the obtained results with the ones of Table 4.3, one can notice that the presence of high-order harmonics worsens the RMSE of the CPTO of circa 2% and the one of the SPTO of about 16%. Due to the better pedaling torque estimation obtainable when employing a sinusoidal pedaling torque model, in the following simulations, only the latter is taken into account.

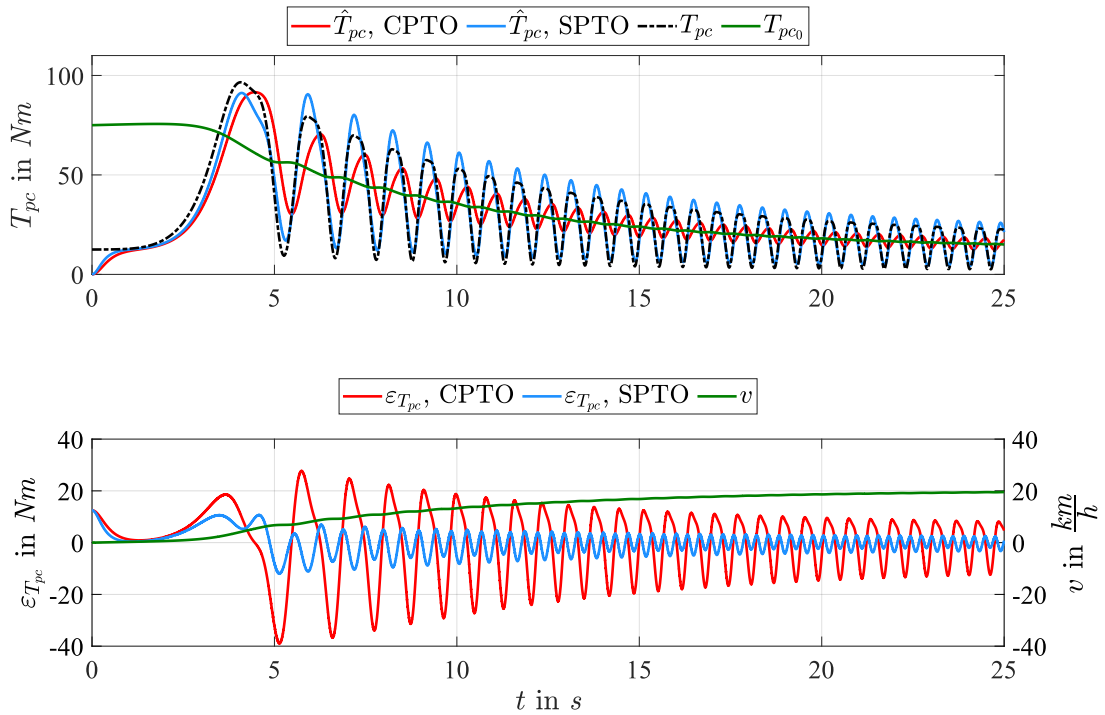


Figure 4.12: Simulated effect of pedaling torque high-order harmonics on the pedaling torque estimation obtained with the two proposed PTOs. From top to bottom: Pedaling torque estimation \hat{T}_{pc} using CPTO and SPTO; corresponding pedaling torque estimation error $\varepsilon_{T_{pc}}$ and bicycle speed v .

Mechanical transmission losses:

Electric bicycle mechanical transmissions are typically characterized by high efficiency with values close to 1. The highest power losses are caused by the bicycle drivetrain chain transmission. Thus, the simulation analysis is performed considering a drivetrain transmission with the worst case efficiency $\eta_d = 0.85$ defined in Section 3.1.1. The obtained results are reported in Figure 4.13. Compared to Figure 4.9, it can be seen that neglecting the drivetrain efficiency introduces an offset in the pedaling torque estimation. Under these hypotheses, the RMSE reported at the back wheel has been calculated resulting in 2.65 Nm . Thus,

its value worsens of circa 101% compared to the case $\eta_d = 1$. Nevertheless, it has to be remarked that the calculated value represents a worst case. In the case unworn and lubricated chains are employed ($\eta_d \simeq 0.97$), the effect of the unmodelled mechanical transmission efficiency can be neglected without affecting the pedaling torque estimation considerably.

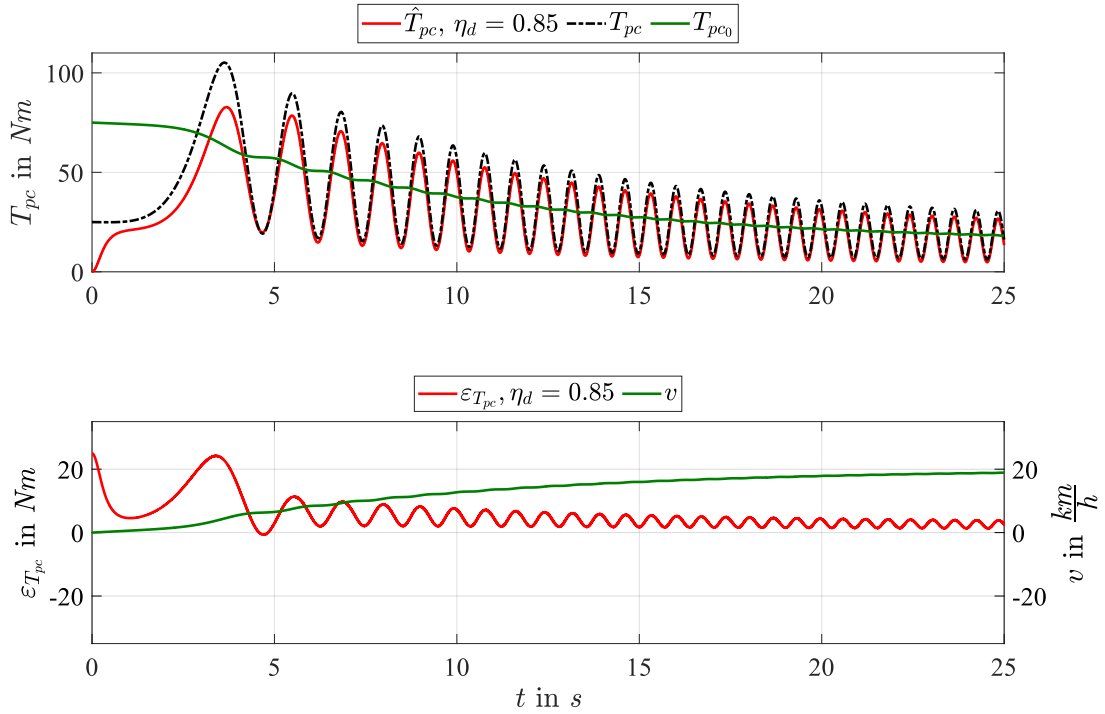


Figure 4.13: Simulated effect of unmodelled drivetrain transmission efficiency η_d on the pedaling torque estimated using the SPTO. From top to bottom: Pedaling torque estimation \hat{T}_{pc} ; corresponding pedaling torque estimation error $\varepsilon_{T_{pc}}$ and bicycle speed v .

External forces:

This paragraph analyzes the effect of unmodelled external forces acting on the longitudinal dynamics such as human forces not generated through the crankset mechanism F_h^e and braking forces F_B . In the performed simulation, it has been assumed that a propulsive human force $F_h^e = 100 \text{ Nm}$ is applied in $t \in [0; 8] \text{ s}$, a pedaling force F_p acts in $t \in [8; 17] \text{ s}$, and the vehicle is braked by a force $F_B = -100 \text{ Nm}$ in $t \in [17; 25] \text{ s}$. It has to be remarked that, to obtain a more realistic profile of the applied forces, a first order LPF with a cut frequency $f_{c_F} = 0.8 \text{ Hz}$ has been employed. The obtained simulation results are reported in Figure 4.14. As one can see, the state observer tracks after a short transient all the applied external forces and cannot distinguish between unmodelled forces and the pedaling one. Therefore, one can conclude that the PTOs consider all the unmodelled forces acting on the vehicle longitudinal dynamics as pedaling force.

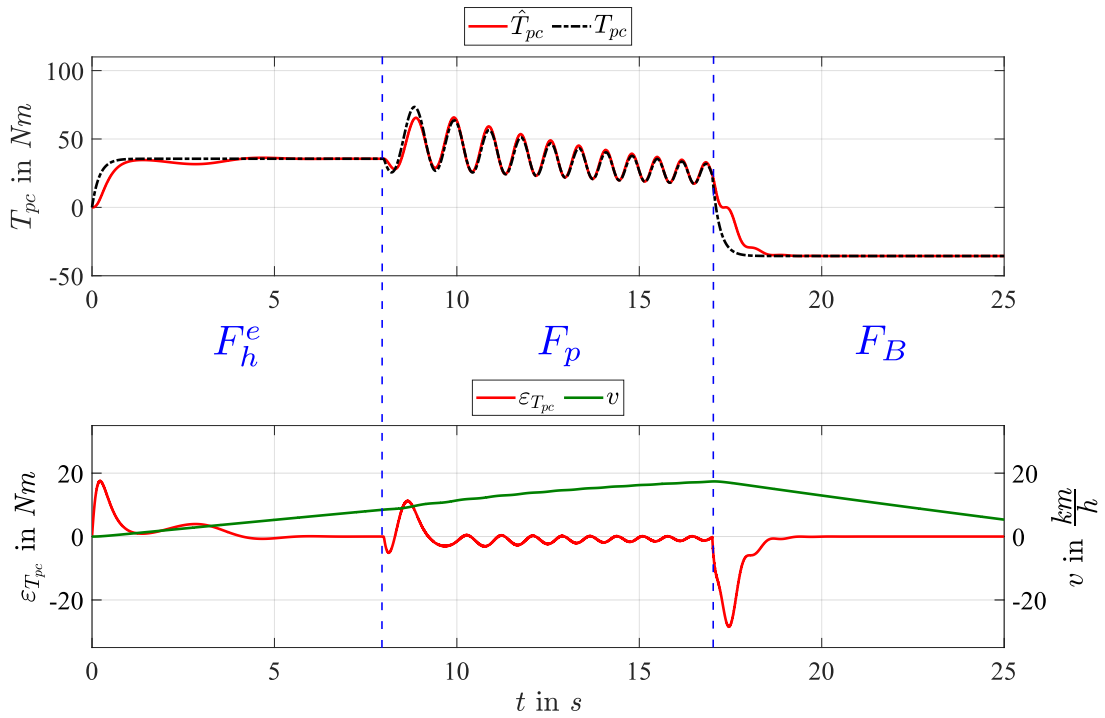


Figure 4.14: Simulated effect of unmodelled external forces (F_h^e and F_B) on the pedaling torque estimated using the SPTO. From top to bottom: Pedaling torque estimation \hat{T}_{pc} ; corresponding pedaling torque estimation error $\varepsilon_{T_{pc}}$ and bicycle speed v .

Wind effect:

Following, the effect of the wind on the pedaling torque estimation is evaluated. In particular, a headwind $v_{w_x} = 10 \frac{km}{h}$ and a tailwind $v_{w_x} = -10 \frac{km}{h}$ are analyzed in Figure 4.15 and 4.16, respectively, because their presence modifies the simulated pedaling torque profile. As one can see, in the presence of a headwind, the cyclist applies a higher torque to reach the desired speed target. The state observer, which does not consider the wind in its model, interprets the lower acceleration due to the resisting effect of the wind as a lower applied pedaling torque. One can notice that the introduced estimation offset increases with the speed where the aerodynamics has a higher impact on the vehicle dynamics. Similarly, in the presence of a tailwind, the cyclist applies a smaller torque and the state observer interprets the propelling effect of the wind and the higher acceleration as a higher applied torque. Also in this case, the introduced estimation offset increases with the speed. The RMSE reported at the back wheel has been calculated resulting in 2.66 Nm in the case of headwind and 2.1 Nm in the presence of tailwind. Thus, the RMSE worsens by circa 102% and 59% respectively compared to the no wind situation. One can notice that the estimation is not affected equally by headwinds and tailwinds. Indeed, contrarily to tailwinds, a headwind always increases the apparent wind determining a higher aerodynamic drag independently of its intensity. This causes a bigger error in the pedaling torque estimation

compared to a tailwind of the same intensity. From this analysis, one can conclude that the presence of wind affects the pedaling torque estimation at high speed and in the presence of strong headwinds even at low speed. Nevertheless, thanks to the high-variable wind direction and intensity strong headwinds occur rarely. Therefore, the effect of wind can be typically neglected in the PTO model.

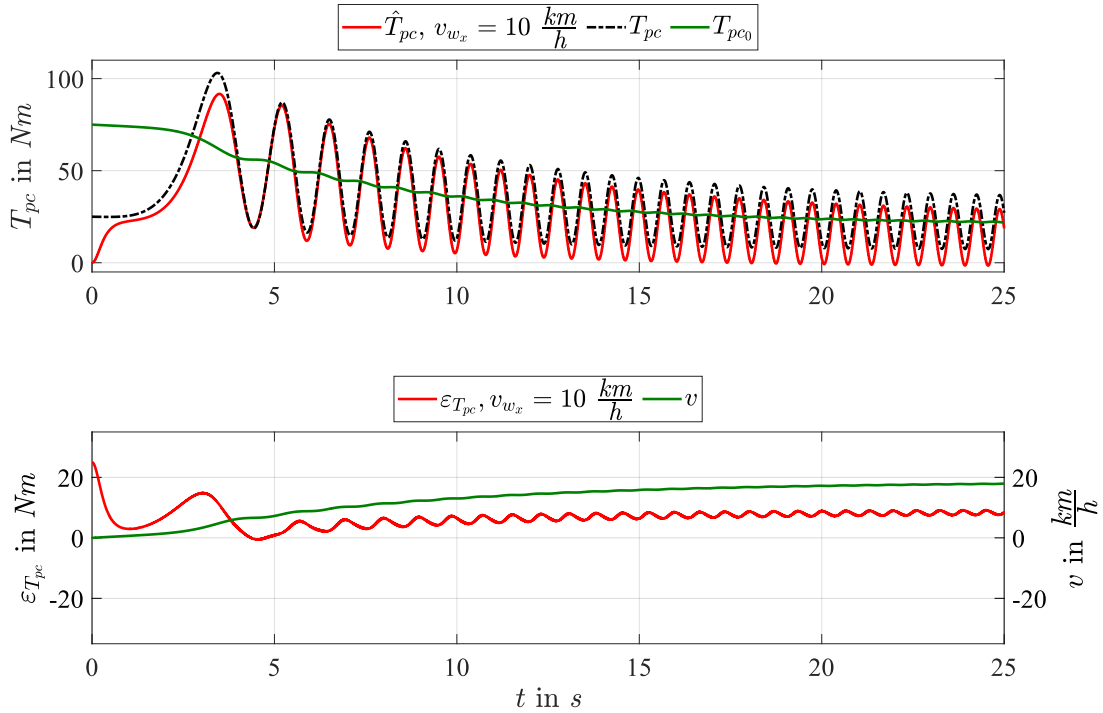


Figure 4.15: Simulated effect of a headwind $v_{w_x} > 0 \frac{km}{h}$ on the pedaling torque estimation obtained using the SPTO. From top to bottom: Pedaling torque estimation \hat{T}_{pc} ; corresponding pedaling torque estimation error $\varepsilon_{T_{pc}}$ and bicycle speed v .

4.4.3 Effect of parametric variations

In this section, the effect of bicycle mass m , drag area A_d , air density ρ , and rolling friction coefficient μ variations are evaluated within the worst case range defined in Section 3.2. Moreover, this section analyses also the effects of road slope estimation errors on the pedaling torque estimation accuracy.

Model parametric variations:

Following, the simulation results obtained in the presence of model parametric variations are analyzed. As one can see in Figure 4.17, worst-case errors in the mass value considerably affect the pedaling torque estimation, especially in the low-speed range, introducing a significant offset in the estimated pedaling torque. Nevertheless, this error decreases with

4.4 Pedaling torque observers simulation

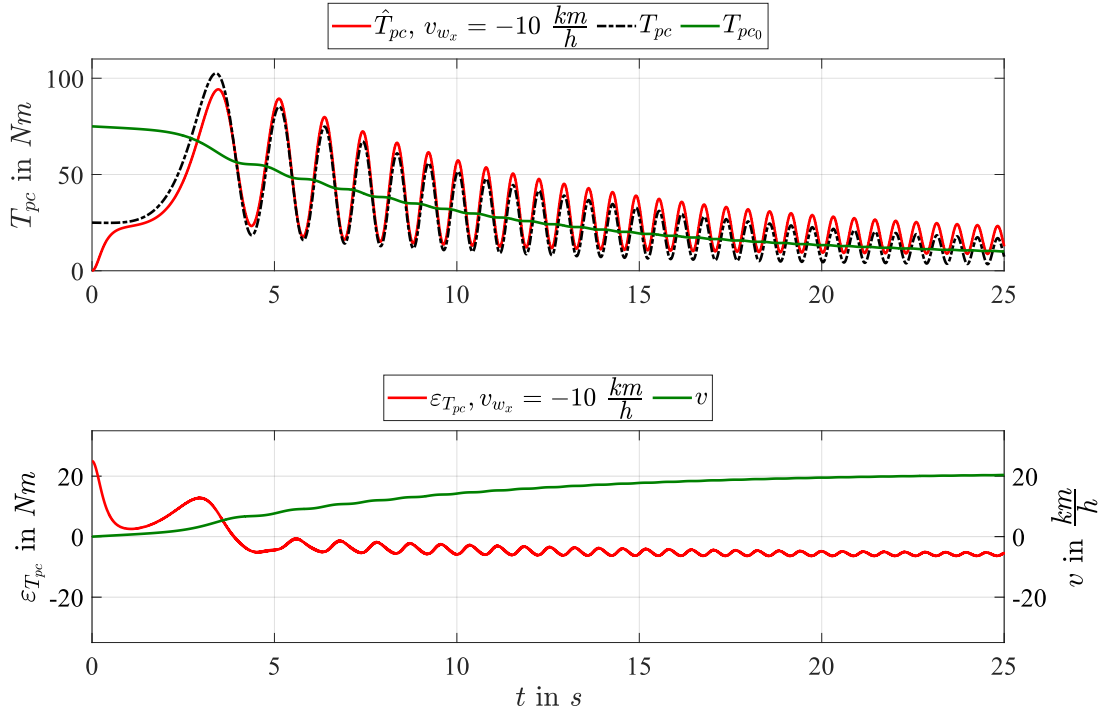


Figure 4.16: Simulated effect of a tailwind $v_{w_x} < 0 \frac{km}{h}$ on the pedaling torque estimation obtained using the SPTO. From top to bottom: Pedaling torque estimation \hat{T}_{pc} ; corresponding pedaling torque estimation error $\varepsilon_{T_{pc}}$ and bicycle speed v .

the speed, and results comparable to the effect of the other parametric variations at high speeds. The RMSE reported at the back wheel has been calculated resulting in 5.12 Nm in the case the filter considers a wrong system mass $m = 60 \text{ kg}$ and 4.93 Nm in the case $m = 140 \text{ kg}$. Thus, an error in the mass value knowledge worsens the RMSE of circa 288% in the worst-case scenario compared to a perfect knowledge of the system mass. On the contrary, Figure 4.18 shows that the drag area variation affects the estimation, especially at high speeds where the aerodynamics is not negligible while it has a small effect on the estimation in the low-speed range. The RMSE reported at the back wheel has been calculated resulting in 1.33 Nm in the case the assumed drag area is $A_d = 0.32 \text{ m}^2$ and 1.7 Nm when $A_d = 0.63 \text{ m}^2$. Therefore, the worst-case error on the knowledge of the drag area worsens the RMSE of circa 29% compared to a perfect knowledge of this value. Compared to the other parametric variations, as illustrated in Figure 4.19, an air density variation results negligible in the entire speed range. Also for air density variations, the RMSE reported at the back wheel has been calculated resulting in 1.32 Nm in the case the assumed air density is $\rho = 1.14 \frac{kg}{m^3}$ and 1.35 Nm in the case $\rho = 1.3 \frac{kg}{m^3}$. Thus, the worst-case error on the air density knowledge worsens the estimation of circa 2% compared to a perfect knowledge of this value. Contrary to drag area variations, Figure 4.20 shows that rolling friction coefficient changes affect the estimation also in the low-speed range. Furthermore, one can notice that the intro-

duced offset is constant and not speed-dependent. The RMSE reported at the back wheel has been calculated resulting in 1.7 Nm in the case the assumed rolling friction coefficient is $\mu = 0.002$ and 2.13 Nm when $\mu = 0.01$. Therefore, the worst-case error in the knowledge of the rolling friction coefficient worsens the estimation of circa 61% compared to a perfect knowledge of this value. The results obtained concerning the worst-case RMSEs reported at the back wheel and the respective increment compared to a perfect knowledge of the system parameters are summarized in Table 4.4. It has to be remarked that the worst case RMSE increments here reported are expressed to the assumed real values of Table 4.2. Higher errors are expected in the case extreme values of the parametric range are considered.

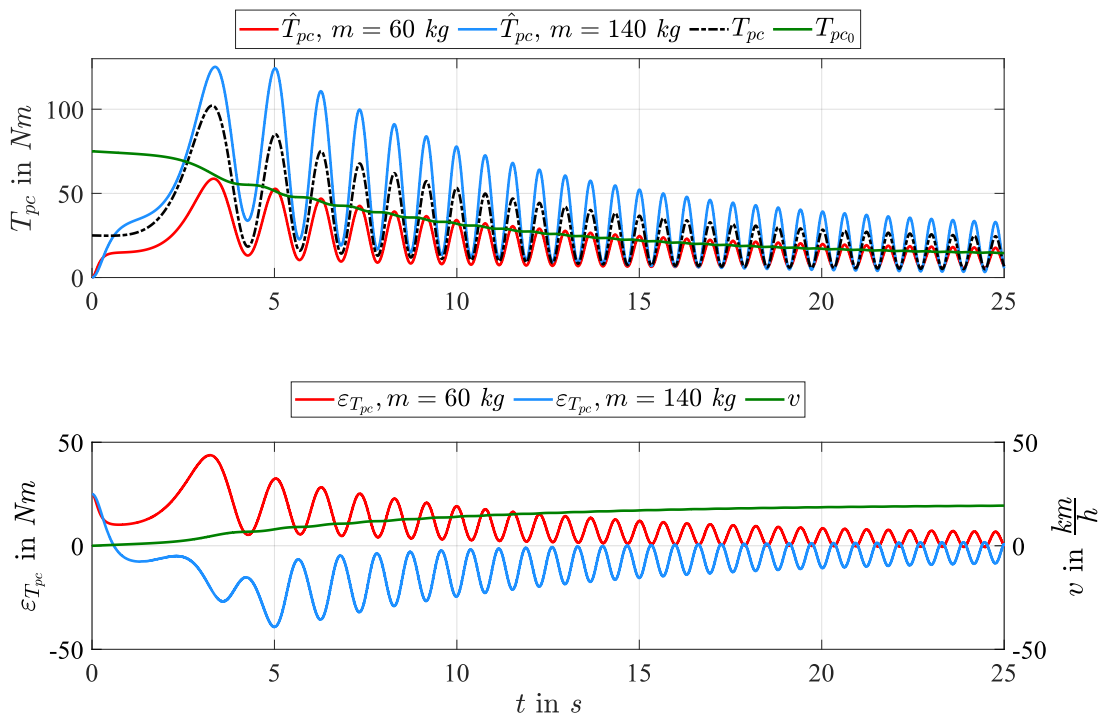


Figure 4.17: Simulated effect of a mass m variation on the pedaling torque estimation obtained using the SPTO. From top to bottom: Pedaling torque estimation \hat{T}_{pc} ; corresponding pedaling torque estimation error $\varepsilon_{T_{pc}}$ and bicycle speed v .

4.4 Pedaling torque observers simulation

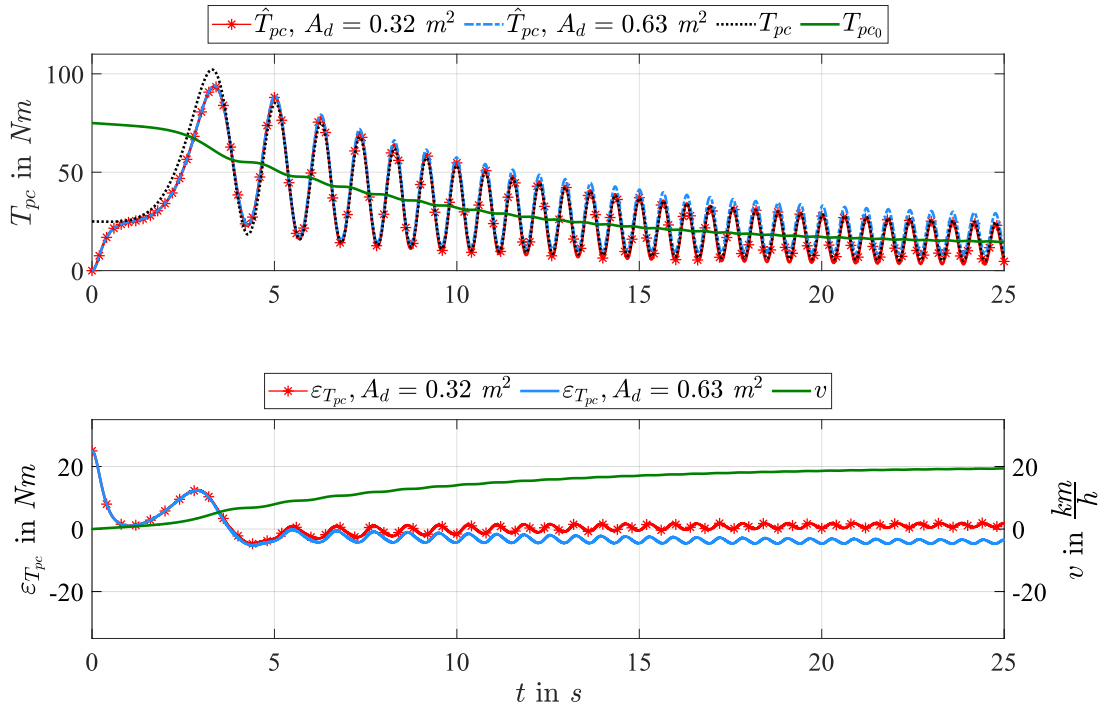


Figure 4.18: Simulated effect of a drag area A_d variation on the pedaling torque estimation obtained using the SPTO. From top to bottom: Pedaling torque estimation \hat{T}_{pc} ; corresponding pedaling torque estimation error $\varepsilon_{T_{pc}}$ and bicycle speed v .

Road slope estimation error:

The effects of a road slope estimation error ε_β on the pedaling torque estimation are reported in Figure 4.21. In particular, the errors $\varepsilon_\beta = 0.1 \text{ deg}$ and $\varepsilon_\beta = 1 \text{ deg}$ are analyzed in simulation. As one can see, road slope estimation errors affect the pedaling torque estimation generating offsets even when tiny road slope estimation errors comparable to barely perceivable slopes occur. Moreover, one can notice that the effect of a road slope estimation error is not speed-dependent. In both cases, the RMSE reported at the back wheel has been calculated resulting in 1.43 Nm in the case a road grade estimation error of 0.1 deg occurs and 6.09 Nm in the case the estimated slope differs of 1 deg from its real value. Considering these two cases, the RMSE worsens by circa 8% and 361% respectively. This analysis clarifies that the road slope estimation error minimization is fundamental to achieve accurate pedaling torque estimates. Indeed, narrow road estimation errors below 1 deg introduce a pedaling torque estimation error comparable to the one caused by a considerable mass identification error.

4.4.4 Considerations

The performed simulation analysis allows us to understand the assets and drawbacks of the proposed pedaling torque estimation approaches. It has been shown that the PTOs estimate the pedaling torque by exploiting the bicycle longitudinal dynamic model, the measured bi-

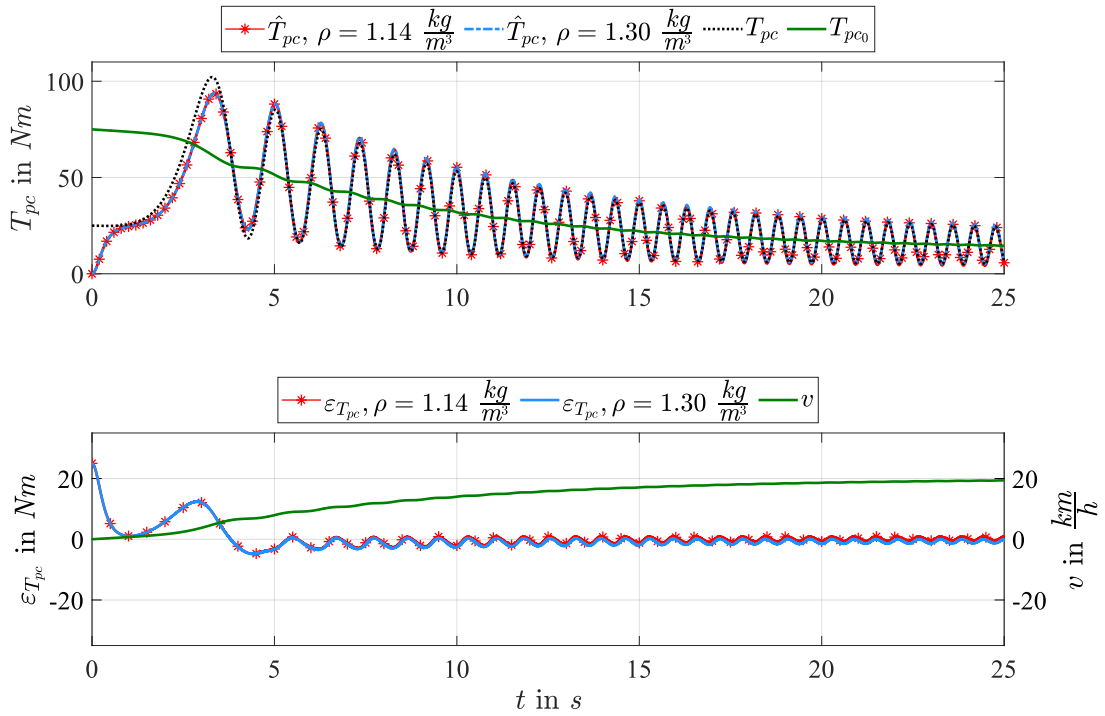


Figure 4.19: Simulated effect of air density ρ variation on the pedaling torque estimation obtained using the SPTO. From top to bottom: Pedaling torque estimation \hat{T}_{pc} ; corresponding pedaling torque estimation error $\varepsilon_{T_{pc}}$ and bicycle speed v .

cycle speed, the motor torque, and the estimated road slope. The simulation results point out that model parametric variations and model simplifications can affect the pedaling torque estimation accuracy. Therefore, accurate parameter knowledge and measurements are fundamental for estimation error minimization. The addition of fictitious process noise in the KF model has been employed to compensate for the simplified pedaling torque modeling. It has been shown that the sinusoidal pedaling torque model exploitation allows for improved estimation compared to a constant one. Nevertheless, the SPTO estimation is more susceptible than the one of the CPTO to the presence of measurement noise and errors.

The modeling hypothesis of Section 4.2.1 can be accepted without influencing the estimation accuracy considerably. In particular, typical high-order pedaling torque harmonics do not alter the estimation accuracy remarkably when employing a SPTO. Moreover, in the case of unworn and lubricated transmissions, also drivetrain losses can be neglected without affecting the estimation considerably. Also, the simulations show that neglecting the effect of the wind does not significantly influence the pedaling torque estimation except in the rare case of a strong headwind. Nonetheless, it has been shown that the proposed methods cannot distinguish between the pedaling torque and external forces acting on the vehicle dynamics not generated through the crankset such as braking forces or thrust forces applied by the cyclist without employing the pedals.

The effect of parametric variations is speed-dependent and can impact significantly on

4.4 Pedaling torque observers simulation

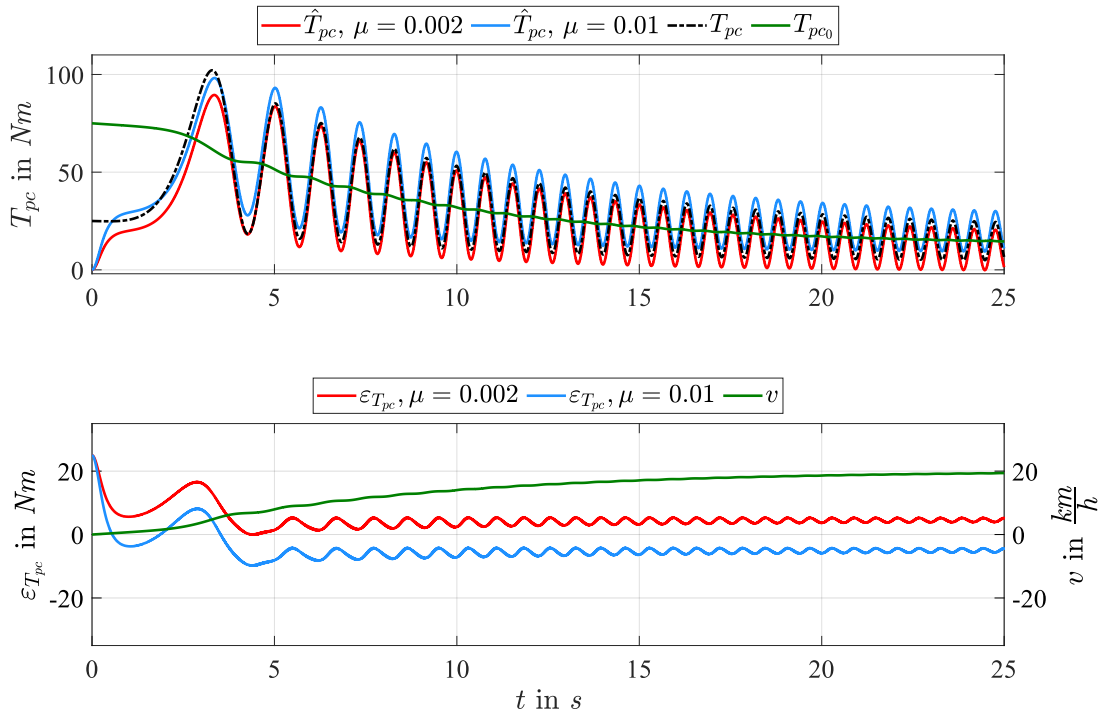


Figure 4.20: Simulated effect of rolling friction coefficient μ variation on the pedaling torque estimation obtained using the SPTO. From top to bottom: Pedaling torque estimation \hat{T}_{pc} ; corresponding pedaling torque estimation error $\varepsilon_{T_{pc}}$ and bicycle speed v .

the estimation especially when combined variations occur concurrently. The simulation results confirm that in the low-speed range, the estimation accuracy depends mainly on the knowledge of the system mass and the road grade. Since the mass is typically a constant parameter while riding, the pedaling torque estimation quality is strongly related to the road slope estimation accuracy. Moreover, it has been shown that errors in the knowledge of the drag area and rolling friction coefficient affect the estimation less than the mass and road slope. Thus, these parameters can be considered constant without influencing the estimation and the provided electrical assistance remarkably. In addition, the simulations showed that the effect of air density variations is entirely negligible on the pedaling torque estimation accuracy.

Parameter	Worst-case RMSE in Nm	Worst-case RMSE increment
Mass m	5.12	288%
Drag area A_d	1.7	29%
Air density ρ	1.35	2%
Rolling friction coefficient μ	2.13	61%

Table 4.4: Worst-case RMSE reported at the back wheel (evaluated considering T_{pw}) in the presence of parametric variations and its increment compared to the RMSE obtained with perfect knowledge of the parameters when using the SPTO.

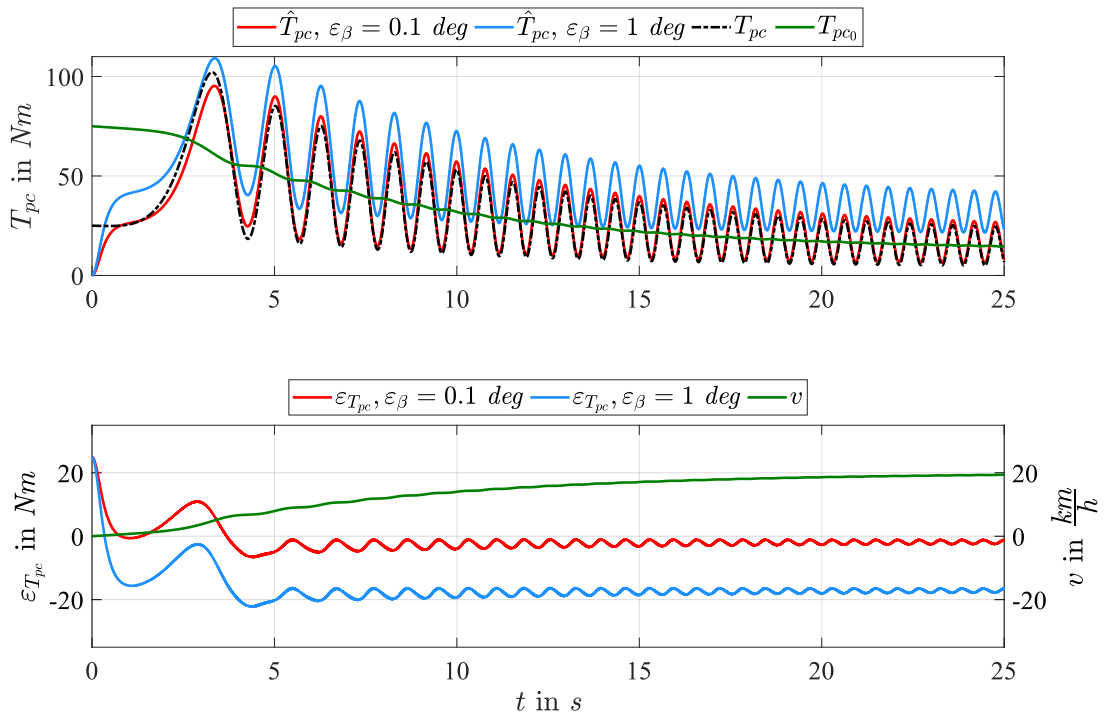


Figure 4.21: Simulated effect of road slope estimation error ε_β on the pedaling torque estimation obtained using the SPTO. From top to bottom: Pedaling torque estimation \hat{T}_{pc} ; corresponding pedaling torque estimation error $\varepsilon_{T_{pc}}$ and bicycle speed v .

5 Experimental results

In this chapter, the previously proposed PTOs are experimentally validated. Tests are performed in realistic riding conditions to analyze the torque estimation error and the cycling effort reduction in a variable sloped environment. In particular, the experiments are performed on a pedelec prototype programmed to generate electrical aid utilizing a simple fixed-gain control strategy.

Firstly, a description of the implemented torque-sensorless control method and the design choices made in the prototype development phase is provided. After that, the proposed algorithm employed to estimate the road angle is analyzed performing outdoor tests. A particular focus is placed on the selection of the tuning parameters and the angle estimation error analysis in the presence of vehicle accelerations, variable slopes, and curves. Then, the PTOs tuning is analyzed in the absence of road grade variations and electrical assistance. Afterwards, the effect of road angle estimation errors and motor control on the pedaling torque estimation is evaluated under noteworthy riding conditions, namely during the starting phase and uphill riding. Then, the cycling performances obtained with the proposed torque-sensorless approaches, expressed in terms of cycling power and energy reduction, are compared with the ones achieved when employing a torque sensor. Eventually, a qualitative analysis of the proposed electrical assistance methods is performed by letting several people test the prototype and answer a survey.

5.1 Bicycle prototype

This section describes the bicycle prototype that has been developed to perform the experimental validation in this work. Firstly, a generic system description that provides an overview of the proposed torque-sensorless control strategy implementation in the pedelec prototype is given. Then, mechanical and electrical design characteristics of the bicycle prototype are discussed.

5.1.1 System description

Figure 5.1 contains a schematic representation of the system functionalities. As one can see, the sensorless pedaling torque estimation is achieved by substituting the torque sensor with current sensors, a rotor position sensor, and a six-axes IMU. In particular, the measured currents \mathbf{i}_{abc} and the electrical rotor position θ_e are employed to control the motor torque T_m to the desired value T_m^* relying on a FOC. By differentiating the position sensor measurement, the vehicle longitudinal speed v is obtained. The latter together with the longitudinal acceleration measurement provided by the IMU a_{s_x} are the inputs of a road slope observer that estimates the road angle $\hat{\beta}$. To compensate for cornering effects on the road slope estimation, the measured angular speed ω_{s_z} given by the IMU is also employed. Afterwards,

5.1 Bicycle prototype

the applied motor torque, the measured bicycle speed, and the estimated road angle are provided to the PTO to estimate the pedaling torque \hat{T}_{pc} . The obtained estimation can be employed to control the motor torque to the desired reference generated according to the chosen pedelec control strategy. It has to be remarked that a pedaling torque sensor is anyway installed in the designed prototype for validation purposes.

Since the focus of this work is to analyze the accuracy of the pedaling torque estimation and to prove that the estimated signal can be used to assist the bicycle motion and reduce cycling efforts, a simple power-oriented fixed-gain control strategy has been chosen among the possible electrical assistance strategies. To reduce system complexity, regenerative braking has also not been implemented in the prototype.

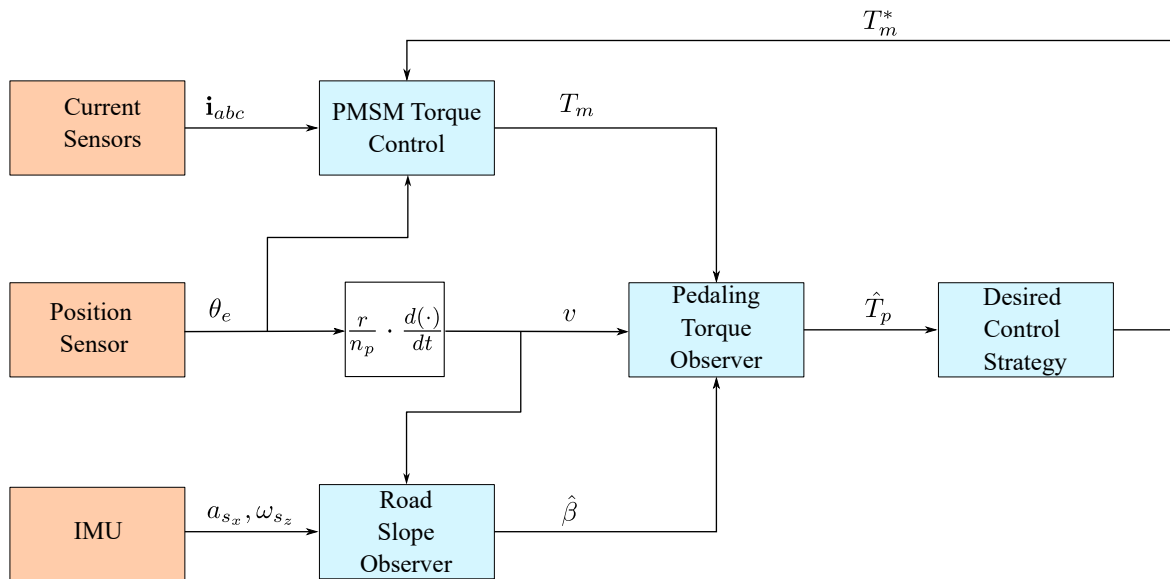


Figure 5.1: Schematic representation of the proposed pedelec torque-sensorless assistance.

5.1.2 Mechanical design

The main objective of the prototype mechanical design was to create an easy-to-access and -maintain system that simplifies testing procedures. Figure 5.2 contains a picture of the pedelec prototype employed for testing the proposed sensorless control approach. The considered bicycle has a standard diamond frame and mounts 28" tires and a drivetrain with a fixed and known gear ratio $\tau_d = 2.8$. The electrical assistance is provided through a hub direct-drive motor mounted on the back wheel. The choice of mounting the motor on the pedelec rear wheel reduces the possibility of the wheel slipping at the cost of increased weight unbalance between the wheels. The battery and the control electronics are placed inside a rear bicycle basket increasing the system compactness and reducing power losses because the cable length is minimized. Nonetheless, the installation of the motor, battery, and control electronics in the rear part of the bicycle determines an increment of the weight unbalance and thus worsens the rideability of the vehicle. A hub motor has been chosen

since it can be easily mounted on the bicycle without the need to modify the frame as in the case of many mid-drive solutions. Friction drives have been discarded due to the high power losses and tire wear that they cause. A direct-drive motor has been preferred to a geared one to simplify the system modeling. Indeed, these motors do not contain internal mechanical transmissions that are often not accessible and have gear ratios that are not explicitly declared by manufacturers. Moreover, thanks to their large dimensions, direct-drive motors offer the possibility of integrating the control electronics inside the motor hub. This feature could be exploited for future developments of the bicycle prototype. Additionally, the absence of a freewheeling mechanism would allow for the implementation of regenerative braking in further developments of the system.

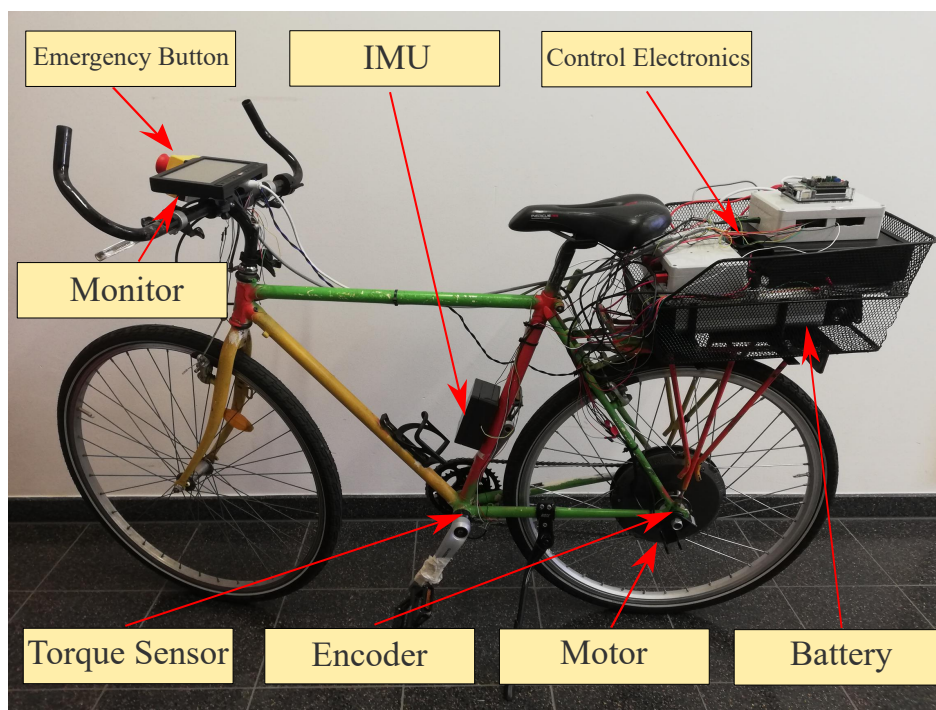


Figure 5.2: Designed pedelec prototype for the torque-sensorless control validation.

5.1.3 Electrical design

A hub direct-drive motor *HS3540* produced by *Crystalyte Europe* is employed to provide electrical assistance in the designed prototype. The considered motor is a PMSM with superficially mounted magnets whose main characteristics are reported in [143]. A PMSM has been preferred to a BLDC motor because it offers the possibility of employing FOC to control the motor torque and thus achieve better dynamical performances and reduced torque ripple. Among the possible energy storage sources employable in a pedelec, a Li-Ion battery has been selected due to the high energy density and lifetime that characterize these batteries compared to other technologies. In particular, the *Maratronic SilverFish XH259 24 V* battery pack has been utilized. The chosen battery has a maximum output voltage of 25.9 V and a capacity of 12 Ah. It can be noticed that for safety reasons in the prototype testing

phase, the minimum battery voltage applicable to the motor has been chosen. For the sake of brevity, further details about the designed control electronics and the employed sensors are provided in the appendix (Section 7.2).

The achievement of a highly efficient motor torque control requires a correct knowledge of the motor electrical parameters. However, their value is often not provided by manufacturers that rather give information regarding the rated quantities (power, speed, voltage, and current), the weight, and the dimensions of the motor. Since motor parameters are not provided in the specific manufacturer datasheet, in this work an offline parametric identification has been performed. Table 5.1 contains the electrical motor parameters of the designed pedelec prototype obtained by performing an offline identification based on LCR-meter measurements and the guidelines provided in [144].

Motor parameter	Value
Number of pole pairs n_p	23
Rated DC voltage \tilde{U}_{DC}	48 V
Rated DC current \tilde{i}_{DC}	45 A
Rated power \tilde{P}	2 kW
Rated torque \tilde{T}_m	80 Nm
Rated mechanical speed $\tilde{\omega}_m$	25 $\frac{rad}{s}$
Phase resistance R	105 m Ω
Inductance d-axis L_d	207 μH
Inductance q-axis L_q	252 μH
Permanent magnet flux linkage Ψ_{PM}	0.028 Vs
Torque constant K_T	0.966 $\frac{Nm}{A}$

Table 5.1: Identified motor electrical parameters of the *HS3540* hub direct-drive motor utilized in the designed pedelec prototype.

5.2 Road slope estimation

This section analyses the experimental results obtained with the proposed road slope estimation approaches under different riding conditions. In each scenario, the algebraic method (4.64) and the suggested KF are compared with the reference road angle measured with a digital inclinometer. In particular, the confidence interval at 95% $CI_{95\%}$ of the performed static angle measurements is evaluated employing the following formula:

$$CI_{95\%} = \bar{\chi} \pm \kappa \frac{\sigma_{\chi}}{\sqrt{n}}, \quad (5.1)$$

where $\bar{\chi}$ is the measurement sample average value, σ_{χ} is its standard deviation, n is the number of considered observations, and κ is the critical value of the assumed standard normal distribution equal to $\kappa = 1.96$ in the case a confidence interval of 95% is evaluated. Considering the confidence interval allows to account for the measurement errors caused by local surface irregularities and the device uncertainty by expressing the confidence on the measured angle mean value. It has to be remarked that the algebraic method (4.62) has been neglected in this analysis due to its ineffectiveness in practical applications where bicycle leaning is not negligible. The estimation algorithms are implemented on the microcontroller with a sampling frequency of $f_s = 500 \text{ Hz}$. Besides, the wheel speed and IMU measurements are low-pass filtered with a bandwidth of $f_{c_v} = f_{c_{a_s}} = f_{c_{\omega_s}} = 1 \text{ Hz}$ to reduce the effects of vibrations and differentiation.

In the following, the tuning of the proposed KF is first discussed. After selecting the KF parameters, the road angle estimation is compared with the algebraic method in a level ground and a variable-sloped scenario. Finally, the proposed method to reduce the estimation error caused by cornering is experimentally analyzed.

5.2.1 Kalman filter tuning

In this section, the tuning of the KF employed for the road slope estimation is discussed and experimentally verified in different scenarios. Due to the modeling errors on which the proposed algorithm is based, tuning the filter means selecting the covariance matrices to weigh the confidence in the model and the measurements. In this case, more emphasis can be given to the measurements v and a_{s_x} to compensate for the modeling simplifications. Therefore, the measurement equation variances must be chosen smaller than the ones of the process $\sigma_w^2 \gg \sigma_v^2$. Besides, the model is based on the simplifying assumption that the acceleration and the slope angle are constant in time. Thus, to obtain a reliable state estimation, the confidence in each model equation must be weighted by choosing the elements of the covariance matrix \mathbf{Q} . Since a and g_x are coupled through the measured a_{s_x} , a variance ratio $\zeta_{\sigma_w^2} = \frac{\sigma_{w_a}^2}{\sigma_{w_{g_x}}^2}$ representative of the variability of the states a and g_x , i.e. of the mistrust on the respective equation, must be selected.

Based on the previous analysis, the experiments have been performed considering the following values for the covariance matrices (4.72):

$$\mathbf{Q} = \begin{bmatrix} \sigma_{w_a}^2 & 0 & 0 \\ 0 & 1 & 0 \\ 0 & 0 & \sigma_{w_{g_x}}^2 \end{bmatrix} \quad \mathbf{R} = \begin{bmatrix} 10^{-2} & 0 \\ 0 & 10^{-2} \end{bmatrix}, \quad (5.2)$$

where increasing values for the ratio $\zeta_{\sigma_w^2}$ have been evaluated considering $\sigma_{w_{g_x}}^2 = 1 \frac{m^2}{s^4}$. Figure 5.3 reports the road slope estimation results obtained with the proposed KF when pedaling on an almost flat road. In this scenario, the measured reference evaluated on the entire route presents a $CI_{95\%} = 0.16 \pm 0.17 \text{ deg}$. The calculated reference is reported in the figure with black dashed lines. Figure 5.4 contains the same analysis performed when riding on a variable sloped environment. In addition, the two figures enclose the bicycle longitudinal acceleration in each scenario that allows an analysis of the road angle estimation dependency on the vehicle acceleration. To evaluate the estimated road slope accuracy, the obtained

5.2 Road slope estimation

results are related to the traveled distance x in Figure 5.5. This allows to compare the estimated angle with the slope reference statically calculated employing the digital inclinometer. The reference slope has been evaluated at several points along the track at circa 2 m distance between each other. For each measurement point, the confidence interval at 95% of the sample is reported with a black line in Figure 5.5. As one can see, for small values of the ratio $\zeta_{\sigma_w^2}$, the estimated road slope is too sensitive to the bicycle acceleration but reacts faster to angle variations. Increasing the ratio, the filter estimate reduces its sensitivity to the acceleration at the cost of a less reactive road angle estimation. Table 5.2 contains the RMSE calculated considering the differently tuned KFs in each scenario. For increasing values of $\zeta_{\sigma_w^2}$, the RMSE decreases by circa 86% in the flat ground experiment and of the 22% in the variable sloped ground one. Based on the experimental results, higher ratios seem to be more suitable to obtain an insensitive to the vehicle acceleration grade estimation at variable slope levels. A good solution is represented by the filter with $\zeta_{\sigma_w^2} = 100$ (highlighted in Table 5.2) that will be employed in the next experiments in this work.

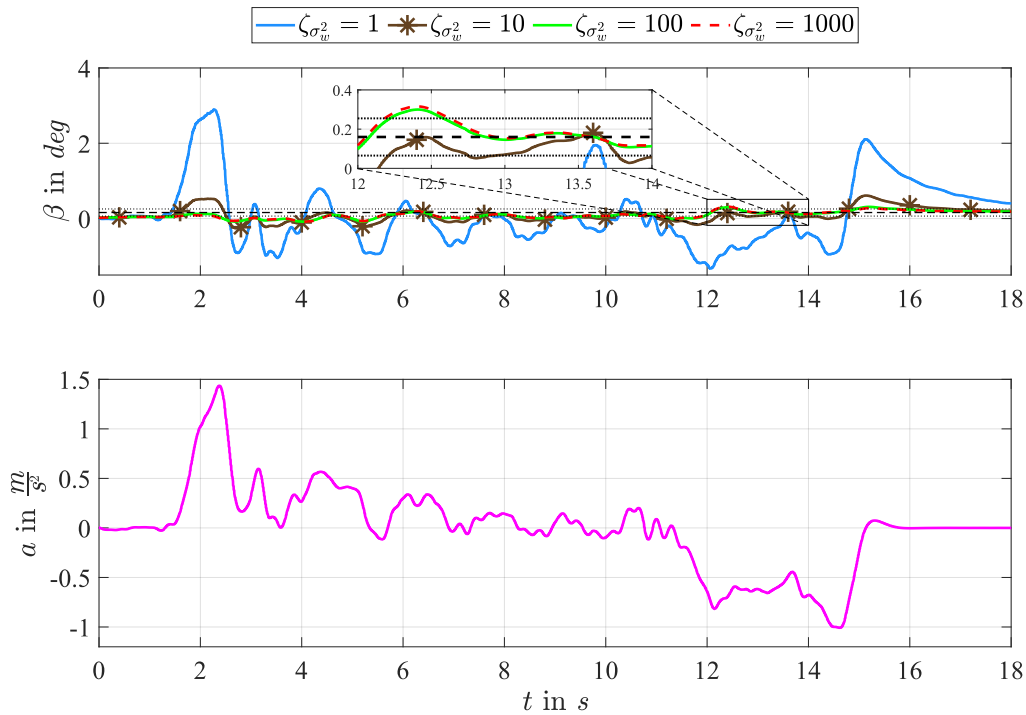


Figure 5.3: KF road slope estimation $\hat{\beta}$ dependency on the covariance matrices tuning ($\zeta_{\sigma_w^2} \in \{1; 10; 100; 1000\}$) in flat ground test ($\beta \simeq 0$ deg). The measured road slope reference confidence interval is reported with black dashed lines. From top to bottom: road slope estimation $\hat{\beta}$ and bicycle longitudinal acceleration a .

RMSE in deg				
Ground condition	$\zeta_{\sigma_w^2}$			
	1	10	100	1000
Flat ground	0.745	0.171	0.107	0.104
Variable sloped ground	0.5759	0.4476	0.4459	0.4462

Table 5.2: KF road slope estimation $\hat{\beta}$ RMSE dependency on the covariance matrices tuning in different scenarios.

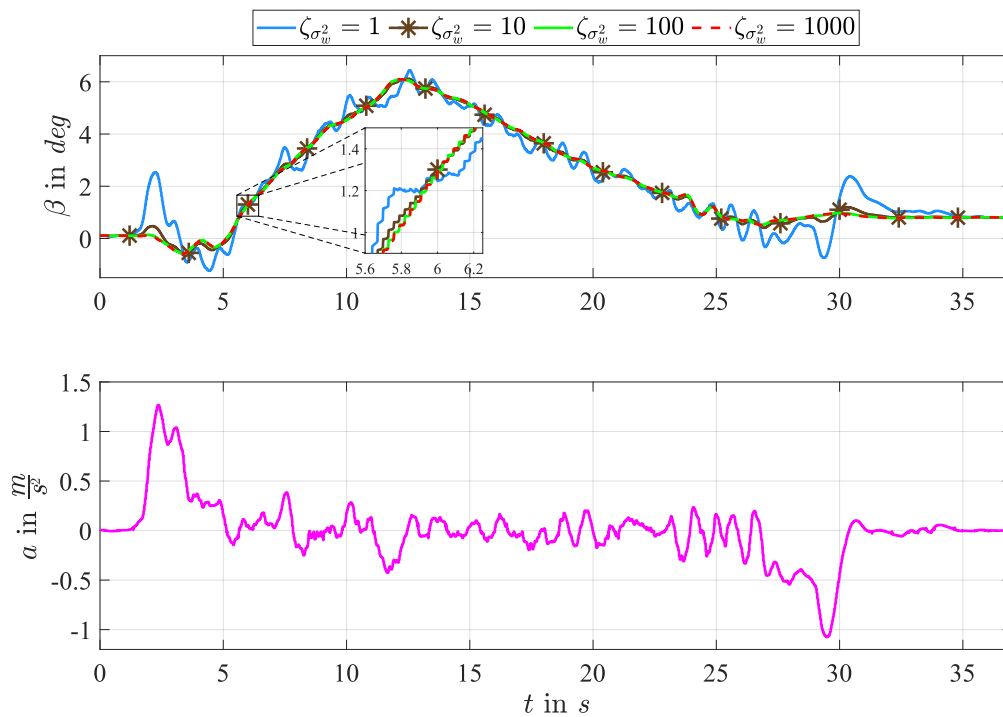


Figure 5.4: KF road slope estimation $\hat{\beta}$ dependency on the covariance matrices tuning ($\zeta_{\sigma^2} \in \{1; 10; 100; 1000\}$) in a variable sloped ground test ($\beta \neq 0$ deg). From top to bottom: road slope estimation $\hat{\beta}$ and bicycle longitudinal acceleration a .

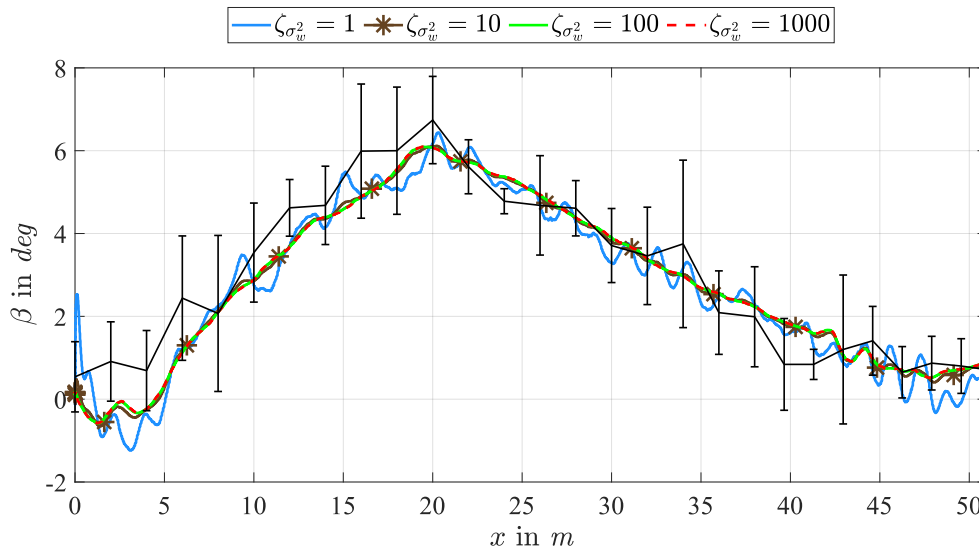


Figure 5.5: Road slope estimation $\hat{\beta}$ error analysis (related to the traveled distance x) for different KF covariance matrices tuning ($\zeta\sigma_w^2 \in \{1; 10; 100; 1000\}$) in a variable sloped ground test ($\beta \neq 0 \text{ deg}$). The measured road slope reference and its confidence interval is reported in black.

5.2.2 Level ground riding

In this section, the road slope estimations obtained with the algebraic method and the KF are compared in the case of level ground riding. Figure 5.6 contains the estimation results obtained on an almost flat road. In this scenario, the road angle has been measured with static measurements of an inclinometer resulting in a $CI_{95\%} = 0.25 \pm 0.16 \text{ deg}$. One can notice that the angle estimation obtained with the algebraic method is more noisy than the one obtained with the proposed KF. To obtain a low noise slope estimation with the algebraic method, the difference between a and a_{s_x} should be precisely equal to g_x . However, even in the absence of road slope $g_x = 0 \frac{m}{s^2}$, the acceleration signals are not the same due to the effect of measurement errors, differentiating, and filtering. As one can see, a smoother angle estimation less sensitive to acceleration variations is obtained by employing the proposed KF. For each algorithm, the RMSE has been calculated resulting in 0.434 deg for the algebraic method and 0.084 deg for the KF. Thus, a reduction of the RMSE of circa 80% is obtained by employing the KF in level ground riding.

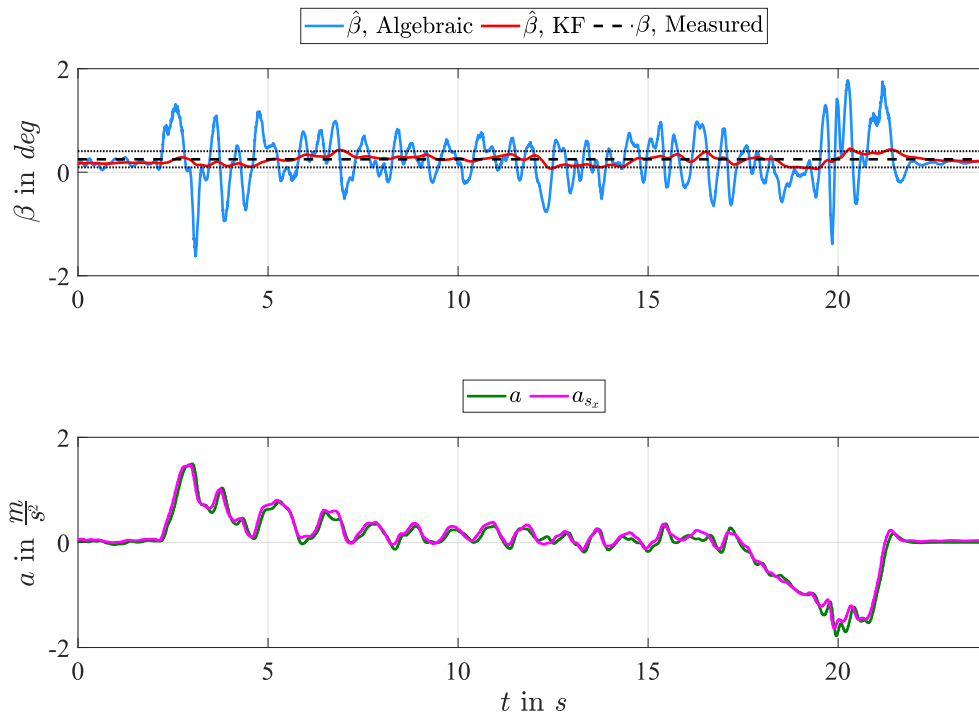


Figure 5.6: Road slope estimation $\hat{\beta}$ in level ground riding ($\beta \simeq 0 \text{ deg}$). From top to bottom: road slope estimation $\hat{\beta}$ and measured longitudinal accelerations (obtained from the wheel speed a and from IMU measurements a_{s_x}).

5.2.3 Variable sloped environment

Following, the road slope estimations obtained in a sloped environment with the algebraic method and the proposed KF are analyzed. Figure 5.7 contains the experimental results achieved when riding uphill and downhill the same sloped road of Figures 5.4 and 5.5. One can notice that, in the presence of a non-null road angle, a difference between a and a_{s_x} that corresponds to g_x is noticeable. To evaluate the estimated road slope accuracy, the obtained estimation results are related to the traveled distance x in Figure 5.8. As one can notice both methods follow approximately the calculated slope reference. The KF estimation results are smoother but slower than the one obtained with the algebraic method. The RMSE has been calculated in both cases resulting in 0.92 deg when using the algebraic method and 0.729 deg employing the KF. Thus, a reduction of the RMSE of circa 20% is obtained when estimating the road grade using the proposed KF in a sloped environment. The reduction of the RMSE improvement compared to level ground riding is explainable by the filtering effect of the KF that introduces a time delay on the estimation in the presence of variable road slopes. One can notice that at circa 50 m a considerable estimation error of circa 5 deg is present. This error is caused by the U-turn performed while turning back to ride downhill the same route. This considerable angle error would propagate onto the pedaling torque estimation affecting the control system performances. Thus, the cornering effect error must be mitigated to obtain

reliable control performances when riding in a curve.

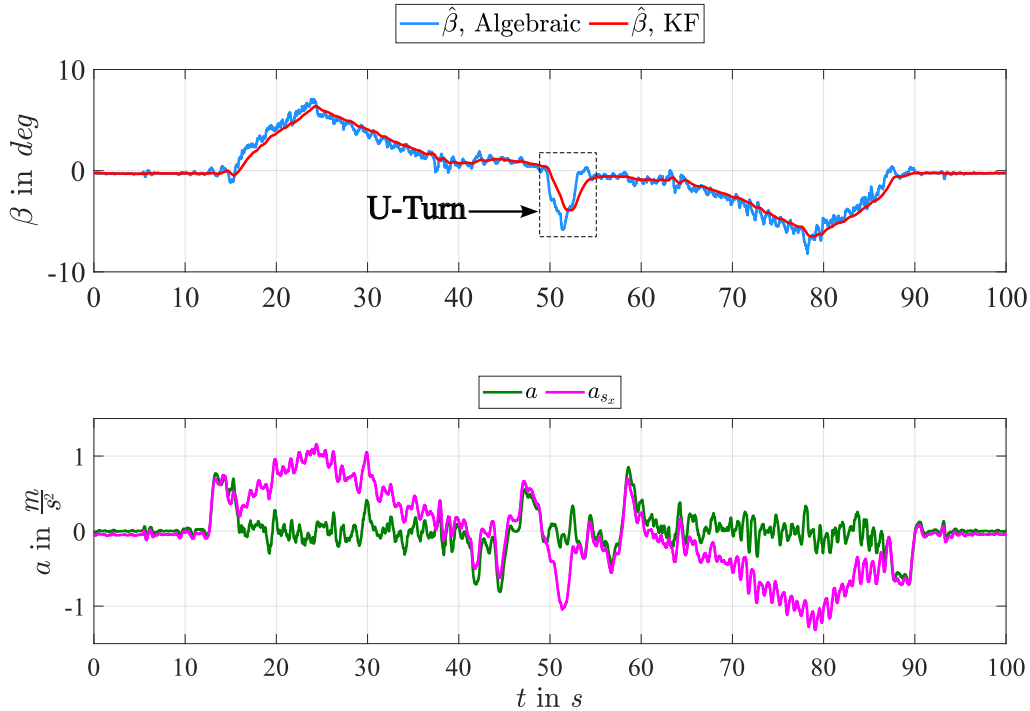


Figure 5.7: Road slope estimation $\hat{\beta}$ in a variable sloped environment ($\beta \neq 0 \text{ deg}$). From top to bottom: road slope estimation $\hat{\beta}$ and measured longitudinal accelerations (obtained from the wheel speed a and from IMU measurements a_{s_x}).

5.2.4 Riding in a curve

In this section, the negative effect of riding in a curve on the slope estimation and the method used to reduce it are analyzed. Table 5.3 contains the tuning parameters employed to compensate for the cornering effect using the proposed approach. These parameters have been experimentally chosen minimizing the estimation error when considering curves of different aggressiveness. Figure 5.9 contains the estimation results when riding in a curve on an almost flat ground. In this scenario, the measured road angle calculated with the digital inclinometer presents a $CI_{95\%} = 0.18 \pm 0.09 \text{ deg}$ over the entire track. This measured reference is reported with dashed black lines in the figure. Moreover, in the experiment, the curve occurs during approximately the interval $t \in [6.5; 11] \text{ s}$. One can notice that thanks to the employed correction method the error introduced by the cornering effect can be reduced. In particular, the RMSEs have been calculated during the cornering interval resulting in 0.924 deg for the algebraic method, 0.565 deg for the KF, and 0.321 deg for the KF with the cornering compensation method. Thus, an RMSE improvement of circa 43% is obtained when employing the proposed curve correction approach compared to the non-compensated estimation. However, it has to be remarked that the obtained results are strictly dependent on the ag-

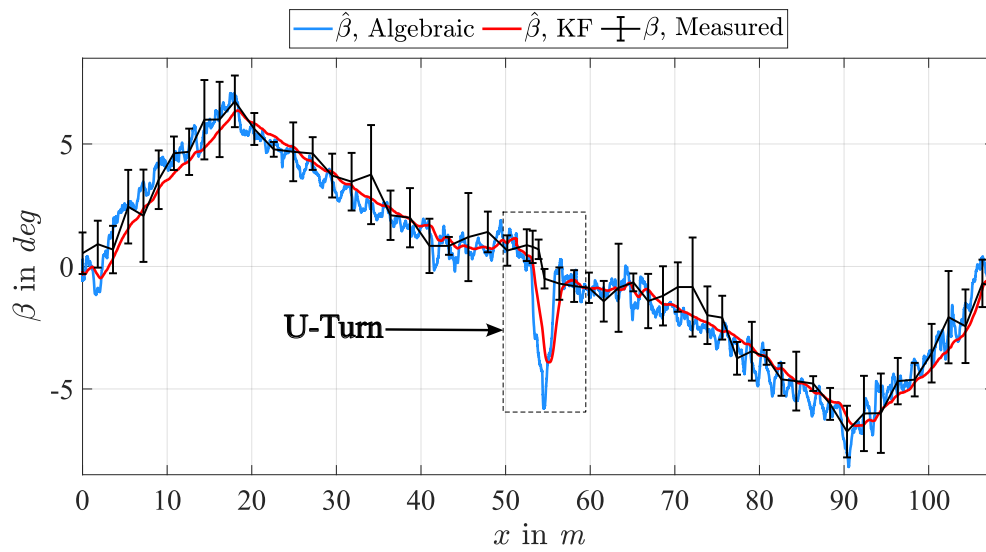


Figure 5.8: Road slope estimation $\hat{\beta}$ error analysis (related to the traveled distance x) in a variable sloped environment ($\beta \neq 0 \text{ deg}$).

gressiveness of the considered curve. Indeed, a worse RMSE improvement is expected when riding in hairpin- or U-turns.

Tuning parameter	Value
Λ_{th}	$0.1 \frac{rad}{s}$
c	75
$f_{c_\beta}^{min}$	0.005 Hz
$f_{c_\beta}^{max}$	3 Hz

Table 5.3: Parameters employed in the proposed curve effect compensation method.

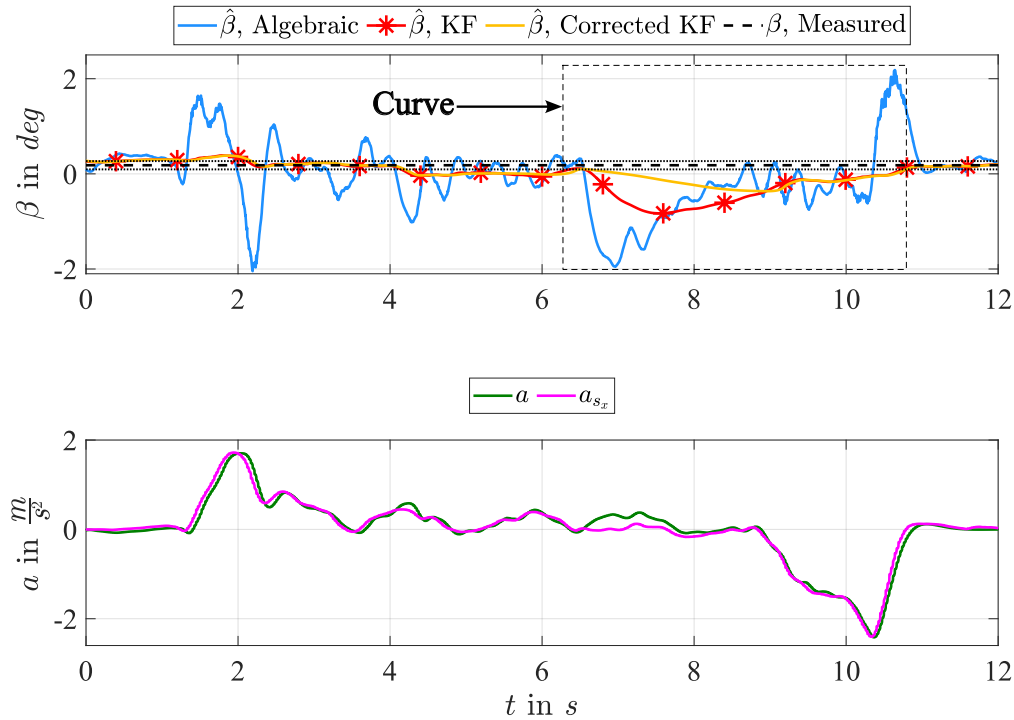


Figure 5.9: Road slope estimation $\hat{\beta}$ cornering effect compensation. From top to bottom: road slope estimation $\hat{\beta}$ and measured longitudinal accelerations (obtained from the wheel speed a and from IMU measurements a_{s_x}).

5.3 Torque-sensorless control

In this section, the proposed pedaling torque estimation algorithms are analyzed and experimentally validated in a realistic riding environment. The PTOs are implemented on a microcontroller with a sampling frequency of $f_s = 500 \text{ Hz}$. Even in this case, a low pass filter corner frequency of $f_{c_v} = 1 \text{ Hz}$ has been utilized to filter the measured bicycle speed. Before performing each experiment, the cyclist mass has been measured with a digital scale and its value updated in the microcontroller firmware. Moreover, the pedaling torque estimation has been performed defining in the PTO models the rolling friction coefficient to its worst case value $\mu = 0.01$ to account for bump losses, and the drag area to the typical upright cycling value $A_d = 0.63 \text{ m}^2$.

Initially, the tuning of the PTOs is analyzed in an indoor scenario without motor assistance assuming the road to be perfectly level $\beta = 0 \text{ deg}$, namely without performing an online angle estimation. Under these conditions, the PTOs tuning that optimizes the torque estimation performances has been selected and employed in the subsequent experiments.

Afterwards, tests are performed on a predefined track, that covers a distance of about 200 m, characterized by sections with a variable slope, curves, and straight-level ground. Figure 5.10 illustrates the track employed for the performance analysis, while Figure 5.11

reports the estimated road slope obtained with the proposed KF over the considered track. As one can notice, the estimated slope in the level ground segment is not perfectly flat but contained in the range $\beta \in [-0.5; 0.5]$ *deg*. The track is characterized by rapid grade changes during the curves, which, in the grade estimation, sum up with cornering effect errors. Moreover, all experiments have been performed riding the bicycle at an average cruise speed of circa $v \in [10; 15]$ $\frac{km}{h}$. Additionally, all the test rides have been performed in low wind speed weather conditions $v_w \in [0; 10]$ $\frac{km}{h}$.

Under these hypotheses, the torque estimation capabilities of the proposed PTOs are evaluated in two noteworthy riding conditions, namely during the starting phase and when riding uphill. These experiments allow the analysis of the online slope estimation and motor assistance effects on the quality of the estimated pedaling torque.

After that, the riding performances are analyzed by evaluating the pedaling power in the same remarkable conditions. Here, the performances are compared with the ones obtained by employing a commercial torque sensor to generate the assistance and without motor aid. In particular, the maximum and average pedaling power reduction are evaluated in the aforementioned conditions. Also, for each assistance approach, the cycling energy is computed and compared to the total delivered energy (motor plus pedaling) to indicate the global effort reduction in the performed riding task.

Eventually, to take into account the preference and riding feeling variability between different users, a qualitative analysis of the implemented assistance approaches is executed. In particular, several people were surveyed by asking question about the perceived assistance characteristics and letting them compare the proposed assistance methods.

5.3.1 Pedaling torque observers tuning

As discussed in Section 4.4.1, tuning a KF in the presence of modeling simplifications means selecting the covariance matrices to weigh the confidence between the model and the measurement equations employed by the filter. In particular, it has been shown in simulation that the measurements and the bicycle longitudinal model can be trusted more than the pedaling torque model selecting the values of the covariance matrices. In the following, the pedaling torque estimation is evaluated for different tuning of the proposed algorithms when riding on a flat ground. It has to be remarked that in these experiments, to exclude from the analysis errors introduced by the slope estimation, the latter is not performed assuming the terrain to be perfectly flat $\beta = 0$ *deg*. Similarly, to exclude errors caused by the motor torque control, the analysis is performed without electrical assistance. Furthermore, the following tests are performed indoors to exclude the effect of wind on the pedaling torque estimation. Under these conditions, the Normalized Root Mean Square Error (NRMSE) of the pedaling torque has been calculated to evaluate the quality of the estimation. In particular, to allow a comparison of the obtained results in different riding conditions, the RMSE has been normalized considering the average value of the measured pedaling torque \bar{T}_p :

$$\text{NRMSE} = \frac{\text{RMSE}}{\bar{T}_p} \cdot 100. \quad (5.3)$$

Besides, the respective $\text{CI}_{95\%}$ have been evaluated over three experiments performed under similar conditions. In the executed trials the following covariance matrices have been

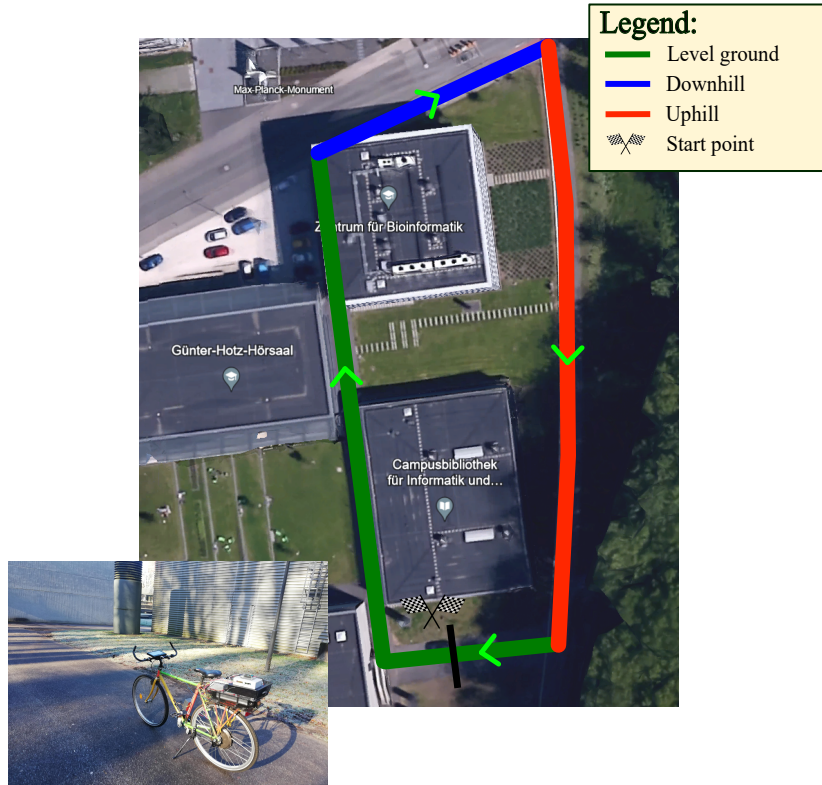


Figure 5.10: Selected track for the torque-sensorless control performance analysis. (Google ©)

selected to assess the CPTO pedaling torque estimation performances:

$$\mathbf{Q} = \begin{bmatrix} 10^{-2} & 0 \\ 0 & \sigma_{w_{T_{pc}}}^2 \end{bmatrix}, \quad R = 10^{-3}. \quad (5.4)$$

Similarly, the same analysis is performed by tuning the SPTO with the following covariance matrices:

$$\mathbf{Q} = \begin{bmatrix} 10^{-2} & 0 & 0 & 0 \\ 0 & \sigma_{w_{\xi}}^2 & 0 & 0 \\ 0 & 0 & \sigma_{w_{\xi}}^2 & 0 \\ 0 & 0 & 0 & \sigma_{w_{\xi}}^2 \end{bmatrix}, \quad R = 10^{-3}. \quad (5.5)$$

For both PTOs values of $\sigma_{w_{T_{pc}}}^2 = \sigma_{w_{\xi}}^2 \in \{10, 100, 500, 1000\} \text{ N}^2 \text{ m}^2$ have been utilized. It has to be remarked that the variances have been evaluated for values $\sigma_{w_{T_{pc}}}^2 = \sigma_{w_{\xi}}^2 \leq 10^3 \text{ N}^2 \text{ m}^2$ since simulations have shown that for higher values, despite the fact the estimation becomes more reactive to torque variations, undesired oscillations appear on the estimated pedaling torque due to errors caused by noise and differentiation of the measured rotor position that affect the highly trusted speed measurement. Besides, values of $\sigma_{w_{T_{pc}}}^2 = \sigma_{w_{\xi}}^2 \leq 10 \text{ N}^2 \text{ m}^2$, has also been excluded from the analysis because they do not allow to obtain a sufficiently reactive

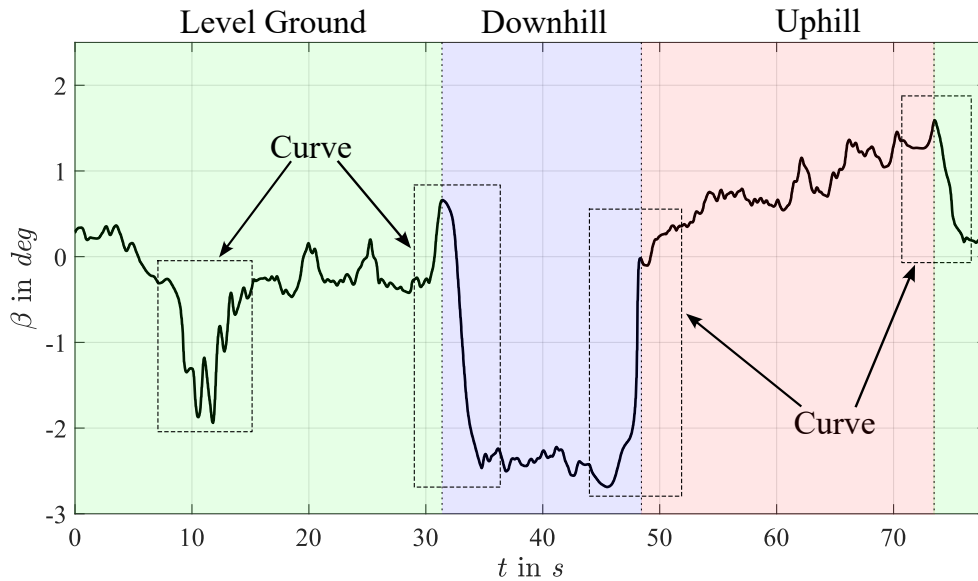


Figure 5.11: Estimated road slope $\hat{\beta}$ with the proposed KF over the testing track.

torque estimation. As an example, the extreme cases $\sigma_{w_{Tpc}}^2 = \sigma_{w_{\xi}}^2 = 1 \text{ N}^2 \text{ m}^2$ and $\sigma_{w_{Tpc}}^2 = \sigma_{w_{\xi}}^2 = 10^4 \text{ N}^2 \text{ m}^2$ are illustrated in Figure 5.12. The experiments confirm the considerations above when variance values beyond the testing range are utilized. Also, it can be noticed that for high values of variance, the speed measurement errors affect more the SPTO than the CPTO causing bigger oscillations on the estimated pedaling torque.

Figure 5.13 and Figure 5.14 contain an example of the results obtained employing the different analyzed tunings of the CPTO and the SPTO, respectively. As one can see when employing a simple constant pedaling torque model high values of the variance $\sigma_{w_{Tpc}}^2$ need to be selected to compensate for the modeling simplification. Moreover, the state estimation results are too slow compared to the pedaling torque dynamics at narrow variance values. For increasing values of $\sigma_{w_{Tpc}}^2$, the estimation gets more reactive to torque variations, especially in the starting acceleration phase. Nevertheless, even for high values of $\sigma_{w_{Tpc}}^2$, the estimation results are delayed and damped compared to the pedaling torque peaks. As shown in Figure 5.14, employing a pedaling torque sinusoidal model allows to improve the estimation even for small values of $\sigma_{w_{\xi}}^2$. Moreover, increasing variance values permit the estimation improvement and the pedaling torque estimation delay reduction. Table 5.4 contains the NRMSE of the pedaling torque for the considered tunings of the PTOs. As one can notice, for both models the NRMSE decreases for increasing values of the the pedaling torque model variance. However, for values $\sigma_{w_{\xi}}^2 > 500 \text{ N}^2 \text{ m}^2$, the estimation of the SPTO starts deteriorating because of the oscillations caused by the highly trusted speed measurement errors. Moreover, it can be seen that the SPTO reduces the NRMSE by about 10 – 20 % compared to the CPTO at the same level of variance. Based on this analysis, it is clear that the employment of a sinusoidal model improves the pedaling torque estimation. To minimize the NRMSE, the effect of the speed measurement noise, and obtain a sufficiently reactive torque estimation, $\sigma_{w_{Tpc}}^2 = \sigma_{w_{\xi}}^2 = 500 \text{ N}^2 \text{ m}^2$ has been selected as optimal variance value and

5.3 Torque-sensorless control

highlighted in Table 5.4. This variance value will be utilized to tune the PTOs in the later experiments of this work.

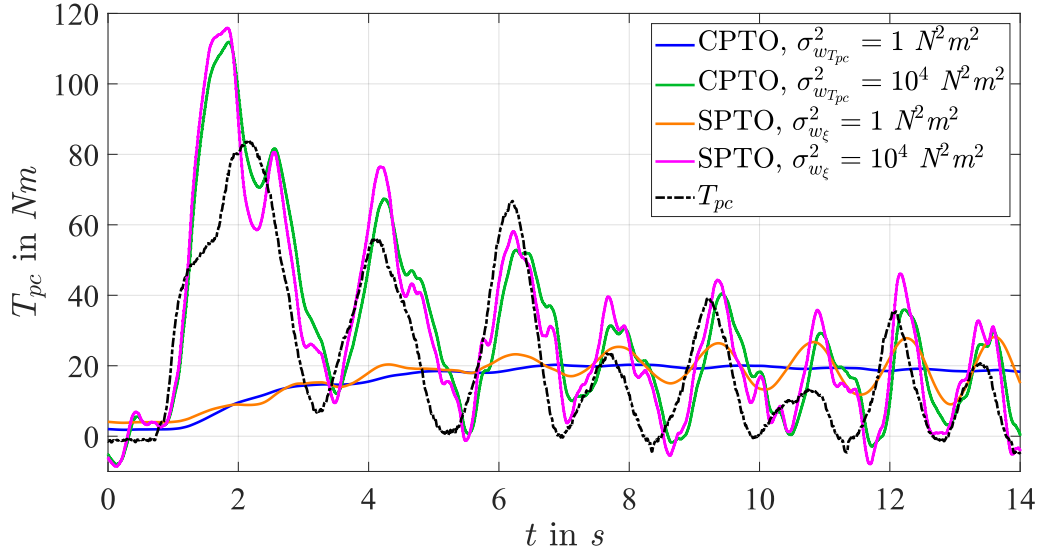


Figure 5.12: Pedaling torque estimation \hat{T}_{pc} obtained with PTO covariance values beyond the considered tuning range ($\sigma_w^2 \notin [10; 1000] \text{ N}^2 \text{ m}^2$) when riding indoor (no road slope $\beta = 0 \text{ deg}$ and no wind $v_{w_x} = 0 \frac{\text{km}}{\text{h}}$) without motor assistance ($T_m = 0 \text{ Nm}$).

NRMSE in %				
PTO	$\sigma_{w_{T_{pc}}}^2 = \sigma_{w_{\xi}}^2$ in $\text{N}^2 \text{ m}^2$			
	10	100	500	1000
CPTO	86.32 ± 5.8	73.56 ± 3.08	68.91 ± 0.7	68.13 ± 3.25
SPTO	74.7 ± 5.6	51.09 ± 5.49	49.87 ± 4.5	52.11 ± 3.7

Table 5.4: Confidence interval at 95% of the estimated pedaling torque \hat{T}_{pc} NRMSE evaluated for different PTO tuning values when riding indoor (no road slope $\beta = 0 \text{ deg}$ and no wind $v_{w_x} = 0 \frac{\text{km}}{\text{h}}$) without motor assistance ($T_m = 0 \text{ Nm}$).

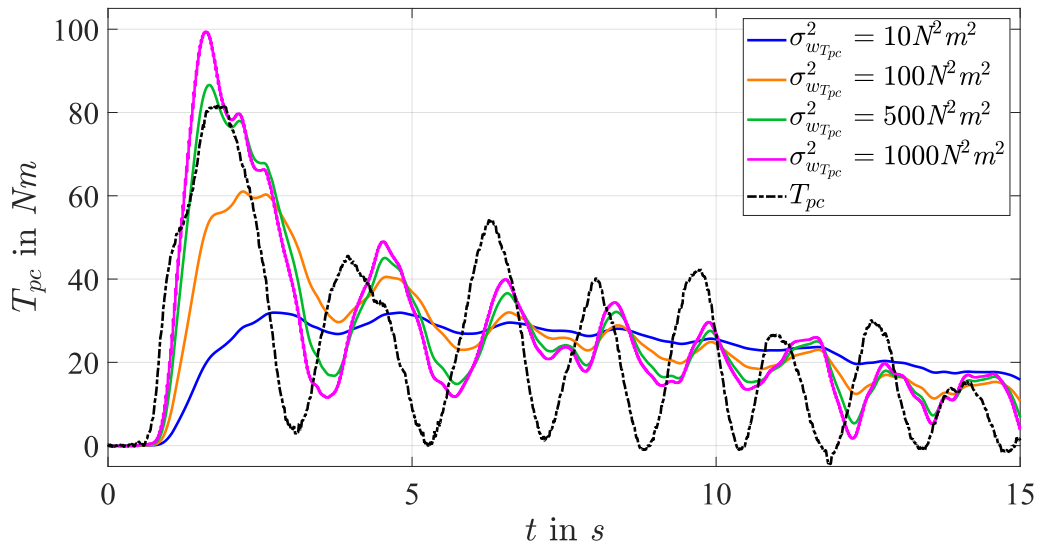


Figure 5.13: Pedaling torque estimation \hat{T}_{pc} for different tuning of the CPTO ($\sigma_{w_{T_{pc}}}^2 \in \{10; 100; 500; 1000\} N^2 m^2$) when riding indoor (no road slope $\beta = 0$ deg and no wind $v_{w_x} = 0 \frac{km}{h}$) without motor assistance ($T_m = 0 Nm$).

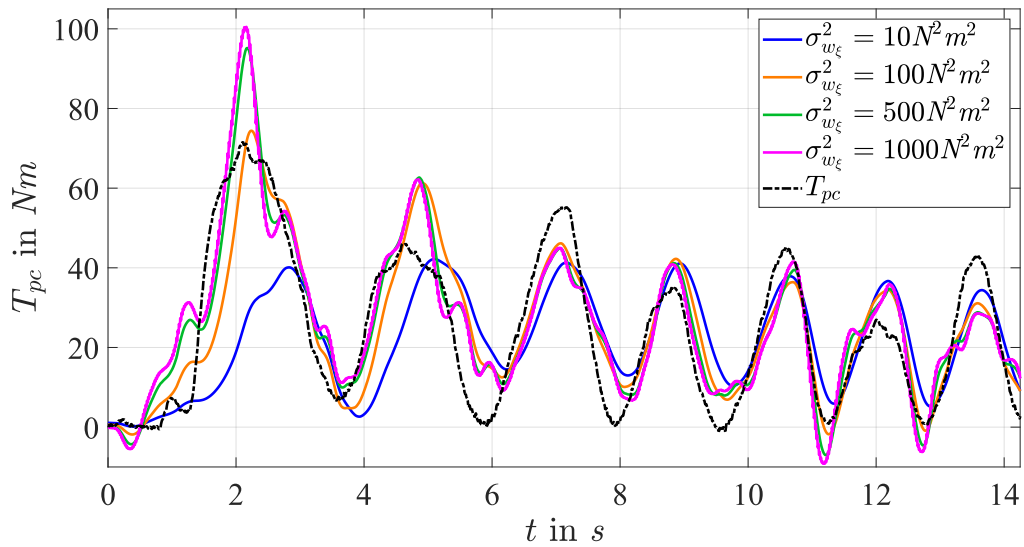


Figure 5.14: Pedaling torque estimation \hat{T}_{pc} for different tuning of the SPTO ($\sigma_{w_{\xi}}^2 \in \{10; 100; 500; 1000\} N^2 m^2$) when riding indoor (no road slope $\beta = 0$ deg and no wind $v_{w_x} = 0 \frac{km}{h}$) without motor assistance ($T_m = 0 Nm$).

5.3.2 Pedaling torque estimation analysis

In this section, the two proposed PTOs, tuned as previously explained, are tested on the road in the defined track. In particular, two noteworthy sections of the track, where higher assistance is required, are analyzed:

- riding behavior during the starting phase (first 10 s);
- riding behavior during the uphill portion of the track.

It has to be remarked that due to the presence of wind, variable riding conditions, and followed path, also in this case the $CI_{95\%}$ of the NRMSE is evaluated over three performed tests. Differently from the previous analysis, all the following experiments are performed with an online estimation of the road slope.

Firstly, the experiments are executed in the absence of motor assistance. Afterwards, the torque estimation capabilities are analyzed when a motor aid based on the estimated pedaling torque and a simple fixed-gain control strategy is provided:

$$T_m^* = K_a \hat{T}_{pw}, \quad (5.6)$$

where $K_a = 1$ represents the selected fixed gain used in the performed experiments. Thus, a motor torque equal to the estimated pedaling torque is set as reference for the FOC according to the considerations of Section 3.1.3 ($i_q^* = \frac{T_m^*}{K_T}$ A, $i_d^* = 0$ A). It has to be remarked that, due to the prototype battery limitations and for safety reasons during testing, a maximum current reference of $i_q^* = 20$ A can be sent to the motor limiting the maximum deliverable motor torque to circa $T_m \simeq 20$ Nm. Moreover, in the presence of estimated braking torques, the electrical assistance is cut off.

Pedaling torque estimation analysis without motor assistance:

Figure 5.15 and 5.16 contain an example of the pedaling torque estimation obtained without electrical assistance during the starting and uphill sections of the track, respectively. The estimation performances without motor assistance expressed in terms of NRMSE are reported in Table 5.5. Analyzing this index, one can notice that the introduction of the road angle online estimation barely affects the CPTO estimate in both starting and uphill riding phases compared to the indoor results. On the other hand, the SPTO estimation visibly degrades only in the case of uphill riding (circa 5%). Thus, the SPTO results are more susceptible to the road angle estimation error caused by the delay introduced by the slope estimator in a variable grade environment. Nonetheless, the NRMSE of the SPTO torque estimation is circa 10% smaller than the one of the CPTO.

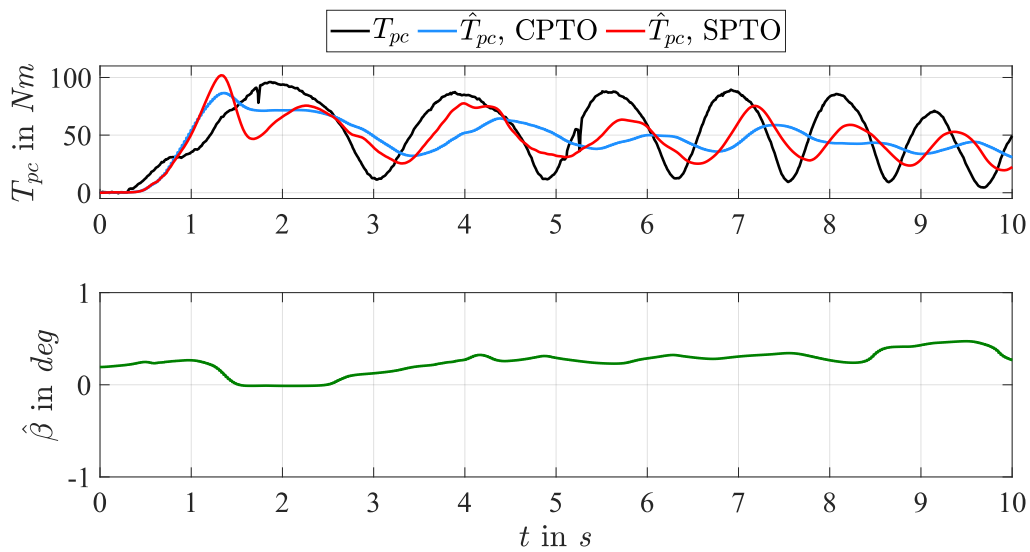


Figure 5.15: Comparison of the PTOs **pedaling torque estimation** obtained during the **starting phase** of the track with **no motor assistance** ($T_m = 0 Nm$). From top to bottom: pedaling torque estimation \hat{T}_{pc} and estimated road slope $\hat{\beta}$.

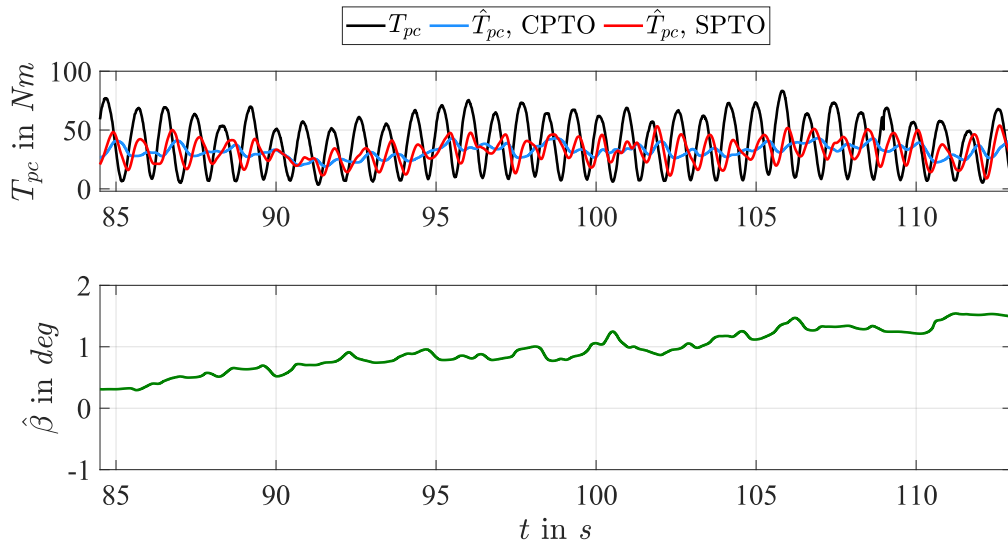


Figure 5.16: Comparison of the PTOs **pedaling torque estimation** obtained during the **up-hill section** of the track with **no motor assistance** ($T_m = 0 Nm$). From top to bottom: pedaling torque estimation \hat{T}_{pc} and estimated road slope $\hat{\beta}$.

NRMSE in %		
PTO	Starting	Uphill
CPTO	68.86 ± 7.35	65.96 ± 4.67
SPTO	50.3 ± 5.01	54.98 ± 3.5

Table 5.5: Confidence interval at 95% of the estimated **pedaling torque** \hat{T}_{pc} **NRMSE** evaluated during the starting and uphill sections of the track **without electrical assistance** ($T_m = 0 Nm$).

Pedaling torque estimation analysis with motor assistance:

Following, the effect of the electrical assistance on the torque estimation performance is analyzed. In particular, to account for the repercussions of the control system inaccuracies and current limitations on the pedaling estimation, the NRMSE of the delivered motor torque $T_m = \hat{T}_{pw}$ compared to the measured pedaling torque reported at the back wheel T_{pw} is evaluated. Figure 5.17 and 5.18 contain an example of the results obtained when providing electrical assistance based on the CPTO estimation in the starting and uphill sections, respectively. Figure 5.19 and 5.20 illustrate whereas the same two riding conditions when the electrical assistance is based on the SPTO torque estimation. In these figures, it can be noticed that the current measurement noise propagates onto the applied motor torque. Table 5.6 contains the motor torque NRMSE evaluated in the starting and uphill sectors of the track. Considering the CPTO, the NRMSE degrades circa 5 – 10% in both sections due to the effects of the motor assistance compared to the previous results. In the case of the SPTO, the NRMSE deterioration is even higher amounting to about 10 – 15% in the two analyzed sectors of the track. Despite its higher susceptibility to errors introduced by the motor assistance, the SPTO provides more accurate estimates with an NRMSE 5 – 10% lower than the CPTO one. Moreover, conversely to the CPTO, the torque estimated with the SPTO keeps a pseudo-sinusoidal shape with a similar frequency to the measured signal.

NRMSE in %		
PTO	Starting	Uphill
CPTO	72.55 ± 4.68	74.37 ± 0.49
SPTO	62.78 ± 7.58	66.87 ± 3.38

Table 5.6: Confidence interval at 95% of the **motor torque** $T_m = \hat{T}_{pw}$ **NRMSE** evaluated during the starting phase and uphill riding.

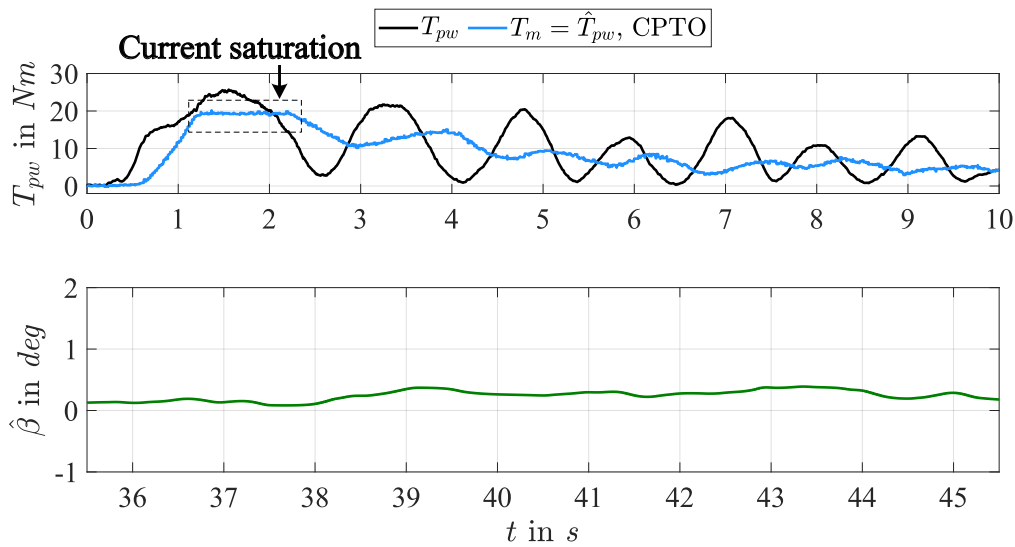


Figure 5.17: **Electrical assistance** $T_m = \hat{T}_{pw}$ based on the **CPTO pedaling torque estimation** during the **starting phase**. From top to bottom: pedaling torque estimation $T_m = \hat{T}_{pw}$ and estimated road slope $\hat{\beta}$ employing the proposed KF.

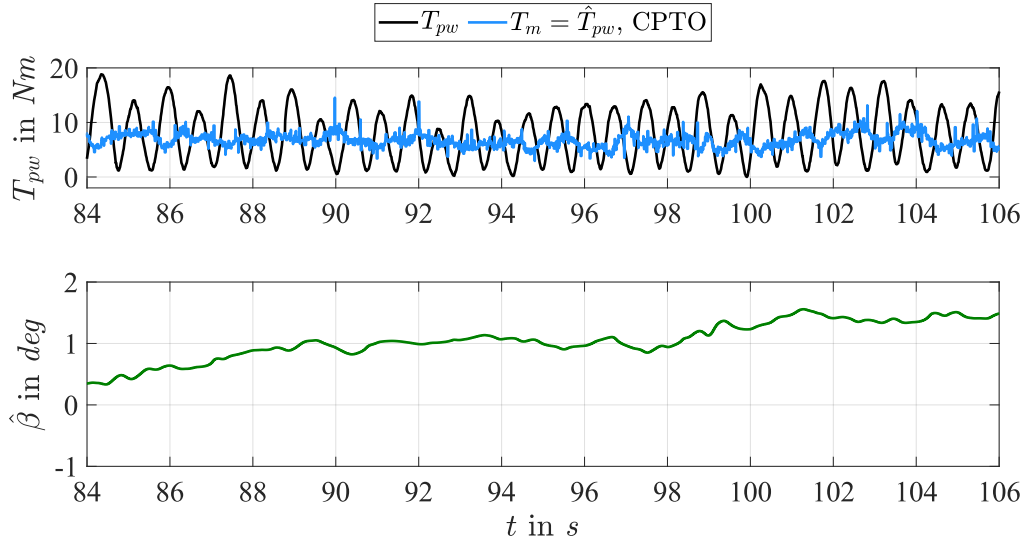


Figure 5.18: **Electrical assistance** $T_m = \hat{T}_{pw}$ based on the **CPTO pedaling torque estimation** during the **uphill section** of the track. From top to bottom: pedaling torque estimation $T_m = \hat{T}_{pw}$ and estimated road slope $\hat{\beta}$.

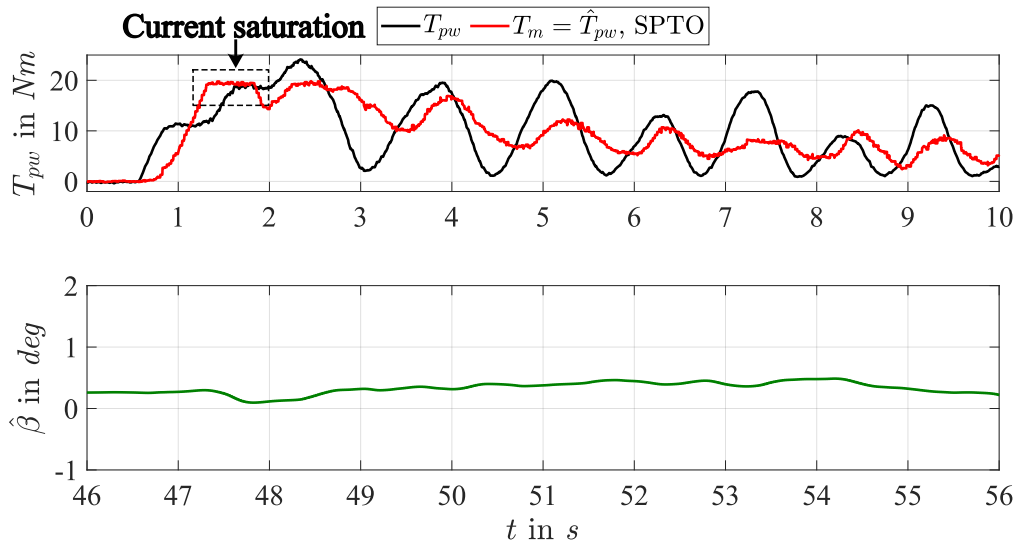


Figure 5.19: **Electrical assistance** $T_m = \hat{T}_{pw}$ based on the **SPTO pedaling torque estimation** during the **starting phase**. From top to bottom: pedaling torque estimation $T_m = \hat{T}_{pw}$ and estimated road slope $\hat{\beta}$.

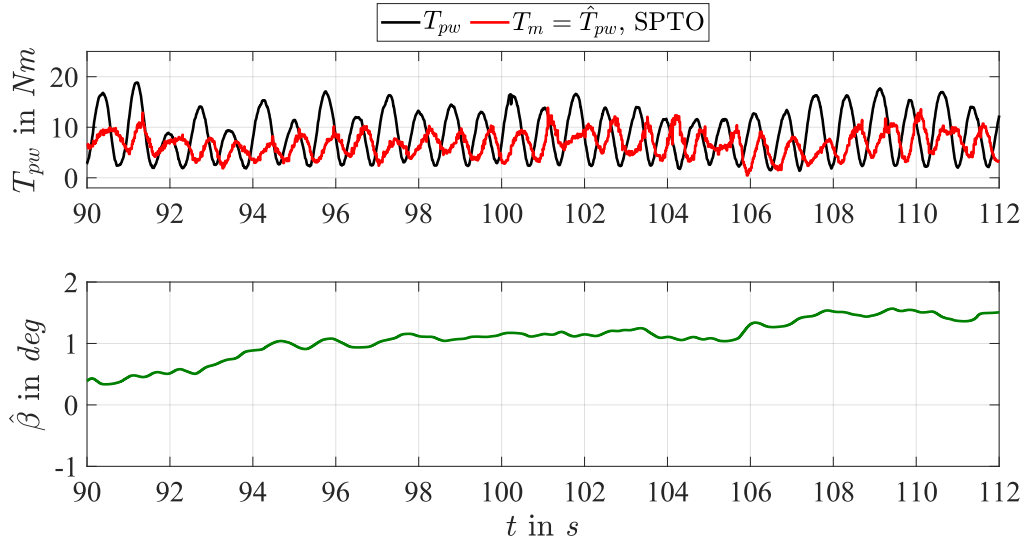


Figure 5.20: **Electrical assistance** $T_m = \hat{T}_{pw}$ based on the **SPTO pedaling torque estimation** during the **uphill section** of the track. From top to bottom: pedaling torque estimation $T_m = \hat{T}_{pw}$ and estimated road slope $\hat{\beta}$.

5.3.3 Riding performance analysis

In this section, the torque-sensorless riding performances are analyzed and compared to the ones obtained when employing a pedaling torque sensor to measure the pedaling torque and apply electrical assistance accordingly. Furthermore, the results obtained without electrical aid are also considered to evaluate the effort reduction of each electrical assistance type. To account for experiment variability, in each test, three laps of the defined track are ridden.

Firstly, the analysis focuses on the delivered pedaling power P_p for each kind of assistance considering the starting and uphill sections of the track. Here, the maximum $\max(P_p)$ and the average pedaling powers \bar{P}_p are analyzed. These two quantities indicate the peak level and the overall intensity of cycling effort on the considered section of the track, respectively. Also, to quantify the maximum and average pedaling power reduction of each electrical assistance method compared to the case without aid, two indexes have been defined, namely the Maximum Pedaling Power Reduction (MPPR) and the Average Pedaling Power Reduction (APPR):

$$\text{MPPR} = \left[1 - \frac{\max(P_{p \text{ assistance}})}{\max(P_{p \text{ no assistance}})} \right] \cdot 100, \quad (5.7)$$

$$\text{APPR} = \left(1 - \frac{\bar{P}_{p \text{ assistance}}}{\bar{P}_{p \text{ no assistance}}} \right) \cdot 100. \quad (5.8)$$

It has to be remarked that to account for experiment variability, the $\text{CI}_{95\%}$ of the average pedaling power and APPR over three experiments performed in similar conditions is calculated. Whereas, in the case of the maximum pedaling power and MPPR, since we are interested in evaluating the maximum cycling effort level under the defined conditions, the highest peak value obtained in the three considered experiments is reported.

Afterwards, an analysis of the global delivered energy E_Σ necessary to perform the task is executed. In particular, the pedaling E_p and motor E_m contributions are evaluated for each electrical assistance type. Their relation gives an indication of the global effort reduction obtained with each assistance method over the entire riding task. In particular, to quantify the pedaling effort reduction, the Pedaling Energy Reduction (PER) index has been defined as:

$$\text{PER} = \left(1 - \frac{E_p}{E_\Sigma} \right) \cdot 100. \quad (5.9)$$

This percentage indicates the pedaling energy reduction compared to the total delivered energy (motor plus cycling) required to perform the experiment when electrical assistance is applied. Also in this case, to account for experiments variability the $\text{CI}_{95\%}$ of the aforementioned quantities has been calculated considering three experiments performed in similar conditions.

Delivered pedaling power analysis:

Following, the experimental results obtained with the different assistance approaches are reported and analyzed. It has to be remarked that examples taken from the performed set

of experiments are illustrated. In each condition, the torques acting on the motorized wheel are reported, namely the transmitted pedaling torque T_{pw} , the motor torque T_m , and the total driving torque $T_\Sigma = T_{pw} + T_m$. Additionally, the corresponding bicycle speed v is shown. Furthermore, the driving power has been calculated. In particular, the delivered pedaling power P_p , the motor power P_m , and the total applied power $P_\Sigma = P_p + P_m$ are shown. Also, the corresponding estimated road slope $\hat{\beta}$ is reported.

Firstly, the riding performances obtained in the starting phase are presented. Figure 5.21 contains the starting behavior without electrical assistance, while Figure 5.22 the results obtained with a torque sensor-based electrical assistance. Besides, Figures 5.23 and 5.24 contain the results obtained when employing the estimated pedaling torque given by the CPTO and SPTO, respectively.

Then, the uphill sector results are presented. Figure 5.25 contains the results obtained when the bicycle is ridden without motor assistance, whereas, Figure 5.26 illustrates the results achieved when a sensor is employed to measure the pedaling torque and apply the electrical assistance. The results obtained when the motor assistance is based on the estimated pedaling torque given by the CPTO and SPTO are reported in Figures 5.27 and 5.28, respectively.

In Figures 5.22 and 5.26, it can be seen that when providing electrical assistance with a fixed gain strategy based on the pedaling torque sensor measurements, the motor aid is an almost perfect amplification of the measured signal, except when the desired torque exceeds the maximum applicable torque limited by the prototype current saturation. Thus, the total delivered power is circa equal to $P_\Sigma \simeq 2P_p$. In the case torque-sensorless assistance is provided, due to the torque estimation inaccuracy, the motor assistance adds a pseudo-sinusoidal offset onto the pedaling power. As seen in the previous sections, this offset, equal to the delivered motor power, results more constant in the case a CPTO is used to estimate the pedaling torque (Figures 5.23 and 5.27). Whereas, in the case of the SPTO, the power offset is more reactive to the pedaling signal variations (Figures 5.24 and 5.28). Nevertheless, the total delivered power obtained with the SPTO does not perfectly coincide with the one provided utilizing the sensor-based electrical assistance.

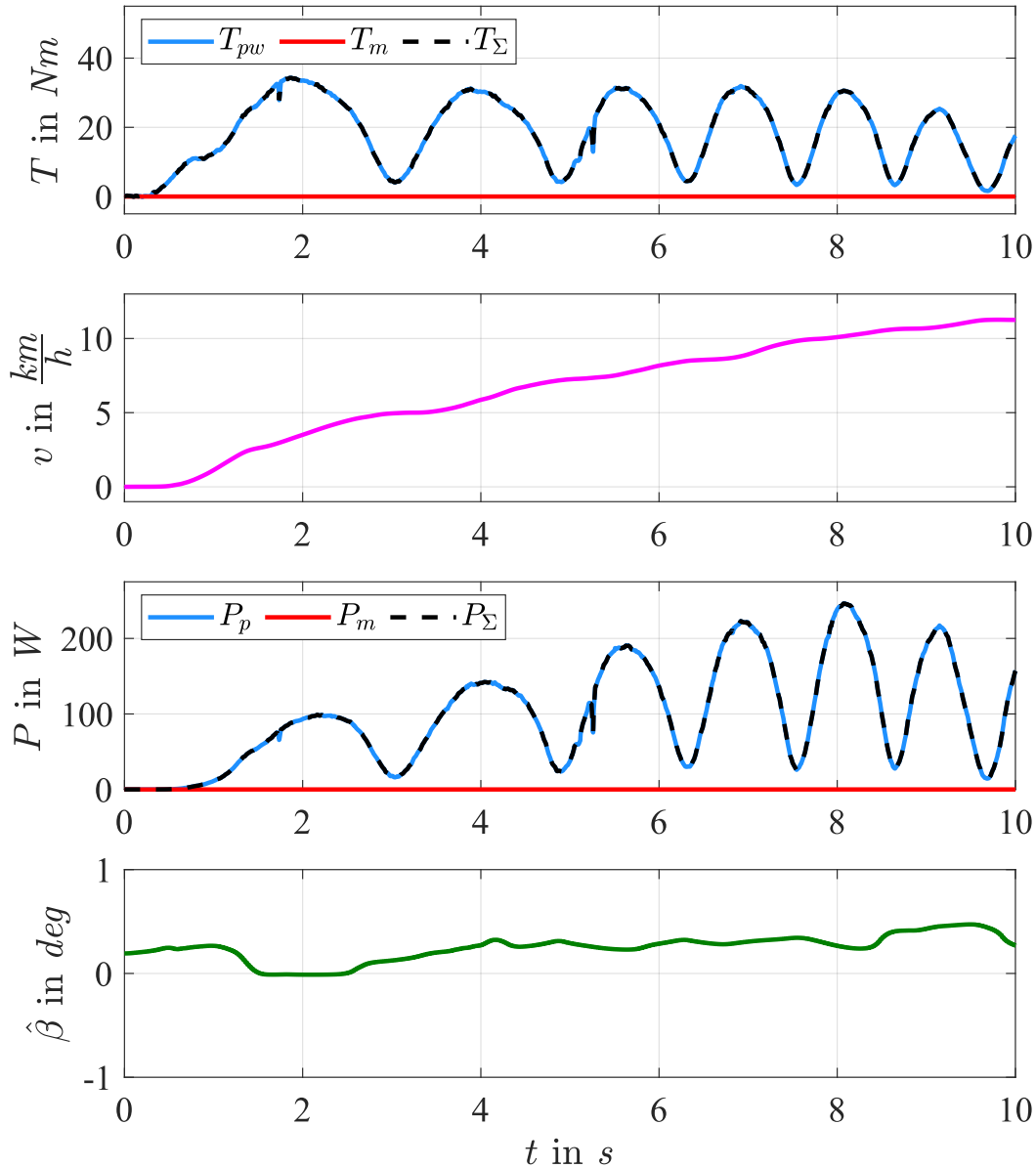


Figure 5.21: **Starting behavior without provided electrical assistance** ($T_m = 0 \text{ Nm}$). From top to bottom: pedaling torques (measured pedaling torque T_{pw} , motor torque T_m , and total delivered torque $T_\Sigma = T_{pw} + T_m$) at the back wheel, bicycle speed v , delivered power (pedaling power P_p , motor power P_m , and total power $P_\Sigma = P_p + P_m$), and estimated road slope $\hat{\beta}$.

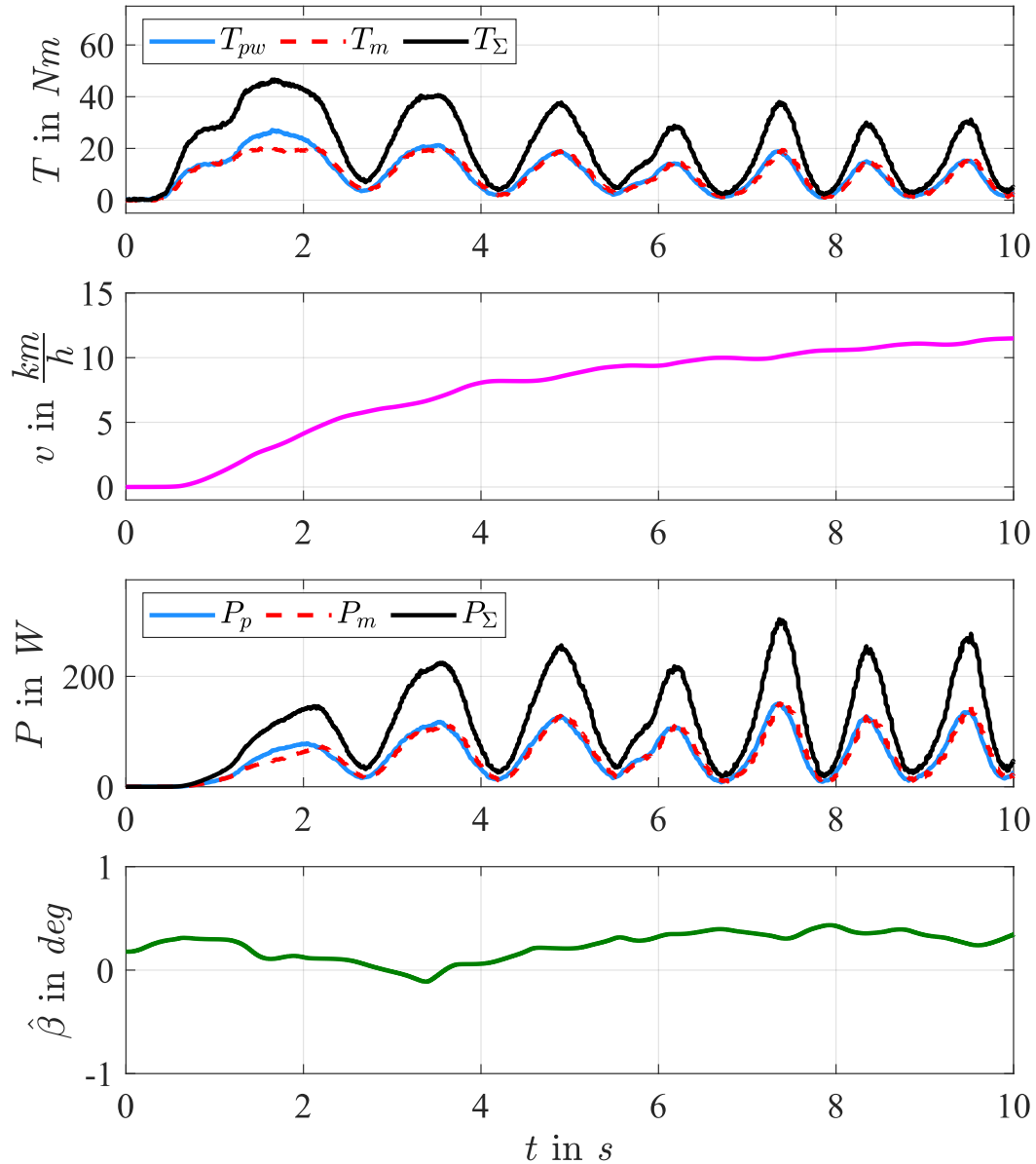


Figure 5.22: **Starting behavior** in the case of an **electrical assistance based on torque sensor** measurements ($T_m = T_{pw}$). From top to bottom: pedaling torques (measured pedaling torque T_{pw} , motor torque T_m , and total delivered torque $T_\Sigma = T_{pw} + T_m$) at the back wheel, bicycle speed v , delivered power (pedaling power P_p , motor power P_m , and total power $P_\Sigma = P_p + P_m$), and estimated road slope $\hat{\beta}$.

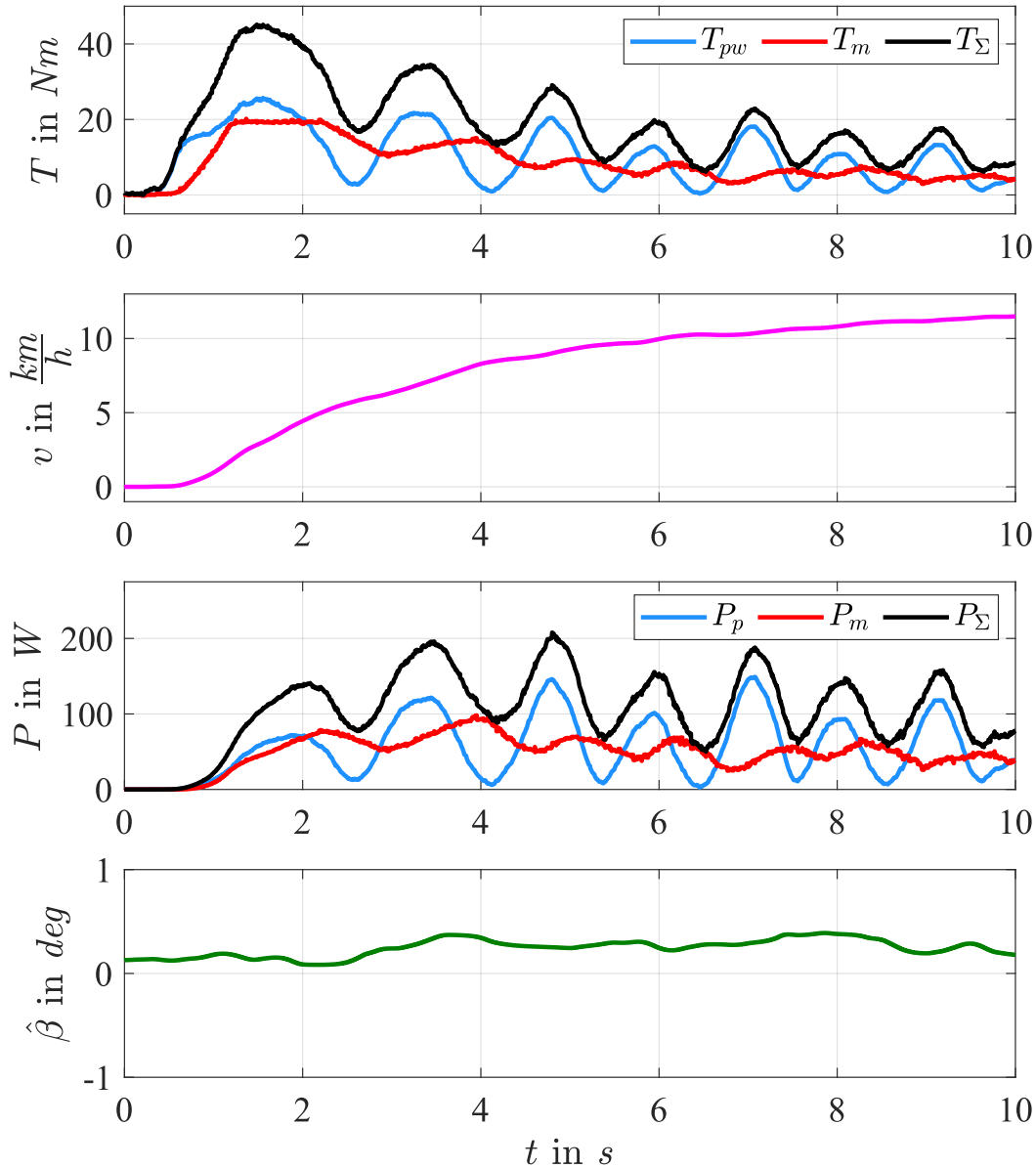


Figure 5.23: **Starting behavior** in the case of an **electrical assistance based on the CPTO** torque estimation ($T_m = \hat{T}_{pw}$). From top to bottom: pedaling torques (measured pedaling torque T_{pw} , motor torque T_m , and total delivered torque $T_\Sigma = T_{pw} + T_m$) at the back wheel, bicycle speed v , delivered power (pedaling power P_p , motor power P_m , and total power $P_\Sigma = P_p + P_m$), and estimated road slope $\hat{\beta}$.

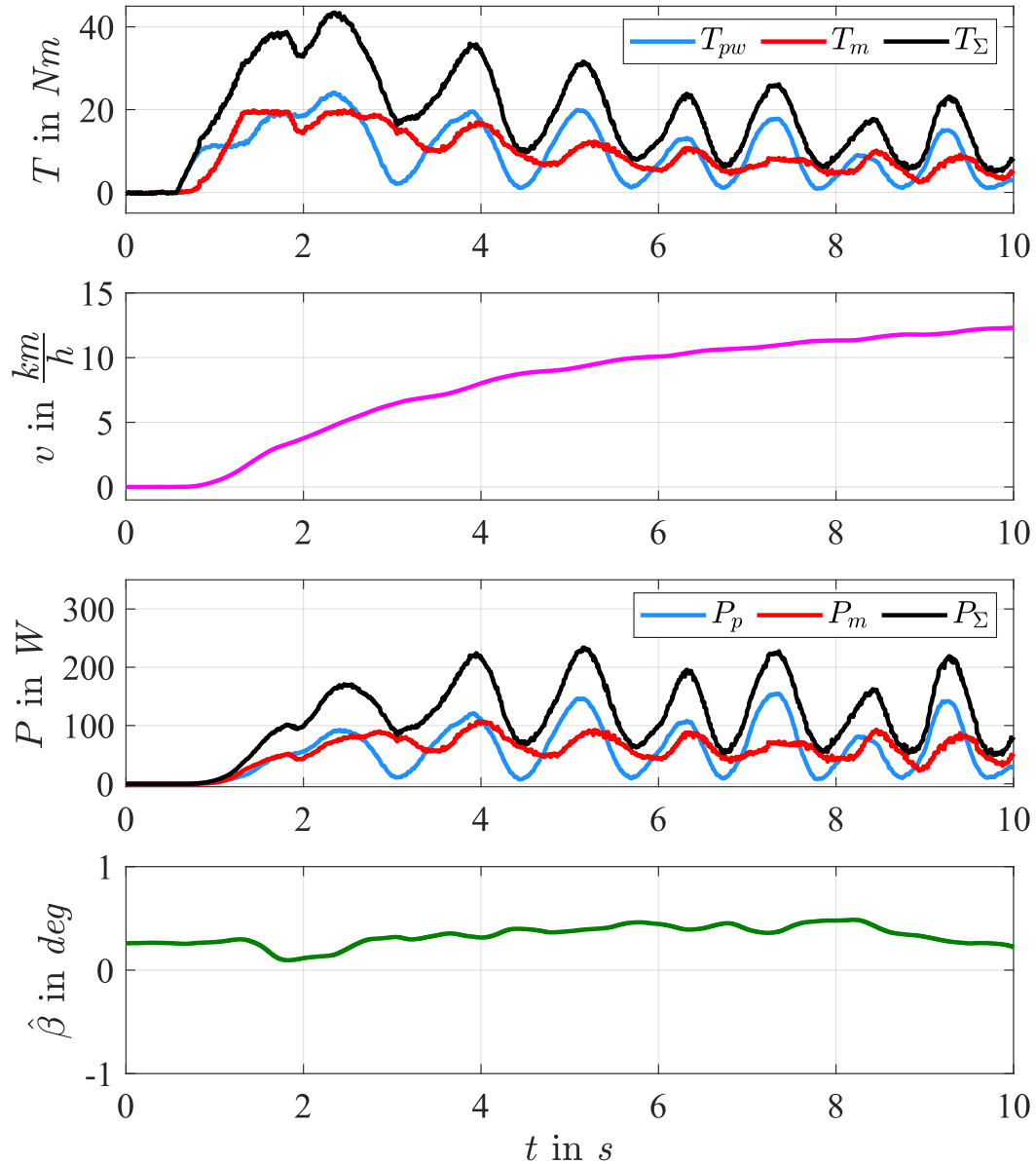


Figure 5.24: **Starting behavior** in the case of an **electrical assistance based on the SPTO** torque estimation ($T_m = \hat{T}_{pw}$). From top to bottom: pedaling torques (measured pedaling torque T_{pw} , motor torque T_m , and total delivered torque $T_\Sigma = T_{pw} + T_m$) at the back wheel, bicycle speed v , delivered power (pedaling power P_p , motor power P_m , and total power $P_\Sigma = P_p + P_m$), and estimated road slope $\hat{\beta}$.

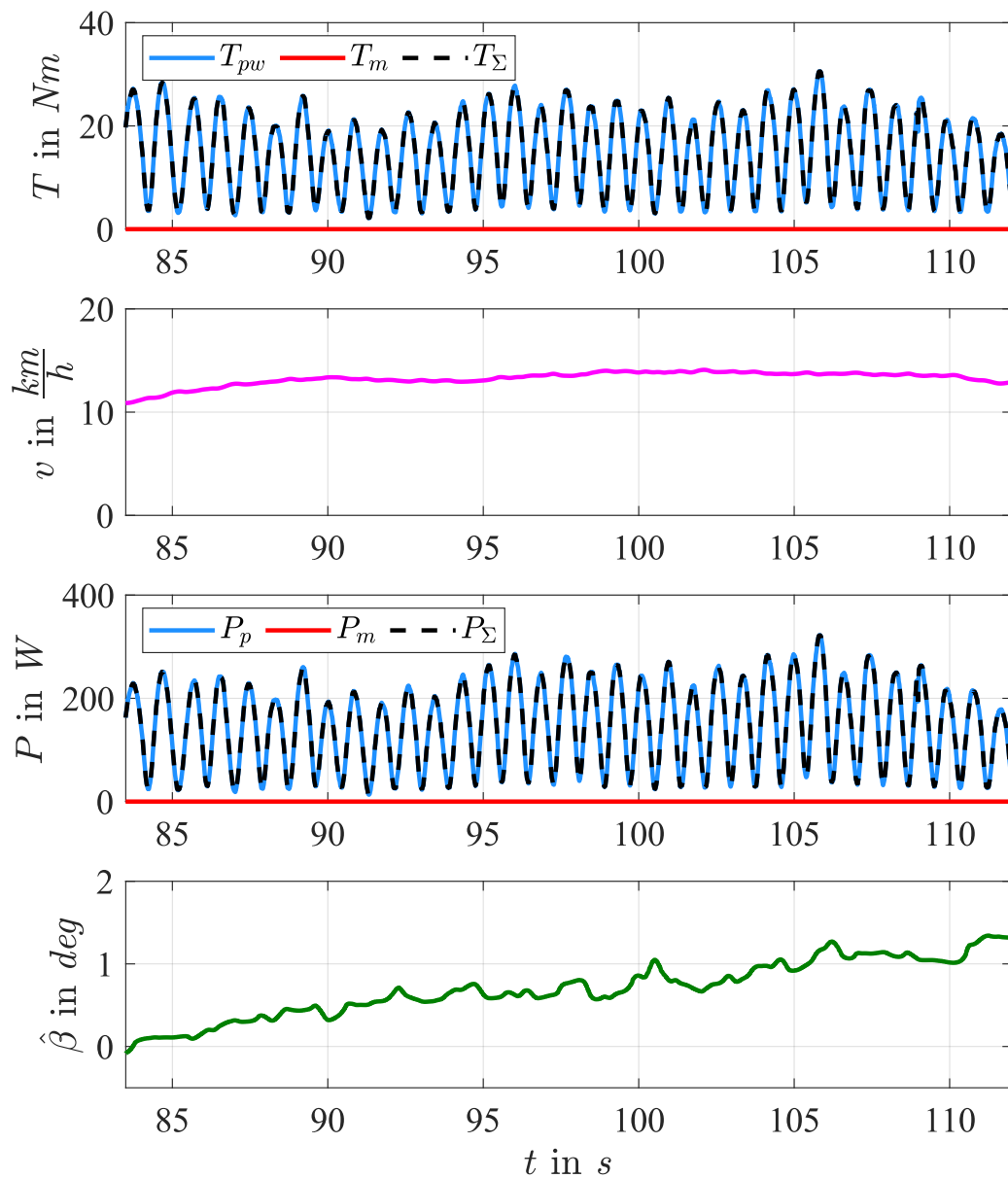


Figure 5.25: **Uphill riding without provided electrical assistance** ($T_m = 0 \text{ Nm}$). From top to bottom: pedaling torques (measured pedaling torque T_{pw} , motor torque T_m , and total delivered torque $T_\Sigma = T_{pw} + T_m$) at the back wheel, bicycle speed v , delivered power (pedaling power P_p , motor power P_m , and total power $P_\Sigma = P_p + P_m$), and estimated road slope $\hat{\beta}$.

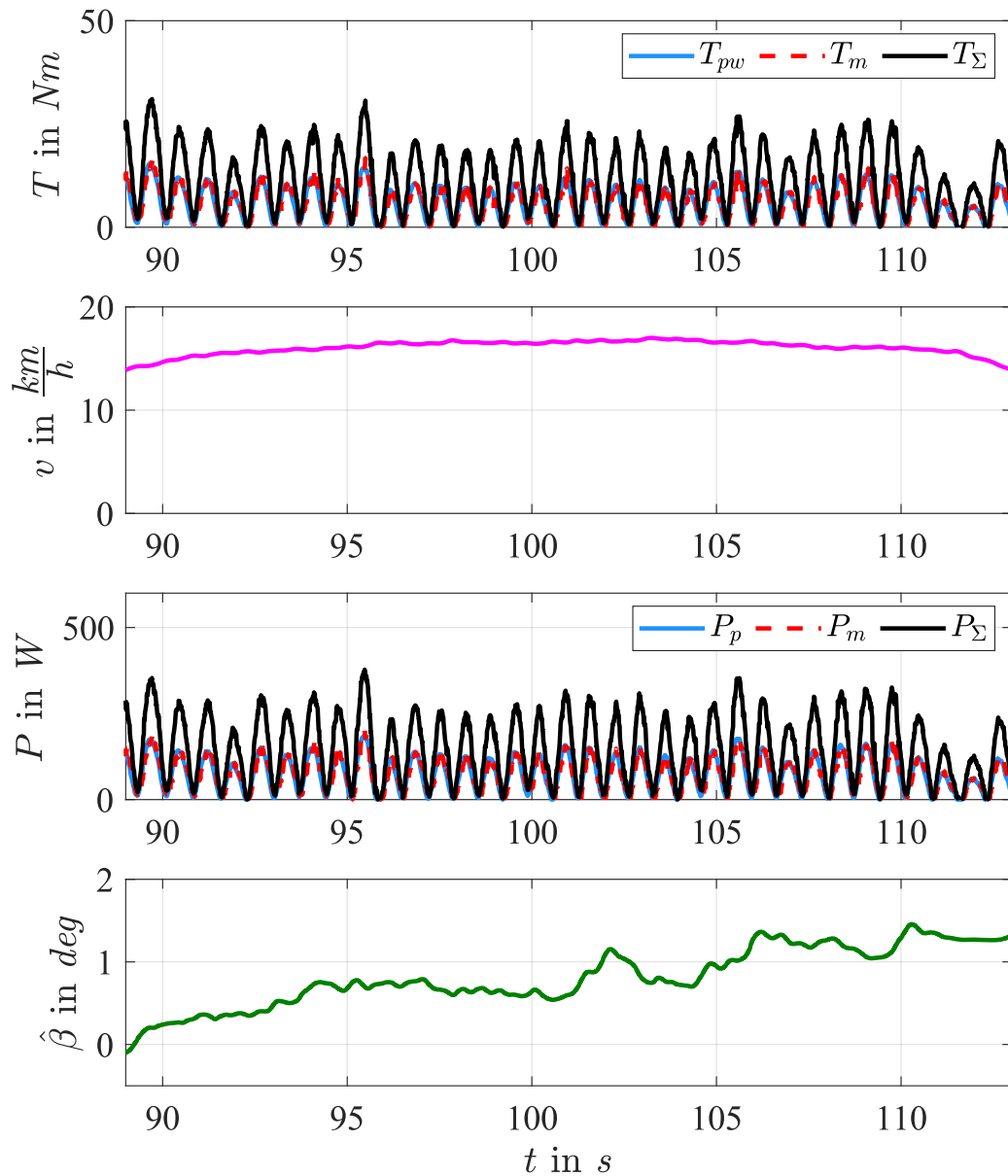


Figure 5.26: **Uphill riding** in the case of an **electrical assistance based on torque sensor** measurements ($T_m = T_{pw}$). From top to bottom: pedaling torques (measured pedaling torque T_{pw} , motor torque T_m , and total delivered torque $T_\Sigma = T_{pw} + T_m$) at the back wheel, bicycle speed v , delivered power (pedaling power P_p , motor power P_m , and total power $P_\Sigma = P_p + P_m$), and estimated road slope $\hat{\beta}$.

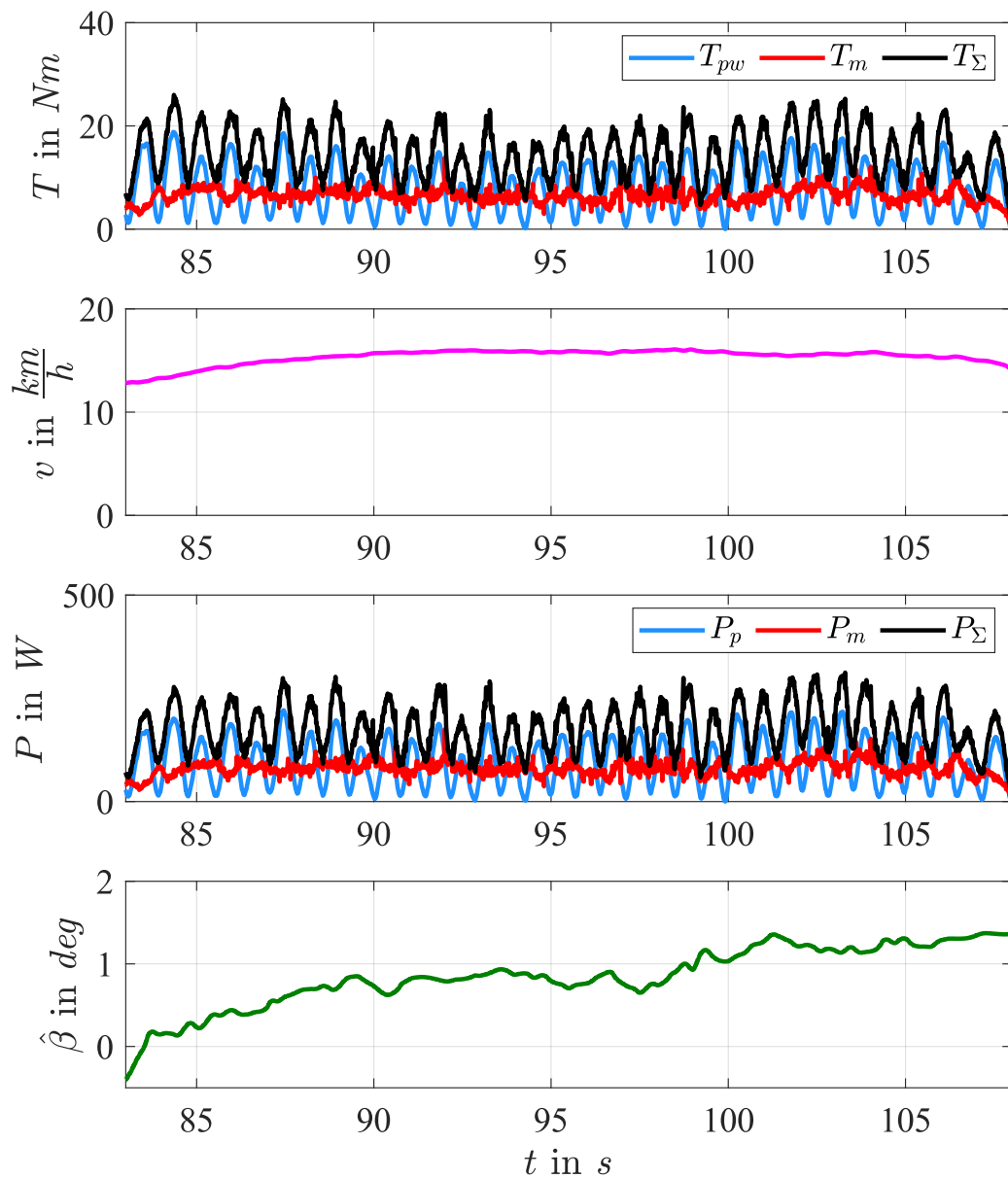


Figure 5.27: **Uphill riding** in the case of an **electrical assistance based on the CPTO** torque estimation ($T_m = \hat{T}_{pw}$). From top to bottom: pedaling torques (measured pedaling torque T_{pw} , motor torque T_m , and total delivered torque $T_\Sigma = T_{pw} + T_m$) at the back wheel, bicycle speed v , delivered power (pedaling power P_p , motor power P_m , and total power $P_\Sigma = P_p + P_m$), and estimated road slope $\hat{\beta}$.

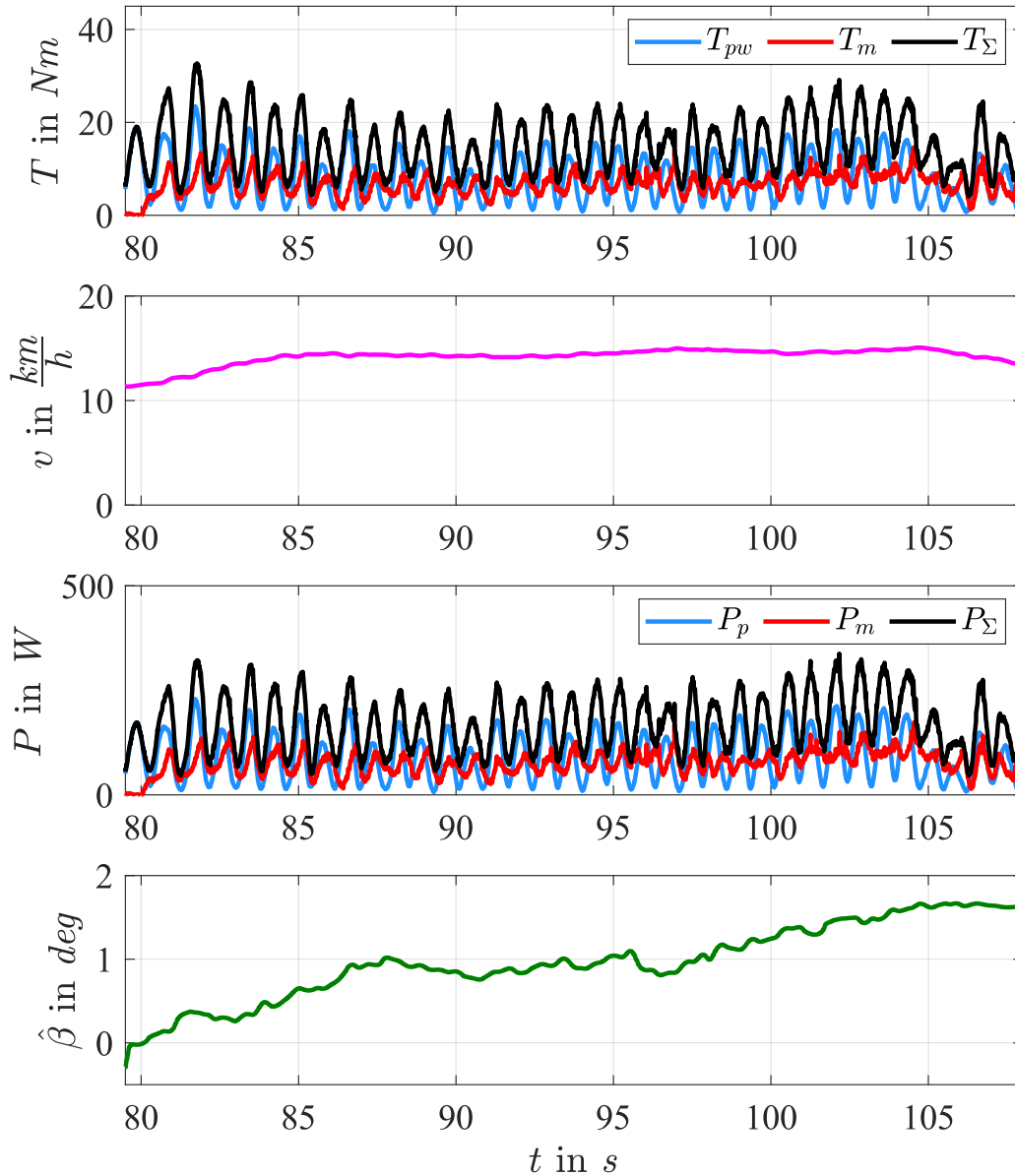


Figure 5.28: **Uphill riding** in the case of an **electrical assistance based on the SPTO** torque estimation ($T_m = \hat{T}_{pw}$). From top to bottom: pedaling torques at the back wheel (measured pedaling torque T_{pw} , motor torque T_m , and total delivered torque $T_\Sigma = T_{pw} + T_m$), bicycle speed v , delivered power (pedaling power P_p , motor power P_m , and total power $P_\Sigma = P_p + P_m$), and estimated road slope $\hat{\beta}$.

In the following, a comparison between the torque-sensorless approaches based on the maximum and average pedaling power is presented. In particular, Table 5.7 contains the

results achieved during the starting section while Table 5.8 the ones obtained in uphill riding.

It can be seen that in the starting section, a similar APPR has been obtained for the two PTOs. In both cases, the average power reduction results even about 5% higher than the one obtained with the pedaling torque sensor. This can be explained by the torque-filling effect caused by the inaccurate torque estimation of the PTOs. Indeed, the electrical assistance is provided even at crank angles where low pedaling torque is applied. Moreover, it can be seen that the MPPR results circa 5% higher in the case of SPTO because it estimates the torque peaks with more accuracy than the CPTO. In particular, its MPPR is comparable to the one achieved with the torque sensor. In the uphill sector, the power reductions obtained with the sensor-based approach result circa 5% higher because, conversely to the starting phase, no saturation caused by the limitation of the motor torque has been experienced in this portion of the track. Moreover, one can notice that the APPR slightly worsens of about 1 – 2% for both PTOs compared to the results obtained in the starting phase. This reduction can be mostly explained by the effect of road slope estimation delays in a variable slope environment and the necessary strong filtering of the speed measurement that reduce the average estimated pedaling torque even in the presence of the filling effect of the sensorless approaches. Besides, it can be seen that slope estimation delays and strong speed filtering also affect the torque peak estimation capability of both PTOs causing a reduction of the MPPR of circa 10% compared to the value obtained when employing the sensor. In particular, a MPPR degradation of circa 5% has been achieved when utilizing the SPTO compared to the results obtained in the starting phase. Whereas, the MPPR obtained with the CPTO has resulted less dependent on the estimated slope and measured speed since comparable values have been achieved in both the starting and uphill sectors of the track.

One can conclude that by analyzing the delivered pedaling power, small differences can be noticed between the sensor and the sensorless approaches, especially in the absence of rapid slope variations, like in the starting phase. It has also been seen that rapid road angle changes and the strong speed measurement filtering affect the pedaling power peaks estimation capability of the PTOs rather than the average delivered power. Indeed, thanks to the torque filling effect caused by the torque estimation inaccuracy, a similar or higher APPR has been obtained with both torque-sensorless electrical assistance approaches compared to the sensor-based one. Moreover, the assistance provided using the SPTO estimation results more similar to the one of the torque sensor in the starting phase. However, this resemblance degrades with variable road angles. Whereas, although slightly worse in the starting phase, the CPTO-based electrical assistance has resulted less dependent on the road angle estimation inaccuracies. Furthermore, it has to be remarked that other sources of error like online model parametric variations, inaccuracies of the motor torque control system, and modeling simplifications can be also responsible for performance degradation when employing torque-sensorless-based electrical assistance approaches.

Assistance type	$\max(P_p)$ in W	\bar{P}_p in W	MPPR in %	APPR in %
No assistance	246.34	84.3 ± 9.95	—————	—————
Sensor	160.61	54.06 ± 5.23	34.8	35.87 ± 0.3
CPTO	173.19	51.29 ± 4.86	29.69	39.15 ± 0.15
SPTO	161.01	50.9 ± 6.01	34.63	39.61 ± 0.17

Table 5.7: **Pedaling power analysis in the starting phase** of the track with different kind of electrical assistance.

Assistance type	$\max(P_p)$ in W	\bar{P}_p in W	MPPR in %	APPR in %
No assistance	322.67	147.65 ± 2.97	—————	—————
Sensor	195.2	88.78 ± 9.32	39.51	39.87 ± 0.1
CPTO	226.44	91.98 ± 5.03	29.82	37.7 ± 0.06
SPTO	228.21	90.86 ± 11.92	29.27	38.46 ± 0.13

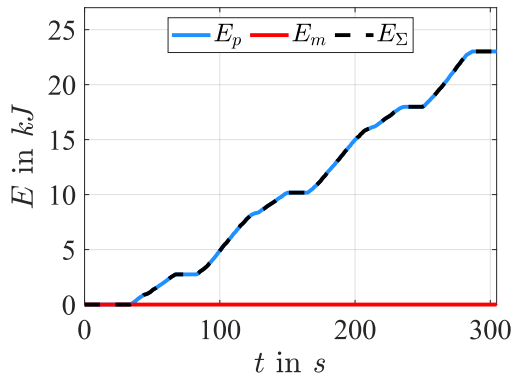
Table 5.8: **Pedaling power analysis in the uphill section** of the track with different kind of electrical assistance.

Delivered energy analysis:

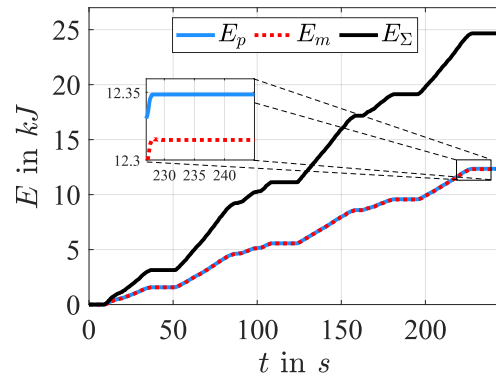
In the following, the total delivered energy on the entire track is analyzed to evaluate and compare the global pedaling effort reduction of each electrical assistance strategy. Figure 5.29 encloses examples of dissipated energy in the four test cases. In particular, each figure contains the cycling energy E_p , the motor energy E_m , and the total one $E_\Sigma = E_p + E_m$ necessary to perform the considered task. One can notice that the total delivered energy slightly varies in each experiment depending on the applied pedaling torque profile, followed path, and environmental conditions. However, its final value is always contained in the range $E_\Sigma \in [20;25]$ kJ. Table 5.9 contains the confidence intervals of the aforementioned quantities considering three experiments executed in similar conditions. Additionally, the PER is evaluated for each assistance type and the relative confidence interval is reported. As one can notice, in the case of a torque sensor based electrical assistance, the energy reduction amounts to circa the 50% with a very small variability. As expected, this assistance approach is independent from external riding and environmental conditions. It has to be remarked that the calculated PER would be exactly equal to 50% in the case of no motor torque saturation. When the CPTO estimation is utilized to provide the electrical aid, the pedaling energy reduction decreases of about 5%. Besides, this reduction has a higher variability than the sensor-based approach due to the dependence of the pedaling torque estimation on environmental and riding conditions. Employing an SPTO, the pedaling effort reduction is only circa 3% lower than the one obtained with a torque sensor based assistance. Although the

PER of the SPTO is higher than the one obtained with the CPTO, one can notice that it is more variable depending on the environmental conditions.

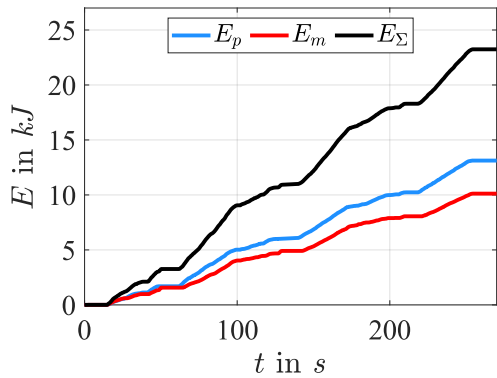
Therefore, from an energy reduction point of view, the torque-sensorless approaches slightly increase the total cycling effort compared to the torque sensor-based assistance. However, the effort reduction capability varies depending on the environmental conditions, especially in the case a SPTO is employed.



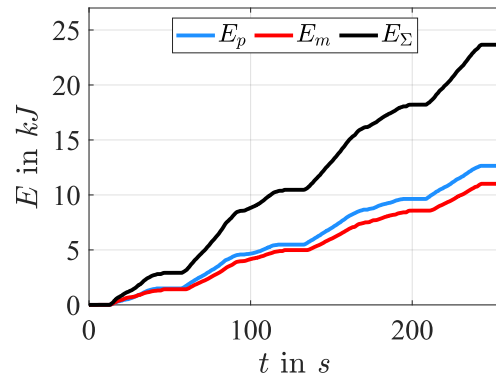
(a) No electrical assistance ($T_m = 0 \text{ Nm}$).



(b) Torque sensor-based electrical assistance ($T_m = T_{pw}$).



(c) CPTO estimation based electrical assistance ($T_m = \hat{T}_{pw}$).



(d) SPTO estimation based electrical assistance ($T_m = \hat{T}_{pw}$).

Figure 5.29: **Delivered energy on the entire track** (pedaling energy E_p , motor energy E_m , total energy $E_\Sigma = E_p + E_m$) with the different electrical assistance approaches.

Assistance type	E_p in kJ	E_m in kJ	E_Σ in kJ	PER in %
No assistance	22.611 ± 1.814	—————	22.611 ± 1.814	—————
Sensor	11.531 ± 1.577	11.443 ± 1.627	22.973 ± 3.204	49.8 ± 0.16
CPTO	12.775 ± 0.396	10.379 ± 0.315	23.154 ± 0.088	44.828 ± 1.513
SPTO	12.315 ± 1.901	10.892 ± 0.144	23.206 ± 1.844	47.103 ± 4.086

Table 5.9: Confidence intervals at 95% of the **delivered energy on the entire track** with different electrical assistance approaches.

5.3.4 Qualitative analysis

The pedaling effort reduction expressed in terms of pedaling power or energy devaluation, cannot be considered as the only index that points out the quality of an electrical assistance strategy. In fact, as stated in [1], riders are mainly interested in usability and good feel while riding electric bicycles, thus in user-dependent and not numerically definable quantities. Therefore, the different electrical aid approaches implemented on the pedelec prototype have been tested by a sample of 10 people of different sex, age, weight (in the range [60;90] kg), height (in the range [170;190] cm), and cycling experience to derive a qualitative analysis of the torque-sensorless riding performances. Each participant was asked to ride the bicycle on the track of Figure 5.10 at a maximum speed of circa $15 \frac{km}{h}$ and test the three different electrical assistance types (sensor-based, CPTO-based, and SPTO-based) in an unknown to the rider randomized order. After performing the required task, the participants were asked to answer a questionnaire related to the electrical assistance strategies characteristics (reported in the appendix of this work), to create a preference ranking of the tested aid approaches, and to guess whether the tested assistance method was a sensor-based or a sensorless control approach. In particular, the following questions were asked the rider:

- “Was the received electrical assistance sufficient?”
- “Was the electrical assistance sufficiently reactive to your pedaling?”
- “Did you experience delays in the delivered electrical assistance?”
- “Do you think that the received electrical assistance is safe enough?”

Figure 5.30 illustrates the survey participant answers to the above-reported questions. As one can see, the majority of participants thought that the received electrical assistance was sufficient for the performed task. However, in the case of the CPTO and the sensor-based approach, the 30% and 20% of persons respectively found the received electrical aid too weak. Surprisingly, no survey participant believed the SPTO to provide insufficient assistance. Concerning the responsiveness of the delivered motor aid, all participants found as expected the sensor-based approach to be the most reactive to the applied pedaling torque. Nevertheless, only the 20% and the 10% of participants believed that the sensorless approaches, CPTO and SPTO respectively, were not sufficiently responsive. Moreover, the

riders have also correctly identified the higher responsiveness of the SPTO compared to the CPTO-based assistance. When asked about the experienced assistance delays, only the 10% of participants felt delays in the sensor-based approach. On the other hand, strong delays were detected in the CPTO-based approach where 70% of people lamented a retarded motor aid compared to the applied pedaling. In the SPTO approach, the people percentage that complained about assistance delays drastically decreased to 30% underlining the higher responsiveness of this approach compared to the CPTO. Nevertheless, many cyclists have reported delays in receiving assistance with both sensorless approaches especially after curves or in the presence of rapid slope changes. This behavior can be explained by the delays and errors introduced by the employed slope estimation approach when fast slope variations or curves occur. Generally, the majority of survey participants found the tested assistance methods safe. Only a few of them considered the unexpected assistance boost received in the presence of rapid road grade variations, when testing the torque-sensorless methods, not acceptable. Additionally, as expected, no one complained about the sensor-based approach safety. Furthermore, some participants denounced power boosts delivered by the sensorless approaches while pushing the bike without being on the saddle. Nevertheless, this behavior was expected and constitutes a known problem of the sensorless approaches, namely the incapability of distinguishing between propulsive forces generated at the pedals from other thrust forces applied to the vehicle.

Afterwards, the survey participants were asked to compare the tested assistance methods. Generally, many cyclists noticed a minimal difference between the proven electrical aid strategies. In particular, many of them recognized that the CPTO-based assistance reacts later compared to the other two and that the SPTO one is a compromise between the sensor and the CPTO. Moreover, some cyclists claimed the SPTO-based assistance to be very similar to the one obtained when employing the sensor, i.e. very reactive to the applied pedaling torque. Furthermore, the participants were asked to create a preference ranking of the tested methods. Figure 5.31 contains the results of this ranking. In particular, Figure 5.31(a) illustrates a Formula One style ranking calculated attributing a score depending on the strategy preference placement for each participant, namely attributing 10 points to a 1st, 5 points to a 2nd, and 0 points to a 3rd placement. Based on this evaluation approach, the sensor-based assistance (65 points) has resulted in the overall best strategy with only 10 points distance from the SPTO (55 points). Whereas, the CPTO has resulted clearly the less favorite approach adding up to only 30 points. Figure 5.31(b) shows in which percentage each assistance method has reached the 1st placement in the user preference. As one can notice, the 50% of participants preferred the highly reactive sensor-based approach, whereas the 30% and 20% favored rather the SPTO or the CPTO respectively. Some cyclists explicitly stated that they preferred the smoother assistance received with the CPTO-based control which aided their motion even when they were not pedaling. In particular, they were satisfied by the torque filling effect and did not like the torque amplification and consequent speed fluctuations typical of a torque-sensor-based fixed gain control. Thus, these results confirm how difficult is to establish a ranking between electrical assistance methods since the results are strongly dependent on the expectations and preferences while riding of each cyclist.

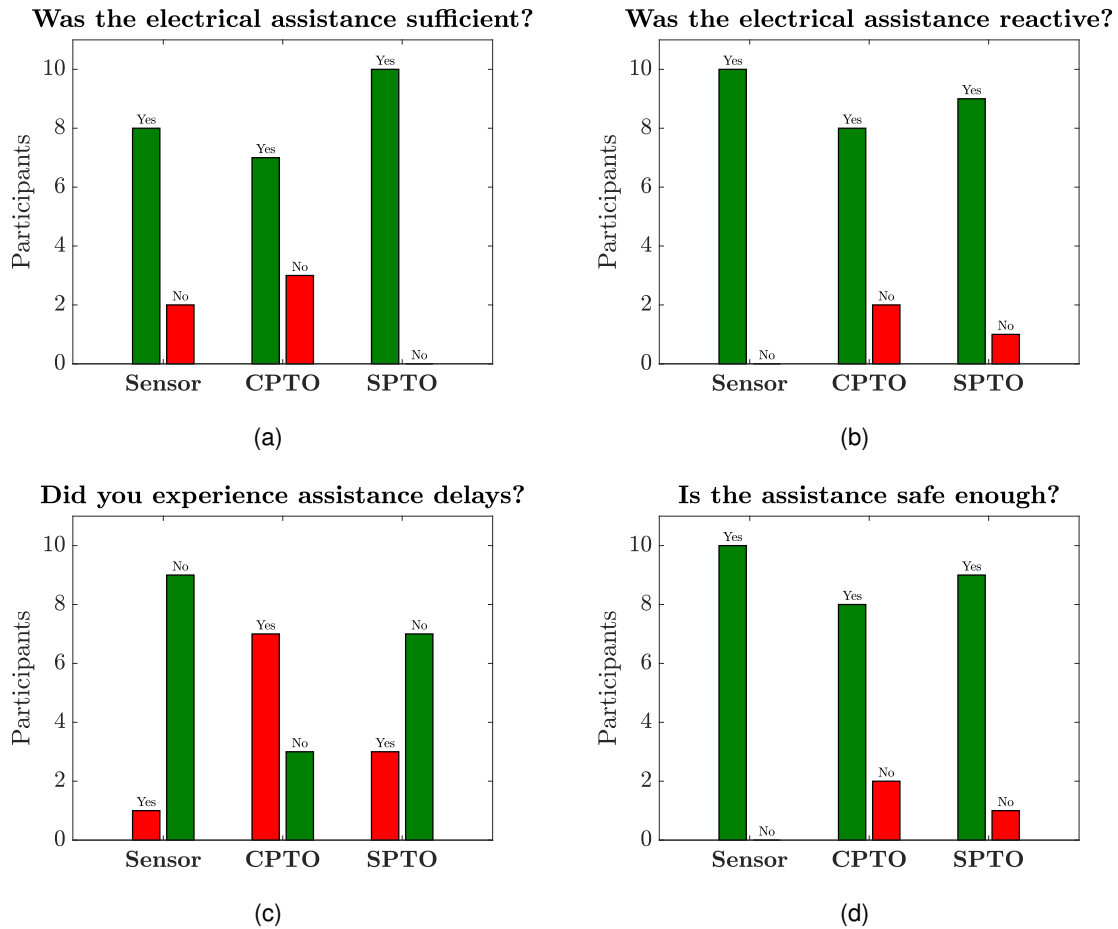


Figure 5.30: Survey participants opinions about the tested electrical assistance characteristics.

Eventually, each survey participant was asked to guess if they were testing a sensor-based or a sensorless control. Only the 50% of interviewed were able to detect the sensor among all the tested assistance approaches. The remaining participants either confused the SPTO-based control with the sensed one or were not able to correctly answer the question because they did not know how to recognize a sensor-based approach from a sensorless one due to probably a lack of electric bicycle riding experience or knowledge about torque-sensorless pedelec control.

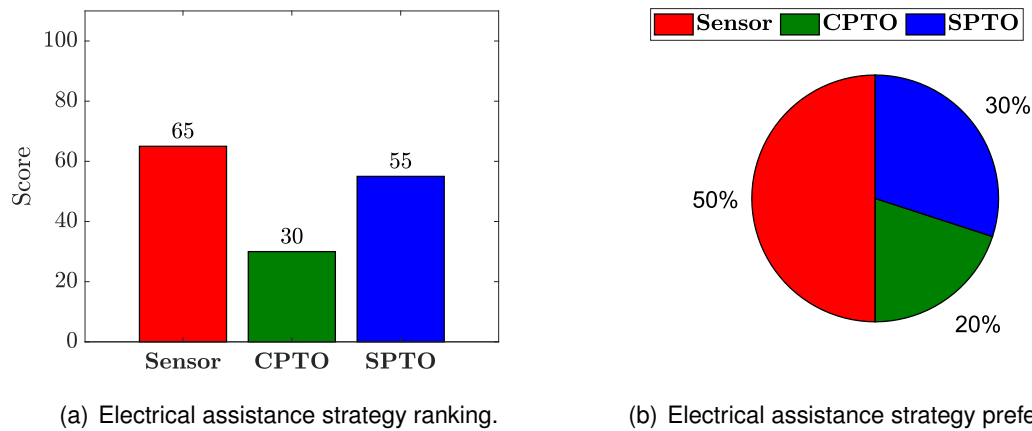


Figure 5.31: Survey participants preferences concerning the tested electrical assistance strategies.

5.3.5 Final considerations

From the previous qualitative analysis, it has emerged that slight differences can be noticed between the sensor-based and the torque-sensorless approaches. In particular, the SPTO has resulted more similar to the sensed approach, confirming the numerical results of Section 5.3.3, since capable of following with higher accuracy the applied pedaling torque compared to the CPTO method. Moreover, the SPTO has resulted in a good compromise between the sensor- and CPTO-based assistances. Nevertheless, considering the aforementioned numerical analysis, the pedaling torque estimation and effort reduction capability obtained with the SPTO have resulted more dependent on model parametric variations, modeling simplifications, variable environmental conditions, and model input errors (vehicle speed, motor torque, and slope estimation) compared to the CPTO. Although capable of providing a sufficiently strong and reactive assistance level, unwanted delays or power boosts have been experienced when utilizing sensorless approaches. These effects can be mainly attributed to the incapability of the slope estimation approach to follow rapidly changing road grades due to the necessary strong filtering of the vehicle speed input measurement. Furthermore, it has been shown that sensorless control approaches are not able to distinguish between pedaling forces and other thrust forces applied to the vehicle. Nonetheless, the majority of cyclists found the torque-sensorless control approaches sufficiently safe to ride. All in all, an explicit user preference between sensor-based and sensorless control did not emerge from the survey, especially when comparing the SPTO with the sensor. Moreover, some participants preferred the CPTO-based control confirming the high user-dependence of evaluating an electrical assistance. As other evidence of the slight difference between the analyzed control approaches, half of the survey participants could not recognize the sensor-based method among the tested control strategies.

6 Conclusions and outlooks

6.1 Content summary

In this work, a state observation approach that addresses the problem of torque-sensorless assistance for electric bicycles has been discussed. The unknown input observation has been applied to extract the delivered pedaling torque from the total disturbance acting on the system employing the so-called PTOs. In particular, two different approaches to describe the external human input have been analyzed, namely a constant (CPTO) and a sinusoidal model (SPTO) of the pedaling torque. Also, the problem of online road grade estimation has been addressed by employing low-computational efforts KF based on low-cost IMU and in-vehicle measurements. Simulations and experiments have highlighted the advantage of using a sinusoidal model to improve the pedaling torque estimation performance. The PTO estimates have been then employed to electrically aid the vehicle and compared with the results achieved when employing a torque sensor. The performed outdoor trials have shown that torque-sensorless control approaches allow, despite the modeling simplifications and estimation errors, to achieve a comparable pedaling power and energy reduction to the sensor-based one without considerably affecting the global riding feeling especially when an SPTO is employed.

6.2 Conclusions

This work has shown that the analysis of the design characteristics of electric bicycles is fundamental to understand and develop torque-sensorless assistance strategies. In particular, a novel classification of electrical assistance approaches, based on the control optimization focus, has been proposed. This provides useful guidelines to the control system designer compared to the commonly used user-oriented classification based on the sensors employed to detect the human input.

Furthermore, this work formalizes a generalized bicycle longitudinal dynamic model. Compared to the literature, here, the commonly employed electric bicycle motor assemblies, i.e. mid-drive, hub, and friction ones are considered. In particular, a generic expression (3.24) of the motor force is derived and included in the vehicle dynamic model (3.40).

The effect of variable environmental and riding conditions has been also considered in the defined bicycle model (3.40). Then, exploiting the results of a sensitivity analysis, a simplified expression (4.29) has been derived and employed in the PTO models. To consider the impact of the assumed modeling simplification and parametric variations on the pedaling torque estimation, the PTOs have been tested in simulation. It has been shown that the estimators are not able to distinguish the pedaling from other external forces applied to the vehicle, such as braking or propulsive forces. Additionally, intense headwinds can degrade the pedaling torque estimation. Moreover, it has been revealed that an accurate pedaling

torque estimation requires the correct knowledge of the system parameters including mass, road slope, and friction. Despite these limitations, outdoor tests have demonstrated that even in the presence of variable environmental conditions, the electrical assistance performance obtained when relying on torque-sensorless strategies has resulted in a narrow degradation compared to the one obtained with the sensor.

The problem of pedaling torque estimation has been addressed by employing models of different complexity to describe the human input in the PTOs. Based on considerations about the periodic nature of pedaling, the utilization of an enhanced sinusoidal model has been discussed and mathematically formalized in the PTO structure. Simulations have shown that the SPTO usage reduces the pedaling torque estimation error in the presence of unmodelled high-order harmonics. Indoor tests have revealed that a sinusoidal model improves the NRMSE at the same model variance level of circa 10 – 20 % compared to a simple pedaling torque constant model. However, an estimation performance degradation has been observed outdoors in the presence of variable sloped environments and motor assistance with both models. In particular, the SPTO has resulted more susceptible by achieving an NRMSE degradation circa 5% higher than the CPTO in the same conditions. Nonetheless, the SPTO estimation accuracy has resulted circa 5 – 10% higher than the one of the CPTO. Moreover, differently from the CPTO, which estimates approximately the pedaling torque mean value, the SPTO estimate presents a pseudo-sinusoidal shape with a similar frequency to the applied cycling torque. A higher variability has been detected also in the delivered SPTO electrical aid, which, although generally performing more similarly to the sensor, has a higher dependence on environmental and riding conditions.

Differently from the current state of the art, the nonlinear state estimation problem has been here addressed by employing EKFs. Such a method represents an easier and more intelligible approach, based on linearizing the system around the nominal state trajectory, compared to other state observers. Moreover, an observer-tuning strategy to handle model simplifications based on the confidence on the model and measurement equations is here described. In particular, to compensate for the pedaling model simplifications, higher trust is given to the bicycle longitudinal model and the measurements by adding fictitious noise to the pedaling torque equations in the PTOs. The validity of the approach, first tested in simulation, has been confirmed by experimental results. Additionally, an operative manner to select the covariance matrices based on the minimization of the estimation error that accounts for errors caused by the highly-trusted speed measurements has been discussed.

Among the components that act on the vehicle longitudinal dynamics, the performed sensitivity analysis and simulations have highlighted that gravity has the highest impact. Thus, the knowledge of the system mass and the road slope is essential to achieve high-quality pedaling torque estimation performance. While the mass can be considered constant during rides, the road angle may vary rapidly and require a real-time estimation. It has been shown that the road grade estimation problem can be solved using approaches of different complexity and costs. Among them, for cost reduction sake, it is worth employing low-cost IMU to address this issue. To improve the performance of standard algebraic estimation methods, the employment of closed-loop approaches is discussed in this work. In particular, a simple low-cost and low-computational KF based on the vehicle speed and a reduced set of inertial measurements is proposed. Guidelines for the covariance matrices selection have been provided by performing outdoor tests in a variable-sloped environment at different vehicle acceleration levels. The experimental results have shown that the employment of the

proposed KF improves the road angle RMSE of circa 80% compared to algebraic methods in a flat ground test. Nevertheless, the performance improvement is reduced to circa 20% in a sloped environment. These results can be principally explained by the necessary low-pass filtering of the measurements to account for vibrations and the noise introduced by the differentiation of the rotor position on the vehicle speed. Additionally, a method that compensates for the modeling error introduced by cornering is here presented. Experiments have shown that this correction improves the angle estimation. Nevertheless, its effectiveness is dependent on the aggressiveness of the curve.

In the majority of the literature, the evaluation of torque-sensorless algorithm quality is expressed in terms of pedaling torque estimation error minimization. Nevertheless, this cannot be considered as the only index to evaluate the received assistance. In this work, the delivered pedaling power and energy reduction are analyzed as a possible metric to evaluate the assistance performances. In particular, the maximum and average power reduction during the starting phase and uphill riding are calculated as well as the total pedaling energy reduction on the performed riding task. Moreover, for the first time in the literature, the riding feeling has been analyzed by surveying people of different sex, age, weight, height, and cycling experience. The experiments have been executed on a defined track that includes variable slopes and curves. In each case, sensed and sensorless approaches have been tested and compared. The results have revealed narrow differences between sensorless and sensed approaches. For instance, from a pedaling energy reduction perspective, the CPTO and SPTO assistance has resulted only about 5% and 3% worse than the one obtained with the sensor, respectively. The survey results have shown that the SPTO resembles the sensor-based assistance more than the CPTO. Nevertheless, some cyclists preferred the CPTO thanks to its capability of offering electrical aid even when not pedaling. These results have underlined the difficulty in assessing the best assistance strategy. Moreover, it has been shown that undesired assistance delays or boosts may be delivered due to road grade estimation errors or while walking with the bicycle. Despite these problems, the 50% of the survey participants preferred sensorless approaches to the sensed one. Also, 50% of the interviewed could not recognize the sensor-based among the tested strategies. Additionally, the majority of the riders felt safe while cycling with torque-sensorless pedelecs.

6.3 Outlooks

Although the performance degradation is minimal when employing the proposed torque-sensorless approaches, some improvements are still required to become a valid alternative to torque-sensors. Nonetheless, when considering possible system enhancements, it is fundamental to keep the overall complexity and costs lower than the ones of the sensed system to avoid losing the advantage of switching to sensorless approaches. Following, possible system improvements that may be topics for further research activities are discussed.

Reduction of the dependency on environmental conditions:

At present, unmodeled environmental conditions such as intense headwinds or vibrations caused by road surface irregularities may affect the torque estimation and the sensorless electrical assistance performances.

Although strong headwinds are rare and affect the vehicle dynamics especially in the high-speed range where low assistance levels are required, their presence might influence the delivered assistance even at low speeds depending on their intensity. The control system would interpret the unmodeled aerodynamic resistance as a reduced applied pedaling. These may lead to performance degradation during windy days or areas of the world representing a limitation for a possible commercial spread of torque-sensorless control strategies. To overcome this issue, a viable solution could be the integration of wind measurements, employing a Pitot tube or an anemometer, and a consequent enhancement of the PTO model to include wind effects.

As seen in Section 3.1.7, vibrations and bumps caused by road conditions and irregularities cause unmodelled power losses that can affect the system performance. Although accounted in this work in the rolling friction coefficient, this hypothesis may not subsist when their intensity is not negligible. Unfortunately, their mathematical modeling is complex due to their high user and situation dependency. Consequently, their implementation in the PTO is hardly feasible. Moreover, vibrations affect the accelerations measured with the IMU and the road grade estimation. Thus, to avoid a strong low pass filtering of inertial measurements and reduce bump losses, mechanical design expediency must be considered in the assembly of the control electronics and the selection of bicycle tires, frames, and suspensions.

External human forces handling:

As seen in the simulations and the experimental results, external unmodelled forces not generated by pedaling are not distinguishable by the proposed torque estimators. While braking forces can be ignored by turning off the electrical assistance or activating electrical braking in the presence of negative estimated torques, thrust forces are always interpreted as pedaling torque and generate assistance. In standard operation status, namely when the rider is on the saddle, this does not represent a problem. However, this leads to dangerous motor activation when walking with the bicycle. Therefore, to increase the system safety, a possible solution is the employment of external switches mounted on the handlebar to turn on the motor assistance. Alternatively, the activation of the electrical aid only at speeds that are not compatible with walking utilizing where possible according to the local legislation a throttle to provide power at low speeds could be considered. A further possibility is the detection of the rider-on-saddle condition based on force sensors or the exploitation of inertial measurements as proposed in [145].

Online parametric estimation:

At the current implementation state, for system complexity reduction sake, the proposed sensorless control approaches estimate only the road slope among all system parameters due to its considerable impact on vehicle dynamics. A system performance improvement would require an online update of all the parameters considered constant in vehicle dynamics modeling, including the mass, friction coefficients, and gear ratio.

As stated in Section 4.2.1, system mass variations occur rarely during standard operation. Moreover, as explained in Section 4.3.2, mass estimation approaches based on vehicle dynamics or exciting input injection cannot be successfully used without force measurements. Thus, to account for cyclist mass variations, possible solutions include using force sensors

mounted in the saddle or a cycling mass value insertion into a display mounted on the handlebar or a mobile app connected with the control electronics before starting riding.

Although less impacting on the bicycle dynamics compared to mass and road grade, rolling friction and drag area variations may affect the received assistance. Their online estimation typically exploits the vehicle longitudinal model. Nevertheless, also in this case, force measurements are required for the parametric estimation. Therefore, a conceivable solution to the problem would be a periodic online update of the parameters when a vehicle coasting down state is detected, namely when no forces are applied, as proposed in [146] in the field of electric scooters.

In this work, the bicycle gear ratio has been considered a fixed and well-known value. This hypothesis stands for many electric bicycles that utilize a fixed gear ratio like the developed one, where the motor aid compensates for the missing pedaling power. Nevertheless, many cyclists like changing gear ratio even when riding electric bicycles. To make possible torque-sensorless pedelecs with variable gears, a solution could be an online gear ratio estimation and update into the PTO models utilizing state observation approaches as proposed in [147, 148] or an online pedaling frequency estimation like the one proposed in [45].

PTO measurement improvements:

As shown in the experimental results, the degradation of the torque estimation and motor aid performances is strongly related to vehicle speed measurement errors introduced by the necessary filtering used to reduce the noise caused by the differentiation of the measured rotor position. To address the problem of speed signal improvement, model-based or signal-processing-based approaches are commonly employed [149]. The first methods are based on model reference adaptive systems, state observation approaches, or neural networks [150–152]. However, such methods require a model of the load that is often not totally known. Thus, they could not be satisfactorily implemented in the case of torque-sensorless approaches, where PTOs estimate the load torque at the same time. Signal-processing-based approaches such as first- or high-order approximations, polynomial interpolation, or numerical integration [153–155] would be therefore preferable.

The velocity filtering also negatively influences the online road slope estimation by causing delayed delivered assistance in highly-variable sloped environment. To avoid the employment of the vehicle longitudinal speed in the angle estimation, more computationally complex methods that involve all the measurements of the 6-axis IMU based on complementary or Kalman filtering, as examined in [139], could be considered. Thanks to the employment of gyroscopic measurements, these methods could reduce problems related to vibrations that affect the measured accelerations.

Position sensorless motor control:

Although a pedaling torque estimation degradation is foreseeable, to further reduce costs and utilized space in the system, the substitution of the rotary encoder with low-cost Hall effect sensors or position-sensorless motor control approaches is worth to be investigated.

Since the angle resolution achievable with Hall sensors is too low to be employed in FOC, either the employment of BLDC motors controlled with electronic commutation or rotor position reconstruction approaches, like the ones proposed in [156, 157], could be considered.

To completely remove position-sensing devices, the employment of sensorless motor control could be alternatively taken into account. Nevertheless, it is fundamental to achieve high-quality position information in the whole speed range. Depending on their working principles, sensorless approaches are known to work better either at low (anisotropy-based) or high (BEMF-based) motor speeds. To overcome this issue, the utilization of strategies that combine the position information obtained with different methods, as the one proposed in [158], might be viable.

Further system improvements:

Further possible system improvements aim at increasing the commercial appeal of torque-sensorless systems. More complex bicycle control strategies than the basic fixed-gain approach could be implemented to improve the smoothness, speed-dependency, and energy-efficiency of the delivered motor power, as seen in Section 2.3. Moreover, thanks to the braking torque detection capability of the PTOs, regenerative braking could be implemented without the necessity of installing electric brakes. This would allow for recovery energy while braking and increase the battery autonomy.

Thanks to the torque sensor removal, a partial or complete in-motor integration of the control electronics could be also achieved. In such a way, an in-wheel and easy-to-install conversion kit that does not require the installation of any additional sensor might be realized. Moreover, the additional development of a mobile app that allows varying the delivered assistance levels and analysis of cycling performances would further increase the appeal of the conversion kit.

7 Appendix

7.1 IMU calibration and mounting offset correction

The IMU calibration procedure consists of the compensation for the zero-g and zero-rate offsets of the sensor caused by the mechanical stress when mounting the MEMS device onto a printed circuit board. The zero-g offset correction may be performed aligning the sensor with the different sensing axes and comparing the output acceleration signals with the expected values in each of the six possible orientations. For each axis, offset, gain, and cross-gains are evaluated and used to correct the accelerometer measurements [159]. The zero-rate correction can also be performed evaluating the measured angular rate when the device does not move and compensating for it.

After calibrating the device, the IMU measurements expressed in the sensor reference frame $x^s - y^s - z^s$ must be reported into the bicycle one $x - y - z$ compensating for the mounting offset of the sensing device expressed in terms of the Euler angles roll φ_s , pitch γ_s , and yaw ψ_s . The angle compensation must be performed in the absence of bicycle longitudinal acceleration $a = 0 \frac{m}{s^2}$ when the device measures only the effect of gravity \mathbf{g} . Thus, the measured accelerations \mathbf{a}_s^s expressed in the sensor reference frame that has a generic orientation compared to the gravitational field result:

$$\mathbf{a}_s^s = \begin{bmatrix} a_{s_x}^s & a_{s_y}^s & a_{s_z}^s \end{bmatrix}^T = \begin{bmatrix} g_x^s & g_y^s & g_z^s \end{bmatrix}^T. \quad (7.1)$$

To calculate the mounting angles, we need to evaluate the accelerometer readings in the absence of bicycle leaning and road grade. Under these hypotheses, the gravity vector results parallel to the z -axis of the bicycle reference frame, i.e. the accelerations reported in the bicycle frame \mathbf{a}_s must result after the coordinate system transformation equal to:

$$\mathbf{a}_s = \begin{bmatrix} a_{s_x} & a_{s_y} & a_{s_z} \end{bmatrix}^T = \begin{bmatrix} 0 & 0 & g \end{bmatrix}^T. \quad (7.2)$$

A reference frame transformation that bounds the two coordinate systems can be defined by applying three consecutive rotations. In this case, the sequence y , x , and z has been chosen:

$$\mathcal{R}_y(\gamma_s) = \begin{bmatrix} \cos(\gamma_s) & 0 & -\sin(\gamma_s) \\ 0 & 1 & 0 \\ \sin(\gamma_s) & 0 & \cos(\gamma_s) \end{bmatrix}, \quad (7.3)$$

$$\mathcal{R}_x(\varphi_s) = \begin{bmatrix} 1 & 0 & 0 \\ 0 & \cos(\varphi_s) & \sin(\varphi_s) \\ 0 & -\sin(\varphi_s) & \cos(\varphi_s) \end{bmatrix}, \quad (7.4)$$

$$\mathcal{R}_z(\psi_s) = \begin{bmatrix} \cos(\psi_s) & \sin(\psi_s) & 0 \\ -\sin(\psi_s) & \cos(\psi_s) & 0 \\ 0 & 0 & 1 \end{bmatrix}, \quad (7.5)$$

where $\mathcal{R}_i(\cdot)$ with $i \in \{x, y, z\}$ represents the generic rotation matrix around the i -axis. Composing the three rotations, one obtains the overall rotation matrix:

$$\mathcal{R}_{yxz}(\gamma_s, \varphi_s, \psi_s) = \mathcal{R}_y(\gamma_s) \mathcal{R}_x(\varphi_s) \mathcal{R}_z(\psi_s) = \begin{bmatrix} c_{\gamma_s} c_{\psi_s} - s_{\gamma_s} s_{\varphi_s} s_{\psi_s} & c_{\gamma_s} s_{\psi_s} + c_{\psi_s} s_{\gamma_s} s_{\varphi_s} & -c_{\varphi_s} s_{\gamma_s} \\ -c_{\varphi_s} s_{\psi_s} & c_{\varphi_s} c_{\psi_s} & s_{\varphi_s} \\ c_{\psi_s} s_{\gamma_s} + c_{\gamma_s} s_{\varphi_s} s_{\psi_s} & s_{\gamma_s} s_{\psi_s} - c_{\gamma_s} c_{\psi_s} s_{\varphi_s} & c_{\gamma_s} c_{\varphi_s} \end{bmatrix}, \quad (7.6)$$

where the functions cosine and sine are written as c_i and s_i with $i \in \{\gamma_s, \varphi_s, \psi_s\}$ for the sake of a compact mathematical representation. Therefore, the acceleration \mathbf{a}_s can be expressed into the sensor frame:

$$\mathbf{a}_s^s = \mathcal{R}_{yxz}(\gamma_s, \varphi_s, \psi_s) \mathbf{a}_s = \begin{bmatrix} -g \cos(\varphi_s) \sin(\gamma_s) \\ g \sin(\varphi_s) \\ g \cos(\gamma_s) \cos(\varphi_s) \end{bmatrix}. \quad (7.7)$$

Solving the system of equations (7.7), only two orientation angles γ_s and φ_s of the device can be calculated since the vector \mathbf{a}_s is invariant to rotations around the z -axis which is parallel to the gravitational field [160]. In particular, the orientation angles can be calculated as follows:

$$\gamma_s = \arctan\left(\frac{-g_x^s}{g_z^s}\right), \quad (7.8)$$

$$\varphi_s = \arctan\left(\frac{g_y^s}{\sqrt{g_x^{s2} + g_z^{s2}}}\right). \quad (7.9)$$

To express the measured accelerations into the bicycle frame one can use the following expression:

$$\mathbf{a}_s = \mathcal{R}_{yxz}^T(\gamma_s, \varphi_s, \psi_s) \mathbf{a}_s^s, \quad (7.10)$$

where $\mathcal{R}_i^{-1}(\cdot) = \mathcal{R}_i^T(\cdot)$ thanks to the orthogonality of the rotation matrices. It can be noticed that to apply the transformation (7.10) the yaw angle mounting offset ψ_s needs to be known. Thanks to the lightness of bicycles, it is possible to evaluate the yaw mounting offset placing the vehicle straight in the vertical plane, i.e. with the gravity parallel to the x -axis of the bicycle. Under this hypothesis, after the coordinate transformation, the acceleration in the bicycle frame must result equal to:

$$\mathbf{a}_s = [g \ 0 \ 0]^T. \quad (7.11)$$

Applying (7.8) and (7.9) in the new position, one obtains the complementary angle to the pitch mounting angle $\frac{\pi}{2} - \gamma_s$ and the yaw offset ψ_s , respectively. Thus, the rotation matrix can be determined and the accelerations can be reported in the bicycle frame using equation (7.10). Similarly, the angular speeds measured in the sensor frame $\omega_s^s = [\omega_{s_x}^s \ \omega_{s_y}^s \ \omega_{s_z}^s]^T$ can be reported into the bicycle one:

$$\omega_s = \mathcal{R}_{yxz}^T(\gamma_s, \varphi_s, \psi_s) \omega_s^s. \quad (7.12)$$

7.2 Prototype control electronics description

In this section, the electronic components and sensors employed in the projected pedelec prototype are described in detail. Figure 7.1 contains a schematic description of the designed control electronics. The system is composed of five electronic boards with different functionalities that communicate with each other over a Controller Area Network (CAN) bus. This communication protocol is typically employed in vehicle applications thanks to its simplicity, low cost, and robustness to electric disturbances and electromagnetic interference. The 24 V battery pack with integrated BMS is connected to the Power Distribution Unit (PDU) which is the electronic board that supplies all the other boards of the distributed system with the required voltages. The voltage level reduction is performed employing two voltage regulators that reduce the battery voltage to 12 V and 5 V respectively. To ensure safety in case of system failure during the testing phase, the PDU contains a relais that disconnects the battery from the system when pressing an emergency button mounted on the bicycle handlebar as shown in Figure 5.2. Furthermore, since no energy recovery mechanism has been considered in the prototype design, the PDU contains a chopper circuit that protects the power electronics from overvoltages caused by electrical braking and dissipates the motor energy over a braking resistor R_B . The battery voltage is used to supply the Motor Control Unit (MCU) which is the electronic board used to control the motor. This board is composed of three parts, namely the inverter, the control, and the position sensing boards. The MCU has been divided into different interconnected boards, to add modularity to the system. The inverter board contains a three-phase inverter and the electronics used to measure the currents and the voltages necessary to control the motor. The inverter is made of 6 Power-MOSFETs dimensioned for a pedelec application (48 V, 45 A) controlled by a gate driver. Phase current measurements are performed employing in-line shunt resistors and current sensor amplifiers. The inverter board is connected to the control one which contains a *STM32H7* microcontroller. The latter performs the current and voltage measurements using Analog-to-Digital Converters (ADCs) with 12-bit resolution, the rotor position sensing, and FOC. Moreover, a Universal Serial Bus (USB) connection allows data plotting. The control boards connect to a position-sensing board that contains the necessary electronics to connect a rotary encoder to the microcontroller. In particular, the *LM10* incremental magnetic rotary encoder from *RLS* [161], has been utilized. The considered encoder is composed of a contactless readhead coupled with a magnetic ring firmly mounted on the motor housing. The device generates two sinusoidal differential-ended analog quadrature-outputs that allow the mechanical rotor position calculation using the arcotangent function. A *Raspberry Pi 4* board allows data collecting, plotting, and streaming using the software *ESPlot* over a monitor mounted on the bicycle handlebar and connected with a High Definition Multimedia

Interface (HDMI) cable as shown in Figure 5.2. Moreover, the *Raspberry Pi 4* connects to the Bicycle Supervision Unit (BSU) over USB. This connection supplies the BSU and allows data streaming. The BSU is a *Nucleo-144* Board that mounts a *STM32H7* microcontroller. Its function is to supervise the entire system, run the road slope observer, estimate the pedaling torque with the proposed PTOs, and generate the torque references for the motor control. Moreover, the BSU connects to a pedaling torque sensor employed for validation purposes. Among the possible mountable sensors described in Section 2.2, the bottom bracket technology has been chosen. In particular, the *ERider ERST* sensor [73] has been installed since, compared to other sensors based on the same technology, it allows the measurement of the complete applied pedaling torque. The IMU Board (IMUB) is firmly mounted to the bicycle frame and contains a *LSM6DSL* six-axes IMU connected to a *STM32F3* microcontroller over Serial Peripheral Interface (SPI). Also, this board allows data plotting with a USB connection. The IMUB sends the IMU measurements while the MCU sends the applied motor torque and measured motor angular speed to the BSU. The latter processes the received information and sends the torque reference used by the MCU to control the motors and provide electrical assistance. Additionally, the system offers the possibility to read CAN messages through a connection to the bus with an external computer.

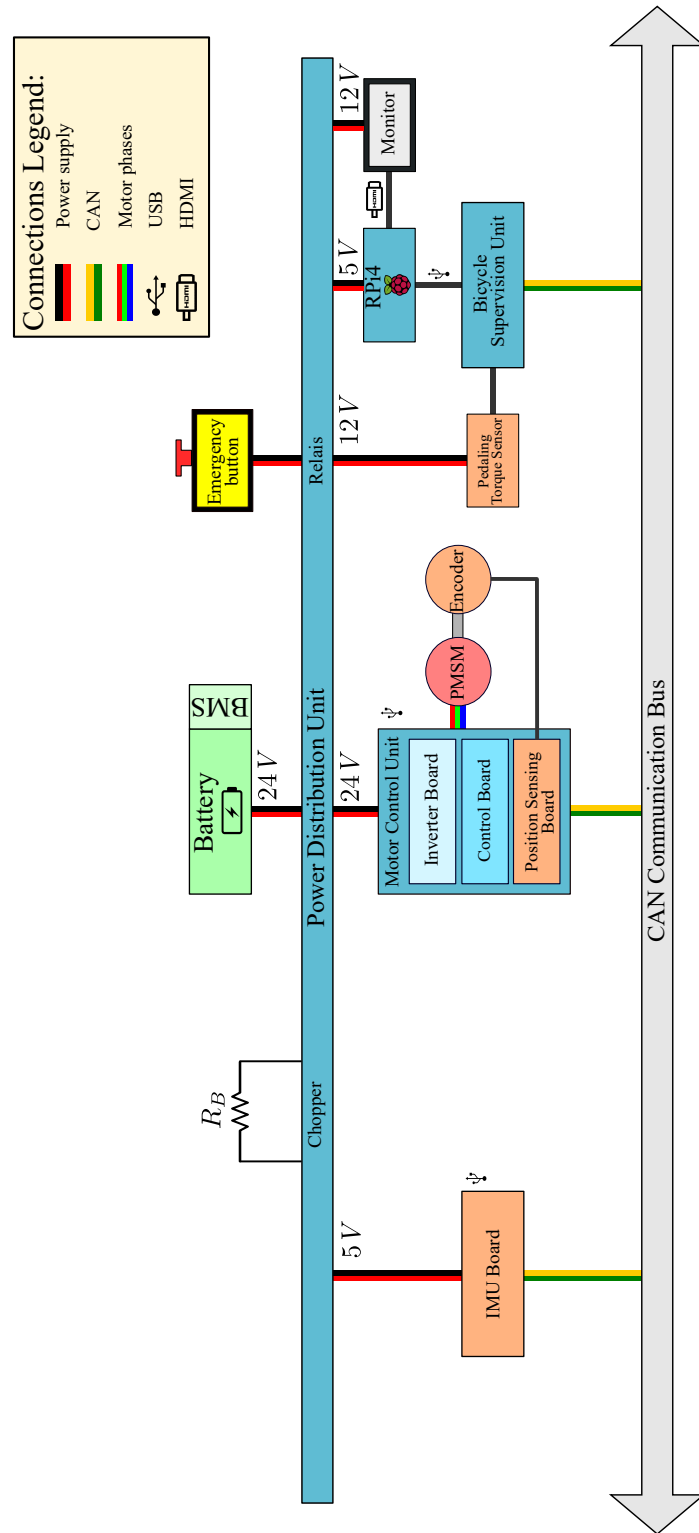


Figure 7.1: Schematic description of the control electronics employed in the developed pedelec prototype.

Torque-sensorless electrical assistance survey

In this survey, you will try and evaluate three different electrical assistance strategies implemented on a pedelec prototype. In particular, you will test one torque-sensored and two torque-sensorless electrical assistance approaches in an unknown order. At the end of the survey, you will be asked to guess which kind of assistance you tried.

Electrical assistance Code

Testing order code: _____

Personal information

1. Name: _____
2. Age: _____
3. Sex: Female Male
4. Height: _____ cm
5. Measured weight: _____ kg

Cycling experience

6. How often do you ride a bicycle?
 - Never
 - Occasionally
 - Daily
 - Professionally
 - Other: _____
7. Do you have experience with electric bicycles? Yes No
8. Do you have an electric bicycle? Yes No
9. If not, would you buy one? (Please motivate)
 - No: _____
 - Yes: _____
10. How often do you ride electric bicycles?
 - Never
 - Occasionally
 - Daily
 - Other: _____
11. What kind of electric bicycle have you ridden before?
 - Power-on-demand
 - Pedelec
 - I don't know

12. What do you expect when riding an electric bicycle? (Please describe your riding performance expectations)

13. In which context do/would you use an electric bicycle rather than other means of transportation? (Please describe)

Electrical assistance 1

14. Was the received assistance sufficient?

- No
- Yes

15. Was the assistance sufficiently reactive to your pedaling?

- No
- Yes

16. Did you experience delays in the delivered assistance? (If yes, please explain when)

- No
- Yes: _____

17. Do you think that the received electrical assistance is safe enough? (Please motivate)

- No: _____
- Yes: _____

Electrical assistance 2

18. Was the received assistance sufficient?

- No
- Yes

19. Was the assistance sufficiently reactive to your pedaling?

- No
- Yes

20. Did you experience delays in the delivered assistance? (If yes, please explain when)

- No
- Yes: _____

21. Do you think that the received electrical assistance is safe enough? (Please motivate)

- No: _____
- Yes: _____

Electrical assistance 3

22. Was the received assistance sufficient?

- No
- Yes

23. Was the assistance sufficiently reactive to your pedaling?

- No
- Yes

24. Did you experience delays in the delivered assistance? (If yes, please explain when)

- No
- Yes: _____

25. Do you think that the received electrical assistance is safe enough? (Please motivate)

- No: _____
- Yes: _____

Comparison between the assistance methods

26. Did you feel differences between the three assistance methods? (Please describe)

27. Can you guess which assistance method you tested? (Answer with Sensor or Sensorless)

- Electrical Assistance 1: _____
- Electrical Assistance 2: _____
- Electrical Assistance 3: _____

28. Please create a ranking of your favorite assistance methods: (Answer with 1,2,3)

1. _____
2. _____
3. _____

8 List of symbols

General:

x, X Quantities.
 \mathbf{x}, \mathbf{X} Vectors and matrices.

Number sets:

\mathbb{R} Real numbers.
 \mathbb{Z} Integer numbers.

Reference systems:

abc Phase reference frame.
 dq Rotor reference frame.
 xyz Bicycle reference frame.
 $x^s y^s z^s$ IMU reference frame.
 $\alpha\beta$ Stator reference frame.

Accents:

$\hat{}$ Estimated quantity.
 $\tilde{}$ Rated quantity.
 $\bar{}$ Average value.

Superscripts:

$*$ Control target.
 $+$ KF *a posteriori* estimate.
 $-$ KF *a priori* estimate.

Quantities:

Note: Some quantities may contain specific subscripts and superscripts whose meaning is explained in the quantity description.

a Bicycle longitudinal acceleration.
 $a_{s_i}^j$ IMU measured acceleration. Subscript i : axis component $\{x, y, z\}$, radial component R , tangential component T . Superscript j : sensor reference frame s ,

	bicycle reference frame <i>no superscript</i> .
A	Frontal area of cyclist and bicycle.
A_d	Drag area.
\mathbf{A}	State space representation continuous time state matrix.
\mathbf{B}	State space representation continuous time input matrix.
c	Curve effect compensation coefficient.
C_d	Drag coefficient.
$CI_{95\%}$	Confidence interval at 95%.
\mathbf{C}	State space representation continuous time output matrix.
d	Distance traveled horizontally or run.
d_{μ}	Rolling friction apparent distance traveled horizontally or run.
e_i	Induced electromotive forces. Subscript i : motor phase $\{a, b, c\}$.
E	Energy.
E_m	Motor energy.
E_p	Pedaling energy.
E_{Σ}	Global delivered energy.
$f_{c_i}^j$	LPF cutoff frequency. Subscript i indicates the filtered quantity. Superscript j : maximum value <i>max</i> , minimum value <i>min</i> .
f_s	Sampling frequency.
F	Force.
F_a	Aerodynamic drag force.
F_b	Bump force.
F_d	Driving forces.
F_g	Gravity force.
F_h^i	Human forces acting on the bicycle longitudinal dynamics. Superscript i : external to the crankset e .
F_m	Motor force acting on the bicycle longitudinal dynamics.
$F_{p_i}^j$	Pedaling force. Subscript i : radial component R , tangential component T . Superscript j : left pedal l , right pedal r .
F_r	Rolling friction force.
F_B	Braking force.
F_I	Inertia force.
\mathcal{F}_{f_i}	Contact surface forces. Subscript i : normal component N , parallel component P .
\mathbf{F}	State space representation discrete time state matrix.
g_i^j	Gravitational acceleration on Earth. Subscript i : axis component $\{x, y, z\}$. Superscript j : sensor reference frame s , bicycle reference frame <i>no superscript</i> .
h	Elevation increase or rise.
h_{μ}	Rolling friction apparent elevation increase or rise.
\mathbf{G}	State space representation discrete time input matrix.
\mathbf{H}	State space representation discrete time output matrix.
i_i	Current. Subscript i : motor phase $\{a, b, c\}$, rotor frame $\{d, q\}$, power inverter DC.
\mathbf{I}	Identity matrix.
\mathbf{J}_F	EKF Jacobian state-state matrix.
\mathbf{J}_H	EKF Jacobian output-state matrix.

\mathbf{J}_L	EKF Jacobian state-noise matrix.
\mathbf{J}_M	EKF Jacobian output-noise matrix.
k	Discrete time variable.
k_j	Discrete time instant. Subscript j : initial i , final f .
K_a	Electrical assistance fixed gain.
K_T	Motor torque constant.
\mathbf{K}	State observer gain.
l_c	Crankarm length.
L_i	Motor inductance. Subscript i : motor phase $\{a, b, c\}$, rotor frame $\{d, q\}$.
m	Total system mass.
n_p	Number of pole pairs.
N	Normal to the surface weight force component.
O	Curve instantaneous center of rotation.
\mathcal{O}	Observability matrix.
\mathcal{O}_v	Time-variant system observability matrix.
p	Absolute pressure.
P	Power.
P_a	Power required to overcome the aerodynamic force.
P_g	Power required to overcome the gravity force.
P_r	Power required to overcome the rolling friction force.
P_{mi}	Motor power. Subscript i : at the crankset c , at the rear cogwheel w .
P_{pi_j}	Pedaling power. Subscript i : at the crankset c , at the rear cogwheel w . Subscript j : with electrical assistance <i>assistance</i> , without electrical assistance <i>no assistance</i> .
P_R	Total power required to overcome the resisting forces.
$P_{\Sigma i}$	Total power. Subscript i : at the crankset c , at the rear cogwheel w .
\mathbf{P}	KF estimation error covariance matrix.
\mathbf{Q}	KF noise on the process covariance matrix.
r	Bicycle wheel radius.
r_c	Crankset radius.
r_f	Friction wheel radius.
r_w	Rear cogwheel radius.
R	Phase resistance.
R_s	Specific gas constant for dry air.
R_B	Braking resistance.
\mathbf{R}	KF noise on the measurements covariance matrix.
s	Laplace domain variable.
S_i	Power inverter MOSFET, with $i \in [1;6]$.
t	Continuous time variable.
T	Torque.
T_{mi}	Motor torque. Subscript i : at the crankset c , at the rear cogwheel w .
$T_{pi_k}^j$	Pedaling torque. Subscript i : at the crankset c , at the rear cogwheel w . Superscript j : left pedal l , right pedal r . Subscript k : continuous component 0, second harmonic component 2, fourth harmonic component 4.
T_s	Sampling time.
T_{sim}	Fixed simulation step time.

List of symbols

T_B	Braking torque.
$T_{\Sigma i}$	Total torque. Subscript i : at the crankset c , at the rear cogwheel w .
u	State space representation input.
U_i	Voltage. Subscript i : motor phase $\{a, b, c\}$, power inverter DC .
v	Bicycle longitudinal velocity.
v_{a_i}	Relative air or apparent wind velocity. Subscript i : axis component $\{x, y, z\}$.
v_{w_i}	Wind velocity. Subscript i : axis component $\{x, y, z\}$.
w_i	KF noise on the process. Subscript i indicates the quantity to which is referred.
x	State space representation state.
y	State space representation measured output.
y_{PI}	PI controller output.
z_c	Crankset number of teeth.
z_w	Rear cogwheel number of teeth.
α	Auxiliary variable including the effect of road slope and rolling friction.
β_i	Road slope angle. Subscript i : expressed as percentage %.
β_μ	Rolling friction apparent road slope angle.
γ_s	IMU pitch mounting offset.
Γ_f	Curve trajectory front wheel radius.
Γ_r	Curve trajectory rear wheel radius.
Γ_s	Curve trajectory IMU radius.
δ	Steering angle.
ε_i	KF estimation error. Subscript i indicates the quantity to which is referred.
$\zeta_{\sigma_w^2}$	Variance ratio in the road slope estimation.
η_d	Drivetrain transmission efficiency.
η_f	Friction motor assembly transmission efficiency.
η_g	Gearbox transmission efficiency.
η_m	Global motor transmission efficiency.
θ_c	Crankset angle.
θ_e	Motor electrical angle.
θ_m	Motor mechanical angle.
Θ	Absolute temperature.
κ	Critical value of the probability distribution.
Λ_i	Index to quantify the curve aggressiveness. Subscript i : threshold value th .
μ	Rolling friction coefficient.
μ_f	Kinetic friction coefficient.
v_i	KF noise on the measurement. Subscript i indicates the quantity to which is referred.
$\tilde{\zeta}_i^j$	SPTO augmented state. Subscript i : continuous component 0, second harmonic component 2. Superscript j : cosine component c , sine component s .
ρ	Density of air.
τ_d	Drivetrain gear ratio.
τ_f	Friction motor assembly transmission ratio.
τ_g	Gearbox gear ratio.
τ_m	Global motor gear ratio.
φ	Bicycle leaning angle.
φ_s	IMU roll mounting offset.

χ	Generic measured value or observation.
ψ_s	IMU yaw mounting offset.
Ψ_i	Magnetic flux linkage. Subscript i : motor phase $\{a, b, c\}$, permanent magnet <i>PM</i> .
ω	Rear wheel angular speed.
ω_c	Crankset angular speed.
ω_{dq}	Rotor frame angular speed.
ω_e	Motor electrical angular speed.
ω_m	Motor mechanical angular speed.
ω_w	Rear cogwheel angular speed.
$\omega_{s_i}^j$	IMU measured angular speed. Subscript i : axis component $\{x, y, z\}$. Superscript j : sensor reference frame s , bicycle reference frame <i>no superscript</i> .
$\mathbf{0}$	Zero vector or matrix.

Operators:

c_i	Cosine of an angle. Subscript i indicates the angle.
$E[\cdot]$	Statistic expected value.
$f(\cdot)$	State space representation nonlinear continuous time state function.
$f_d(\cdot)$	State space representation nonlinear discrete time state function.
$G_i(s)$	LPF transfer function. Subscript i indicates the filtered quantity.
$h(\cdot)$	State space representation nonlinear continuous time output function.
$h_d(\cdot)$	State space representation nonlinear discrete time output function.
$\max(\cdot)$	Maximum value.
$\mathcal{R}_i(j)$	Rotation matrix. Subscript i indicates the reference axis. Subscript j indicates the rotation angle.
s_i	Sine of an angle. Subscript i indicates the angle.
$\text{sgn}(\cdot)$	Sign function.
$[\cdot]^T$	Transpose of a vector or matrix.
$[\cdot]^{-1}$	Inverse matrix.
σ_i	Standard deviation. Subscript i indicates the quantity to which is referred.
σ_i^2	Variance. Subscript i indicates the quantity to which is referred.

Bibliography

- [1] D. G. Wilson and T. Schmidt, *Bicycling Science, fourth edition*. MIT Press, May 2020. ISBN: 9780262538404.
- [2] O. Bolton, "Electrical bicycle," United States Patent 552271, Dec. 31, 1895.
- [3] C. Theryc, "Wheel with electrical motor-hub for vehicles," United States Patent 572036, Nov. 24, 1896.
- [4] J. Schnepf, "Automobile," United States Patent 627066, June 13, 1899.
- [5] E. Salmeron-Manzano and F. Manzano-Agugliaro, "The Electric Bicycle: Worldwide Research Trends," *Energies*, vol. 11, p. 1894, July 2018.
- [6] A. Biderman, C. Ratti, and C. Outram, "Hybrid sensor-enabled electric wheel and associated systems, multi-hub wheel spoking systems, and methods of manufacturing and installing wheel spokes," United States Patent 9027681, May 12, 2015.
- [7] C. Contò and N. Bianchi, "E-Bike Motor Drive: A Review of Configurations and Capabilities," *Energies*, vol. 16, p. 160, Dec. 2022.
- [8] J. E. Bourne, S. Sauchelli, R. Perry, A. Page, S. Leary, C. England, and A. R. Cooper, "Health benefits of electrically-assisted cycling: a systematic review," *International Journal of Behavioral Nutrition and Physical Activity*, vol. 15, p. 116, Dec. 2018.
- [9] A. R. Cooper, B. Tibbitts, C. England, D. Procter, A. Searle, S. J. Sebire, E. Ranger, and A. S. Page, "Potential of electric bicycles to improve the health of people with Type 2 diabetes: a feasibility study," *Diabetic Medicine*, vol. 35, pp. 1279–1282, Sept. 2018.
- [10] H. Mohammadi-Abdar, A. L. Ridgel, F. M. Discenzo, and K. A. Loparo, "Design and Development of a Smart Exercise Bike for Motor Rehabilitation in Individuals With Parkinson's Disease," *IEEE/ASME Transactions on Mechatronics*, vol. 21, pp. 1650–1658, June 2016.
- [11] A. Muetze and Y. Tan, "Electric bicycles - A performance evaluation," *IEEE Industry Applications Magazine*, vol. 13, pp. 12–21, July 2007.
- [12] Y. Ruan, C. Hang, Y. Wang, and R. Ma, "The role of government in an emerging Disruptive Innovation: The case of E-bike in China," in *2012 IEEE International Conference on Management of Innovation & Technology (ICMIT)*, (Bali, Indonesia), pp. 447–451, IEEE, June 2012.
- [13] "Regulation (EU) No 168/2013 of the European Parliament and of the Council of 15 January 2013 on the approval and market surveillance of two- or three-wheel vehicles and quadricycles (Text with EEA relevance)Text with EEA relevance." Jan. 15, 2013.

- [14] A. Bryson and D. Luenberger, "The synthesis of regulator logic using state-variable concepts," *Proceedings of the IEEE*, vol. 58, no. 11, pp. 1803–1811, 1970.
- [15] J. Meditch and G. Hostetter, "Observers for systems with unknown and inaccessible inputs," in *1973 IEEE Conference on Decision and Control including the 12th Symposium on Adaptive Processes*, (San Diego, CA, USA), pp. 120–124, IEEE, Dec. 1973.
- [16] C. Johnson, "Accommodation of external disturbances in linear regulator and servomechanism problems," *IEEE Transactions on Automatic Control*, vol. 16, pp. 635–644, Dec. 1971.
- [17] E. Sariyildiz, R. Oboe, and K. Ohnishi, "Disturbance Observer-Based Robust Control and Its Applications: 35th Anniversary Overview," *IEEE Transactions on Industrial Electronics*, vol. 67, pp. 2042–2053, Mar. 2020.
- [18] K. Ohishi, K. Ohnishi, and K. Miyachi, "Torque -speed regulation of DC motor based on load torque estimation method," *IPEC -Tokyo*, 1983.
- [19] M. Nakao, K. Ohnishi, and K. Miyachi, "A Robust decentralized joint control based on interference estimation," in *Proceedings. 1987 IEEE International Conference on Robotics and Automation*, vol. 4, (Raleigh, NC, USA), pp. 326–331, Institute of Electrical and Electronics Engineers, 1987.
- [20] K. Tamaki, K. Ohishi, K. Ohnishi, and K. Miyachi, "Microprocessor-based robust control of a DC servo motor," *IEEE Control Systems Magazine*, vol. 6, pp. 30–36, Oct. 1986.
- [21] E. Schrijver and J. van Dijk, "Disturbance Observers for Rigid Mechanical Systems: Equivalence, Stability, and Design," *Journal of Dynamic Systems, Measurement, and Control*, vol. 124, pp. 539–548, Dec. 2002.
- [22] A. Radke and Z. Gao, "A survey of state and disturbance observers for practitioners," in *2006 American Control Conference*, (Minneapolis, MN, USA), p. 6 pp., IEEE, 2006.
- [23] Y. Hori, "Disturbance suppression on an acceleration control type DC servo system," in *PESC '88 Record., 19th Annual IEEE Power Electronics Specialists Conference*, (Kyoto, Japan), pp. 222–229, IEEE, 1988.
- [24] T. Murakami, F. Yu, and K. Ohnishi, "Torque sensorless control in multidegree-of-freedom manipulator," *IEEE Transactions on Industrial Electronics*, vol. 40, pp. 259–265, Apr. 1993.
- [25] E. Sariyildiz and K. Ohnishi, "A comparison study for force sensor and reaction force observer based robust force control systems," in *2014 IEEE 23rd International Symposium on Industrial Electronics (ISIE)*, (Istanbul, Turkey), pp. 1156–1161, IEEE, June 2014.
- [26] S. Katsura and K. Ohnishi, "A wheelchair type mobile robot taking environmental disturbance into account," in *7th International Workshop on Advanced Motion Control. Proceedings (Cat. No.02TH8623)*, (Maribor, Slovenia), pp. 500–505, IEEE, 2002.

-
- [27] S. Katsura and K. Ohnishi, "Human interaction by a wheelchair," in *IEEE 2002 28th Annual Conference of the Industrial Electronics Society. IECON 02*, (Sevilla, Spain), pp. 2758–2763, IEEE, 2002.
- [28] H. Yabushita, Y. Hirata, K. Kosuge, and Z. Wang, "Environment-adaptive control algorithm of power assisted cycle," in *IECON'03. 29th Annual Conference of the IEEE Industrial Electronics Society (IEEE Cat. No.03CH37468)*, vol. 2, (Roanoke, VA, USA), pp. 1962–1967, IEEE, 2003.
- [29] X. Fan and M. Tomizuka, "Robust disturbance observer design for a power-assist electric bicycle," in *Proceedings of the 2010 American Control Conference*, (Baltimore, MD, USA), pp. 1166–1171, IEEE, June 2010.
- [30] M. Hosaka and T. Murakami, "Yaw rate control of electric vehicle using steer-by-wire system," in *The 8th IEEE International Workshop on Advanced Motion Control, 2004. AMC '04.*, (Kawasaki, Japan), pp. 31–34, IEEE, 2004.
- [31] Y. Tanaka and T. Murakami, "Self sustaining bicycle robot with steering controller," in *The 8th IEEE International Workshop on Advanced Motion Control, 2004. AMC '04.*, (Kawasaki, Japan), pp. 193–197, IEEE, 2004.
- [32] K. Iuchi, H. Niki, and T. Murakami, "Attitude control of bicycle motion by steering angle and variable COG control," in *31st Annual Conference of IEEE Industrial Electronics Society, 2005. IECON 2005*, (Raleigh, NC, USA), p. 6 pp., IEEE, 2005.
- [33] V. Sankaranarayanan and S. Ravichandran, "Torque sensorless control of a human-electric hybrid bicycle," in *2015 International Conference on Industrial Instrumentation and Control (ICIC)*, (Pune, India), pp. 806–810, IEEE, May 2015.
- [34] H. Kawajiri, S. Sakaino, H. Mizoguchi, and T. Tsuji, "Sensorless pedaling torque estimation by front and rear wheels independently driven power assist bicycle," in *2015 IEEE International Conference on Mechatronics (ICM)*, (Nagoya, Japan), pp. 364–369, IEEE, Mar. 2015.
- [35] T. Li, Q. Yang, X. Tu, and B. Ren, "An improved torque sensorless speed control method for electric assisted bicycle with consideration of coordinate conversion," *IEEE/CAA Journal of Automatica Sinica*, vol. 7, pp. 1575–1584, Nov. 2020.
- [36] D. S. Cheon and K. H. Nam, "Pedaling torque sensor-less power assist control of an electric bike via model-based impedance control," *International Journal of Automotive Technology*, vol. 18, pp. 327–333, Apr. 2017.
- [37] P. Padmagirisan, R. Sowmya, and V. Sankaranarayanan, "Power-assist control of a human–electric hybrid bicycle with energy regeneration and cruise control," *Proceedings of the Institution of Mechanical Engineers, Part I: Journal of Systems and Control Engineering*, vol. 233, pp. 179–191, Feb. 2019.
- [38] T. Li, Q. Yang, B. Ren, and X. Tu, "A Torque Sensor-less Speed Control Method of Electric Assisted Bicycle," in *37th Chinese Control Conference*, (Wuhan, China), 2018.

- [39] R. Mandriota, S. Fabbri, M. Nienhaus, and E. Grasso, "Sensorless Pedalling Torque Estimation Based on Motor Load Torque Observation for Electrically Assisted Bicycles," *Actuators*, vol. 10, p. 88, Apr. 2021.
- [40] B. J. Misgeld, L. Bergmann, B. Szilasi, S. Leonhardt, and D. Greven, "Virtual torque sensor for electrical bicycles," *IFAC-PapersOnLine*, vol. 53, no. 2, pp. 8903–8908, 2020.
- [41] T. Kurosawa, Y. Fujimoto, and T. Tokumaru, "Estimation of pedaling torque for electric power assisted bicycles," in *IECON 2014 - 40th Annual Conference of the IEEE Industrial Electronics Society*, (Dallas, TX, USA), pp. 2756–2761, IEEE, Oct. 2014.
- [42] N. Fukushima and Y. Fujimoto, "Estimation of pedaling torque for electric power-assisted bicycle on slope environment," in *2017 IEEE International Conference on Advanced Intelligent Mechatronics (AIM)*, (Munich, Germany), pp. 1682–1687, IEEE, July 2017.
- [43] T. Kurosawa and Y. Fujimoto, "Torque Sensorless Control for an Electric Power Assisted Bicycle with Instantaneous Pedaling Torque Estimation," *IEEJ Journal of Industry Applications*, vol. 6, no. 2, pp. 124–129, 2017.
- [44] N. Fukushima and Y. Fujimoto, "Experimental verification of torque sensorless control for electric power-assisted bicycles on sloped environment," in *2018 IEEE 15th International Workshop on Advanced Motion Control (AMC)*, (Tokyo, Japan), pp. 66–71, IEEE, Mar. 2018.
- [45] K. Hatada, K. Hirata, and T. Sato, "Energy-Efficient Power Assist Control with Periodic Disturbance Observer and Its Experimental Verification Using an Electric Bicycle," *SICE Journal of Control, Measurement, and System Integration*, vol. 10, pp. 410–417, Sept. 2017.
- [46] T. Narikiyo, K. Fuwa, and T. Murano, "Implementation of Disturbance Attenuation System Based on Frequency Estimation," *IFAC Proceedings Volumes*, vol. 41, no. 2, pp. 2702–2707, 2008.
- [47] V. Dimitrov, "Overview of the Ways to Design an Electric Bicycle," in *2018 IX National Conference with International Participation (ELECTRONICA)*, (Sofia, Bulgaria), pp. 1–4, IEEE, May 2018.
- [48] M. Corno, D. Berretta, and S. M. Savaresi, "Human machine interfacing issues in SeNZA, a Series Hybrid Electric Bicycle," in *2015 American Control Conference (ACC)*, (Chicago, IL, USA), pp. 1149–1154, IEEE, July 2015.
- [49] T. Lipowsky, J. Stegmaier, M. Lang, and P. Li, "Simulative potential assessment of regenerative braking with electric bicycles under consideration of realistic boundary conditions," in *2017 International Conference on Research and Education in Mechatronics (REM)*, (Wolfenbuettel, Germany), pp. 1–7, IEEE, Sept. 2017.
- [50] M. Guarisco, F. Gao, and D. Paire, "Autonomy and user experience enhancement control of an electrically assisted bicycle with dual-wheel drive," in *2015 IEEE Industry Applications Society Annual Meeting*, (Addison, TX, USA), pp. 1–8, IEEE, Oct. 2015.

-
- [51] W. C. Morchin and H. Oman, *Electric Bicycles: A Guide to Design and Use*. Electric Bicycle Manual, 2006. ISBN: 978-0-471-67419-1.
- [52] D. Xu, L. Wang, and J. Yang, "Research on Li-ion Battery Management System," in *2010 International Conference on Electrical and Control Engineering*, (Wuhan, China), pp. 4106–4109, IEEE, June 2010.
- [53] M. Bertoluzzo and G. Buja, "Development of Electric Propulsion Systems for Light Electric Vehicles," *IEEE Transactions on Industrial Informatics*, vol. 7, pp. 428–435, Aug. 2011.
- [54] T. Yalcinoz, "A Dynamic Model and Analysis of PEM Fuel Cells for an Electric Bicycle," in *2018 IEEE International Conference on Environment and Electrical Engineering and 2018 IEEE Industrial and Commercial Power Systems Europe (EEEIC / I&CPS Europe)*, (Palermo, Italy), pp. 1–5, IEEE, June 2018.
- [55] S.-C. Li, C.-Y. Gao, and F.-C. Wang, "Control and development of a PEMFC electric bicycle," in *2014 Proceedings of the SICE Annual Conference (SICE)*, (Sapporo, Japan), pp. 1017–1022, IEEE, Sept. 2014.
- [56] N. Hatwar, A. Bisen, H. Dodke, A. Junghare, and M. Khanapurkar, "Design approach for electric bikes using battery and super capacitor for performance improvement," in *16th International IEEE Conference on Intelligent Transportation Systems (ITSC 2013)*, (The Hague, Netherlands), pp. 1959–1964, IEEE, Oct. 2013.
- [57] K. Malan, M. Coutlakis, and J. Braid, "Design and development of a prototype super-capacitor powered electric bicycle," in *2014 IEEE International Energy Conference (ENERGYCON)*, (Cavtat, Croatia), pp. 1434–1439, IEEE, May 2014.
- [58] E. Starschich and A. Muetze, "Comparison of the Performances of Different Geared Brushless-DC Motor Drives for Electric Bicycles," in *2007 IEEE International Electric Machines & Drives Conference*, (Antalya, Turkey), pp. 140–147, IEEE, May 2007.
- [59] A. Adnan and D. Ishak, "Finite element modeling and analysis of external rotor brushless DC motor for electric bicycle," in *2009 IEEE Student Conference on Research and Development (SCOReD)*, (UPM Serdang, Malaysia), pp. 376–379, IEEE, 2009.
- [60] T. Chan, L.-T. Yan, and S.-Y. Fang, "In-wheel permanent-magnet brushless DC motor drive for an electric bicycle," *IEEE Transactions on Energy Conversion*, vol. 17, pp. 229–233, June 2002.
- [61] W. Chlebosz, G. Ombach, and J. Junak, "Comparison of permanent magnet brushless motor with outer and inner rotor used in e-bike," in *The XIX International Conference on Electrical Machines - ICEM 2010*, (Rome, Italy), pp. 1–5, IEEE, Sept. 2010.
- [62] Y. Honda, T. Nakamura, T. Higaki, and Y. Takeda, "Motor design considerations and test results of an interior permanent magnet synchronous motor for electric vehicles," in *IAS '97. Conference Record of the 1997 IEEE Industry Applications Conference Thirty-Second IAS Annual Meeting*, vol. 1, (New Orleans, LA, USA), pp. 75–82, IEEE, 1997.

- [63] K.-S. Kim, S.-H. Lee, H.-R. Cha, K.-S. Lee, and S.-J. Park, "Design and analysis of outer rotor type IPMSM for an electric bicycle," in *INEC 2009 - 31st International Telecommunications Energy Conference*, (Incheon, South Korea), pp. 1–4, IEEE, Oct. 2009.
- [64] A. Vagati, G. Pellegrino, and P. Guglielmi, "Comparison between SPM and IPM motor drives for EV application," in *The XIX International Conference on Electrical Machines - ICEM 2010*, (Rome, Italy), pp. 1–6, IEEE, Sept. 2010.
- [65] S. Kawano, H. Murakami, N. Nishiyama, Y. Ikkai, Y. Honda, and T. Higaki, "High Performance Design of an Interior Permanent Magnet Synchronous Reluctance Motor for Electric Vehicles," *Proceedings of Power Conversion Conference - PCC '97*, (Nagaoka, Japan), pp. 33-36, vol.1, 1997.
- [66] K. Fujii, H. Kumai, E. Ishii, S. Higaki, S. Yamaguchi, and H.-A. Zhao, "Researches on small capacity vehicles driven by induction machine," in *6th International Workshop on Advanced Motion Control Proceedings*, (Nagoya, Japan), pp. 465–468, IEEE, 2000.
- [67] H. Chen, "The switched reluctance motor drive for application in electric bicycle," in *ISIE 2001. 2001 IEEE International Symposium on Industrial Electronics Proceedings (Cat. No.01TH8570)*, vol. 2, (Pusan, South Korea), pp. 1152–1156, IEEE, 2001.
- [68] J. Lin, N. Schofield, and A. Emadi, "External-rotor 6-10 switched reluctance motor for an electric bicycle," in *IECON 2013 - 39th Annual Conference of the IEEE Industrial Electronics Society*, (Vienna, Austria), pp. 2839–2844, IEEE, Nov. 2013.
- [69] R. A. Inte and F. N. Jurca, "A novel synchronous reluctance motor with outer rotor for an electric bike," in *2016 International Conference and Exposition on Electrical and Power Engineering (EPE)*, (Iasi, Romania), pp. 213–218, IEEE, Oct. 2016.
- [70] F. N. Jurca, R. Mircea, C. Martis, R. Martis, and P. P. Florin, "Synchronous reluctance motors for small electric traction vehicle," in *2014 International Conference and Exposition on Electrical and Power Engineering (EPE)*, (Iasi, Romania), pp. 317–321, IEEE, Oct. 2014.
- [71] P. Acarnley and J. Watson, "Review of position-sensorless operation of brushless permanent-magnet machines," *IEEE Transactions on Industrial Electronics*, vol. 53, pp. 352–362, Apr. 2006.
- [72] Sensitivus, "Sensitivus Gauge SG2Q Torque/Cadence Sensor Technology Datasheet.," SM10635-9 SG2Q datasheet, July 2022.
- [73] "ERider ERS Sensors." Available:<https://www.erider.com//sensors>. [Accessed June 17, 2024].
- [74] S. Duc, V. Villerius, W. Bertucci, and F. Grappe, "Validity and Reproducibility of the Ergomo®Pro Power Meter Compared With the SRM and Powertap Power Meters," *International Journal of Sports Physiology and Performance*, vol. 2, pp. 270–281, Sept. 2007.

-
- [75] Thun, “Datasheet Thun X-Cell RT 3.0. Magnetoelastic bottom bracket torque and cadence sensor.” X-Cell RT 3.0 datasheet, July 2019.
- [76] P. Spagnol, M. Corno, and S. M. Savaresi, “Pedaling torque reconstruction for half pedaling sensor,” in *2013 European Control Conference (ECC)*, (Zurich), pp. 275–280, IEEE, July 2013.
- [77] TDCM, “TDCM BB Torque Sensor Installation & 66 Operation Guide,” TDCM BB torque sensor datasheet, 2016.
- [78] “Electrical bike foot pedaling moment detection method,” China Patent 101539466A, Sept. 23, 2009.
- [79] “Chain type torque sensor for electric bicycle,” China Patent 2700157Y, May 18, 2005.
- [80] G. Roovers and B. D’Herripon, “Method and device for measuring the chain force in a bicycle,” United States Patent 0120211, May 14, 2009.
- [81] C. Abagnale, M. Cardone, P. Iodice, S. Strano, M. Terzo, and G. Vorraro, “Theoretical and Experimental Evaluation of a Chain Strength Measurement System for Pedelecs,” *Engineering Letters*. vol. 22. pp. 102-108. 2014.
- [82] BionX, “BionX conversion kit User Manual.” BionX user manual, 2016.
- [83] Forehorse, “Forehorse FEP1 Datasheet.” Forehorse FEP1 datasheet. Available: <https://www.forehorse.com/Products>. [Accessed March 6, 2023].
- [84] J.-H. Lee, J.-S. Choi, D.-W. Kang, J.-W. Seo, J.-Y. Kim, D.-H. Kim, S.-T. Yang, and G.-R. Tack, “Development of a System for Measuring the Three-Axis Pedal Force in Cycling and Its Applications,” *World Academy of Science, Engineering and Technology, International Journal of Mechanical, Aerospace, Industrial, Mechatronic and Manufacturing Engineering* vol. 9, pp. 235-238, 2015.
- [85] M. Hull and R. Davis, “Measurement of pedal loading in bicycling: I. Instrumentation,” *Journal of Biomechanics*, vol. 14, pp. 843–855, Jan. 1981.
- [86] G. Álvarez and J. Vinyolas, “A New Bicycle Pedal Design for On-Road Measurements of Cycling Forces,” *Journal of Applied Biomechanics*, vol. 12, pp. 130–142, Feb. 1996.
- [87] A. V. Pigatto, K. O. Moura, G. W. Favieiro, and A. Balbinot, “A new crank arm based load cell, with built-in conditioning circuit and strain gages, to measure the components of the force applied by a cyclist,” in *2016 38th Annual International Conference of the IEEE Engineering in Medicine and Biology Society (EMBC)*, (Orlando, FL, USA), pp. 1983–1986, IEEE, Aug. 2016.
- [88] E. Martín-Sosa, V. Chaves, I. Alvarado, J. Mayo, and J. Ojeda, “Design and Validation of a Device Attached to a Conventional Bicycle to Measure the Three-Dimensional Forces Applied to a Pedal,” *Sensors*, vol. 21, p. 4590, July 2021.
- [89] A. Balbinot, C. Milani, and J. Nascimento, “A New Crank Arm-Based Load Cell for the 3D Analysis of the Force Applied by a Cyclist,” *Sensors*, vol. 14, pp. 22921–22939, Dec. 2014.

- [90] L. Stilo, H. Lugo, D. S. Velandia, P. P. Conway, and A. A. West, "Personalised Controller Strategies for Next Generation Intelligent Adaptive Electric Bicycles," *IEEE Transactions on Intelligent Transportation Systems*, vol. 22, pp. 7814–7825, Dec. 2021.
- [91] S. Mammari, N. A. Oufroukh, and S. Glaser, "Reducing rider effort for electric bicycles by environment disturbance compensation," in *2011 IEEE International Conference on Control Applications (CCA)*, (Denver, CO, USA), pp. 550–555, IEEE, Sept. 2011.
- [92] Z. Kai and Y. Dejun, "A control approach adaptive to load and road slope for electric power assisted bicycle," in *2017 36th Chinese Control Conference (CCC)*, (Dalian, China), pp. 3414–3418, IEEE, July 2017.
- [93] B. Zaghari, A. Stuijck, A. S. Weddell, and S. Beeby, "Efficient Energy Conversion in Electrically Assisted Bicycles Using a Switched Reluctance Machine Under Torque Control," *IEEE Access*, vol. 8, pp. 202401–202411, 2020.
- [94] C. Abagnale, M. Cardone, P. Iodice, S. Strano, M. Terzo, and G. Vorraro, "Model-based Control for an Innovative Power-assisted Bicycle," *Energy Procedia*, vol. 81, pp. 606–617, Dec. 2015.
- [95] M. Cardone, S. Strano, and M. Terzo, "Optimal power-assistance system for a new pedelec model," *Proceedings of the Institution of Mechanical Engineers, Part C: Journal of Mechanical Engineering Science*, vol. 230, pp. 3012–3025, Oct. 2016.
- [96] Z. HaoBin, L. Bo, and C. BingGang, "H Infinity Robust Controller for Electric Bicycles," in *2008 Workshop on Power Electronics and Intelligent Transportation System*, (Guangzhou, China), pp. 131–135, IEEE, Aug. 2008.
- [97] P.-C. Chen, C.-C. Hsiao, S.-L. Wu, and S.-B. Chang, "The Torque Control with Multi-Objective Performance for E-Bike Systems with Human Power Assistance," *WSEAS Transaction on Systems and Control*, vol. 6, no. 10, 2011.
- [98] P.-H. Chen, "Application of fuzzy intelligence to Elebike control design," in *Proceedings of 6th International Fuzzy Systems Conference*, vol. 1, (Barcelona, Spain), pp. 199–206, IEEE, 1997.
- [99] S. Indulal and P. Nair, "A novel approach in automatic control of a hybrid bicycle," in *IET-UK International Conference on Information and Communication Technology in Electrical Sciences (ICTES 2007)*, (Tamil Nadu, India), pp. 296–301, IEE, 2007.
- [100] P.-H. Chen, "Intelligence application: Elebike fuzzy control part I," in *2008 International Conference on Machine Learning and Cybernetics*, (Kunming, China), pp. 3581–3585, IEEE, July 2008.
- [101] J.-S. Lee and J.-W. Jiang, "Enhanced fuzzy-logic-based power-assisted control with user-adaptive systems for human-electric bikes," *IET Intelligent Transport Systems*, vol. 13, no. 10, pp. 1492–1498, 2019.
- [102] O. Uyar, M. Çunkaş, and H. Karaca, "Enhanced intelligent control with adaptive system for electrically assisted bicycle," *Engineering Science and Technology, an International Journal*, vol. 30, p. 101047, June 2022.

-
- [103] K. Hatada and K. Hirata, "Energy-efficient power assisting methods for periodic motions and its experimental verification," in *2012 IEEE International Conference on Industrial Technology*, (Athens, Greece), pp. 858–863, IEEE, Mar. 2012.
- [104] R. Hatano, D. Namikawa, R. Minagawa, and M. Iwase, "Experimental verification of effectiveness on driving force assist control based on repetitive control for electrically-assisted bicycles," in *2014 IEEE 13th International Workshop on Advanced Motion Control (AMC)*, (Yokohama, Japan), pp. 237–241, IEEE, Mar. 2014.
- [105] K. Hatada and K. Hirata, "Power assisting control for electric bicycles using an adaptive filter," in *2014 IEEE International Conference on Industrial Technology (ICIT)*, (Busan, South Korea), pp. 51–54, IEEE, Feb. 2014.
- [106] T. Nagata, S. Okada, and M. Makikawa, "Electric motor assisted bicycle as an aerobic exercise machine," in *2012 Annual International Conference of the IEEE Engineering in Medicine and Biology Society*, (San Diego, CA, USA), pp. 1933–1935, IEEE, Aug. 2012.
- [107] S. Sweeney, R. Ordonez-Hurtado, F. Pilla, G. Russo, D. Timoney, and R. Shorten, "A Context-Aware E-Bike System to Reduce Pollution Inhalation While Cycling," *IEEE Transactions on Intelligent Transportation Systems*, vol. 20, pp. 704–715, Feb. 2019.
- [108] S. Mohammad, T. M. Guerra, J. M. Grobois, and B. Hecquet, "Heart rate control during cycling exercise using Takagi-Sugeno models," *IFAC Proceedings Volumes*, vol. 44, pp. 12783–12788, Jan. 2011.
- [109] M. Corno, P. Giani, M. Tanelli, and S. M. Savaresi, "Human-in-the-Loop Bicycle Control via Active Heart Rate Regulation," *IEEE Transactions on Control Systems Technology*, vol. 23, pp. 1029–1040, May 2015.
- [110] R. C. Hsu, C.-T. Liu, W.-M. Lee, and C.-H. Chen, "A Reinforcement Learning Based Power Assisted Method with Comfort of Riding for Light Electric Vehicle," in *2010 IEEE 71st Vehicular Technology Conference*, (Taipei, Taiwan), pp. 1–5, IEEE, 2010.
- [111] R. C. Hsu, C.-T. Liu, and D.-Y. Chan, "A Reinforcement-Learning-Based Assisted Power Management With QoR Provisioning for Human–Electric Hybrid Bicycle," *IEEE Transactions on Industrial Electronics*, vol. 59, pp. 3350–3359, Aug. 2012.
- [112] M. Corno, D. Berretta, P. Spagnol, and S. M. Savaresi, "Design, Control, and Validation of a Charge-Sustaining Parallel Hybrid Bicycle," *IEEE Transactions on Control Systems Technology*, vol. 24, pp. 817–829, May 2016.
- [113] A. Dardanelli, M. Tanelli, and S. Savaresi, "An active energy management system for light two-wheeled electric vehicles," *IFAC Proceedings Volumes*, vol. 46, no. 21, pp. 213–218, 2013.
- [114] M. Giliberto, F. Arena, and G. Pau, "A fuzzy-based Solution for Optimized Management of Energy Consumption in e-bikes," *Journal of Wireless Mobile Networks, Ubiquitous Computing, and Dependable Applications*, vol. 10, pp. 45–64, Sept. 2019.

- [115] I. Tal, B. Ciobotaru, and G.-M. Muntean, "Vehicular-Communications-Based Speed Advisory System for Electric Bicycles," *IEEE Transactions on Vehicular Technology*, vol. 65, pp. 4129–4143, June 2016.
- [116] K. Aström and A. Lennartsson, "Bicycle dynamics and control: adapted bicycles for education and research," *IEEE Control Systems*, vol. 25, pp. 26–47, Aug. 2005.
- [117] S. Capmal and H. Vandewalle, "Torque-velocity relationship during cycle ergometer sprints with and without toe clips," *European Journal of Applied Physiology*, vol. 76, pp. 375–379, Sept. 1997.
- [118] W. Bertucci, F. Grappe, A. Girard, A. Betik, and J. D. Rouillon, "Effects on the crank torque profile when changing pedalling cadence in level ground and uphill road cycling," *Journal of Biomechanics*, vol. 38, pp. 1003–1010, May 2005.
- [119] D. Too and C. D. Williams, "Determination of the optimal crank arm length to maximize peak power production in an upright cycling position," 2018.
- [120] R. Krishnan, *Permanent Magnet Synchronous and Brushless DC Motor Drives*. CRC Press, Dec. 2017. ISBN: 9781315221489.
- [121] F. Pradko, R. Lee, and V. Kaluza, "Theory of human vibration response," *U.S. Army Tank-Automotive center.*, (Warren, MI, USA), 1966.
- [122] D. Luenberger, "Observers for multivariable systems," *IEEE Transactions on Automatic Control*, vol. 11, pp. 190–197, Apr. 1966.
- [123] D. Simon, *Optimal State Estimation: Kalman, H infinity, and Nonlinear Approaches*. Wiley, Jan. 2006. ISBN: 9780471708582.
- [124] X. Wang, P. Cui, and H. Cui, "Local observability of nonlinear systems based on linearization," in *2008 2nd International Symposium on Systems and Control in Aerospace and Astronautics*, (Shenzhen, China), pp. 1–4, IEEE, Dec. 2008.
- [125] J. C. Gerdes and H. S. Bae, "Parameter Estimation and Command Modification for Longitudinal Control of Heavy Vehicles," *Institute of Transportation Studies, UC Berkeley, Research Reports, Working Papers, Proceedings*, Apr. 2003.
- [126] M. Witczak, V. Puig, D. Rotondo, and P. Witczak, "A necessary and sufficient condition for total observability of discrete-time linear time-varying systems," *IFAC-PapersOnLine*, vol. 50, pp. 729–734, July 2017.
- [127] M. S. Rafiq and J.-W. Jung, "A Comprehensive Review of State-of-the-Art Parameter Estimation Techniques for Permanent Magnet Synchronous Motors in Wide Speed Range," *IEEE Transactions on Industrial Informatics*, vol. 16, pp. 4747–4758, July 2020.
- [128] H. S. Bae, J. Ryu, and J. C. Gerdes, "Road Grade and Vehicle Parameter Estimation for Longitudinal Control Using GPS," *IEEE Conference on Intelligent Transportation Systems*, 2001.

-
- [129] P. Sahlholm and K. H. Johansson, "Road Grade Estimation for Look-Ahead Vehicle Control," *IFAC Proceedings Volumes*, vol. 41, no. 2, pp. 3380–3385, 2008.
- [130] K. Jo, J. Kim, and M. Sunwoo, "Real-Time Road-Slope Estimation Based on Integration of Onboard Sensors With GPS Using an IMM-PDA Filter," *IEEE Transactions on Intelligent Transportation Systems*, vol. 14, pp. 1718–1732, Dec. 2013.
- [131] A. Vahidi, A. Stefanopoulou, and H. Peng, "Experiments for Online Estimation of Heavy Vehicle's Mass and Time-Varying Road Grade," in *Dynamic Systems and Control, Volumes 1 and 2*, (Washington, DC, USA), pp. 451–458, ASME/EDC, Jan. 2003.
- [132] A. Vahidi, A. Stefanopoulou, and H. Peng, "Recursive least squares with forgetting for online estimation of vehicle mass and road grade: theory and experiments," *Vehicle System Dynamics*, vol. 43, pp. 31–55, Jan. 2005.
- [133] M. Zhao, F. Yang, D. Sun, W. Han, F. Xie, and T. Chen, "A joint dynamic estimation algorithm of vehicle mass and road slope considering braking and turning," in *2018 Chinese Control And Decision Conference (CCDC)*, (Shenyang), pp. 5868–5873, IEEE, June 2018.
- [134] M. N. Mahyuddin, J. Na, G. Herrmann, X. Ren, and P. Barber, "Adaptive Observer-Based Parameter Estimation With Application to Road Gradient and Vehicle Mass Estimation," *IEEE Transactions on Industrial Electronics*, vol. 61, pp. 2851–2863, June 2014.
- [135] V. Winstead and I. V. Kolmanovskiy, "Estimation of road grade and vehicle mass via model predictive control," in *Proceedings of 2005 IEEE Conference on Control Applications, 2005. CCA 2005.*, (Toronto, Canada), pp. 1588–1593, IEEE, 2005.
- [136] I. Boniolo, S. Corbetta, and S. M. Savaresi, "Attitude estimation of a motorcycle in a Kalman filtering framework," *IFAC Proceedings Volumes*, vol. 43, pp. 779–784, July 2010.
- [137] M. Corno, P. Spagnol, and S. M. Savaresi, "Road Slope Estimation in Bicycles without Torque Measurements," *IFAC Proceedings Volumes*, vol. 47, no. 3, pp. 6295–6300, 2014.
- [138] C.-F. Huang, B.-H. Dai, and T.-J. Yeh, "Observer-based sensor fusion for power-assist electric bicycles," in *2016 American Control Conference (ACC)*, (Boston, MA, USA), pp. 5486–5491, IEEE, July 2016.
- [139] J. Jauch, J. Masino, T. Staiger, and F. Gauterin, "Road Grade Estimation With Vehicle-Based Inertial Measurement Unit and Orientation Filter," *IEEE Sensors Journal*, vol. 18, pp. 781–789, Jan. 2018.
- [140] X. Meng, K. Pang, B. Di, W. Li, Y. Wang, J. Zhang, and Y. Xu, "Road grade estimation for vehicle emissions modeling using electronic atmospheric pressure sensors," *Frontiers in Environmental Science*, Jan. 2023.

- [141] B. Feng, G. Yin, Y. Ren, T. Shen, and F. Wang, "A Joint Vehicle Mass and Road Slope Estimation of Distributed Drive Electric Vehicles Considering Road Environment Factors," in *2022 IEEE 25th International Conference on Intelligent Transportation Systems (ITSC)*, (Macau, China), pp. 817–824, IEEE, Oct. 2022.
- [142] T. Chai and R. R. Draxler, "Root mean square error (RMSE) or mean absolute error (MAE)? – Arguments against avoiding RMSE in the literature," *Geoscientific Model Development*, vol. 7, pp. 1247–1250, June 2014.
- [143] Crystalyte Europe, "Crystalyte Europe HS3540 Technical details." Available: <http://shop.crystalyte-europe.com/product.php?productid=16447cat=295page=1>. [Accessed: June 17, 2024].
- [144] V. Bobek, Freescale Semiconductor, "PMSM Electrical Parameters Measurement," Tech. Rep. AN4680, Feb. 2013.
- [145] M. Corno, D. Berretta, and S. M. Savaresi, "An IMU-Driven Rider-on-Saddle Detection System for Electric-Power-Assisted Bicycles," *IEEE Transactions on Intelligent Transportation Systems*, vol. 17, pp. 3184–3193, Nov. 2016.
- [146] M. Corno and S. M. Savaresi, "Design and Control of an All-in-the-Wheel Assisted Kick Scooter," *IEEE/ASME Transactions on Mechatronics*, vol. 21, pp. 1858–1867, Aug. 2016.
- [147] G. Rallo, S. Formentin, M. Corno, and S. M. Savaresi, "Real-time pedaling rate estimation via wheel speed filtering," *IFAC-PapersOnLine*, vol. 50, pp. 6010–6015, July 2017.
- [148] G. Rallo, S. Formentin, M. Corno, and S. M. Savaresi, "Real-time cycling cadence estimation via wheel speed measurement," *International Journal of Adaptive Control and Signal Processing*, vol. 32, pp. 1052–1066, July 2018.
- [149] L. Bascetta, G. Magnani, and P. Rocco, "Velocity Estimation: Assessing the Performance of Non-Model-Based Techniques," *IEEE Transactions on Control Systems Technology*, vol. 17, pp. 424–433, Mar. 2009.
- [150] P. Belanger, "Estimation of angular velocity and acceleration from shaft encoder measurements," in *Proceedings 1992 IEEE International Conference on Robotics and Automation*, (Nice, France), pp. 585–592, IEEE Comput. Soc. Press, 1992.
- [151] L. Ben-Brahim and S. Tadakuma, "Speed control of induction motor without rotational transducers," in *Conference Record of 1998 IEEE Industry Applications Conference. Thirty-Third IAS Annual Meeting (Cat. No.98CH36242)*, vol. 1, (St. Louis, MO, USA), pp. 625–632, IEEE, 1998.
- [152] E. Levi and M. Wang, "A speed estimator for high performance sensorless control of induction motors in the field weakening region," *IEEE Transactions on Power Electronics*, vol. 17, pp. 365–378, May 2002.

- [153] F. Janabi-Sharifi, V. Hayward, and C.-S. Chen, "Discrete-time adaptive windowing for velocity estimation," *IEEE Transactions on Control Systems Technology*, vol. 8, pp. 1003–1009, Nov. 2000.
- [154] R. Kavanagh, "Performance analysis and compensation of M/T-type digital tachometers," *IEEE Transactions on Instrumentation and Measurement*, vol. 50, pp. 965–970, Aug. 2001.
- [155] Y. Su, C. Zheng, D. Sun, and B. Duan, "A Simple Nonlinear Velocity Estimator for High-Performance Motion Control," *IEEE Transactions on Industrial Electronics*, vol. 52, pp. 1161–1169, Aug. 2005.
- [156] F. Giulii Capponi, G. De Donato, L. Del Ferraro, O. Honorati, M. Harke, and R. Lorenz, "AC brushless drive with low-resolution Hall-effect sensors for surface-mounted PM Machines," *IEEE Transactions on Industry Applications*, vol. 42, pp. 526–535, Mar. 2006.
- [157] J. Gu, M. Ouyang, J. Li, D. Lu, C. Fang, and Y. Ma, "Driving and braking control of PM synchronous motor based on low-resolution hall sensor for battery electric vehicle," *Chinese Journal of Mechanical Engineering*, vol. 26, pp. 1–10, Jan. 2013.
- [158] S. Fabbri, K. Schuhmacher, M. Nienhaus and E. Grasso, "Combination of two different sensorless techniques for complete speed range sensorless drive and control of small sized PMSMs," *IKMT 2019 - Innovative small Drives and Micro-Motor Systems; 12. ETG/GMM-Symposium*, (Wuerzburg, Germany), pp. 1-6, 2019.
- [159] A. Vitali, ST Microelectronics, "ST-Microelectronics Design Tip DT0053: 6-point tumble sensor calibration.," Design Tip DT0053, Nov. 25, 2015.
- [160] I. Frosio, F. Pedersini, and N. Borghese, "Autocalibration of MEMS Accelerometers," *IEEE Transactions on Instrumentation and Measurement*, vol. 58, pp. 2034–2041, June 2009.
- [161] RLS, "LM10 Incremental Magnetic Encoder," LM10 datasheet, April 20, 2023.